Development of 3D leaf shape:
Utricularia gibba as a model system

Claire Bushell

Thesis submitted for the Degree of Doctor of Philosophy

University of East Anglia
John Innes Centre

Submitted September 2016

Abstract

The development of diverse organ shapes involves genetically specified growth patterns which may differ across a tissue in rate and/ or orientation. Understanding specified growth is not intuitive since observed (resultant) growth rates and orientations are the result of specified growth combined with the effects of mechanical constraints in a connected tissue. Growth dynamics in leaves of *Arabidopsis* have previously been studied experimentally and modelled using a polarity field to orient growth, and regional factors which control local specified growth rates parallel and perpendicular to the polarity. It is unclear whether the mechanisms invoked for the development of 2D leaf shape can be applied to more complex 3D leaf shapes. In this work, I developed *Utricularia gibba* as a new model system and studied the development of *U. gibba* 3D epiascidiate (cup-shaped) leaves (known as bladders). I investigated bladder shape changes through development and modelled these transitions using isotropic (equal in all directions) or anisotropic (preferentially in one orientation) specified growth, showing that specified anisotropy is required to generate the full mature bladder shape. The shape of the main body of the bladder could be accounted for by both specified isotropic or anisotropic models. I tested predictions on growth dynamics and polarity made by each model using sector analysis and by investigating markers of tissue cell polarity in bladders. Sector analysis supported an anisotropic specified growth model, while quadrifid gland and UgPIN1 analysis provided evidence of a polarity field in *U. gibba*. Together, these observations suggest a common underlying mechanism for the generation of 3D and 2D leaves. This work shows how computational modelling can be combined with experimentation in a biological system to allow for a better understanding of the specified growth patterns underlying the generation of an organ shape.

Acknowledgements

I would like to give a big thank you to all members of the Coen lab for their support and friendship, and for the many journeys we shared together. My PhD would not have been as special without you all and I couldn't have hoped for a better group of people to spend the past four years with.

Thank you to my supervisor, Rico who taught me the importance of storytelling and always encouraged me to think about the bigger picture. Also, for encouraging me to travel to conferences and for breaking down the barriers between art and science. His way of thinking will be imprinted on me for a very long time.

Thank you to my examiners, Andrew Hudson and Kirsten Bomblies for carefully reading my thesis and for an enjoyable viva.

Thank you to Kay Yeoman who hosted me for a diverse and enriching three-month internship during my PhD and who has been an inspiration to me since my undergraduate degree.

Thank you to my friends outside of the lab for all the fun adventures we have had over the past four years - they really kept me going! Special thanks to Tim Hicks, Helen Duffield, Steve Rudder, Gemma Neale, and Rachel Jones.

A big thank you to my Mum, Heather Bushell and Grandmother, Joan Warwick for their support and encouragement throughout my studies. I wouldn't have got this far without the freedom and inspiration they have given me.

Finally, I would like to give a massive thank you to my partner Robert Green for all the love and support he has given me. He made my home life wonderful and was always there for me with encouraging words when I needed them.

"What is that feeling when you're driving away from people and they recede on the plain till you see their specks dispersing? –it's the too-huge world vaulting us, and it's good-bye. But we lean forward to the next crazy venture beneath the skies."

Jack Kerouac, On the Road

Contents

List of figures

1   General introduction

The diversity of organ shape is astounding: from flat outgrowths such as the wing discs of insects and flat leaves of plants, to complex 3D organs such as the heart or lung, carnivorous plant leaves, specialised flowers, and fruits. Understanding the processes behind the development of such diversity of forms presents one of the major questions in developmental biology and much work has been conducted to try to understand the principles and genetic interactions underlying morphogenesis (the generation of a particular shape). One of the main challenges associated with understanding the development of form is that patterns of growth are usually not intuitive. This is because the growth dynamics that we observe in a tissue can differ to those specified by the activity of genes due to the effect of tissue connectivity.

We can explore growth hypotheses taking into account specified growth patterns and tissue connectivity using computer modelling. In the Growing Polarised Tissue Framework (GPT framework), a canvas represents a continuous sheet of growing tissue and differential growth rates can be specified (Green *et al.*, 2010; Kennaway *et al.*, 2011). Circular clones can be added that deform with the canvas as it grows, enabling different patterns of resultant growth (growth that occurs as a result of specified growth dynamics and the effect of tissue connectivity) on the final shape to be explored. In the example below, the circle has grown to become a lobed shape and some clones are elongated (Figure 1.1, A-B). We might assume, that programmed (or specified) growth was directional (anisotropic) such that growth rate oriented parallel with the elongation of the clones was highest. However, specified growth in this model was isotropic (equal in all directions) across the canvas. The lobed shape was generated by a higher areal growth rate at the sides of the canvas (Figure 1.1, C, red regions). Elongation of the clones near the middle is as a result of the constraints of the growing tissue which is mechanically connected. The two sides are unable to grow as fast as they would if they were free and unconnected, since the middle stripe is growing more slowly (Figure 1.1, C, blue), restricting their growth. This causes clones in side regions to elongate perpendicular with the central stripe of slower growth (Figure 1.1, B). This example illustrates how patterns of growth in 2D can be non-intuitive and how it is useful to distinguish between specified growth (growth which would occur if each region of tissue was disconnected from its neighbour) and resultant growth (emerging

growth that includes effects of tissue connectivity). The problem associated with trying to understand specified growth by observing resultant growth becomes amplified when we consider the development of 3D structures where there are no free edges and the role of tissue connectivity plays an even greater role.
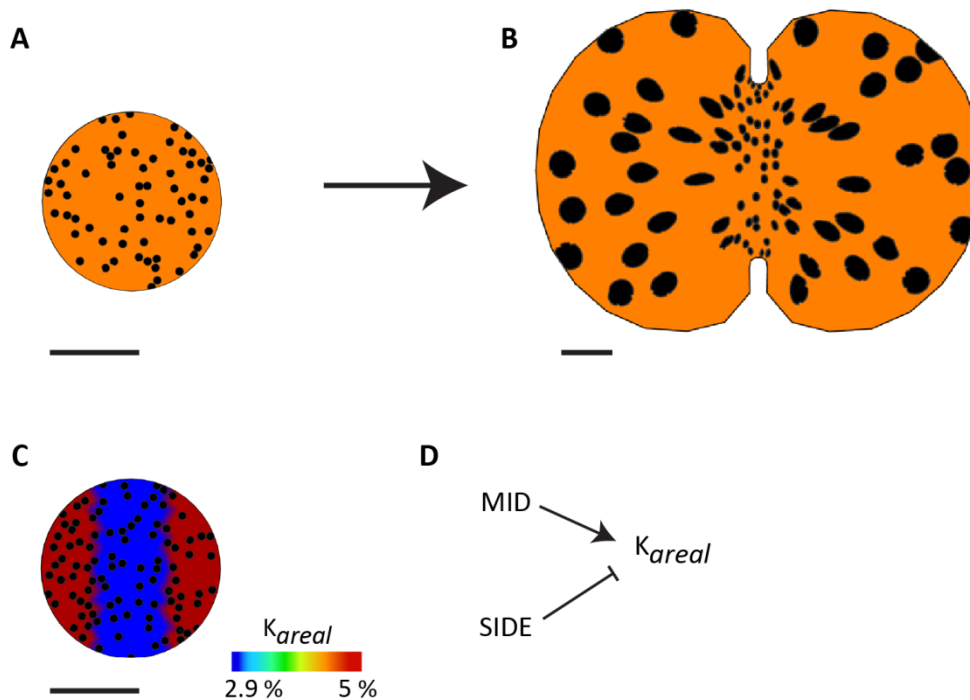
Figure 1.1: Resultant growth patterns can be non-intuitive. (A) Initial shape - a 2D circular canvas with circular clones marked which deform with the canvas as it grows. (B) End shape generated from (A) after growth. Black clones have deformed and are now elliptical near the middle regions of the canvas. (C) Specified areal growth rate mapped on the circular start shape where the factor MID (in the blue region) inhibits isotropic growth, and SIDE (in the red region) promotes isotropic growth. (D) Growth regulatory network (KRN) for the model where areal isotropic growth rate is promoted by MID and inhibited by SIDE. Models were generated using the GPT framework (Kennaway *et al.*, 2011).

Plants are a particularly good system in which to study the development of complex forms since, unlike animals, plant cells are held in place by rigid cell walls and therefore cells in growing plant tissue do not slide relative to each other during development. This provides us with a simplified system for studying the genetic control of shape where morphogenesis

can be described in terms of differential growth rates and orientations without the need to take cell movements and rearrangements into account (Green *et al.*, 2010).

1.1 Plant growth and morphogenesis

Specified growth can be described by two main parameters: the growth rate (rate of expansion), and the growth anisotropy (the extent to which growth is biased in a particular orientation). These can be explored at a discrete, cellular level or at a continuous, tissue level.

1.1.1 Plant growth at the cellular level

At the cellular level, specified growth is driven by cell expansion. The major driving force of cell expansion is internal turgor pressure (Lockhart, 1965). Turgor pressure can be ten times the atmospheric pressure, generating high stresses in the cell walls (Boudaoud, 2010). Elastic expansion in the cell wall occurs in response to turgor pressure and this becomes irreversible (plastic) by cell wall re-modelling which controls growth rate (Lockhart, 1965; Cosgrove, 2005). Cell wall synthesis and remodelling allow cells to increase in size and change shape in response to turgor pressure which acts isotropically, leading to isotropic expansion of cells with even mechanical properties, or anisotropic expansion of cells with uneven mechanical properties. In plants, control of cell growth occurs through modifications of cell wall extensibility (Mirabet *et al.*, 2011). Properties of the cell wall may be modified through the activity of enzymes such as expansins which loosen the cell wall (Cosgrove *et al.*, 2002; McQueen-Mason *et al.*, 1992), or pectin methylesterases (PMEs) which alter the rigidity of the cell wall (Bosch *et al.*, 2005). One important property of the cell wall is cellulose reinforcement. Cellulose is laid down in microfibril layers by cellulose synthase enzymes which are associated with microtubule arrays in the cell. Cellulose stiffens the cell wall, enabling it to resist stress generated by the turgor pressure of the cell (Lockhart, 1965; Heath, 1974; Baskin, 2001). Cellulose deposition has been shown to restrict wall expansion in the direction of the microfibrils. Anisotropy of cell wall properties can therefore determine the orientation of cell growth, for example perpendicular to the walls with the most cellulose reinforcement (Williamson, 1990). In this way, cell wall stiffness and turgor pressure determine the extent and orientation of cell growth.

1.1.2 Plant growth at the tissue level

Plant cells are connected via the cell wall matrix to form plant tissue. This means that cells are not free to expand independently, but are mechanically constrained by neighbouring cells. At the tissue level, growth of complex shapes can involve differential growth along axes (anisotropic growth). Anisotropic growth requires rates and orientations. Since the growing tissue is mechanically connected, differential growth rates and orientations of growth across a tissue can cause conflict between neighbouring regions, reviewed by Coen & Rebocho (2016 in press). This conflict generates stresses in the cell wall matrix which results in tissue deformations such as buckling and therefore changes in shape. Some aspects of this deformation in shape is a resultant property of growth and was not specified (Kennaway *et al.*, 2011). This interaction between specified growth rates and orientations, and the resolution of tissue conflict has been explored using computational modelling (Green *et al.*, 2010; Kennaway *et al.*, 2011; Kuchen *et al.*, 2012; Richardson *et al.*, 2016; Sauret-Güeto *et al.*, 2013). Through this modelling, growth hypotheses can be generated and tested in a cycle of modelling and biological experiments. This has been useful for exploring the major components underlying the generation of certain organ shapes and has been reviewed in Coen & Rebocho (2016 in press). Such work has found that growth across a tissue is rarely uniform, instead differing in rate and orientation across a growing tissue. For example, in the *Arabidopsis* leaf, growth rates decrease towards the distal tip and are higher in lateral domains compared to medial domains. Anisotropic growth was also found to vary during leaf development: growth is biased along the proximal-distal axis of the primordium at early stages, and it is biased along the mediolateral axis of the lamina at later stages (Kuchen *et al.*, 2012).

1.1.3 Control of growth rate

As discussed above, growth rates in a developing plant tissue are controlled by turgor pressure and resistance of the cell wall. The balance between these factors is influenced by growth regulator genes which act to transcriptionally control genes, modify cell wall properties, or regulate growth hormones (such as auxin). The expression of these genes may differ across a developing tissue, generating regions which have different specified growth rates and orientations. These genetically specified growth rates influence how regions of tissue or cells would grow in isolation. However, the rate at which the tissue or

cells actually grow is affected by the mechanical connectivity of the tissue. Growth rates measured in a developing tissue should therefore be considered as resultant growth rates which arise as a combination of specified growth rate and the effect of mechanical constraints in the growing tissue. Two main types of resultant growth may be observed: anisotropic (directional) growth and isotropic growth (equal in all directions). Anisotropic resultant growth may arise through specified anisotropy or, indirectly due to conflict within the tissue (e.g Figure 1.1). It has been proposed that two types of signal might contribute towards coordinated tissue growth (Coen *et al.*, 2004). The first are 'regionalising' signals which provide differences between regions of tissue, allowing growth rate and anisotropy to be regulated locally across a tissue. The second are 'polarising' signals which provide directional information to cells in the growing tissue, providing axial information so that growth specified in regions of tissue may occur preferentially in one orientation.

1.1.4 Growth orientation

For specified anisotropic growth to occur, axial information is required so that growth rates may be specified in orientations relative to a local axis within the tissue. There are currently two main hypotheses for how growth orientation can be specified: through tissue cell polarity, or through stress-based axiality.

1.1.4.1 Polarity-based axiality

Polarity can be described as an asymmetry along an axis. Like most processes in development, this can be considered at the discrete, cellular level or at the continuous, tissue level.

1.1.4.1.1 Cell polarity

A polarised cell exhibits an asymmetry whereby certain molecules or structures are located preferentially towards one end of the cell. This can lead to aspects of the cell's development or function occurring preferentially in one direction or along one axis. For example, in *Caulobacter* polar asymmetry generates different progeny (stalked or flagellum possessing swarmer) at each cell division, reviewed in Shapiro *et al.* (2002). Cells of

multicellular organisms may also be polarised. For example, in *Arabidopsis thaliana,* BREAKING OF ASYMMETRY IN THE STOMATAL LINEAGE (BASL) accumulates in a polarised crescent at the cell periphery of asymmetrically dividing stomatal-lineage cells prior to division (Dong *et al.*, 2009).

1.1.4.1.2 Tissue cell polarity

In many tissues, the polarity of individual cells is coordinated between neighbouring cells and with respect to the overall tissue axes. This coordination of cell polarity fields is referred to as tissue cell polarity and mathematically corresponds to a field of vectors associated with positions in space (a vector field) (Lawrence *et al.*, 2007). This is evident in tissues which display an inherent directionality through polarised external features. For example, cells of the *Drosophila melanogaster* wing are polarised along the proximal-distal axis of the wing. This polarity is established as an asymmetric distribution of proteins early in wing development, leading to the development of a hair from a site at the distal end of each cell and a coordinated pattern of hairs across the wing which point proximal-distally (Strutt, 2001, 2002). A proximal-distal polarity pattern has also been observed in the distribution of the PIN-FORMED 1 (PIN1) protein in the epidermis of the *Arabidopsis* leaf which is localised towards the distal end of each cell (Scarpella *et al.*, 2006). This coordinated PIN polarity may be responsible for specifying principle orientations of leaf growth, since patterns of PIN localisation in the developing *Arabidopsis* leaf primordium match polarity patterns employed in a model of leaf growth (Kuchen *et al.*, 2012).

Tissue cell polarity can also be coordinated in different layers of tissue. For example, while PIN1 polarity points distally in the epidermis of the *Arabidopsis* leaf, polarities in the sub-epidermal cells of the developing midvein are proximally oriented (Scarpella *et al.*, 2006; Wenzel *et al.*, 2007). Roots also exhibit a complex polarity pattern, whereby PIN proteins are oriented towards the root tip in the central tissue, towards the shoot in the outer cells, and inwardly in the cells in between (Blilou *et al.*, 2005). PIN proteins function as exporters of the plant hormone auxin. The coordinated polar distribution of PIN proteins in cells therefore allows for the polarised transport of auxin through a tissue (Wiśniewska *et al.*, 2006). These polarised patterns of PIN localisation are essential for plant morphogenesis since auxin distribution plays an important role in regulating cell fate and growth: for example, in the initiation of lateral organs, the control of leaf vascular patterning, and the

control of root development (Reinhardt *et al.*, 2000; Scarpella *et al.*, 2006; Overvoorde *et al.*, 2010).

1.1.4.1.3 The basis of tissue cell polarity coordination in plants

Several models have been proposed for how tissue cell polarity may be generated with PIN1: the up-the-gradient model (Jönsson *et al.*, 2006; Smith *et al.*, 2006), the with-the-flux model (Mitchison, 1980; Stoma *et al.*, 2008), and the indirect coupling model (Abley *et al.*, 2013). These are reviewed and explored experimentally by Abley *et al* (2016). In the up-the-gradient model, PIN1 localises towards the neighbouring cell with the highest concentration of intracellular auxin (Jönsson *et al.*, 2006; Smith *et al.*, 2006; Bilsborough *et al.*, 2011). Molecular mechanisms behind this model have been proposed and include a mechanical based polarity involving the detection of auxin-induced stress gradients which bias the cellular localisation of PINs (Heisler *et al.*, 2010), and sensing of auxin concentration and transport using a chemical based mechanism (Cieslak *et al.*, 2015).

The with-the-flux model proposes that PIN1 becomes localised according to the rate of auxin efflux across the membrane (localising to the face of the cell which has the highest efflux) and may be coordinated across tissue based on gradients of auxin flux (Mitchison, 1980; Stoma *et al.*, 2008). Ways in which cells may sense auxin flux using biochemical circuits have been explored (Cieslak *et al.*, 2015). However, predictions made by the model include a drop in intracellular auxin concentration during the formation of PIN1 convergence points which is not supported experimentally (Heisler *et al.*, 2005; Brunoud *et al.*, 2012).

An alternative is the indirect coupling model which does not require cells to respond to auxin gradients between cells or sense auxin flux. Instead, intracellular polarity components function to establish cell polarity without external asymmetries in auxin distribution (Abley *et al.*, 2013). There are two polarity components in the model, each of which exist in two forms: the diffusible cytoplasmic form (A and B), and a more slowly diffusing form which is membrane bound (A* and B*). A* and B* are localised at opposite ends of the cell (A* promotes deactivation of B* and *vice versa*). PIN1 is recruited to the membrane by A* which causes polarisation of PIN1. Coordination of PIN polarity across the

7

tissue occurs because the polarities of neighbouring cells are coupled indirectly using a feedback mechanism where extracellular auxin inhibits A* and therefore PIN1 recruitment.

In each model, auxin dynamics can account for the coordination of tissue cell polarity. Testing the models using mutant *Arabidopsis* plants which develop outgrowths revealed that patterns of auxin production in growing leaves are more compatible with the with-the-flux and indirect-coupling models than the up-the-gradient model (Abley *et al.*, 2016).

1.1.4.1.4 *Modelling plant morphogenesis using polarity based axiality*

In a polarity-based axiality model, tissue cell polarity is generated through self-organising chemical signals, providing an underlying polarity field in the tissue. Growth rates may then be specified parallel and perpendicular to this field which is specified independently of growth. This may occur through cellular polarities influencing anisotropy of cell wall properties defining growth orientation. For example, microtubule alignment may be modified, or cell wall stiffness may be altered. Auxin is a strong candidate as the chemical signal (morphogen) for such a polarity system since it has been shown to be transported across tissue in a polar fashion, and is important in a number of developmental processes (outlined above). Models implementing polarity-based axiality have aided our understanding of development of a range of plant organ shapes such as the *Arabidopsis* leaf, *Antirrhinum* petal and whole flower, and *Arabidopsis* and *Capsella* fruit (Green *et al.*, 2010; Kuchen *et al.*, 2012; Sauret-Güeto *et al.*, 2013; Eldridge *et al.*, 2016). These models were generated using the Growing Polarised Tissue (GPT) framework in which plant tissue is treated as a continuous sheet termed the canvas. A polarity field propagates through the canvas and may correspond to a tissue cell polarity field, although the setup of polarity in these models abstracts away from the cell level. Instead, a polarity regulatory network (PRN) is set up and defines the distribution of diffusible POLARISER (POL). POL propagates away from a plus organiser and towards a minus organiser, generating a gradient of POL which determines the polarity field (Kennaway *et al.*, 2011). Once this polarity field has been set up, growth rates parallel (K_{par}) and perpendicular (K_{per}) to the polarity field may be specified.

Several candidate organiser genes have been proposed which may underlie this organiser-based model. For example, the *Arabidopsis* leaf model has a proximal-distal polarity

pattern, with a plus organiser located at the base of the primordium (Kuchen *et al.*, 2012). *CUP SHAPED COTYLEDON* (*CUC*) genes have been proposed to regulate this proximal-distal tissue polarity since *CUC* genes are expressed at the base of the leaf and *CUC2* loss of function mutants show disrupted formation of PIN1 convergence points which are essential for serration development (Bilsborough *et al.*, 2011). This suggests that *CUC2* could regulate the serration formation through generating polarity along the proximal-distal axis of the leaf. Other candidate organiser genes include auxin importers such as *AUX* and *LAX* (Yang *et al.*, 2006; Péret *et al.*, 2012) (candidate minus organisers), and auxin biosynthesis genes such as *YUCCA*s (Cheng *et al.*, 2006, 2007) (candidate plus organisers).

Candidates for growth rate regulator genes in *Arabidopsis* have also been suggested. These include *ROTUNDIFOLIA* (*ROT3*) and *ANGUSTIFOLIA* (*AN*). Cell expansion along the proximal-distal axis of the leaf is decreased in *rot3* mutants (Tsuge *et al.*, 1996; Kim *et al.*, 1999), while cell expansion along the mediolateral axis of the leaf is decreased in *an* mutants, resulting in narrower leaves (Tsuge *et al.*, 1996). *AN* and *ROT3* may therefore be players in specifying growth rates parallel and perpendicular to the proximal-distal axis of polarity set up in the *Arabidopsis* leaf.

1.1.4.2   Stress-based axiality

An alternative hypothesis to the polarity-based system for the generation of tissue orientations is a stress-based axiality system whereby the axiality of a tissue is determined by the orientation of maximal stress patterns in cell walls. Mechanical stress (force per unit area) at a tissue level is evident when cuts are made in tissue and the edges of the tissue either close (the tissue was under mechanical compression), or they pull apart (the tissue was under tension) (Boudaoud, 2010). Mechanical stress is proposed to define axial information through positioning microtubules and modifying mechanical properties of the cell (Heisler *et al.*, 2010). Heisler *et al.*, (2010) proposed that mechanical signals could coordinate PIN1 polarities and microtubule orientations in the shoot apical meristem (SAM). If tissue is under directional stress, cortical microtubules will align parallel to the main stress orientation and resist this stress through modifying the cell walls parallel to the stress orientation, thus leading to anisotropic growth perpendicular to the orientation of the cortical microtubules. This indicates that there may be a complex interplay between chemical and mechanical signals during tissue growth regulation. Stress-based axiality may

be set up using tissue geometry/morphology (Hamant *et al.*, 2008), or through a mechanical feedback system which reads the stress generated by differential growth rates within a connected tissue (Hervieux *et al.*, 2016) (detailed below).

Models of organ emergence at the SAM which use geometry/morphology based stress patterns have been explored (Hamant *et al.*, 2008). In such mechanical models, the epidermis is assumed to be under tension and the meristem is therefore modelled as a pressure vessel (a shell inflated by an inner pressure), and a feedback loop functions to link tissue morphology, stress patters, and microtubule-mediated cellular properties (Hamant *et al.*, 2008). The flanks of the meristem are represented as a cylinder where stress is greater in the circumferential direction than along the meridian, leading to strongly anisotropic stress on the flanks of the meristem. Microtubule orientation in each 2D cell of the model is parallel with the local direction of principal stress. Stiffness of the wall material increases in walls parallel to the directions of the cortical microtubules. Microtubule direction is then updated, with microtubules aligning along the maximal stress direction. This introduces stress feedback into the system which is implemented as a weighted average of each cell's directional wall stresses. Growth of primordia from the flanks of the SAM is initiated by a local decrease in cell wall stiffness which generates an outgrowth (Hamant *et al.*, 2008)

Mechanical stresses can also be generated through differential growth patterns and the resulting differences in mechanical stresses across a tissue have been hypothesised to orient growth. This has been explored and modelled for orienting anisotropic specified growth in the development of the *Arabidopsis* sepal (Hervieux *et al.*, 2016). In this model, residual stresses are generated by differential rates of specified isotropic growth. These residual stresses are then proposed to feed back to reinforce tissue in the direction of the local stress, producing specified anisotropic growth. Simulations in this work show that orienting growth in this manner, using local stresses, does not produce a coherent pattern of orientations (Hervieux *et al.*, 2016). Since growth is directed by residual stress patterns, growth feeds back to modify the stresses and therefore destabilise their orientations. To overcome this, simulations were run where orientations are specified by averaging the stress orientation across the sepal. A sensing mechanism for such averaging is not known and it is unclear how local and average stresses may be distinguished by cells.

1.1.4.3 Growth without axiality (isotropic growth)

In some cases, models of morphogenesis have been explored using only isotropic specified growth. This is perhaps the simplest form of growth because no axial information is required. For example, proximal-distal growth of the chick limb bud can be modelled using specified isotropic growth and a gradient of areal growth rate which is highest near the tip of the bud. In this model, areal growth rate is proportional to the concentration of a growth factor which diffuses from the tip of the growing bud (at the apical ectodermal ridge, AER). Proximal-distal growth of the limb bud is controlled by the rate of growth factor secretion, diffusion, and decay, and the inhibition of growth at the AER (tip). Local growth is isotropic (Popławski *et al.*, 2007). On the other hand, models exploring mouse limb bud development use specified anisotropic growth, matching observed local anisotropy in clonal analysis (Marcon *et al.*, 2011). In this model, signals coming from the AER are thought to promote anisotropic behaviour rather than isotropic growth.

Developmental stages of the liverwort *Marchantia* thallus have been captured using isotropic specified growth whereby a factor termed APEX is placed at apical regions and inhibits growth. Isotropic growth is promoted such that growth is highest in regions near to APEX, but inhibited at APEX itself. This model is able to capture outward expansion of the lobes, bifurcation, branching, apex divergence, and concave branch point formation (Solly, 2015). A role for anisotropic growth was also explored for the generation of longer or wider thallus shapes such as the thinner thallus of *Riccia fluitans* (Solly, 2015).

The modelling of these systems highlights the need to study growth patterns in the biological system as well as computational models when trying to understand specified growth patterns. Both examples here can be considered in 2D. Understanding growth dynamics of 3D organs requires even more careful analysis of growth dynamics due to further tissue connectivity and growth out of the plane. The GPT framework allows both isotropic specified growth models and anisotropic specified growth models to be explored and takes into account the connectivity of the tissue. Hypotheses on resultant growth of tissue can be made by studying clones induced early in the model and can be tested biologically.

1.2 Leaves as a model for plant growth and morphogenesis

Leaves exhibit some of the greatest diversity of shapes, ranging from conventional flat leaves to complex 3D structures such as those seen in carnivorous plant traps which have evolved to attract and capture prey. Extensive work has been conducted to understand the development of flat leaves such as those of *Arabidopsis.* However, the development of complex plant shapes remains poorly understood. Previously, the *Arabidopsis* leaf has been subjected to live tracking from early stages of development and a model has been generated which accounts for *Arabidopsis* leaf growth and development using polarity as an axiality system and regional factors which specify growth rates parallel and perpendicular to the local polarity (Kuchen *et al.*, 2012). In this work, final leaf shape is determined by patterns of growth rates and orientations established early in development as well as resultant growth generated by a mechanically connected tissue (the details of which are discussed above) (Kuchen *et al.*, 2012).

A key question is whether common mechanisms underlie the generation of diverse and more complex forms. Perhaps some of the most complex leaf structures to consider are those of the carnivorous plants, whose complexity has fascinated biologists for centuries. Darwin was one of the earliest scientists to devote attention to their study, providing the first detailed description of eight carnivorous plants (Darwin, 1875). Now, more than 600 species of carnivorous plant have been identified in four of the major angiosperm lineages and in five orders (Ellison & Gotelli, 2008). In some cases, similar complex forms have evolved independently, supporting the hypothesis that there may be simple principles underlying their development. For example, epiascidiate (cup or tubular-shaped) leaves of carnivorous pitcher plants have evolved four times independently: in the families Nepenthaceae, Sarraceniaceae, Cephalotaceae, and Lentibulariaceae (Lloyd, 1942; Ellison & Gotelli, 2008). Examples of epiascidiate leaves from each family are shown in Figure 1.2. Epiascidiate leaves are perhaps some of the most complex leaf shapes. In each case, the leaf develops to form a lidded vessel in which small prey are trapped and digested. The convergent evolution of epiascidiate leaves makes this complex leaf shape particularly applicable as a system to explore possible underlying simplicity in the generation of complex forms.
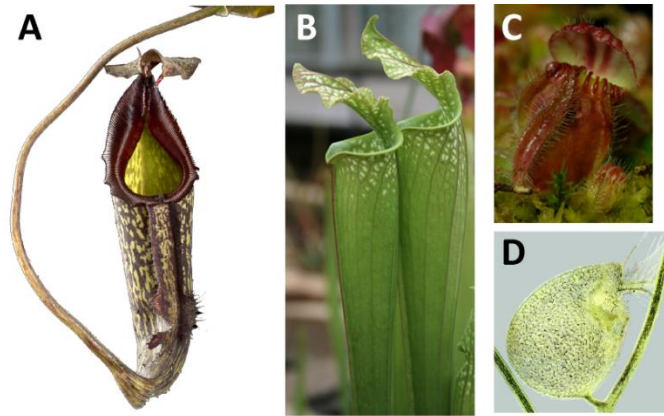
Figure 1.2: Epiascidiate (cup-shaped) leaves have evolved four times independently. (A) *Nepenthes maxima* (Nepenthaceae), (B) *Sarracenia* (Sarraceniaceae), (C) *Cephalotus* (Cephalotaceae), (D) *Utricularia gibba* (Lentibulariaceae). A-C provided by Andrew Davis, JIC.

1.2.1 The development of epiascidiate leaves in relation to flat leaves

To relate epiascidiate leaf growth to our current understanding of leaf development, it is important to consider the relationship between conventional flat leaves such as those from *Arabidopsis* or *Antirrhinum* and 3D epiascidiate leaves. During conventional flat leaf development, leaf founder cells are specified on the flanks of the SAM and transform into the leaf primordia which undergo an elaborate developmental program to give rise to a fully formed leaf (Byrne, 2012). During development, three axes of polar growth are established; the proximal-distal axis (from the base to the tip of the leaf), the medial-lateral axis (from the midvein to the margin of the leaf), and the adaxial-abaxial axis (ad-ab), (from the upper, or ventral to the lower, or dorsal side of the leaf) (Byrne, 2012). The establishment of this third axis (ad-ab) has been studied extensively and we now have an understanding of the gene regulatory network (GRN) involved in establishing a leaf lamina which is flattened in the transverse plane and exhibits distinct adaxial and abaxial surfaces. This is reviewed in Townsley & Sinha (2012) and Yamaguchi *et al* (2012). Ad-ab polarity is established very early, before the leaf primordia begins to grow out, such that the adaxial domain is established on the side of the primordium closest to the SAM (Townsley & Sinha, 2012). Early work on potato and tomato suggested that ad-ab specification was required for lamina outgrowth, since the loss of adaxial identity through separation of the leaf primordia and SAM restricted lamina outgrowth and generated radial leaves (Reinhardt *et*

al., 2005; Sussex, 1951). These findings have been supported by the study of mutants lacking genetic specification of adaxial and abaxial identity. One of the first genes identified for its role in ad-ab identity was the *PHANTASTICA* (*PHAN*) gene of *Antirrhinum majus* (Waites & Hudson, 1995). The leaves of *phan* mutants display a range of morphologies including radially-symmetrical leaves which have a complete lack of adaxial identity and fail to expand laterally, suggesting that *PHAN* promotes leaf adaxial identity and that the juxtaposition between adaxial and abaxial identities promotes lamina outgrowth (Waites & Hudson, 1995). This work paved the way for the characterisation of many genes involved in the establishment of ad-ab identity in the *Arabidopsis* leaf which is now understood to be controlled by a GRN involving transcription factors, small RNAs and other regulatory genes (Townsley & Sinha, 2012; Yamaguchi *et al.*, 2012). In *Arabidopsis* the main regulatory genes include the adaxial specifying *ASYMMETRIC LEAVES 1* (*AS1*)*, ASYMMETRIC LEAVES 2* (*AS2*)*, and class III HOMODOMAIN-LEUCINE ZIPPER genes (HD-ZIPs), and the abaxial fate promoting KANADIs and YABBYs (Townsley & Sinha, 2012; Yamaguchi *et al.*, 2012).

It is It is generally thought that the inner surface of the epiascidiate leaf is equivalent to the adaxial surface of a conventional flat leaf while the outside is equivalent to the abaxial surface (Arber, 1941; Franck, 1976; Fukushima & Hasebe, 2014; Lloyd, 1942). A number of theories have been proposed for the development of *Nepenthes* pitchers and their structural relationship to a conventional flat angiosperm leaf (Franck 1976). A popular theory which attempts to account for all epiascidiate leaves is the modified peltation theory. This theory makes correlations between epiascidiate leaves and peltate leaves which both consist of a base and a petiole with is attached to the lamina at a point away from the lamina margins (Franck, 1976). In this theory, the initial primordia of peltate and epiascidiate leaves are assumed to be similar and epiascidiate leaves acquire their tubular shape through specific patters of tissue growth, starting with the formation of an adaxial outgrowth (the querzone), followed by a secondary adaxial growth which gives rise to the lid. An apex remains in a dorsal position and is thought to give rise to the spur. Interpretations of this theory are shown in Figure 1.3 and are reviewed in Franck (1976). Using this hypothesis, we may consider the opening (or mouth region) of epiascidiate leaves as being equivalent to the margin of a conventional flat or peltate leaf.
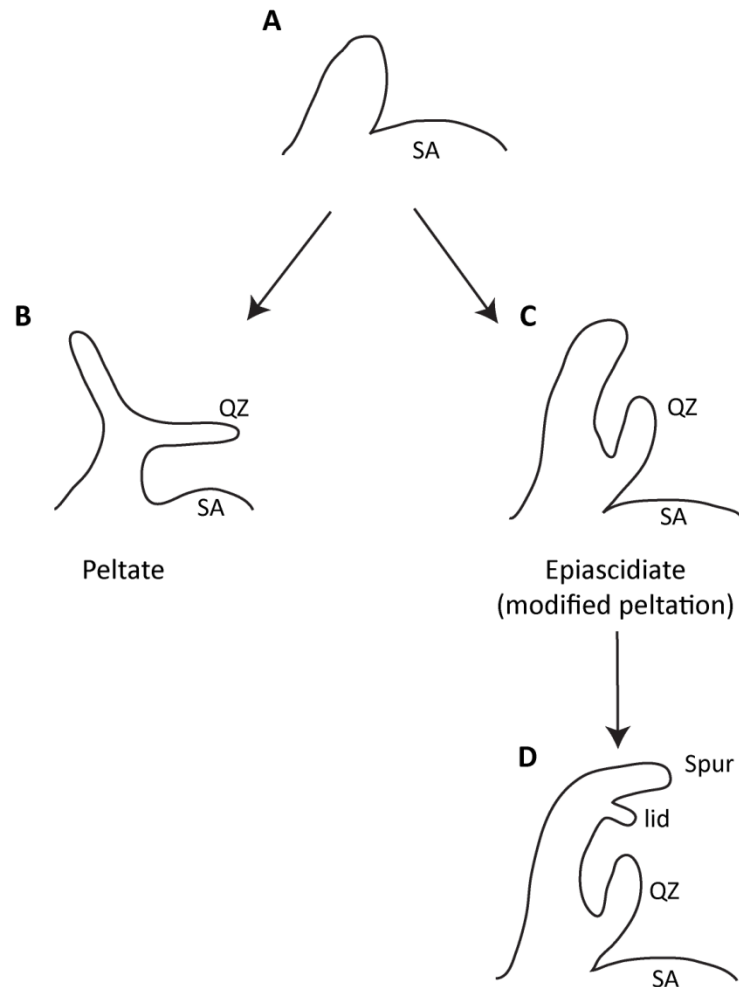
Figure 1.3: Illustration of the modified peltation theory for the development of epiascidiate leaves. Diagrams represent longitudinal sections of developing primordia. (A) Initial leaf primordium. (B) Formation of a peltate leaf through the growth of an adaxial outgrowth termed the querzone (QZ). (C) Modified peltation giving rise to a tubular epiascidiate leaf through the growth of the querzone followed by the generation of a lid (D) through a secondary adaxial outgrowth. SA, shoot apex. Drawings are adapted and interpreted from Franck (1976).

Studies on the development of *Darlintonia californica* (Sarraceniaceae family) epiascidiate leaves, showed that the primordium does develop an adaxial outgrowth (the querzone) which grows upwards to form a tube (Franck, 1975). A similar querzone (referred to as a cross zone) forms during primordial stages of development in the peltate leaf of *Tropaeolum majus* (Gleissberg *et al.*, 2005). During the early stages of *T. majus* development, the abaxial identity gene *TmFIL* (*FILAMENTOUS*) (a YABBY transcription factor) is expressed in a narrow band on the adaxial side of the primordium, coinciding with

15

the formation of the querzone/ cross zone (Gleissberg *et al.*, 2005). This suggests that evolution of the peltate leaf form may be associated with localised derepression of YABBY abaxial identity genes in the adaxial side of the primordium. More recently, this idea was explored in the development of epiascidiate leaves in *Sarracenia purpurea* where the spatiotemporal expression of abaxial *FIL* and adaxial *PHB* (PHABULOSA) (a HD-ZIPIII transcription factor) were explored (Fukushima *et al.*, 2015). The primordia of *S. purpurea* begins in a similar fashion to that discussed above, starting as a relatively flat structure and then forming a cross zone which connects both sides of the leaf margin (Fukushima *et al.*, 2015). Unlike the expression patterns observed in *Tropaeolum*, *SpFIL* and *SpPHB* expression patterns were indistinguishable between the cross zone and more distal regions of the young leaf, and it was suggested that development relied on cell division planes rather than modified expression patterns of surface identity genes (Fukushima *et al.*, 2015). Since only one epiascidiate leaf example has been examined in such a way, it is difficult to rule out the importance of ad-ab identity genes in generating the epiascidiate form or the likelihood of the modified peltation theory.

To date, most theories have focussed on the primordial stages of epiascidiate leaf development and morphological events after this point have not been addressed in detail. To fully understand the development of epiascidiate leaves, we need to apply imaging, molecular genetics, and modelling methods to the morphogenesis of these complex 3D structures at various stages of development. One aim of this work is therefore to establish a new model system for the study of complex leaf shapes which can be studied through development from early stages to maturity. Out of the four examples of epiascidiate leaf evolution, the genus *Utricularia* (belonging to the family Lentibulariaceae and the order Lamiales) presents us with a promising system for study due to a number of qualities.

1.3 Exploring *Utricularia*

The genus *Utricularia*, commonly known as the bladderworts, is made up of over 200 species which are spread worldwide (Lloyd, 1942; Taylor, 1994). Bladderworts are aquatic or terrestrial plants which lack roots and obtain their nutrition through capturing live prey in epiascidiate leaf traps known as bladders (Taylor, 1994; Vincent *et al.*, 2011). Unlike most angiosperms, *Utricularia* species do not exhibit clearly defined stems, roots and leaves with predictable positional relationships to each other (Lloyd, 1942; Taylor, 1994; Chormanski &

Richards, 2012; Rutishauser, 2015). Rather, the main vegetative body of *Utricularia* species is made up of long, branching, stem-like structures referred to as stolons. In aquatic species such as *U. gibba*, these structures grow as dense, floating mats (shown in Figure 1.4, A) with other structures such as bladders and leaves, sometimes referred to as 'leaf like structures' (LLS) (Chormanski & Richards, 2012; Taylor, 1994). The leaves show dichotomous branching, sometimes branching twice. Bladders are sometimes formed on the leaves and may be associated with a single leaf or two. In some aquatic species, the bladders begin their development within the circinnate apex of the stolon (Figure 1.4, B) Inflorescences are produced on the floating matt of stolons, and project above the water (Figure 1.4, D).
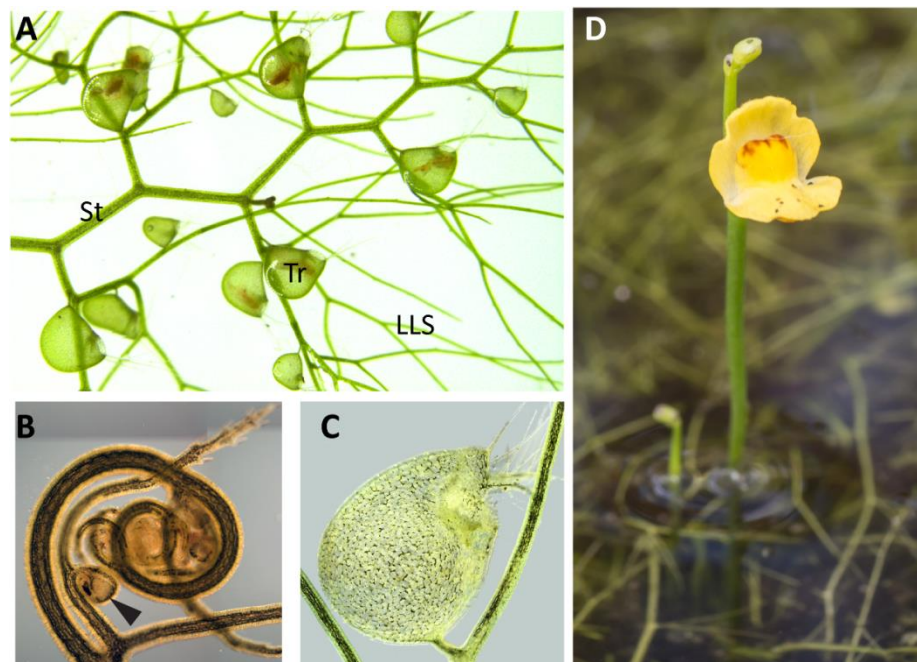
Figure 1.4: *Utricularia gibba* floating aquatic plant morphology. (A) Vegetative body made up of branching stolons (St) which possess bladder traps (Tr) and leaf like structures (LLS). (B) Circinnate apex with young developing bladders (arrow). (C) *U. gibba* bladder. (D) *U. gibba* flower. Images by (A) Karen Lee, (B) Patrick Diaz, and (D) Andrew Davis.

1.3.1 *Utricularia gibba* as a potential model species

Utricularia offers a number of advantages as a potential model system for the study of morphological complexity and diversity. *Utricularia* represent one of the four cases where epiascidiate leaves have evolved. Unlike other epiascidiate leaves, the traps of *Utricularia*

are small and transparent making them amenable to imaging by confocal microscopy or optical projection tomography (OPT) (Lee *et al.*, 2006). The walls of the bladders are also only two cells thick (Rutishauser & Brugger, 1992) which simplifies analysis. Using these imaging techniques on the bladders of *Utricularia,* preliminary work in our lab has revealed their overall 3D morphology as well as cellular details such as quadrifid glands on the inner (adaxial) surface. The bladders appear soon after germination which means that large numbers of plants could potentially be screened on plates for mutants. *Utricularia gibba,* in particular, has the second smallest genome known in angiosperms, with an estimated size 88 Mb (Greilhuber *et al.*, 2006) compared to 157 Mb for *Arabidopsis.* This small genome could allow whole genome sequencing for the isolation of genes identified by mutant screening to be carried out. *U. gibba* has a chromosome number of 2n=14, diploid, allowing for traditional genetic studies (Rahman *et al*., 2001). Furthermore, *U. gibba* is an aquatic species which is easily grown and propagated in culture and can flower in the glasshouse.

1.3.2 *Utricularia* bladder development and morphology

1.3.2.1 Mature bladder morphology

The mature bladders of *Utricularia* species consist of a vessel shape with a lid that functions as a trap door. In aquatic species, the trap mechanism works via suction and has two phases: in the first phase, glands actively pump water out of the trap lumen, leading to a lower internal hydrostatic pressure. At this point the bladder has concave walls and the trap door (with its trigger hairs) is closed to keep the entrance watertight. When a small animal brushes past the trigger hairs (connected to the lid/ trap door) the lid is triggered to open, leading to the second phase: the bladder wall relaxes and prey is passively sucked in, followed by the closing of the trap door and the digestion of prey with the aid of digestive enzymes secreted by internal quadrifid glands (Vincent *et al.*, 2011).

Utricularia species show a wide range of mature bladder morphologies. The hollow traps have been described as either globose or ovoid, they may be stalked or sessile and can vary largely in the position of the opening or mouth region relative to the stalk: the mouth may be basal (adjacent to the stalk), terminal (opposite to the stalk), or lateral (in an intermediate position) (shown in Figure 1.5). Different species also exhibit varied dorsal,

lateral or ventral appendages, usually near the mouth region (Taylor, 1994; Rutishauser, 2015).
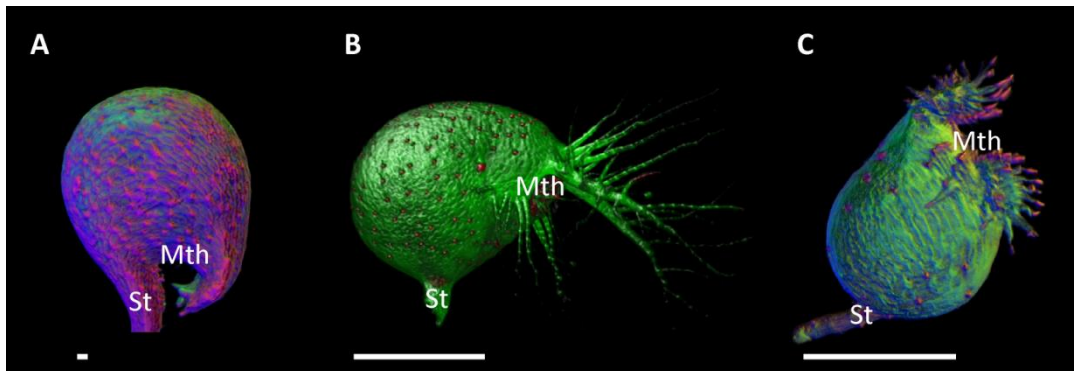
Figure 1.5: Trap diversity in *Utricularia* species. (A) *U. praelonga* which exhibits a basal mouth. (B) *U. gibba* which exhibits a lateral mouth. (C) *U. bisquamata* which exhibits a terminal mouth. Scale bars are 500 μm. All bladders were imaged using optical projection tomography (OPT) and images are courtesy of Karen Lee.

Specifically, *U. gibba* bladders (Figure 1.5, B) are ovoid, stalked and have a lateral mouth with two larger dorsal, branched appendages (antennae), and further dorsal, lateral, and ventral smaller appendages (Taylor, 1994). A mature *U. gibba* bladder is shown in various perspectives in Figure 1.6. Here the stalk and mouth regions (Figure 1.6, green region and pink arrow) are shown as well as the threshold region just below the mouth (Figure 1.6, purple), and the trap door and associated trigger hairs (Figure 1.6, orange and red). The majority of the bladder is two cells thick, apart from the threshold region which is situated just below the mouth opening and consists of several cell layers (Rutishauser & Brugger, 1992).
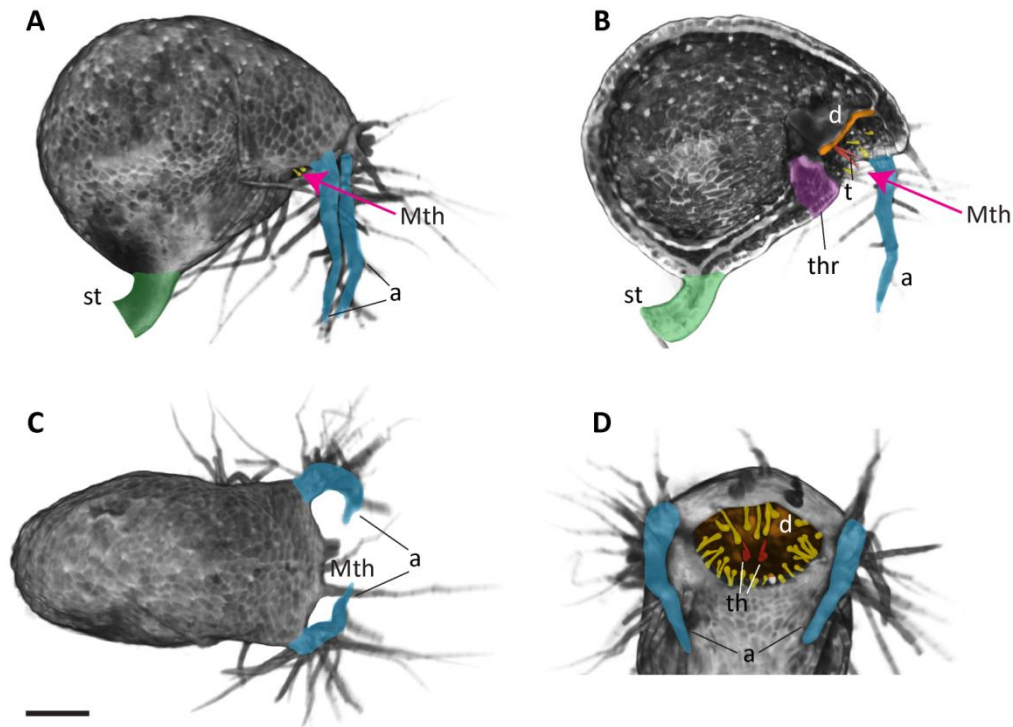
Figure 1.6: *Utricularia gibba* **bladder morphology.** Mature *U. gibba* bladder (A) side, (B) side section, (C) top, (D) entrance to the trap. Labels are stalk (st, green), mouth (Mth, pink arrow) antennae (a, blue), door (d, orange), threshold (thr, purple), and trigger hairs (t, red). Yellow structures are pyriform glands. Bladder was fixed and stained with propidium iodide and imaged using OPT (imaged by Karen Lee). Scale bar is 250 µm.

1.3.2.2   Early stages of Utricularia bladder development

In many aquatic species, such as *U. gibba,* the early stages of bladder development occur within the circinnate apex. This means that the bladder primordium is hidden from view and the youngest stages of bladder development are obscured by a spiral of stolon tissue (Chormanski & Richards, 2012) making the characterisation of early stages and the primordia difficult. The early stages of several terrestrial and aquatic species have been imaged using scanning electron microscopy by Rutishauser & Brugger (1992). From their images it appears that the *Utricularia* bladder primordium begins as an outgrowth similar in appearance to a conventional flat leaf primordium, and then forms an invagination that produces the lumen. However, the stages captured by Rutishauser & Brugger are few for each species and it is difficult to say whether the different species are similar in their developmental morphology. For example, the primordial stage of the terrestrial species *U.*

alpine is described as well as a later stage with the initial formation of the invagination for terrestrial *U. livida.* However, it is unclear how these stages may relate to one another (Rutishauser & Brugger, 1992).

No primordial stages of *U. gibba* have been described, possibly due to difficulties in imaging within the circinnate apex. Perhaps the most complete study of *Utricularia* bladder early development to date is presented in Meierhofer's study from 1902 (Meierhofer, 1902). In this work, the early stages of aquatic *U. vulgaris* bladders which appear to develop outside of the circinnate apex, are illustrated in cross section. These cross sections show the growth of a querzone and formation of a lid, reminiscent of the modified peltation theory discussed above. A compilation of drawings adapted from Meierhofer (1902) is shown below (Figure 1.7).
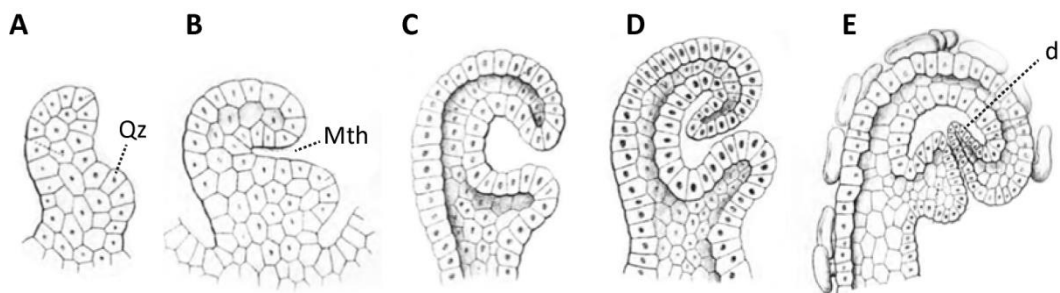
Figure 1.7: Early stages of bladder development interpreted from Meierhofer (1902). Side sections of *U. vulgaris* bladders at various developmental stages. (A) Primordium with the initial formation of the querzone (Qz). (B) Formation of the hollow mouth region. (C-D) continued growth of the querzone and arching of the distal tip. (E) Formation of the lid/ trap door (d). Drawings are adapted from Meierhofer (1902).

Studies to date provide an overview of the developing plant and bladder with no time series of development and no information on the later shape changes that occur during bladder development. Such information will be required to gain an understanding of the growth dynamics of the *Utricularia* bladders. There are also no studies performed on the earliest stages of aquatic species where bladders develop within the circinnate apex as in *U. gibba.* With modern methods such as confocal microscopy, it should be possible to investigate bladder stages which are within the circinnate apex and confirm the morphology of these stages.

1.4 The aim of this work

This work aims to explore underlying principles of tissue growth in the generation of 3D complex forms. Specifically, with regards to isotropic or anisotropic specified growth patterns. This work will take an integrative approach using computational modelling, molecular genetic studies, and imaging techniques to characterise the developmental stages of the *U. gibba* bladder, and generate and test hypotheses on how shape transitions in the bladder can occur. In this context the project has a number of goals:

1. To produce a detailed description of developmental stages of *U. gibba* bladder development and the shape transitions that occur.

2. To generate computational models accounting for the main transitions in bladder shape, exploring specified isotropic and specified anisotropic growth.

3. To test predictions on resultant growth rates and orientations made by the models to arrive at an understanding of specified growth patterns underlying *U. gibba* bladder development.

4. To explore the role of tissue cell polarity in *U. gibba* bladder development.

5. To develop *U. gibba* as a model system to explore the morphogenesis of complex leaf shape. This will involve optimising growth and life cycle conditions, protocols for forward and reverse genetics, and generating resources such as a fully sequenced genome and mutant populations.

2 Bladder developmental dynamics

2.1 Introduction

2.1.1 *Utricularia* bladder development

The *Utricularia gibba* bladder meristem starts its development within the circinnate apex of growing stolons and the first stages of morphogenesis occur while the bladder is wrapped up in this spiral of tissue. Existing studies on *U. gibba* morphology have focussed on mature bladders (Poppinga *et al.*, 2015) and any studies of younger bladders have relied on scanning electron microscopy (SEM) (Rutishauser & Brugger, 1992) and are limited in the case of *U. gibba* since the very early stages of bladder development occur when bladders are wrapped in tissue and not accessible to view (Chormanski & Richards, 2012). This has meant that the internal morphology and bladder shape changes through development have not been described in detail. In this work I aim to study the morphology and shape changes that occur during bladder development in time and space. This will allow me to generate theoretical models of *U. gibba* bladder development that capture the shape changes observed.

2.1.2 Specified growth versus resultant growth

The final shape of an organ is often not a direct readout of local properties specified by patterns of gene activities. Instead, tissue deformation also depends on mechanical constraints from neighbouring regions of tissue (Kennaway *et al.*, 2011). It is therefore difficult to intuitively understand how patterns of gene activity relate to the final form of an organ. In order to consider this relationship, it is useful to distinguish between two types of growth: *specified growth* and *resultant growth*. Specified growth describes the growth that would occur if each region of tissue grew in isolation. Resultant growth describes the growth observed in mechanically connected tissue (which grows with mechanical constraints of neighbouring regions) (Kennaway *et al*., 2011). This is true in both plants and animals: models dealing with *Drosophila* embryo invagination make a similar distinction,

considering the total deformation as imposed active deformation combined with elastic passive deformation (Conte *et al.*, 2008).

2.1.2.1 Growth rates and orientations

Specified and resultant growth can each be either isotropic (equal in all directions) or anisotropic (where growth rate is higher in one orientation). Resultant anisotropic growth can be generated by either isotropic or anisotropic specified growth. This was studied at the single cell level by Green (1965). Here, Green showed how a similar change in form from a cylinder to a flaring cylinder may be generated in two ways (Figure 2.1). In the first instance specified growth is isotropic and there is a gradient in areal growth rate where growth rate is highest at the top of the cylinder and lowest at the bottom (Figure 2.1, A). In the second instance, there is a gradient of specified anisotropic growth in which growth in height is greatest at the base and growth in width is greatest at the top (Figure 2.1, B). The final shape achieved in each case is very similar (both are flared cylinders). Clues to the specified growth pattern can be found by looking at the resultant growth of each segment of the shape. In the specified isotropy example, segments maintain their proportions but are larger at the top, getting smaller towards the base (Figure 2.1, A). In the specified anisotropy example, segments near the bottom are taller, while segments near the top are shorter and elongated (Figure 2.1, B). This means that resultant growth dynamics observed in a tissue can provide information about specified growth (Green, 1965). This work highlights the fact that there are multiple ways of specifying growth to produce a similar final shape. When trying to understand the specified growth pattern of a given form, it is therefore important to consider multiple specified growth patterns and make predictions that can distinguish between them.

A

Specified isotropic growth

Areal growth rate

B

Specified anisotropic growth

Specified anisotropy
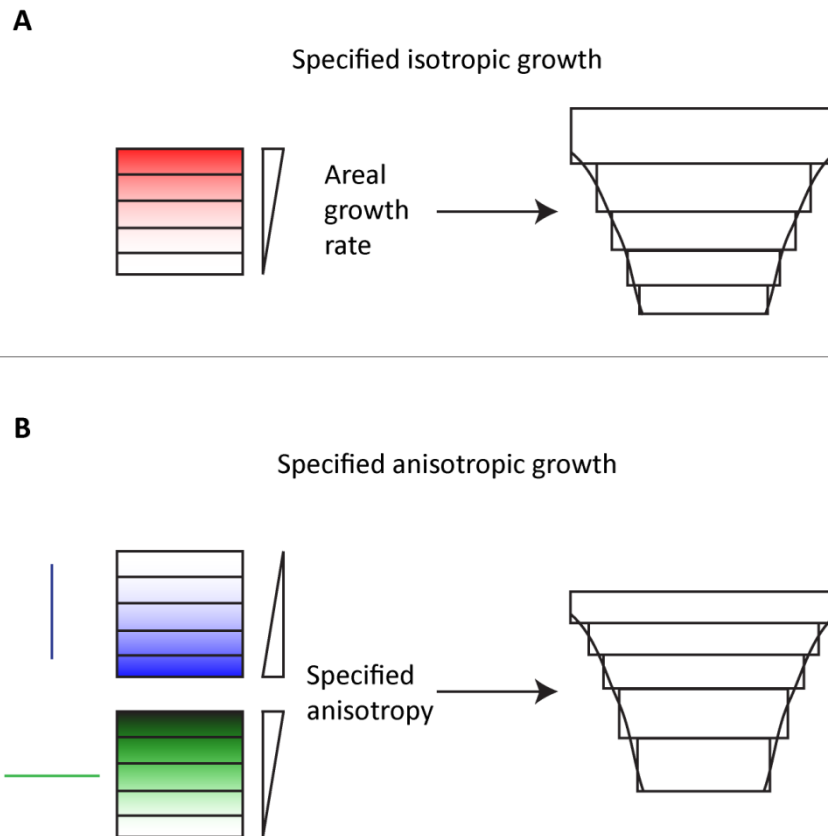
Figure 2.1: Resultant anisotropic growth generated from specified isotropic growth and specified anisotropic growth. Illustration of how a change in shape may be generated through (A) specified isotropic growth with a gradient in specified areal growth rates (red), or (B) specified anisotropic growth with gradients in specified anisotropy (blue and green gradients). Blue and green lines in (B) indicate the orientation in which specified growth rate is highest in each gradient: growth in height is greatest at the base, growth in width is greatest at the tip. (Green, 1965).

2.1.2.2 The role of conflict resolution in development

To understand development at a tissue level, it is important to consider the effect of tissue connectivity on resultant growth. Three types of tissue interactions which can give rise to resultant anisotropic growth and 3D deformations have been described and modelled. These are reviewed in Coen & Rebocho (2016 in press) and are outlined in Figure 2.2.

Areal conflict

Surface conflict

Directional conflict
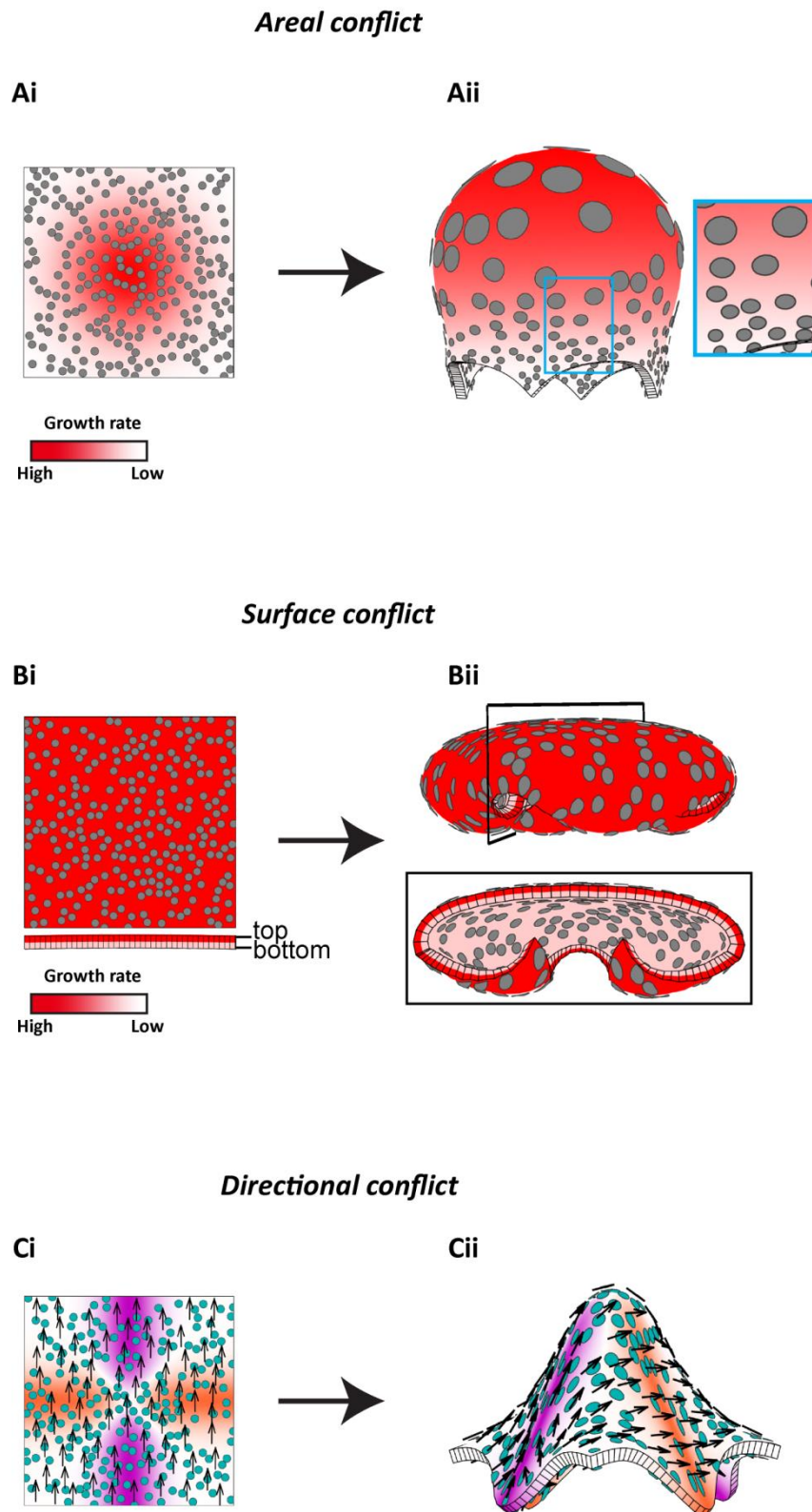
Figure 2.2: Generation of tissue deformations through different tissue conflicts. (Ai-Aii) *Areal conflict*. (Ai) Specified growth is isotropic and growth rate is highest in the centre of the square. (Aii) Final shape generated. Box shows zoomed in regions for clone size comparison. Clones are larger near the centre and smaller around the outside. (Bi-Bii) *Surface conflict*. (Bi) Specified growth is isotropic, and growth rate on the top surface is

higher than the bottom surface. (Bii) Clones on the final shape are equal in size across the top surface, and are smaller on the bottom surface (seen in cross section inside the black box). (Ci-Cii) *Directional conflict.* (Ci) Specified growth is anisotropic: growth is specified parallel with the polarity in the purple region, and perpendicular to the polarity in the orange region. (Cii). Clones on the final shape are elongated parallel with the orientation of highest growth rate in regions of specified anisotropic growth. Clones in between these regions are elongated in the opposite orientation. Images provided by Xana Rebocho.

The first type is *areal conflict*. Here, specified growth is isotropic and areal growth rates differ across the initial shape (growth rates are highest in the centre). This gives rise to a dome due to different regions trying to grow at different rates. This is reflected in the size of clones induced at the start of the model which are larger in the centre and smaller around the outside (Figure 2.2, A). The second type is *surface conflict* where specified growth is still isotropic, and this time growth on the top surface is higher than the bottom surface. This generates a dome due to the interaction between two connected surfaces growing at different rates. Here, clones are equal in size across the top surface, and are smaller on the bottom surface (Figure 2.2, B). The third type is *directional conflict* whereby specified growth is anisotropic and different regions are specified to grow in opposite orientations. Clones are elongated parallel with the orientation of highest growth rate in regions of specified anisotropic growth. Clones in between these regions are elongated in the opposite orientation due to these regions being pulled by the faster growing lines of specified anisotropy (Figure 2.2, C). In each case, the final dome shape is generated through the resolution of conflicts generated by different regions of tissue exhibiting different patterns of specified growth.

This understanding of the relationship between specified and resultant growth is important for understanding the morphogenesis of plant tissue. Directional conflict has been found to play a key role in the development of the *Antirrhinum* palate where opposite orientations of anisotropic growth lead to a deformation of tissue out of the plane (Rebocho *et al.*, 2016 submitted) . Areal conflict may be in play when auxin is applied to the margin of a leaf, and specified growth rate at the margin is higher than that at the centre of the leaf. This causes a wavy edge to emerge through the interaction between specified growth and the constraints of the connected tissue (Eran *et al*., 2004).

Anisotropic specified growth is more complicated than isotropic specified growth, since in the case of specified isotropic growth, genes need only control the local growth rate. However, for anisotropic specified growth to occur, orientations are also required (Kennaway *et al.*, 2011). Since similar shapes can often be accounted for through specified isotropic growth or specified anisotropic growth, a key question is whether specified anisotropy and therefore axiality is required for the development of a given organ.

2.1.3 Understanding morphogenesis and growth through modelling

The relationship between patterns of specified growth and resultant growth are usually not intuitive. It is therefore useful to explore hypotheses in a modelling environment and generate predictions which can be tested in the biological system. The modelling framework GFtbox (Kennaway *et al.*, 2011) allows the exploration of tissue growth and deformation to be explored through the interaction of specified growth patterns and resultant growth generated through the interaction between regions of connected tissue. This framework has provided a means to test hypotheses and explore genetic control of organ shape in a number of organs including the *Antirrhinum* flower (Green *et al.*, 2010), the *Arabidopsis* leaf (Kuchen *et al.,* 2012) and petal (Sauret-Güeto *et al.*, 2013), fruit shape in *Arabidopsis* and *Capsella* (Eldridge *et al.*, 2016), and the maize leaf (Richardson, 2015).

GFtbox uses polarity as a working hypothesis for the setup of tissue axiality, thereby allowing isotropic and anisotropic growth hypotheses to be explored. It also allows a number of testable predictions to be made by studying the shape and size of clones induced before growth. These can be compared to biological data to assess hypotheses on specified growth patterns based on observations made on resultant growth (Kuchen *et al.*, 2012; Sauret-Güeto *et al.*, 2013; Eldridge *et al.*, 2016).

In this framework, tissue is treated as a continuous sheet termed the canvas. Regional factors can be expressed across the canvas and can interact and propagate. Local growth rates can be specified by regional factors across the growing canvas. Axial information may be provided by a polariser regulatory network (PRN) which generates a polarity field via signals propagating through the canvas. This signal is anchored by tissue polarity organisers (polarity points away from + organisers and towards − organisers). Anisotropy can be introduced by specifying growth rates parallel (K_{par}) and perpendicular (K_{per}) to the local

polarity through a growth regulatory network (KRN). Elasticity theory is used to compute the deformation of the canvas. As growth occurs through a series of small deformations, stresses are generated in the canvas (Kennaway *et al.*, 2011). This allows the canvas to deform in response to conflicts generated during growth which can lead to anisotropic resultant growth even when specified growth is isotropic. This means that resultant growth can be studied across a canvas with mechanical constraints that can deform in 3D. Resultant growth of the canvas therefore depends on a combination of specified growth patterns and the constraints of mechanically connected tissue. Shape deformations and local growth rates can therefore contain features (e.g. rotations and curvature) which were not specified, since they are the result of the conflict caused by the interaction between local growth rates with the constraints of a connected tissue.

2.1.4 Aim of this work

The aim of this work is to characterise stages during *U. gibba* bladder development, to explore the principles of bladder morphogenesis using computer modelling, and to make key predictions of the mechanisms underpinning bladder morphogenesis based on models generated.

2.2 Results

2.2.1 Bladder developmental stages

To investigate the early stages of *U. gibba* bladder development when the bladders are inside the circinnate apex (Figure 2.3, A), I fixed and stained several circinnate apices with propidium iodide and imaged them using confocal microscopy (Figure 2.3). The primordium is a flattened structure which looks similar to an *Arabidopsis* leaf primordium except for a small invagination which begins to form (Figure 2.3, Bii, yellow arrow). This invagination progresses to give rise to a flattened sphere-like bladder which is circular from the front and flattened from the side (Figure 2.3, C). At later stages this flattened sphere transforms into a shape resembling a squashed capsule or 'caplet' shape which appears as a horizontal oval from the front and as a vertical oval in side section (Figure 2.3, D). The transition to this caplet shape from bladder initiation is difficult to study in real time since the circinnate

apex masks these early stages of development, making them difficult to track. However, from still images we can see how the bladder progresses through development with invagination and the formation of a trap door and antennae (Figure 2.3, orange), and threshold (Figure 2.3, pink) from the rim generated at the primordium. This is similar to observations made in *Utricularia vulgaris* over 100 years ago by Meierhofer (1902).
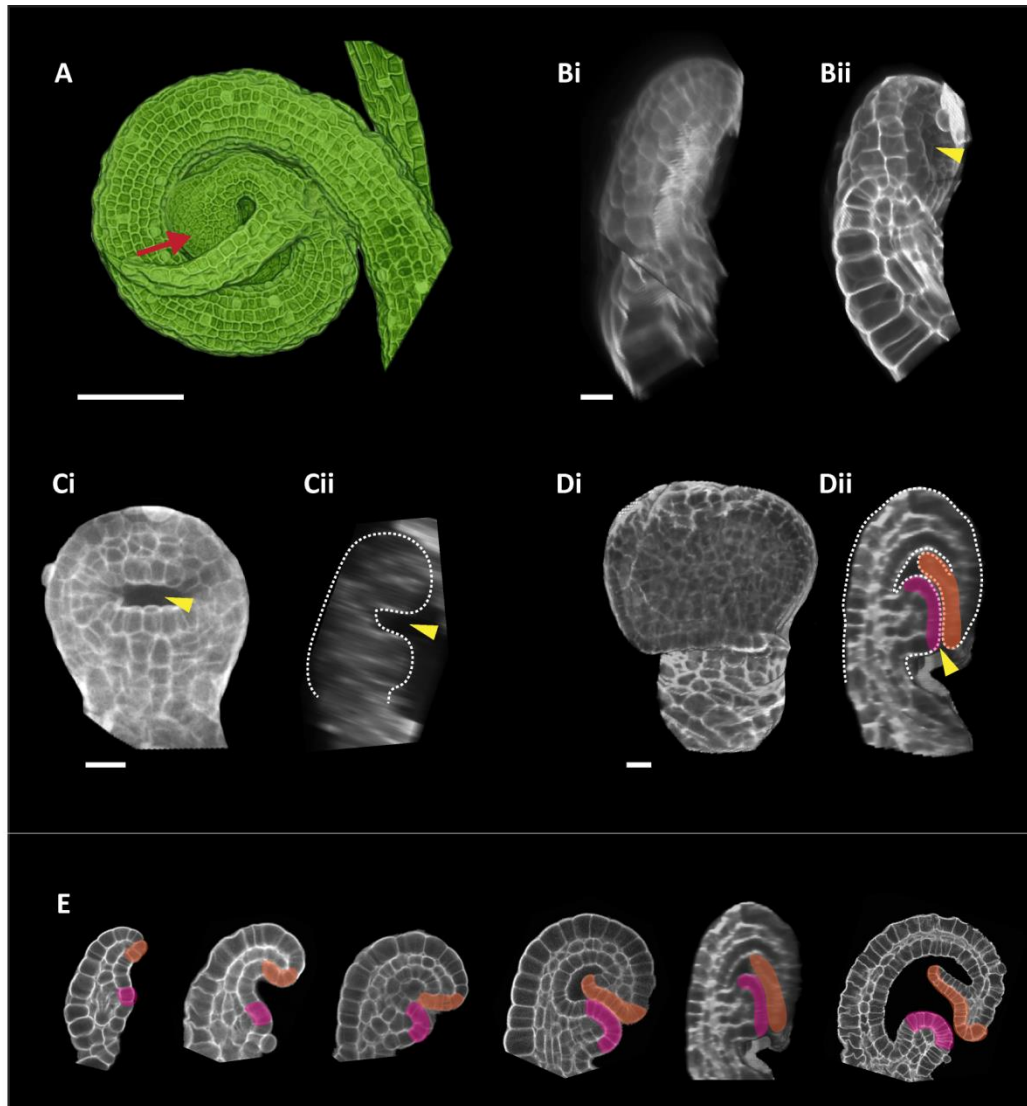
Figure 2.3: Early stages of *U. gibba* bladder development in the circinnate apex. (A) Circinnate apex with young bladder visible (red arrow). (B) Bladder primordium viewed from the side (Bi) and front oblique (Bii) in which the invagination has started to form (yellow arrow). (C) Young bladder after invagination (yellow arrow) viewed from the front (Ci) and in side section (Cii). (D) Young bladder after the formation of the trap door and antennae (orange) and threshold (pink) regions, viewed from the front (Di) and in side section (Dii). (E) Series of young bladders in side section showing some of the key developmental transitions including the development of the trap door and antennae (orange) and threshold regions (pink). Regions in (E) are marked based on appearance

alone and are not an indication of cell divisions in the region. (A) Scale bar is 100 µm. (B-D) Scale bars are 10 µm. (E) Bladders are not to scale. (B) and some sections from (E) were imaged and processed by Christopher Whitewoods.

Once the circinnate apex has uncurled, bladders continue to grow and deform, eventually reaching maturity (Figure 2.4). To assign stages to bladder development I took the maximum size of a mature bladder based on its length from antennae to the furthest point on the back (1400 µm) and then assigned stages in increments of 1.5 fold smaller than this, giving size categories of 1400 µm, 933 µm, 622 µm, 415 µm, 277 µm, 185 µm, 123 µm, 82 µm and so on. I allowed +/- 20 % of the value for each category based on bladder length. I found that the smallest bladders outside of the circinnate apex fell into the 185 µm category. Before this stage, bladders of *U. gibba* are within the circinnate apex. A convenient starting point for my analysis is when the bladders are within the 82 µm length category, (e.g. Figure 2.3, D). At this stage, invagination has occurred so that the bladder is hollow, internal biological landmarks (such as the trap door) have formed and useful external biological landmarks have started to form (such as the antennae).
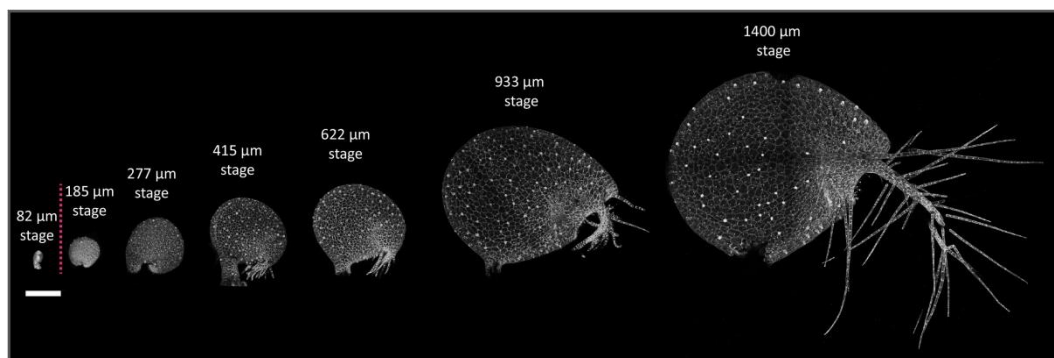
Figure 2.4: *Utricularia gibba* bladder developmental series. Bladders staged using 1.5 fold decrease from maximum bladder length of 1400 µm (antennae to furthest point at the back) +/- 20 %. Stages 185 µm – 1400 µm are found on stolons out of the circinnate apex. The 82 µm stage (before the pink line) is found within the circinnate apex. Scale bar is 200 µm. All bladders imaged using confocal microscope. Stages 185 µm-1400 µm are transgenic GFP line. 82 µm stage bladder is fixed and stained with propidium iodide.

To assign times to these bladder stages and to calculate how long bladder development from the 82 µm stage takes, I tracked the growth of bladders daily until they reached maturity (Figure 2.5, A). Measurements were made from the antennae to the furthest point

on the back of the bladder (bladder length) (Figure 2.5, B, yellow line). As the starting size of each bladder was different, I used the length measurement to place each data set on a normalised timescale of development. I used the length measurements from one sample as a reference and then aligned each subsequent data series to this reference based on the starting length (maintaining the original time interval). I plotted the natural log of bladder length against time and fitted a line to the points before the plateau (up to 192 hours) (Figure 2.5, D). I shifted all times by 96 hours so that I could extrapolate back from my data to give an estimate time for younger bladders developing within the circinnate apex (assuming the growth rate is approximately equal throughout development). The gradient of the graph gives a growth rate of 1.6 % per hour which is similar to that observed for *Arabidopsis* leaf development (Kuchen *et al.*, 2012). I was able to stage any given bladder size using the equation x = (y-c)/m where x is the value on the x axis, y is the value on the y axis, c is the y intercept, and m is the gradient. For example, the estimated time point for an 82 μm bladder based on this measure of length is 36 hours (Figure 2.5, D, red dotted line). It therefore takes approximately 170 hours for the bladder to fully develop from the 82 μm stage, through which time, the bladder increases by over 17 times in length.
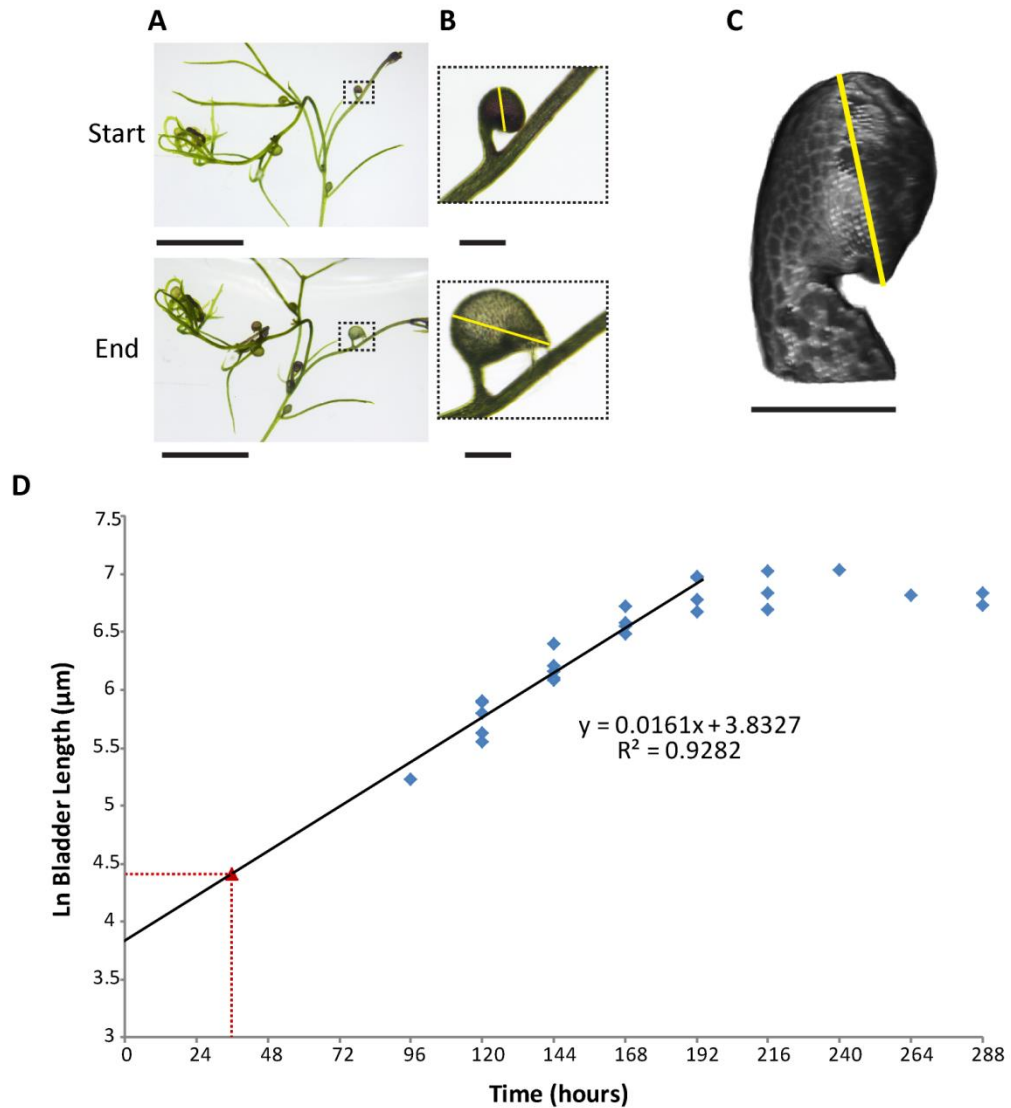
Figure 2.5: Bladder growth analysis. (A) *U. gibba* stolon embedded in low melting point agarose with free stolons and bladders for growth tracking (black dotted boxes). Start and end represent a difference in 72 hours in this example (scale bars are 5 mm). (B) Close up of bladder seen in (A) at the start and end of tracking (scale bars are 500 μm). (C) 82 μm stage bladder viewed from the side (scale bar is 50 μm). All yellow lines show where the length measurements were taken (from the antennae to the furthest point at the back). (D) Natural logarithm of bladder length against time and fitted line on points before the plateau. The gradient of the line is the bladder relative growth rate in length (1.61 % per hour). The red triangle and dotted line gives the calculated position of an 82 μm stage bladder based on the extrapolation of the graph. An R^2 value for the graph is also shown (R^2 = 0.9282) and gives a statistical measure of how close a regression line fits the data (R^2 = 1 indicates a perfect fit).

2.2.2 Characterising bladder shape change

To study bladder development from the 82 μm stage to maturity in more detail, I looked at bladder shape change in cross sections from the front, top, and side of fixed samples using optical projection tomography (OPT) and confocal microscopy (Figure 2.7). The shape of these fixed samples reflects bladder shape in the absence of any negative pressure which would have been present in live specimens at later stages. This is most notable in views from the top where bladder walls appear convex at later stages as opposed to their concave appearance when the trap is set under negative pressure (it is not clear when this negative pressure is generated during development). Therefore, fixed samples are comparable to bladders in the triggered state. I made the cross sections consistent throughout bladder stages by always cropping to biological landmarks: front sections were made by cropping parallel to the stalk, from the mouth back to where the stalk intersects the bladder. Top sections were made perpendicular to the stalk and down to where the trap door of the bladder became visible. Side sections were made by cropping to the bladder midvein (Figure 2.6).
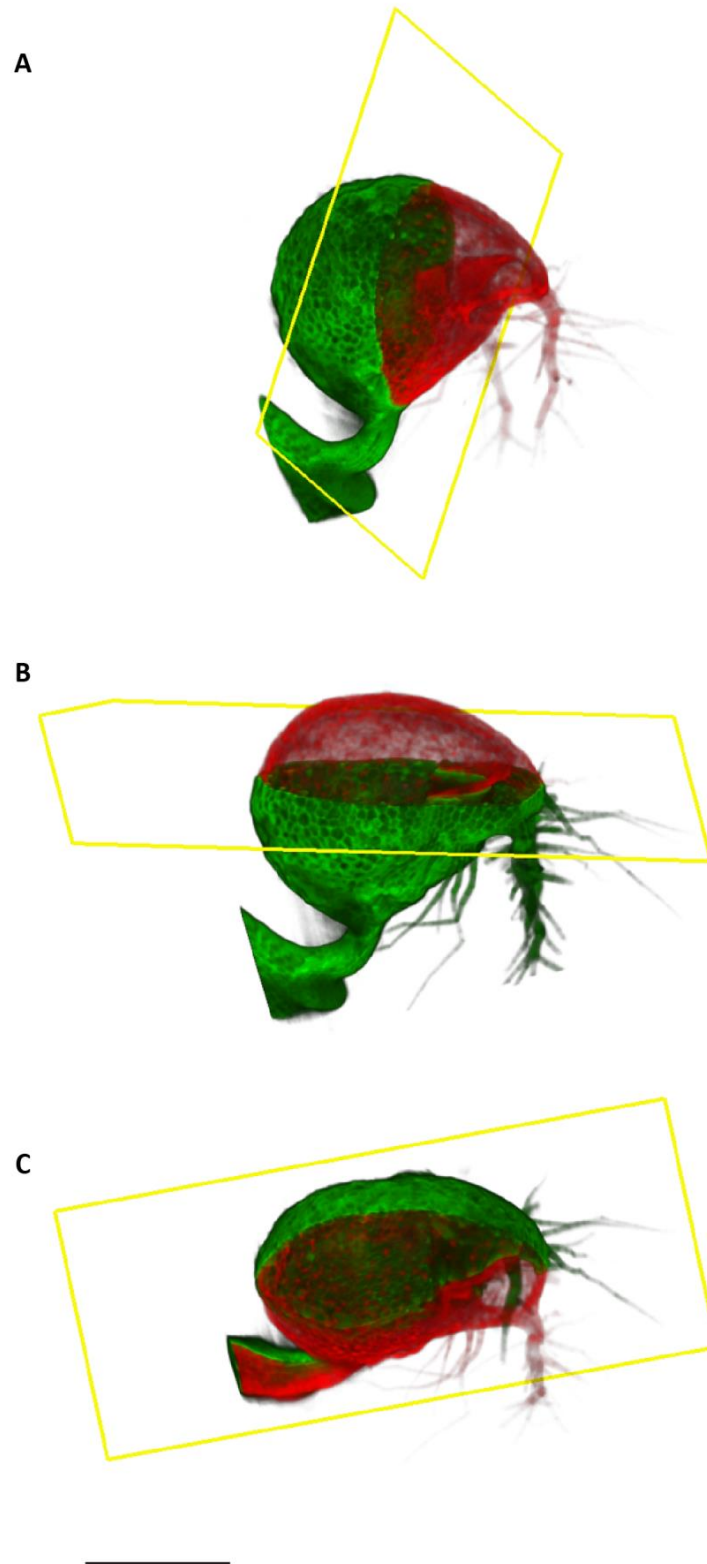
Figure 2.6: Clipping planes used to study *U. gibba* bladders in cross section. Mature bladder with clipping planes indicated for a (A) front section, (B) top section, and (C) side section. Green indicates the volume left after clipping. Red indicates the volume clipped away. Yellow boxes indicate the clipping planes. Scale bar is 550 μm.

	Front section	Top section	Side section

82 µm stage — Ai, Aii, Aiii

185 µm stage — Bi, Bii, Biii

277 µm stage — Ci, Cii, Ciii

415 µm stage — Di, Dii, Diii

622 µm stage — Ei, Eii, Eiii

933 µm stage — Fi, Fii, Fiii
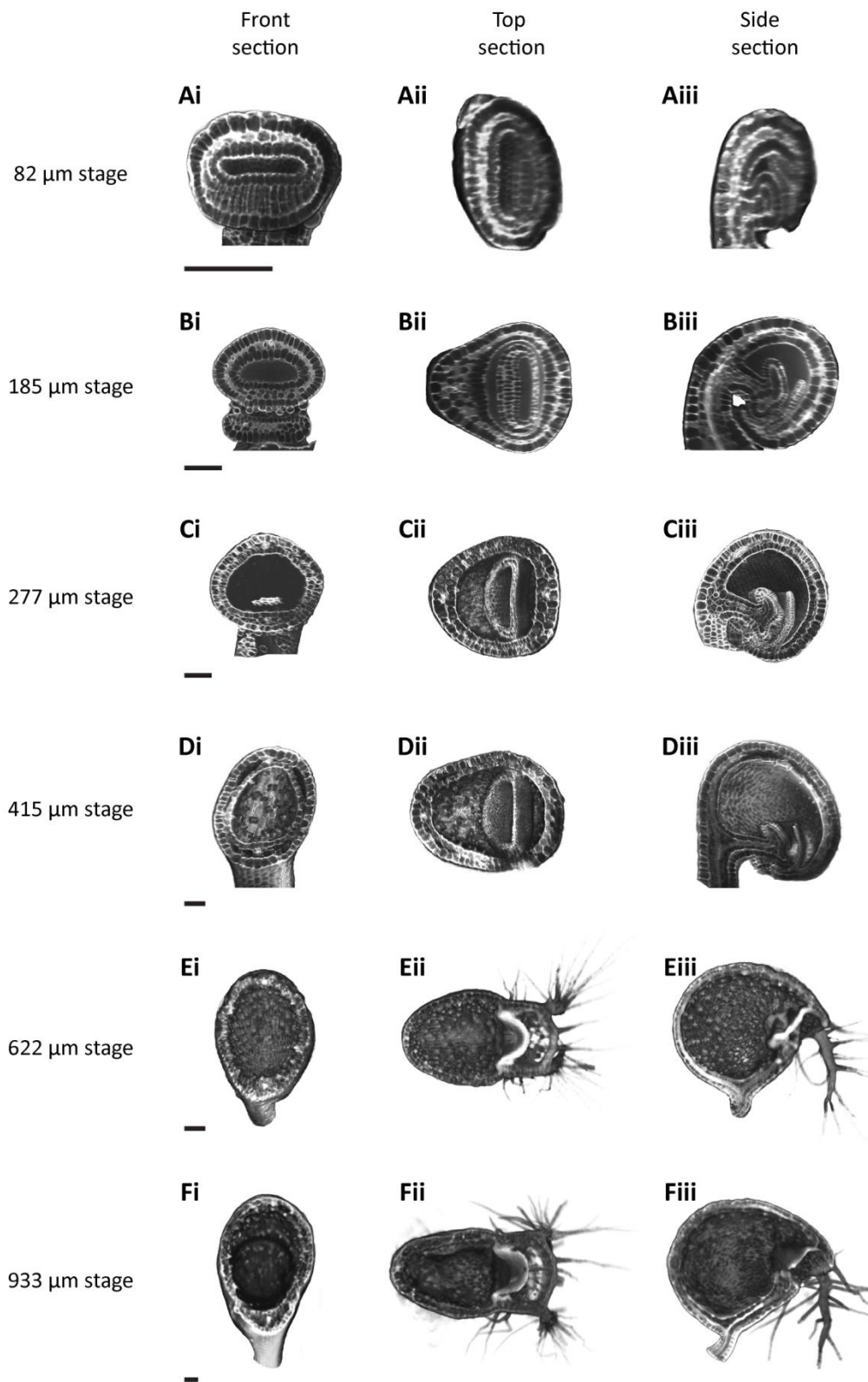
Figure 2.7: *Utricularia gibba* **bladder shape through development.** *U. gibba* bladders in cross section from the front, top, and side. Front sections were made parallel to the stalk up to the stalk intersect. Top sections are down to the trap door and perpendicular to the stalk. Side sections are to the midvein. All bladders were fixed and stained with propidium

iodide. (A-D) Imaged using confocal microscopy (Scale bars are 50 μm). (E-F) Imaged using optical projection tomography (OPT) by Karen Lee (scale bars are 100 μm).

In front section, bladders transition from an ellipse that is wider than it is tall to an ellipse that is taller than it is wide (Figure 2.7, left column). At the 82 μm stage, bladder width is approximately 25 % greater than bladder height. By maturity, bladder height is approximately 42 % greater than width. I plotted the natural logarithm of bladder width against the natural logarithm of bladder height during bladder development and found that the gradient of the line was 1.29, showing that growth rate in height is about 130 % of the growth rate in width (Figure 2.8, B).

Cross sections from the top of bladders at different stages show a transition in shape from an ellipse which is wider than it is deep to an ellipse which is deeper than it is wide (Figure 2.7, middle column). At the 82 μm stage, bladder width is approximately 56 % greater than bladder depth. By maturity, bladder depth is approximately 83 % greater than width. I plotted the natural logarithm of bladder width against the natural logarithm of bladder depth during development and found that the gradient of the line was 1.47, showing that growth rate in depth is about 150 % of the growth rate in width (Figure 2.8, D).
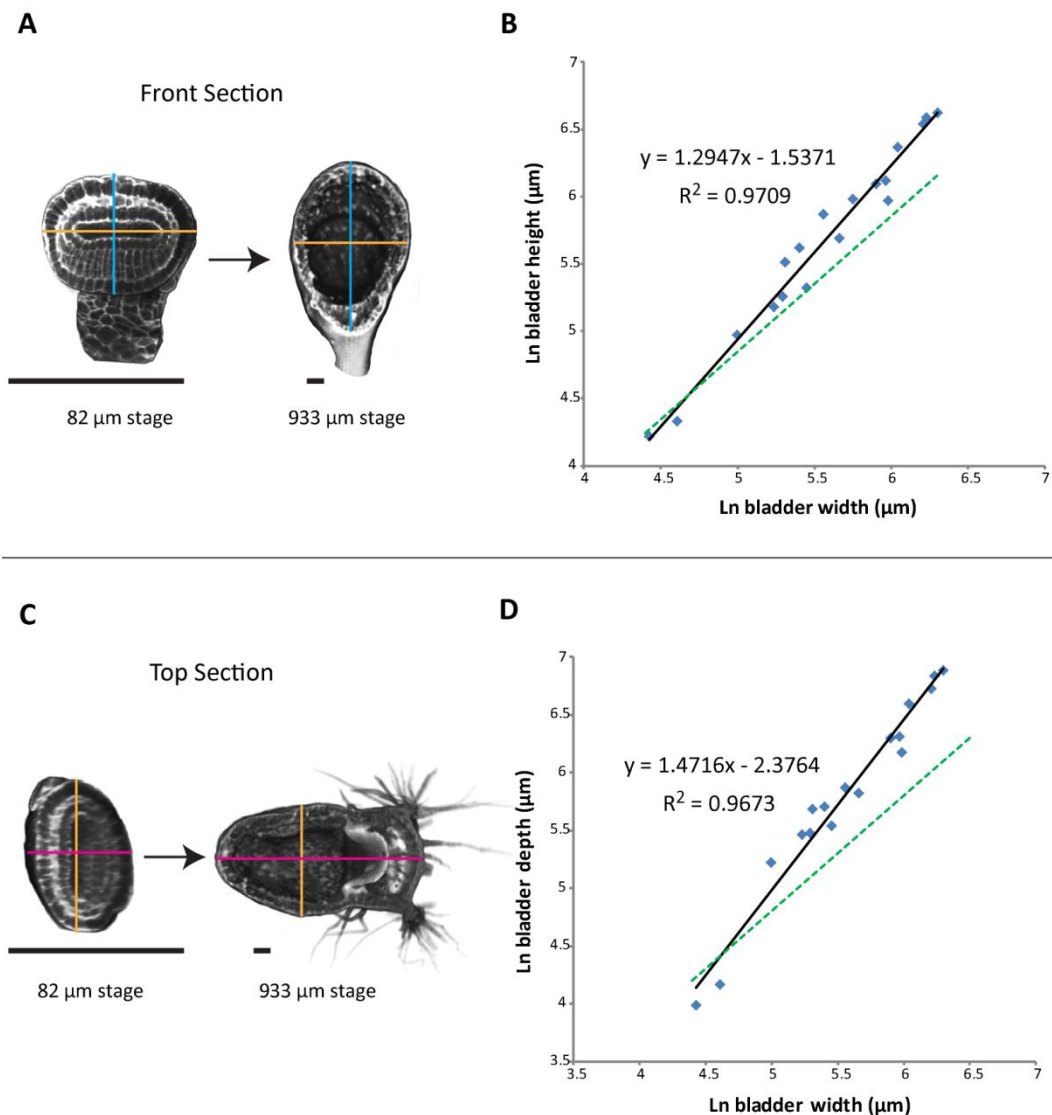
Figure 2.8: Bladder growth in height, weight, and depth. (A) Bladder viewed in cross section from the front at the 82 μm and 933 μm stage. Lines indicate how measurements were made for bladder height (blue line), and bladder width (orange line). (B) Natural log of bladder height plotted against the natural log of bladder width. The gradient of the fitted line is 1.29, showing that growth in width is less than in height. For comparison, there is a fitted line with a gradient of 1 (dotted green). (C) Bladder viewed in cross section from the top at the 82 μm and 933 μm stage. Lines indicate how measurements were made for bladder depth (pink line) and width (orange line). (D) Natural log of bladder depth plotted against the natural log of bladder width. The gradient of the fitted line is 1.47, showing that growth in width is less than in depth. For comparison, there is a fitted line with a gradient of 1 (dotted green). Bladder images are of fixed tissue stained with propidium iodide (82 μm stage was imaged using confocal microscopy and the 933 μm stage was imaged using OPT by Karen Lee). All scale bars are 100 μm.

From the side, bladders start as vertical ellipses in cross section and become more elongated through development (Figure 2.7, right column). This elongation reflects the increase in bladder depth as well as a change in the position of the mouth relative to the stalk. At early stages of development, the stalk and mouth are in close proximity (Figure 2.9, A). As the bladder develops, the stalk and mouth regions become further and further apart until the mouth is at roughly 90 º to the stalk (Figure 2.9, F).
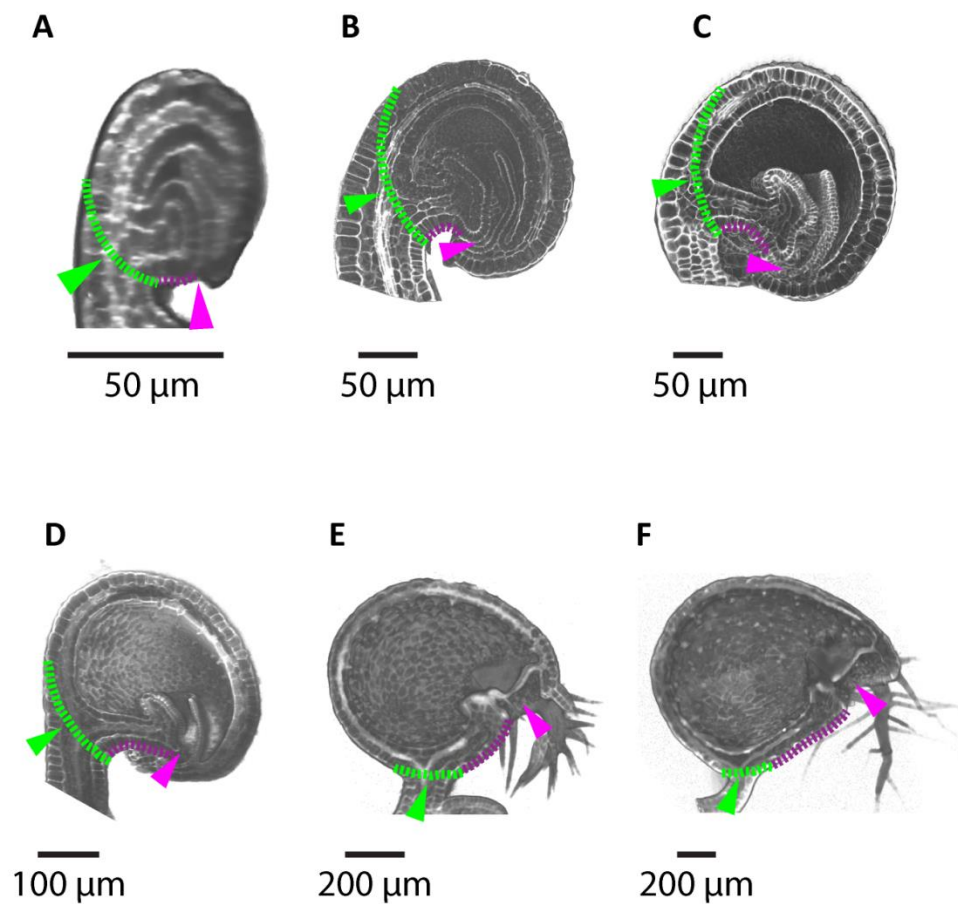
Figure 2.9: Stalk and mouth positions through development of the *U. gibba* bladder. Developmental series of *U. gibba* bladders shown in longitudinal section. The stalk intersect (green dotted line and arrow) and mouth region (pink arrow) are marked along with the region between the stalk and mouth (purple dotted line). (A) 82 µm stage, (B) 185 µm stage, (C) 277 µm stage, (D) 415 µm stage, (E) 622 µm stage, (F) 933 µm stage. Bladders are shown at different scales for comparison. All bladders were fixed and stained with propidium iodide. (A-D) Confocal microscopy (E-F) Optical projection tomography (OPT).

For the displacement of the stalk and mouth regions to occur, the region between stalk and mouth (which I termed 'chin') (Figure 2.9, purple dotted line) must grow proportionally more in length, becoming over 25 times longer from the 82 μm stage to maturity. I plotted the natural logarithm of chin length against time. I assigned a time to each bladder based on bladder length and the growth curve shown in Figure 2.5. While the bladder length has a growth rate of 1.6 % per hour (Figure 2.5), the chin region between stalk and mouth has a growth rate of 2.0 % per hour (Figure 2.10, D).
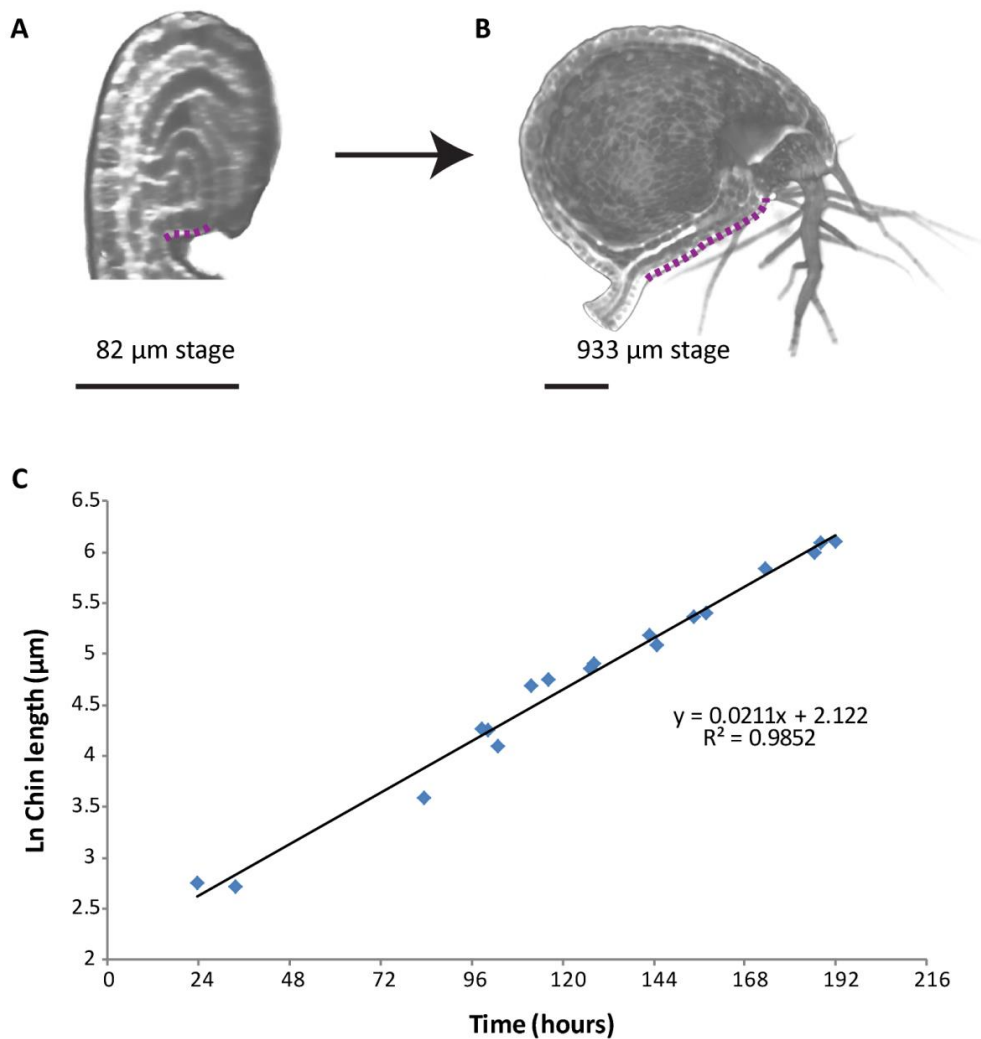
Figure 2.10: Growth analysis of the chin region. Bladder viewed in cross section from the side at (A) the 82 μm stage (scale bar is 50 μm), and (B) the 933 μm stage (scale bar is 250 μm). Lines indicating how measurements were made for chin length (purple dotted line) are shown. (C) Natural log of chin length plotted against time calculated based on bladder length. The gradient of the fitted line shows the growth rate of chin (2.11 % per hour). (A-B) Fixed tissue stained with propidium iodide and imaged using (A) confocal microscopy, or (B) OPT (by Karen Lee).

In summary, I have found that bladders go through three major shape changes:

1.) A greater increase in height versus width.

2.) A greater increase in depth versus width.

3.) An elongation in the chin region (between the stalk and mouth).

2.2.3 Modelling bladder shape change

To explore how the major shape changes in bladder development could arise, I took a computational modelling approach using the Growing Polarised Tissue (GPT) framework (Kennaway *et al.*, 2011; Green *et al.*, 2010; Kuchen *et al.*, 2012; Sauret-Güeto *et al.*, 2013).

2.2.3.1 Shape changes through isotropic and anisotropic growth

To illustrate how simple shape changes may arise through specified isotropic or specified anisotropic growth, I first considered a 2D circular canvas (Figure 2.11). I added circular clones (black) which deform with the canvas as it grows so that local growth orientations can be studied. When specified growth is isotropic and uniform, the circular canvas simply grows into a larger circle, and the clones enlarge isotropically, also remaining circular (Figure 2.11, A).

Isotropic growth

A

B

K_{areal} ← MID

C

D

MID → K_{areal}

SIDE →

E

K_{areal}

4 % — 6.8 %

Anisotropic growth

F   **G**   **I**   **K**   **L**

H

BASE → POL ⊢ TOP

J

$K_{par} > K_{per}$

M   **O**   **N**   **P**
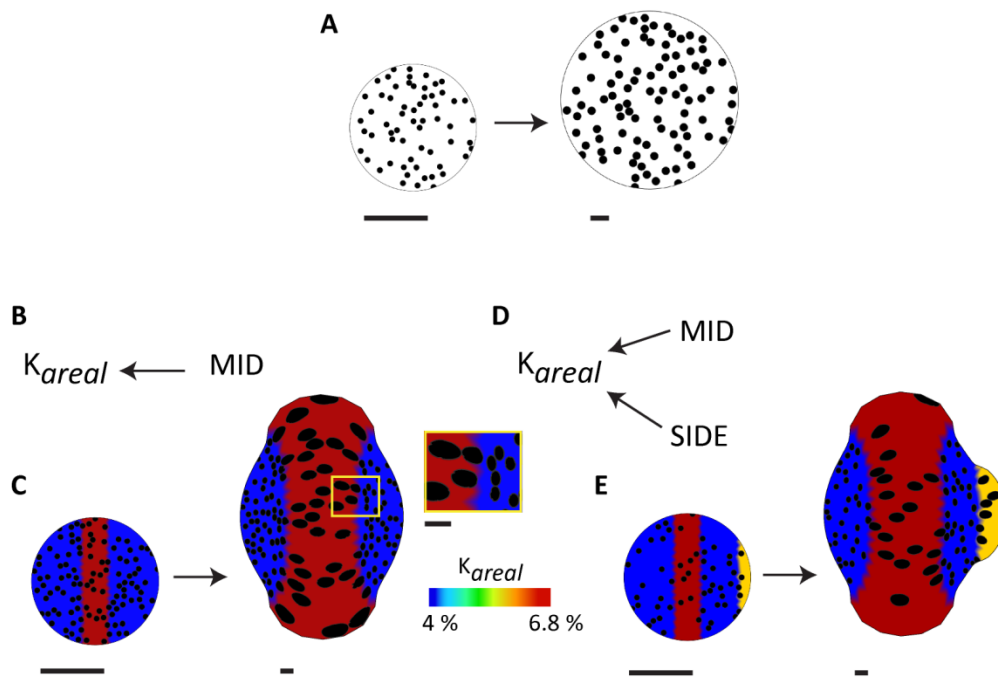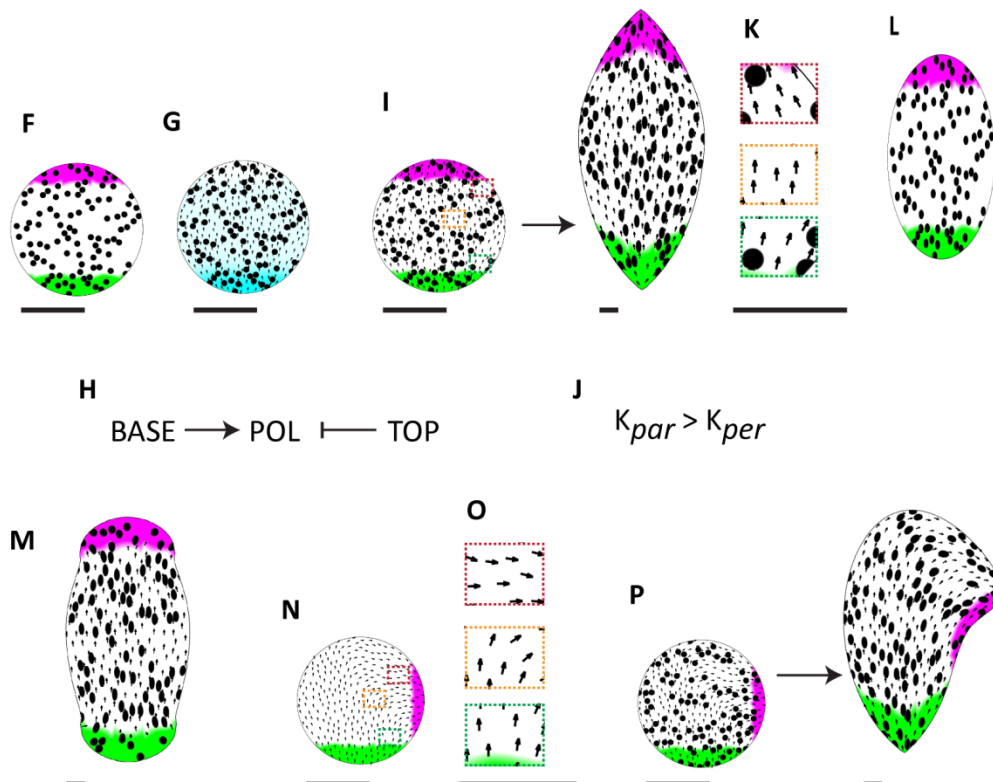
Figure 2.11: 2D shape changes through isotropic and anisotropic growth. (A-E) Isotropic growth models. (A) 2D circular canvas grown isotropically with uniform growth rates across the tissue. (B) Growth regulatory network for (C) where areal growth is promoted by the MID factor (red). (C) 2D circular canvas with MID factor where areal growth is promoted. Start and final shapes of the canvas are show with K_{areal} plot. Yellow box indicates zoomed in region where clone orientations can be viewed more clearly. (D) Growth regulatory network for (E) where areal growth rate is promoted by MID (red region) and SIDE (yellow region). (E) Start and end shape of the canvas are shown with K_{areal} plot. (F-O) Anisotropic growth models. (F) 2D circular canvas with BASE (green) and TOP (pink) factors shown. (G) Diffusible POLARISER (blue) which propagates from the + organiser (BASE, green) and is absorbed by the - organiser (TOP, pink). This generated a poarity field which is represented by arrows. (H) Polarity regulatory network (PRN) for anisotropic models. (I) Start and end shapes of the canvas grown where $K_{par} > K_{per}$ (J). (K) Local polarities in different regions of the canvas shown in (I). (L) Shape generated when the circular canvas is digitally stretched in one direction. (M) Final canvas shape when BASE and TOP are specified to grow isotropically. (N) Canvas start shape with the − organiser displaced by 90 °. The resulting polarity field is indicated (arrows). (O) Local polarities in different regions of the canvas shown in (N). (P) Start and end shape of canvas grown with displaced − organiser. Black clones are induced as circles from the start and deform with the canvas as it grows. Scale bars are 1 mm (except for in K and O where scale bar is 500 μm).

Different shapes may be generated with isotropic growth when growth rates across the canvas are no longer uniform. For example, when I add a factor termed MID down the middle of the circle, and specify areal growth rate here to be higher than the rest of the canvas (Figure 2.11, C, red), the canvas deforms, becoming taller than it is wide (Figure 2.11, C). Although specified growth is isotropic, clones are no longer circular across the canvas. Clones at MID are larger and more elliptical than those in the region of lower specified growth rate. This is because the introduction of differential growth rates causes areal conflict across the tissue. Where growth rate is highest at MID, tissue is constrained by neighbouring regions which are growing more slowly. This conflict results in the MID region being unable to grow as tall as would if it were not constrained. Clones in this region are therefore elliptical due to resultant anisotropic growth caused by areal conflict. More complex shapes can be created when I introduce asymmetry to the model (Figure 2.11, E). If I add another factor to one side of the canvas (SIDE) (Figure 2.11, E, yellow) and promote areal growth here, a bulge in the canvas is generated on this side.

To consider specified anisotropic growth, axiality is required. To introduce axiality I set up a polarity field in the canvas. I added two organisers to the canvas: a plus organiser termed

BASE (green) and a minus organiser termed TOP (pink) (Figure 2.11, F). POL was introduced which can propagate throughout the canvas from the plus organiser and is absorbed by the minus organiser (Figure 2.11, G, turquoise). This generates a polarity field which is represented as arrows across the canvas (Figure 2.11, G). When areal growth rate is equal across the canvas but K_{par} is higher than K_{per}, the canvas deforms to be taller than it is wide (Figure 2.11, I). Here, all clones are elliptical, parallel with the polarity field and are the same size across the canvas. This is because areal growth rate is equal across the canvas and growth is uniformly anisotropic. In this model, the canvas forms points at the base and top. This is because the polarity field is not simply pointing from the BASE to TOP but diverges from BASE and converges at TOP (Figure 2.11, K). Therefore, local polarities vary across the tissue. Since polarity is orienting growth, this introduces a difference in local growth orientations. This generates directional conflict in the canvas, as growth in some regions is oriented differently to growth in neighbouring regions. The shape is therefore different from simply stretching the circular canvas to make it taller (Figure 2.11, L). For the polarity field model, the base and top can be made smoother by specifying these regions to grow isotropically (Figure 2.11, M). Asymmetry can be generated in this model simply by displacing the minus organiser. For example, when the minus organiser is displaced by 90 ° (Figure 2.11, N) the level of directional conflict increases, since there is more difference between the local polarities of the canvas. This causes the canvas to grow in width as well as in height.

These simple 2D models show how deformation in shape can occur through specified isotropic or specified anisotropic growth and how GFtbox can be used to explore such deformations and make predictions on resultant growth orientations using clones which deform with the canvas.

2.2.3.2   Setting up the canvas to model bladder shape changes

To explore these principles in the context of bladder development I generated a 3D hollow caplet shaped canvas to use as my start shape and scaled this to an 82 µm stage bladder (Figure 2.12). I then explored isotropic and anisotropic specified growth to see if I could capture the major shape changes in bladder development by using simple growth parameters.
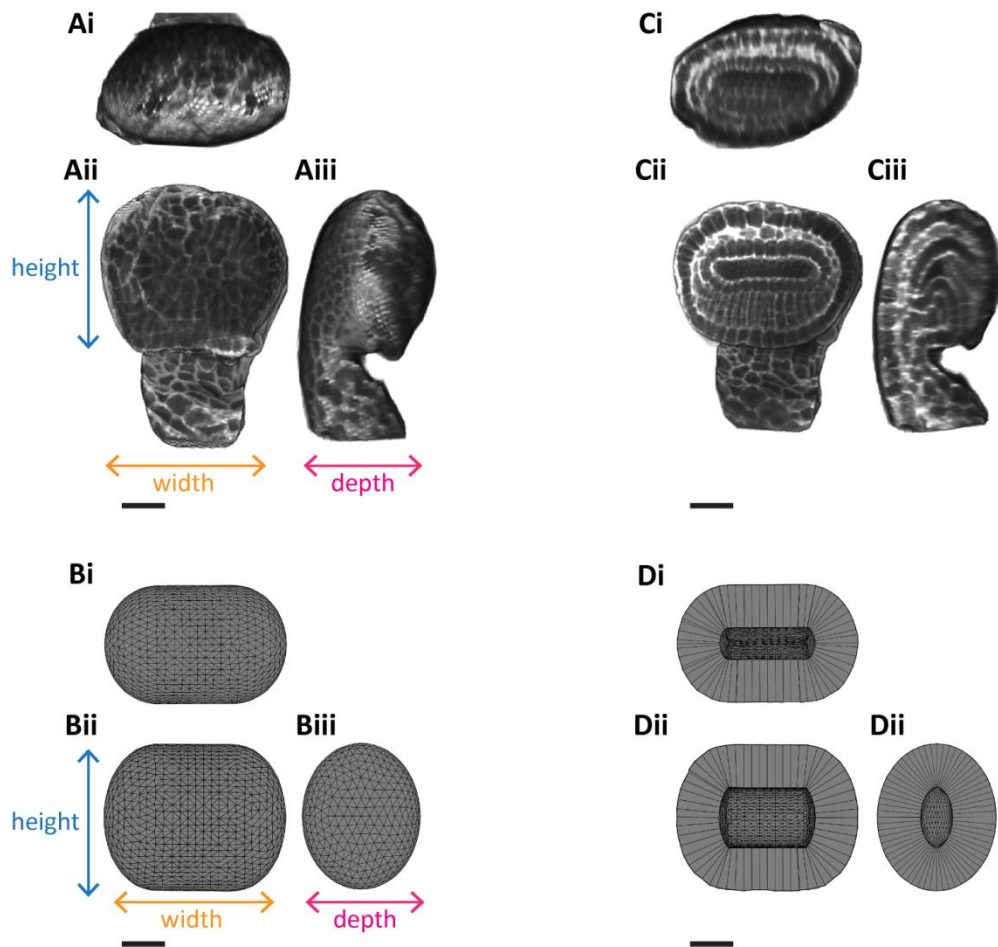
Figure 2.12: Canvas start shape based on measurements of an 82 μm stage bladder. (A) An 82 μm stage bladder viewed from the top (Ai), front (Aii), and side (Aiii). (B) Whole canvas start shape viewed from the top (Bi), front (Bii), and side (Biii) and scaled to an 82 μm stage bladder. (C) Cross sections through the top (Ci), front (Cii), and side (Ciii) of the same 82 μm stage bladder shown in (Ai-Aiii). (D) Cross sections through the canvas shown in (Bi-Biii) from the top (Di), front (Dii), and side (Diii). Height, depth, and width axes are shown in (A and B). (A and C) Confocal images of a fixed sample stained with propidium iodide. All scale bars, 20 μm.

2.2.3.3 Isotropic bladder growth models

I first explored bladder morphogenesis with isotropic specified growth, since this does not require any axiality and is therefore the simplest model to start with. I began with my caplet start shape and explored bladder shape changes using areal conflict alone. I started by considering a simple change in height relative to width, similar to the transition dealt with in 2D above (Figure 2.11, C). In the bladder, this shape transition occurs in 3D and may be thought of as the flattening of a capsule from the sides and a growth in height around

45

the midvein. This is illustrated in Figure 2.13. In the capsule shape (Figure 2.13, A) the blue circumference is larger than the red circumference. In the flattened disc (Figure 2.13, B), the red circumference is larger than the blue circumference. If we imagine the capsule shape growing into the flattened disc, more growth must occur in the red circumference compared to the blue circumference to account for the change in their relative sizes. This is very similar to the transition seen in the *U. gibba* bladder which becomes flattened in width and grows in height.
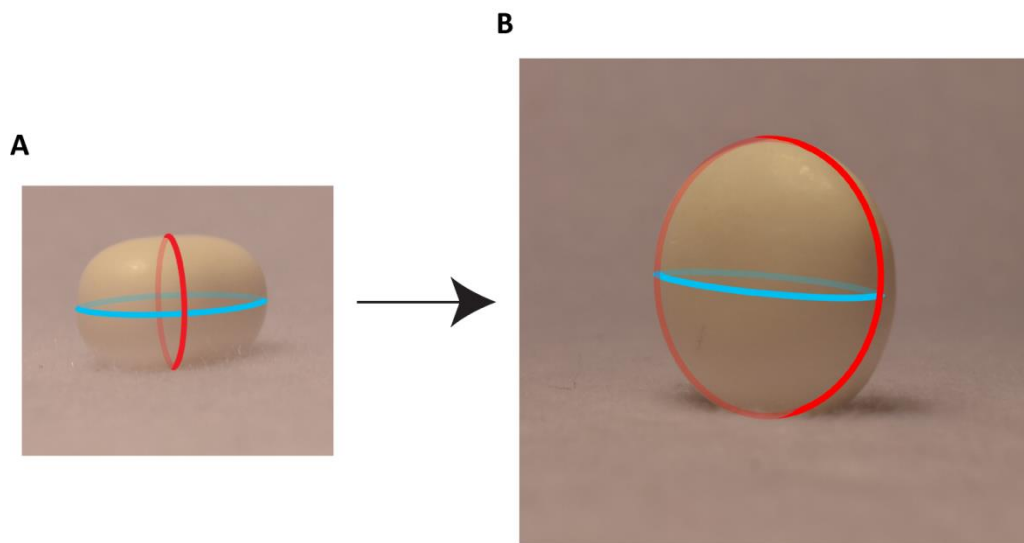
Figure 2.13: 3D shape transitions from a capsule to a flattened disc. (A) Capsule where the blue circumference is larger than the red circumference. (B) Flattened disc where the red circumference is greater than the blue circumference. Photographs kindly provided by Robert Green.

To model this shape transition using isotropic specified growth, I introduced a MIDVEIN factor round the centre of the canvas (Figure 2.14, A) and diffusible factor S_MIDVEIN which diffuses from here (Figure 2.14, B). I then specified areal growth rate to be promoted relative to the local level of S_MIDVEIN so that specified areal growth was highest near the midvein region and lowest at the two sides.
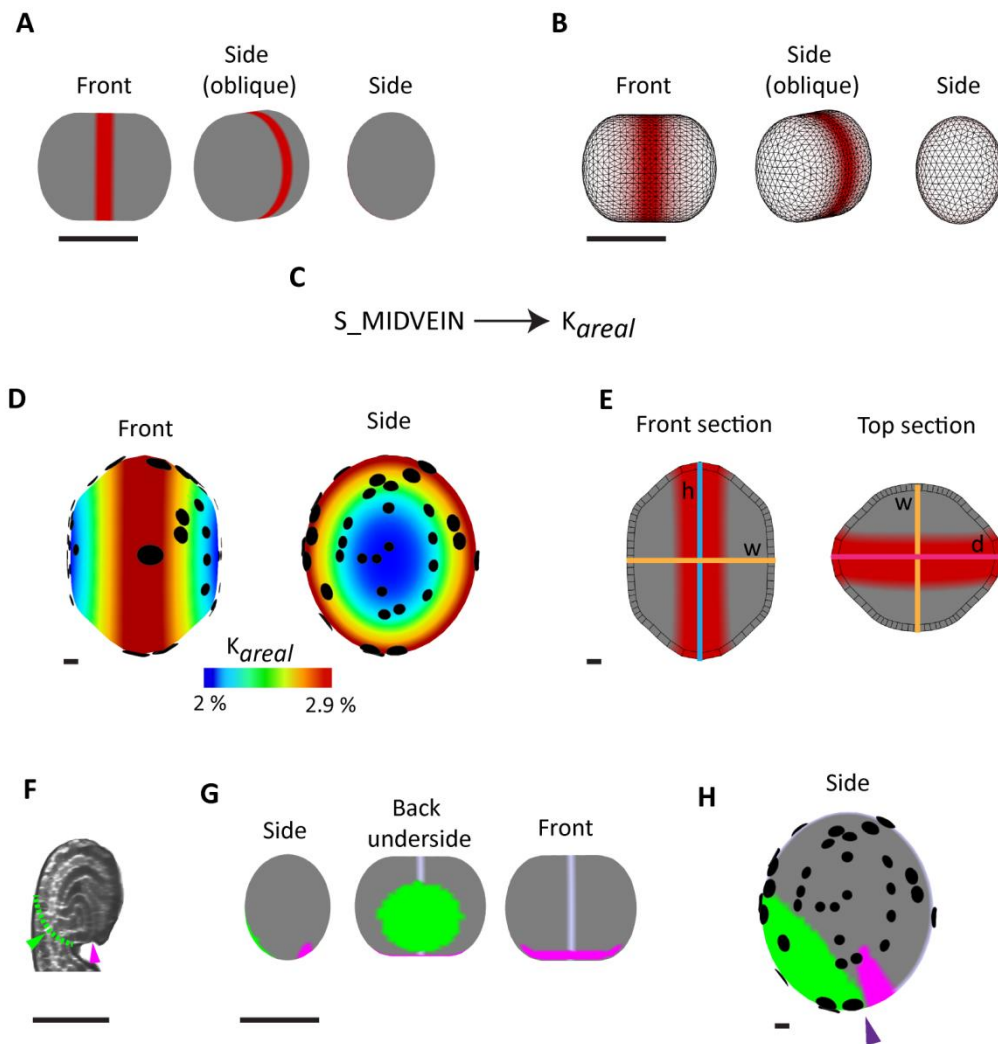
Figure 2.14: Model 1-isotropic specified growth with a gradient of areal growth rates. (A) Canvas start shape with MIDVEIN factor shown (red). (B) Diffusible factor S_MIDVEIN (red) propagates from MIDVEIN to form a gradient across the canvas (elements are shown to allow visualisation of white regions where the level of S_MIDVEIN is very low). (C) Growth regulatory network (KRN) where areal growth rate is promoted at S_MIDVEIN. (D) Canvas end shape with K$_{areal}$ plot. (E) Cross sections from the front and top of the canvas end shape. Lines mark where measurements were made for height (blue line), width (orange line), and depth (pink line). (F) Side section through an 82 μm stage bladder with the stalk intersect (green dotted line and arrow), and mouth region (pink arrow) indicated. (G) Canvas start shape with STALK (green), and MOUTH (pink) regions which were scaled to an 82 μm stage bladder. The pale lilac stripe is used for reference of the front view of the canvas. (H) Model end shape (viewed from the side) with biological landmarks, STALK (green) and MOUTH (pink) marked. Purple arrow indicates the region between STALK and MOUTH. All scale bars are 50 μm.

This gradient in specified areal growth rates can be seen at the final stage of the model (Figure 2.14, D). This model grows more in height relative to width. This height is achieved

due to the areal conflict in the growing canvas. Regions which are closer to the midvein have higher specified areal growth rates, while regions further from the midvein have lower specified areal growth rates. This is reflected in the clone size and shape; clones nearest the midvein appear larger and more elliptical while clones further away from the midvein appear smaller and less elliptical. The end shape of the canvas is about 34 % taller than it is wide (figure Figure 2.14, E, front section), compared to a 42 % difference in the mature bladder. This restriction in the growth rate in width also causes the model to become 16 % deeper than it is wide (Figure 2.14, E, top section). This is substantially lower than the 83 % difference in depth versus width seen in the mature bladder.

In side view, the canvas remains oval (Figure 2.14, D, side). To explore the displacement of the stalk and mouth seen in the bladder, I added two factors for visual reference. I called these factors STALK and MOUTH and positioned them based on measurements of the stalk intersect and mouth of an 82 µm stage bladder (Figure 2.14, F-G). For ease of viewing I have included a visual factor at the midvein for reference (Figure 2.14, G, pale lilac) which runs around the centre of the canvas so that it is visible from the front but not from the side. When I run the model with these regions marked, STALK and MOUTH remain in close proximity (figure, purple arrow) and we do not see the displacement of these regions observed in the bladder (Figure 2.9).

<u>Displacing the STALK and MOUTH regions</u>

To generate a displacement between the STALK and MOUTH regions, I first tried increasing the growth rate in the region between STALK and MOUTH alone, since the resultant growth rate of this region is higher than that of the main body of the bladder (Figure 2.10). I added a factor termed CHIN to the canvas which I positioned between STALK and MOUTH based on an 82 µm stage bladder (Figure 2.15, A-B). I then increased areal growth at CHIN in the model so that it was greater than the highest areal growth rate specified in the original gradient from MIDVEIN. Now that I am considering biological landmarks such as the STALK region of the bladder, for consistency, I will always show the final canvas with the stalk intercept at the base to represent the same orientation as the bladder shown in (Figure 2.9). All measurements will be made with the canvas in this orientation.
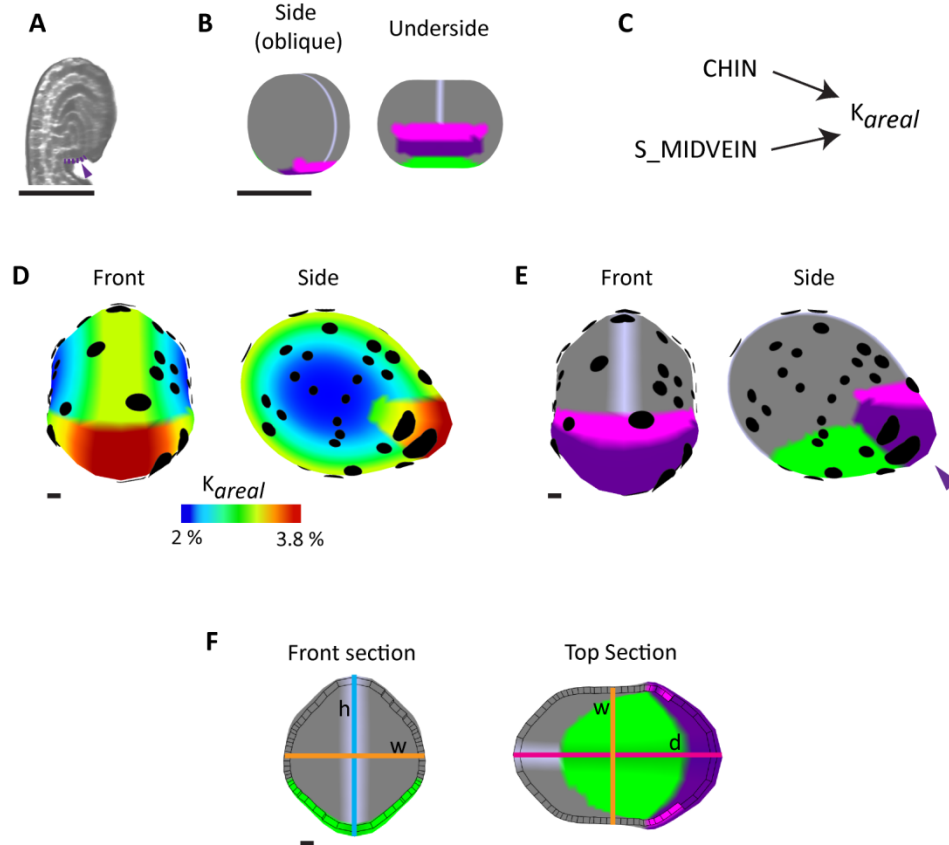
Figure 2.15: Model 2- isotropic specified growth with increased areal growth rate at CHIN. (A) Side section through an 82 µm stage bladder indicating the chin region between the stalk and mouth (purple dotted line and arrow). (B) Canvas start shape with added CHIN factor (purple), in between STALK (green) and MOUTH (pink). (C) KRN where areal growth rate is promoted at CHIN as well as S_MIDVEIN. (D) Canvas end shape with K$_{areal}$ plot. (E) Canvas end shape with CHIN (purple), STALK (green), and MOUTH (pink) regions plotted. (F) Cross sections from the front and top of the canvas end shape. Lines mark where measurements were made for height (blue line), width (orange line), and depth (pink line). All scale bars are 50 µm.

I found that increasing the areal growth rate at CHIN displaced the STALK and MOUTH regions. However, the CHIN region only increased in length by around 18 times (compared to 25 times in the bladder) and bulged out. This bulging of the canvas at CHIN is due to areal conflict which arises as the CHIN region grows faster than neighbouring regions of the canvas. The CHIN region is restricted in growth by connected tissue which is growing at a slower rate.

This model does not fully achieve the change in length versus width or depth; the model grows to become around 19 % taller than it is wide and 52 % deeper than it is wide

(compared to 42 % and 82 % in the bladder). Changing parameters in the model may be able to solve this.

These models suggest that isotropic growth with differential growth rates can achieve a transition from a shape that is wider than it is tall to a shape that is taller than it is wide and from a shape that is wider than it is deep to a shape that is deeper than it is wide. However, these models do not achieve the full bladder proportions. Furthermore, isotropic growth with higher areal growth rate at CHIN is not sufficient to generate the elongation at CHIN required and instead leads to a bulge in the tissue.

2.2.3.4   Adding specified anisotropy to the CHIN region alone

I next explored generating the displacement of STALK and MOUTH in a way that would not cause the canvas to bulge. Since the bulging is due to higher areal growth at CHIN, I tried using specified anisotropic growth in the CHIN region alone to see if directional growth combined with an increase in areal growth rate could generate an elongation of the CHIN region without causing the canvas to bulge.

I first introduced axiality to this model by considering the STALK and MOUTH regions as plus and minus organisers respectively. This gave me an initial canvas with a polarity pointing from STALK to MOUTH (Figure 2.16, A). Local growth rates could then be specified in an anisotropic manner by specifying differences in K_{par} and K_{per}. To try to create a displacement of STALK and MOUTH, I specified anisotropic growth at CHIN where $K_{par} > K_{per}$. Specified isotropic growth was maintained in the rest of the canvas. I also restricted growth at STALK isotropically to reflect the smaller stalk region seen in the mature bladder.
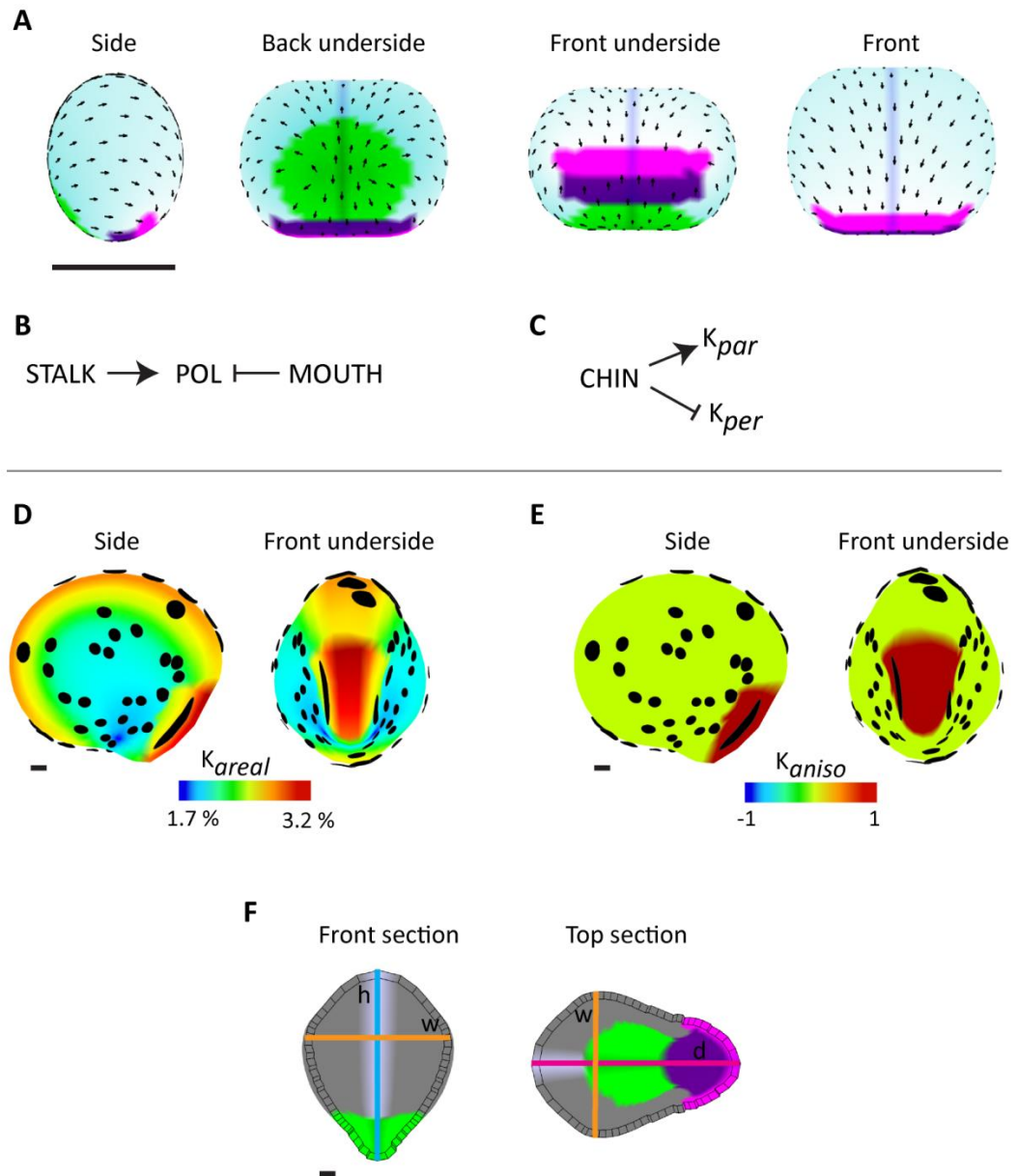
Figure 2.16: Model 3- isotropic specified growth with specified anisotropic growth at CHIN to remove bulge. (A) Set up of a polarity field which propagates forn the + organiser (STALK, green) to the - organiser (MOUTH, pink). The polarity field is represented by arrows across the canvas. (B) PRN for the model. (C) KRN for the model where CHIN promotes K_{par} and inhibits K_{per}. (D) Model with K_{areal} plot. (E) Model with K_{aniso} plot. (F) Front and top sections of the canvas end shape with lines showing where measurements of height (blue line), width (orange lines), and depth (pink line) were made. All scale bars are 50 μm.

Specified areal growth rate is highest at CHIN compared to the rest of the canvas and there is now also specified anisotropy at the CHIN region alone. This is reflected in plots of resultant areal growth rate and anisotropy (Figure 2.16, D & E). The combination of increased areal growth and specified anisotropy at CHIN was able to generate an

elongation at CHIN so that the CHIN region increased in length by around 25 times (the same as that in the bladder). This promoted a displacement of the STALK and MOUTH without generating a bulge in the canvas. The canvas increases more in height versus width and more in depth versus width, becoming 25 % taller that it is wide and 38 % deeper than it is wide (compared to 42 % and 83 % in the mature bladder respectively) (Figure 2.16, F). The bladder therefore manages to achieve the major shape transitions but not to the full extent of the mature bladder. Changing the parameters used may be able to generate a final canvas size more comparable to the mature bladder.

This modelling makes a number of predictions about bladder growth which I explored in more detail:

1.) That anisotropic growth, and therefore axiality, is necessary to generate an elongation of the CHIN region.

2.) Clones near the MIDVEIN are larger than those at the sides of the canvas.

3.) The orientation of the clones differs across the canvas: clones near the MIDVEIN are perpendicular to the MIDVEIN.

Model 3, prediction 1: Clones in the CHIN region are more anisotropic compared to the rest of the canvas.

The first prediction is that specified anisotropic growth, and therefore axiality, is necessary to generate an elongation of the CHIN region without causing the tissue to bulge. In model 3, clones at CHIN therefore appear more anisotropic to those on the rest of the canvas.

To quantify the difference in anisotropy between the main body of the canvas and the CHIN region, I calculated the rate of increase in anisotropy per hour using the following equation:

$$\frac{\text{Ln(major/ minor)}}{200}$$

Where 200 is the total growth time (hours) of the model and it is assumed that the rate of increase in anisotropy is exponential (as growth is exponential).

I then plotted the mean rate of increase in anisotropy per hour of the clones in the CHIN region versus the rest of the canvas (Figure 2.17).
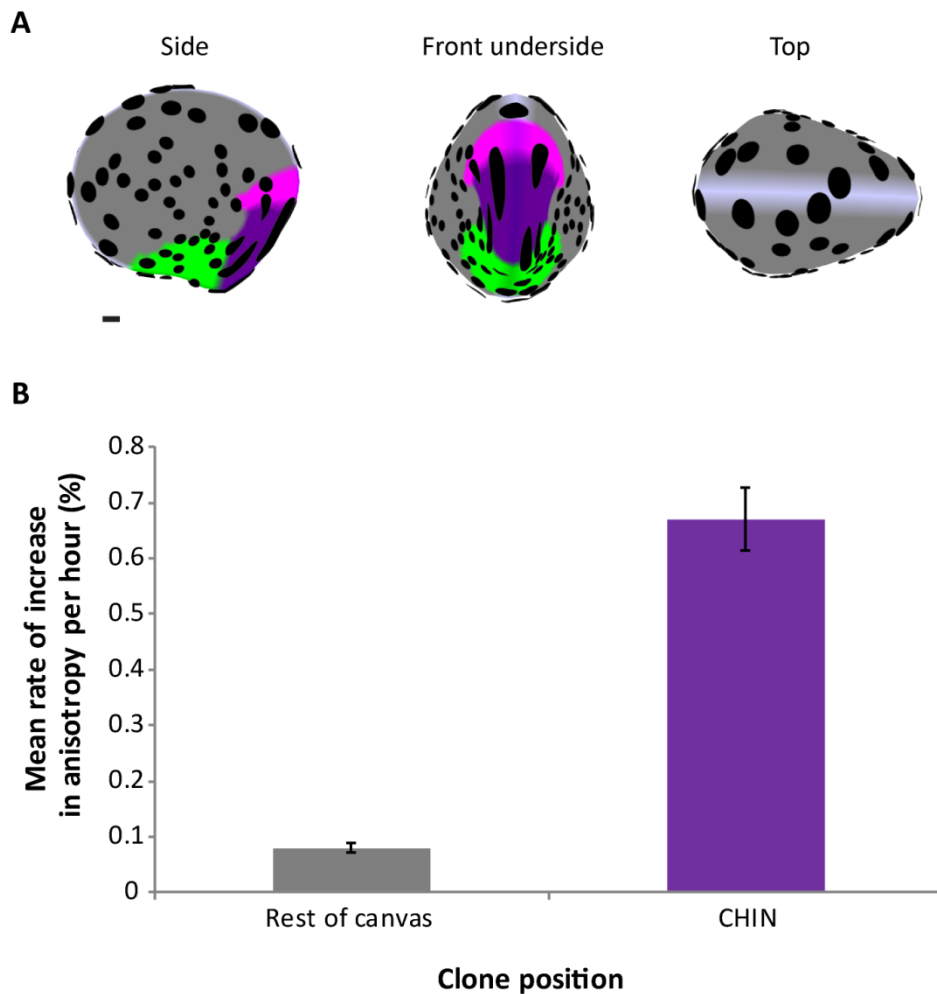
Figure 2.17: Percentage rate of increase in anisotropy per hour at the CHIN region versus the rest of the canvas (model 3). (A) Model end shape viewed from the side, front underside, and top. The CHIN (purple), MOUTH (pink), and STALK (green) regions are shown. Clones are also shown (black) which start as isotropic circles and deform with the canvas. Scale bar is 50 µm. (B) Percentage rate of increase in anisotropy per hour at the CHIN region versus the rest of the canvas. Rate of increase in anisotropy per hour = (Ln (major/minor))/ 200. Bars are standard error of the mean.

I found that the mean rate of increase in anisotropy per hour in the CHIN region of the model is over 8 times greater than that of the rest of the canvas (around 0.67 % per hour at the CHIN region compared to around 0.08 % per hour in the rest of the canvas).

Model 3, prediction 2: Clones are larger near the MIDVEIN and smaller at the sides of the canvas.

There appears to be a difference in the size of clones from the MIDVEIN and the sides of the canvas. Clones near the MIDVEIN appear to be larger than clones near the side of the canvas which appear smaller and more rounded (Figure 2.17, A). To quantify the area of clones in relation to their distance from the MIDVEIN, I used the level of S_MIDVEIN as a proxy for clone position in relation to the MIDVEIN, since S_MIDVEIN diffuses from MIDVEIN and creates a gradient across the canvas. The further from the MIDVEIN, the lower the level of S_MIDVEIN (Figure 2.18, A).

To explore clone area across the canvas, I first plotted the natural logarithm of clone area against the level of S_MIDVEIN (Figure 2.18, B). As the level of S_MIDVEIN increases, clone area increases, showing that clones closest to the MIDVEIN have a larger area compared to those at the sides of the canvas. This is expected because the specified areal growth rate is set by the level of S_MIDVEIN. Smaller clones (Figure 2.18, B, green circles) are from the STALK region of the canvas where growth is restricted.
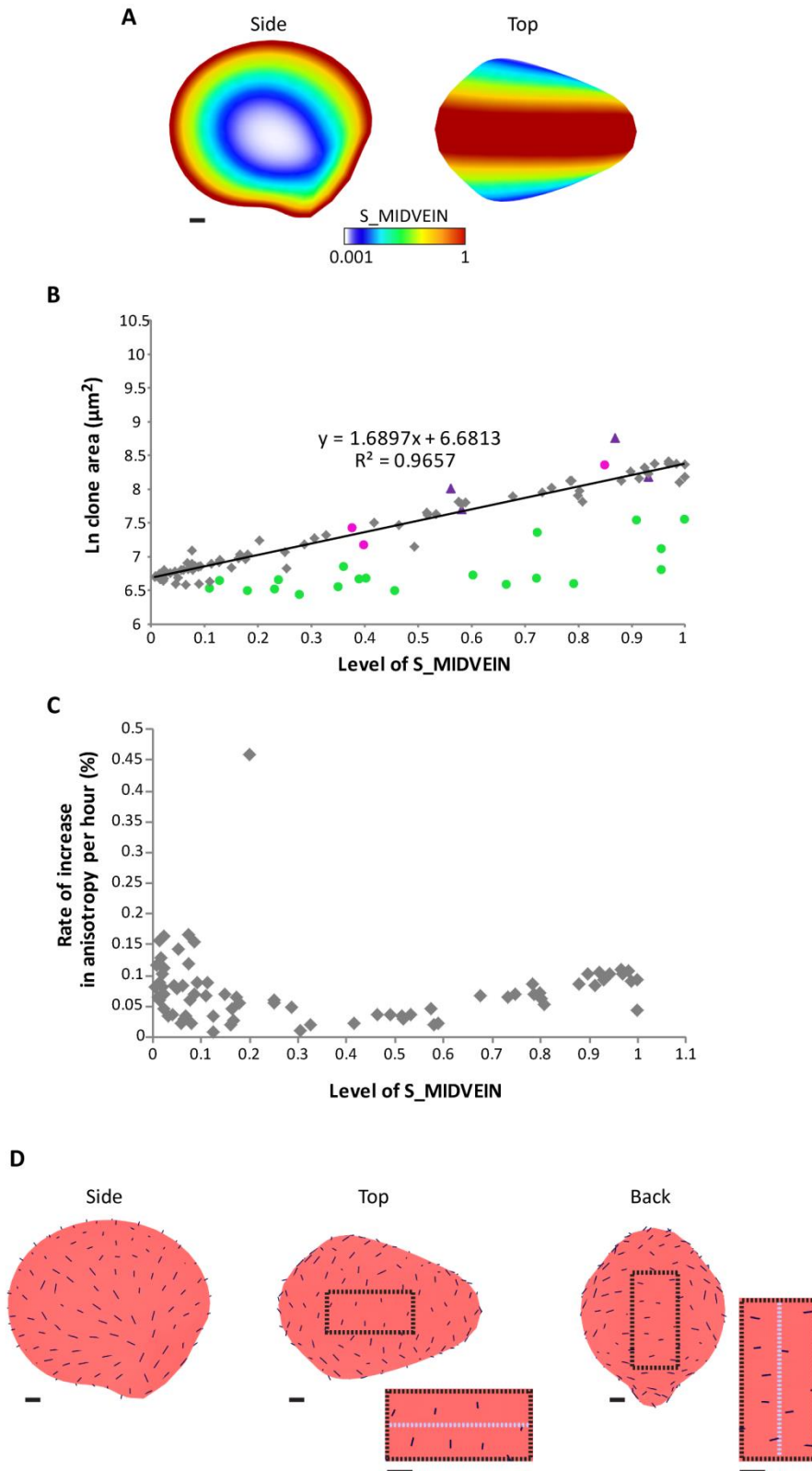
Figure 2.18: Clone area and rate of increase in anisotropy per hour in regions of the canvas at different distances from MIDVEIN (model 3). (A) Model end shape shown from the side and top with S_MIDVEIN plot. S-MIDVEIN diffuses from MIDVEIN and creates a gradient across the canvas. This gives a proxy for clone position on the canvas according to the local level of S_MIDVEIN (higher at the MIDVEIN- red region, lower near the sides of the

canvas- white region). (B) Natural logarithm of clone area against the level of S_MIDVEIN. Data points are coloured to indicate their position on the canvas: main body of the canvas (grey), CHIN (purple triangles), MOUTH (pink circles), and STALK (green circles). Line was fitted to data from the main body of the canvas (grey diamonds). The equation of the line is shown where 1.6897 is the gradient of the line. The R^2 value is given (where 1 indicates a perfect fit of the line to the data). (C) Rate of increase in anisotropy per hour for each clone on the main body of the canvas plotted against the level of S_MIDVEIN at that clone's position. All data is from the main body of the bladder. (D) End shape of the canvas shown from the side, top, and back with the major axis of growth marked (black lines). Boxes show zoomed in regions from the top and back. Orientation of the MIDVEIN is indicated (pale lilac dotted line) for reference. All scale bars are 50 μm.

Model 3, prediction 2: Clones nearest to the MIDVEIN are oriented perpendicular to the MIDVEIN.

Clones near the MIDVEIN appear to be oriented perpendicular to the MIDVEIN (Figure 2.17, A, top view). To study resultant anisotropy across the canvas, and to see if clones are more anisotropic nearer the MIDVEIN region, I plotted the rate of increase in anisotropy per hour against the level of S_MIDVEIN (Figure 2.18, C). I plotted clones from the main body of the bladder only so that the data was not skewed by higher anisotropy in the CHIN region. There is a low level of anisotropy across the canvas; however, I found no correlation between clone proximity to the MIDVEIN and the rate of increase in anisotropy per hour. Most data points on the graph are below 0.2 % per hour (with the exception of one outlier).

To test whether clones nearer the MIDVEIN are oriented perpendicular to the MIDVEIN, I plotted the major axis of growth across the canvas (Figure 2.18, D). The major axis of growth near the MIDVEIN at the top and back of the canvas is perpendicular to the MIDVEIN, compared to the major axis of growth on the sides of the canvas which, in general, is more parallel to the MIDVEIN. This pattern of clone orientation is due to the resolution of areal conflict between the tissue which is growing fastest around the MIDVEN, and the more slowly at the sides. The tissue in the MIDVEIN is unable to expand as much as it would in isolation, and so the clones are elliptical. This is similar to the clone elongation observed 2D when a band of high growth was included in the centre of a growing circle of tissue (Figure 2.11, C).

<u>**Conclusions**</u>

Model 3 predicts that there is a higher level of resultant anisotropy at the CHIN region of the bladder which arises through specified anisotropy in this region alone. The model also predicts that growth near the midvein is higher than at the sides of the bladder and that there is a low level of resultant anisotropy across the main body of the bladder which is oriented perpendicular to the midvein at regions closer to the midvein, and more parallel to the midvein at the sides.

In summary, models using specified isotropic growth alone (Figure 2.14 & Figure 2.15) show that, while shape changes in the main body of the bladder can be partly accounted for with isotropic growth alone, elongation of the chin region in a pure isotropic model leads to a bulge in the canvas at this region. This is due to the resolution of areal conflict in the model. A mixed model which has specified anisotropy at the CHIN region was successful at generating an elongation at the CHIN region without generating a bulge (Figure 2.16). This suggests that anisotropy is required to generate elongation of the chin region and separation of the stalk and mouth regions in the bladder. It is unclear here what effect anisotropy across the main body of the canvas would have on the final shape.

2.2.3.5 Anisotropic bladder growth models

To address what effect specified anisotropy across the main body of the bladder would have, I next explored modelling bladder morphogenesis with uniform anisotropic specified growth across the canvas. In order to transition from a caplet to a flattened disk (like that illustrated in Figure 2.13) using specified isotropic growth, I used an increase in areal growth rate at the MIDVEIN. To explore how a similar transition in 3D shape may be achieved with specified anisotropy alone (no difference in areal growth rate across the canvas), I set up a simple simulation using my caplet start shape, where I could manipulate the level of specified anisotropy across the whole canvas. I started by considering anisotropic specified growth with a polarity field from BASE to TOP (similar to that explored in 2D in Figure 2.11) since this is the most intuitive way to generate a preferential increase in height. I introduced a plus organiser at the base of the canvas and a minus organiser at the top (Figure 2.19, A).

Ai

Aii

Aiii

Bi

Bii

Biii   BASE → POL ⊣ TOP

Front

K_{par} = 0.15
K_{per} = 0.15

D

Isotropic
growth

C

Anisotropic
growth

E

K_{par} = 0.16
K_{per} = 0.14

F

K_{par} = 0.17
K_{per} = 0.13

G

K_{par} = 0.18
K_{per} = 0.12

I

J

K

Side

H

Anisotropic
growth

L

Front section

Top section

K_{par} = 0.17
K_{per} = 0.13
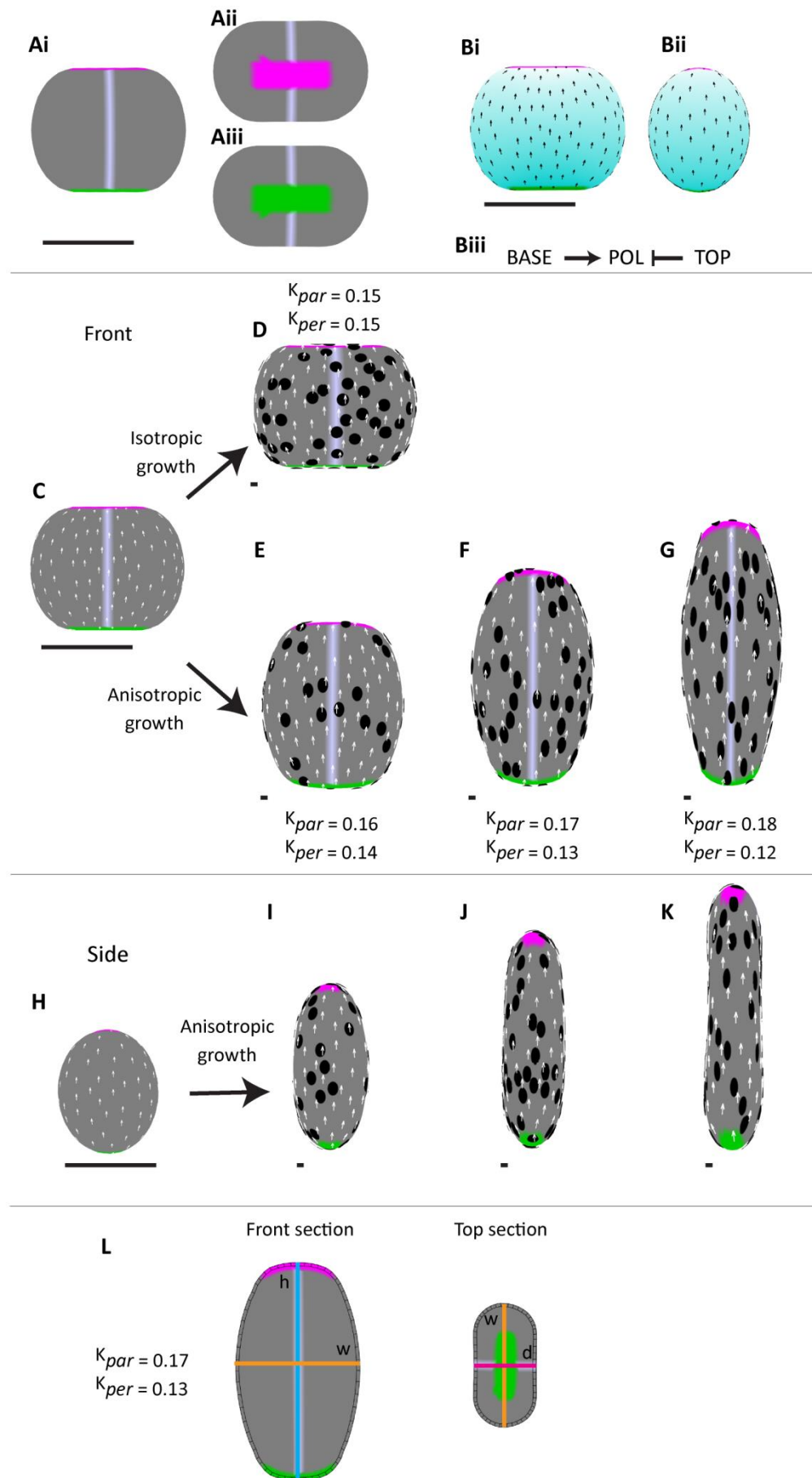
Figure 2.19: Model 4- modelling a growth in height versus in width with anisotropic specified growth. (A) Canvas start shape viewed from the front (Ai), top (Aii), and base (Aii) showing the presence of the factors BASE (green) and TOP (pink). Pale lilac line down centre is for reference in the front view. (B) POL gradient (turquoise) is shown on the canvas viewed from the front (Bi), and the side (Bii). (Biii) Polarity regulatory network (PRN): POL propagates from the + organiser (BASE, green) and is absorbed by the − organiser (MOUTH, pink). (C-G) Canvas viewed from the front at time 0 (C), after isotropic growth for 200 hours (D) or after anisotropic growth where growth in K_{par} is higher than growth in K_{per} (E-G). Anisotropy increases from (E-G). (H-K) Canvas viewed from the side at time 0 (H) and after anisotropic growth for 200 hours (I-K) with K_{par} and K_{per} values in (E-G) respectively. (L) Cross sections of model end shape where K_{par}= 0.17 and K_{per} = 0.13. Lines indicate where measurements of height (blue line), width (orange line), and depth (pink line) where made. All arrows show the polarity field. Black clones are induced as circles from the start and deform with the model. All scale bars, 50 μm.

When this model is run with isotropic growth ($K_{par} = K_{per}$) the canvas grows in size but the shape remains the same (Figure 2.19, D). To introduce anisotropy, I specified a promotion in K_{par}. I kept areal growth ($K_{par} + K_{per}$) constant by reducing K_{per} whenever I increased K_{par}. This anisotropy was sufficient to drive a transition from a start shape that is wider that it is tall to a final shape that is taller that it is wide (Figure 2.19, E). This transition can be accentuated by increasing the level of anisotropy to generate taller, thinner shapes. (Figure 2.19, E-G). However, from the side, where the bladder becomes longer, the model simply grows in height, becoming taller and thinner with greater anisotropy.

In the second example, the difference between K_{par} and K_{per} (K_{par} = 0.17 and K_{per} = 0.13) is equal to 1.3. This is comparable with the difference in the rate of growth in height versus width observed in the bladder which was 1.29 (Figure 2.8, B). Measurements made in cross section of this model (Figure 2.19, L) show that this model becomes 79 % taller than it is wide. However, the model remains 94 % wider than it is deep where the bladder becomes approximately 83 % deeper than it is wide by maturity. Therefore, axiality generated from a polarity running from BASE to TOP is not sufficient to capture both shape transitions seen in the bladder (height versus width and depth versus width).

In order to understand how the bladder may grow, to become more elongated in side view and to consider an increase in depth versus width, I again considered biological landmarks and how these could be used to place the + and − organisers. I replaced the BASE and TOP organisers with the STALK (+ organiser) and MOUTH (- organiser) (Figure 2.20).
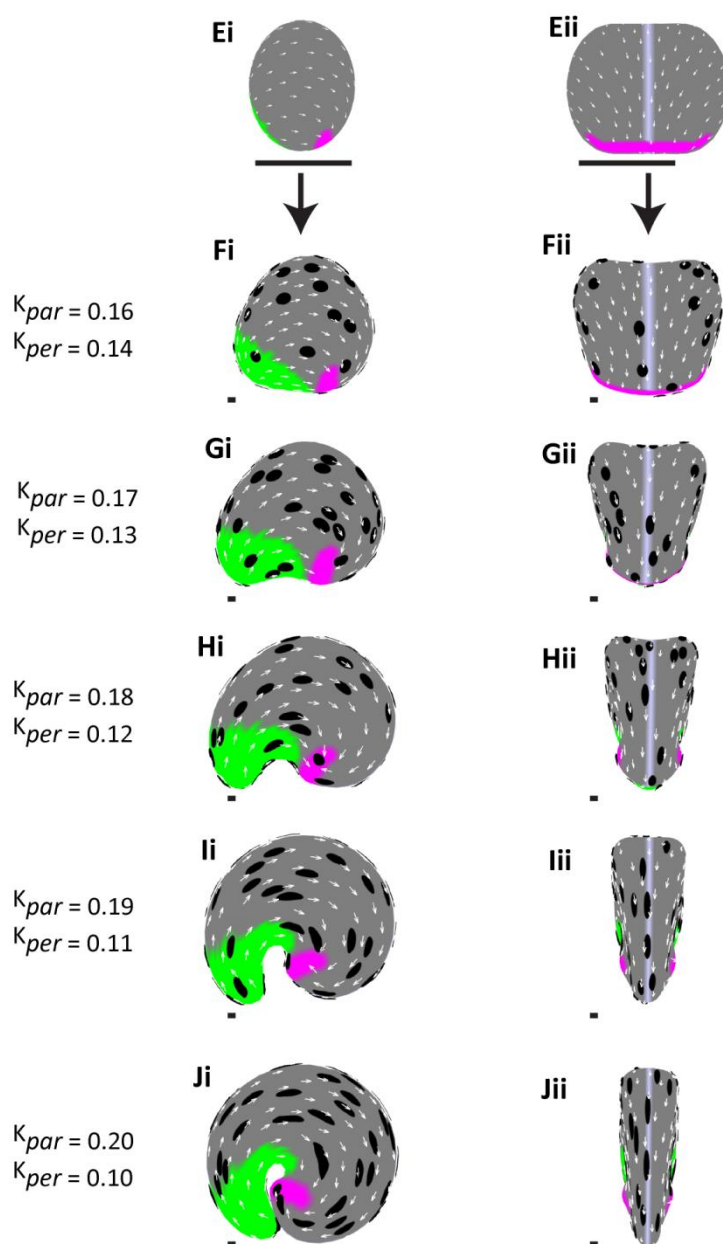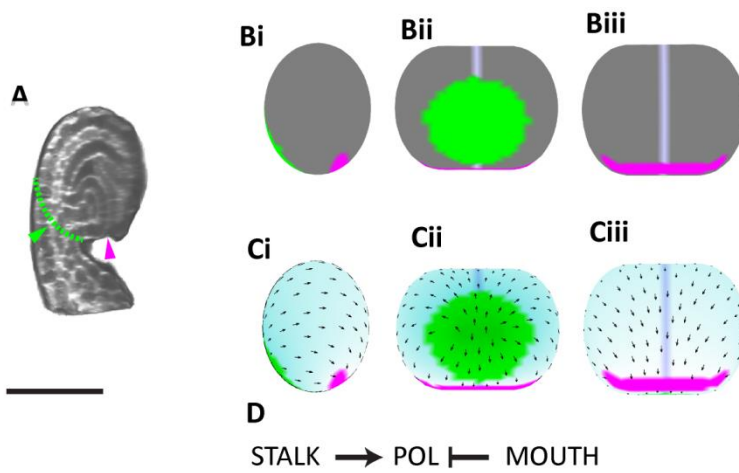
Figure 2.20: Model 5- changing the position of the + and − organisers to the STALK and MOUTH regions. (A) side section through an 82 μm stage bladder with the stalk intersect (green dotted line and arrow) and mouth region (pink arrow) indicated. (B) Canvas start shape viewed from the side (Bi), back underside (Bii), and front (Biii). Pale lilac stripe is used for reference of the front view of the canvas. STALK (green) and MOUTH (pink) regions are shown and were scaled using the 82 μm stage bladder shown in (A). (C) POL propagates from the + organiser (STALK, green) and is absorbed by the − organiser (MOUTH, pink). The POL gradient (turquoise) is shown on the canvas viewed from the side (Ci), back underside (Cii), and front (Ciii). Arrows show the polarity field. (D) Polarity regulatory network (PRN). (E) Canvas start shape viewed from the side (Ei) and the front (Eii). (Fi-Ji) Final canvas shapes viewed from the side with increasing levels of anisotropy where K$_{par}$ is greater than K$_{per}$. (Fii-Jii). Final canvas shapes viewed from the front with increasing levels of anisotropy where K$_{par}$ is greater than K$_{per}$. (A) Confocal image of a fixed bladder stained with propidium iodide. All arrows show the polarity field. Black clones are induced as circles from the start and deform with the model. All scale bars, 50 μm.

This time, a polarity field was generated from STALK to MOUTH (Figure 2.20, C). I kept all other parameters the same; areal growth was kept constant and I varied uniform anisotropy by increasing the value of K$_{par}$ and reducing the value of K$_{per}$ (Figure 2.20, E-J). To keep the model as simple as possible, I did not include the CHIN region.

The end shape of the canvas viewed from the side (Figure 2.20, Fi-Ji), shows the canvas transformation in depth and height at varying levels of anisotropy compared to the start shape (Figure 2.20, Ei). At the lowest level of anisotropy (when K$_{par}$=0.16 compared to K$_{per}$=0.14) (Figure 2.20, Fi), the canvas is still wider than it is tall and wider than it is deep. When anisotropy in the model was increased (Figure 2.20, Gi), the canvas became approximately 18 % taller than it is wide, and approximately 34 % deeper than it is wide (compared to 42 % and 83 % in the mature bladder respectively). This model therefore achieves the broad shape changes but not to the full extent of the bladder. An increase in anisotropy past this point causes the canvas to curl under and we see the formation of an indentation at the STALK-MOUTH boundary (Figure 2.20, Hi-Ji). This is because, due to the displacement of the minus organiser, there was more variability in the orientation of local polarities across the canvas. Since the local polarity influences growth orientations, there is variability in local growth orientations across the canvas, which introduces directional conflict during growth. This conflict is resolved by the curling of the canvas. The region between STALK and MOUTH is also much shorter on the underside of the canvas when compared to the distance from STALK to MOUTH round the back of the canvas. Therefore,

the accumulative growth of the top of the canvas is much greater than the bottom. These differences in accumulative growth coupled with directional conflict cause the canvas to deform with an arch, curling around itself. The STALK region also grows too much, generating a protrusion.

When viewed from the front (Figure 2.20, Fii-Jii), we can see that the canvas becomes thinner with increased anisotropy. In the first instance (Figure 2.20, Fii), the canvas is still wider than it is tall. By the second instance (Figure 2.20, Gii), the canvas is approximately 30 % taller than it is wide (compared to approximately 42 % in a mature bladder). By the third instance (Figure 2.20, Hii), the canvas becomes too thin when compared to a mature bladder.

This model has demonstrated that a displacement of the plus and minus organisers, generating directional conflict can still allow the canvas become taller than it is wide, while also allowing the canvas to become deeper than it is wide. However, the canvas is not able to achieve full growth without curling under. Furthermore, the STALK and MOUTH regions remain in in close proximity; we do not see the characteristic displacement of mouth relative to stalk that we see in the bladder developmental series (Figure 2.9).

Displacing the STALK and MOUTH regions in the anisotropic specified growth model and removing the protrusion at STALK

To investigate how the displacement of STALK and MOUTH could be achieved, I continued with the model that best represented bladder shape change so far. The model that fits the biological scale best, does not have a pronounced curvature, and manages to capture the transitions in shape best, is the case where K_{par} = 0.17 and K_{per} = 0.13 (Figure 2.20, G). I first restricted the growth at STALK in order to prevent the generation of a protrusion in this area (Figure 2.21).
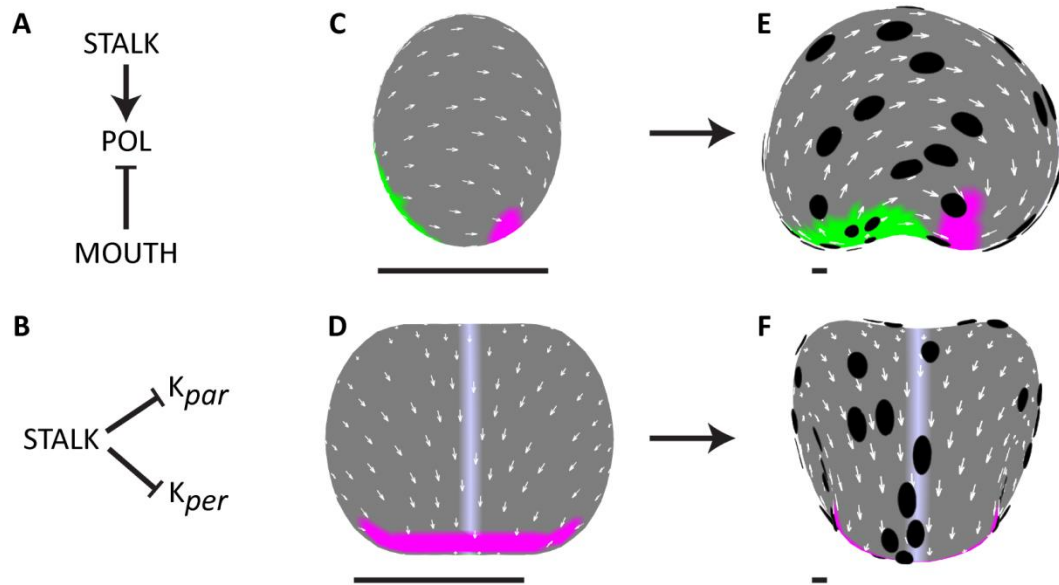
Figure 2.21: Restricting growth at STALK to prevent a protrusion in this region. (A) PRN is the same as in previous models: POLARISER propagates from STALK (C & E, green) and is absorbed by MOUTH (C-E, pink). (B) KRN: K_{par} and K_{per} are both restricted by STALK. The canvas is shown at 0 hours viewed from the side (C) and front (D), and at 200 hours viewed from the side (E) and front (F). All scale bars are 50 µm.

To displace the STALK and MOUTH regions, I re-introduced the CHIN factor in the region between STALK and MOUTH on the underside of the canvas (Figure 2.22, B purple) where I explored increasing growth in this region as I did when exploring isotropic growth models above. I first tried generating an elongation at CHIN by increasing the specified anisotropy in this region. I kept K_{per} fixed and promoted K_{par} at CHIN so that the specified growth rate parallel to the polarity field in this region was 0.2 (Figure 2.22, E), matching the resultant growth rate observed in my time course (Figure 2.10). I found that this was not sufficient to generate the full length of CHIN (Figure 2.22, Ei). However, the STALK and MOUTH regions were displaced (Figure 2.22, Eiv, purple). I then increased the promotion of K_{par} at CHIN so that the specified growth of this region was equal to 0.22, 0.26, and finally 0.28 (Figure 2.22, F, G, H respectively). As anisotropy was increased, the CHIN region became longer and the STALK and MOUTH regions became further apart (Figure 2.22, Ei-Hi). Clones in this region which were induced from the start are longer with each increase in K_{par} at CHIN (Figure 2.22, Eii-Hiv). When K_{par}= 0.28, a CHIN region of approximately biological length is achieved. However, the CHIN region began to bulge outwards (Figure 2.22, Hi). This bulging could be remedied by an inhibition of K_{per} at CHIN, increasing specified anisotropy further (Figure 2.22, Ji). Measurements made of the model in cross section show that this model

grows to be 37 % taller than it is wide and 63 % deeper than it is wide (compared to 42 %
and 83 % in the mature bladder respectively). Further alterations to the parameters may
allow the canvas to reach mature bladder proportions.

A

Bi **Bii** **Biii**

C

STALK ⟶ POL ⊢ MOUTH

D

CHIN ⟶ K_{par} ⊢
K_{per} ⊢ STALK

I

CHIN ↗ K_{par} ⊢
↘ K_{per} ⊣ STALK

Ei **Fi** **Gi** **Hi** **Ji**

inh K_{per} at CHIN ⟶

Eii **Fii** **Gii** **Hii** **Jii**

Eiv **Fiv** **Giv** **Hiv** **Jiv**

Ev **Fv** **Gv** **Hv** **Jv**

K_{par} at CHIN = 0.20

K_{par} at CHIN = 0.22

K_{par} at CHIN = 0.26

K_{par} at CHIN = 0.28

K_{par} at CHIN = 0.28

K

Front section   Top section
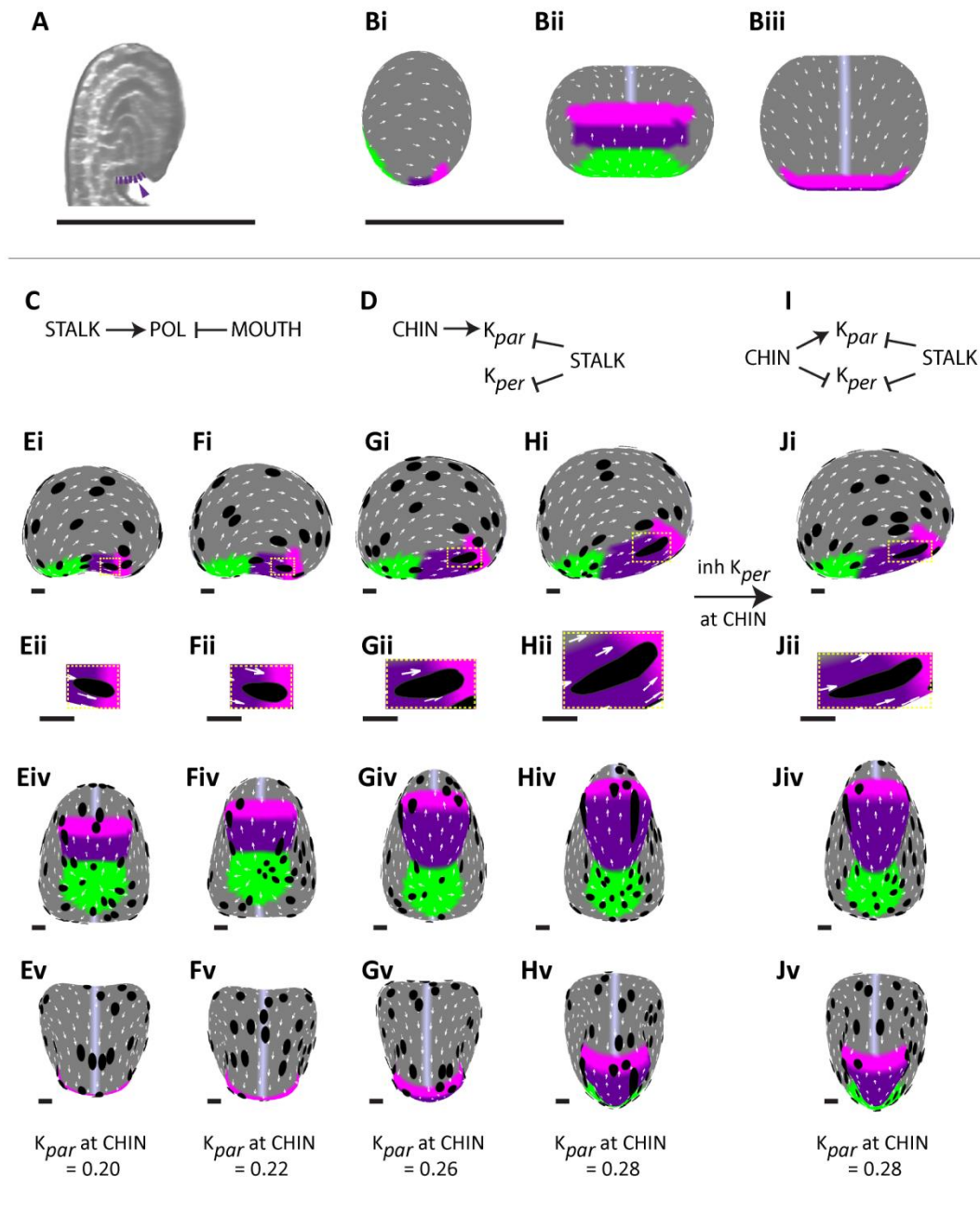
Figure 2.22: Model 6- adding increased anisotropy in the CHIN region. (A) Longitudinal section through an 82 μm stage bladder indicating the chin region between the stalk and mouth (purple dotted line and arrow). (B) Canvas with CHIN factor (purple) in between STALK (green) and MOUTH (pink) and scaled to the 82 μm bladder shown in (A). The canvas is shown viewed from the side (Bi), underside (Bii), and front (Biii). (C) The PRN is the same as previous models. (D) The KRN in models (E-H) where K_{par} and K_{per} are inhibited by STLAK and K_{par} is promoted by CHIN. (E- H) Canvas at time 200 at increasing values of K_{par} at CHIN. Canvas viewed from the side (Ei-Hi), zoomed in on a clone at CHIN (Eii-Hii), viewed from underneath (Eiv-Hiv), and viewed from the front (Ev-Hv). K_{par} = 0.20 (E), Kpar = 0.22 (F), K_{par} = 0.26 (G), K_{par} = 0.28 (H). (I) KRN in model (J) where K_{per} is inhibited by CHIN. (J) Views of the model in which K_{per} is inhibited by CHIN in same views as (E-H). All scale bars are 100 μm.

This model captures a change in height relative to width, as well as the change in depth relative to width (although not quite to biological scale), and growth of the CHIN region. I found that a higher specified growth rate was necessary to generate the full elongation of the CHIN region than the resultant growth rate measured. This is because growth of the tissue in this region is restrained by neighbouring tissue which is not growing as fast.

Exploring the contribution of increased anisotropy and increased areal growth rate in the CHIN region.

To understand how the final shape of this model is generated, I considered what is happening in terms of specified anisotropy and areal conflict in the CHIN region. By increasing K_{par} at CHIN, while keeping K_{per} fixed, I have not only increased the level of anisotropy in this region, but I have also introduced differential growth rates across the canvas. This introduces areal conflict in the growing tissue and it is therefore difficult to know to what extent an increase in anisotropy has played on the generation of this shape, and to what extent the level of areal conflict had contributed. To examine this, I first removed areal conflict generated at CHIN, keeping the promotion in K_{par} at CHIN the same but inhibiting growth in K_{per} so that areal growth in this region was equal to the rest of the tissue (Figure 2.23). I kept the STALK region the same as an anchoring point. This generated an arch in the model which can be seen from the side (Figure 2.23, B). The CHIN region is pinched in, due to the inhibition of K_{per} being so great to overcome the necessary promotion in K_{par} at this region. Next, I removed anisotropy in the CHIN region by keeping K_{par} and K_{per} equal at CHIN and increasing areal growth rate in this region so that is was equal to the areal growth rate in the original model (Figure 2.23, C). When growth at CHIN

is purely through areal conflict, the CHIN region bulges out and does not elongate sufficiently. These models indicate that both anisotropy and a higher areal growth rate at CHIN are required to generate bladder shape.
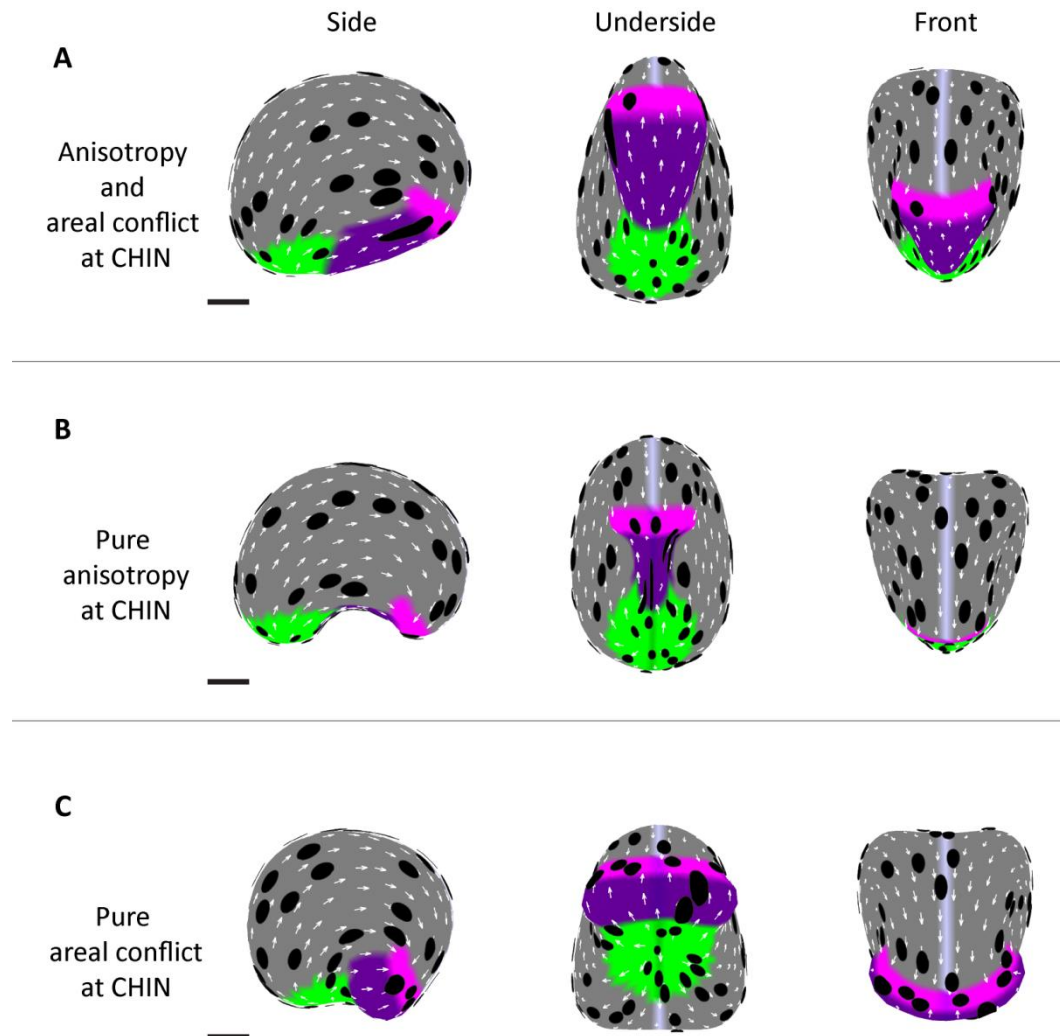
Figure 2.23: Exploring the contribution of specified anisotropy and areal conflict to generate an elongation at CHIN. (A) The original model where growth at CHIN involves both anisotropy ($K_{par} > K_{per}$) and areal conflict (since areal growth rate at CHIN is higher than the rest of the canvas). (B) The model when growth at CHIN is purely anisotropic with no areal conflict. Areal conflict was removed by keeping K_{par} the same as in (A) and reducing K_{per} so that the areal growth rate matched the rest of the canvas. (C) The model growth with pure areal conflict and no anisotropy; $K_{par}=K_{per}$ and areal growth at CHIN is that same as in (A). All scale bars are 200 μm.

To study model 6 further, I looked at what predictions on bladder growth this model could make. One of the most noticeable features of the model is that clones at CHIN appear much more elongated compared to clones on the rest of the canvas (Figure 2.22, Jii). To quantify this, I plotted the mean rate of increase in anisotropy per hour at the CHIN region compared to the rest of the canvas (Figure 2.24).
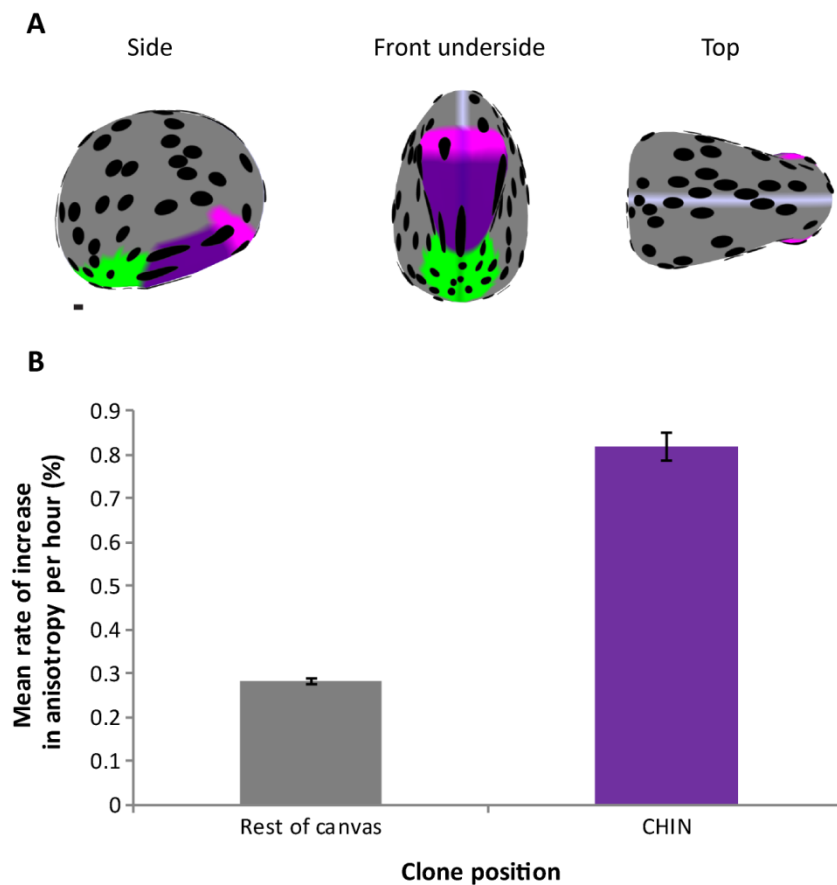
Figure 2.24: Percentage rate of increase in anisotropy per hour (model 6) (A) Model end shape viewed from the side, front underside, and top. The CHIN (purple), MOUTH (pink), and STALK (green) regions are shown. Clones are also shown (black) which start as isotropic circles and deform with the canvas. Scale bar is 50 μm. (B) Mean rate of increase in anisotropy per hour at the CHIN region compared to the rest of the canvas. Rate of increase in anisotropy per hour = (Ln (major/minor))/ 200. Bars are standard error of the mean.

The mean rate of increase in anisotropy per hour is almost 3 times higher in the CHIN region compared to the rest of the canvas (about 0.8 % per hour at CHIN and about 0.3 % per hour in the rest of the canvas) (Figure 2.24, B).

Unlike model 3 where specified growth in the main body of the canvas is isotropic (Figure 2.16), clones in model 6 appear to be even in size and appear to have even levels of anisotropy across the main body of the bladder (excluding the STALK region where clones appear more isotropic, and the CHN region where clones are more elongated). This is not surprising, since specified areal growth rate in the main body of the bladder is even across the canvas. To quantify the clone area and level of anisotropy, I ran the model with the diffusible factor S_MIDVEIN so that I could compare the model with the isotropic specified growth model. I then plotted the natural logarithm of clone area against the level of S_MIDVEIN and the rate of increase in anisotropy per hour against S_MIDVEIN (Figure 2.25).
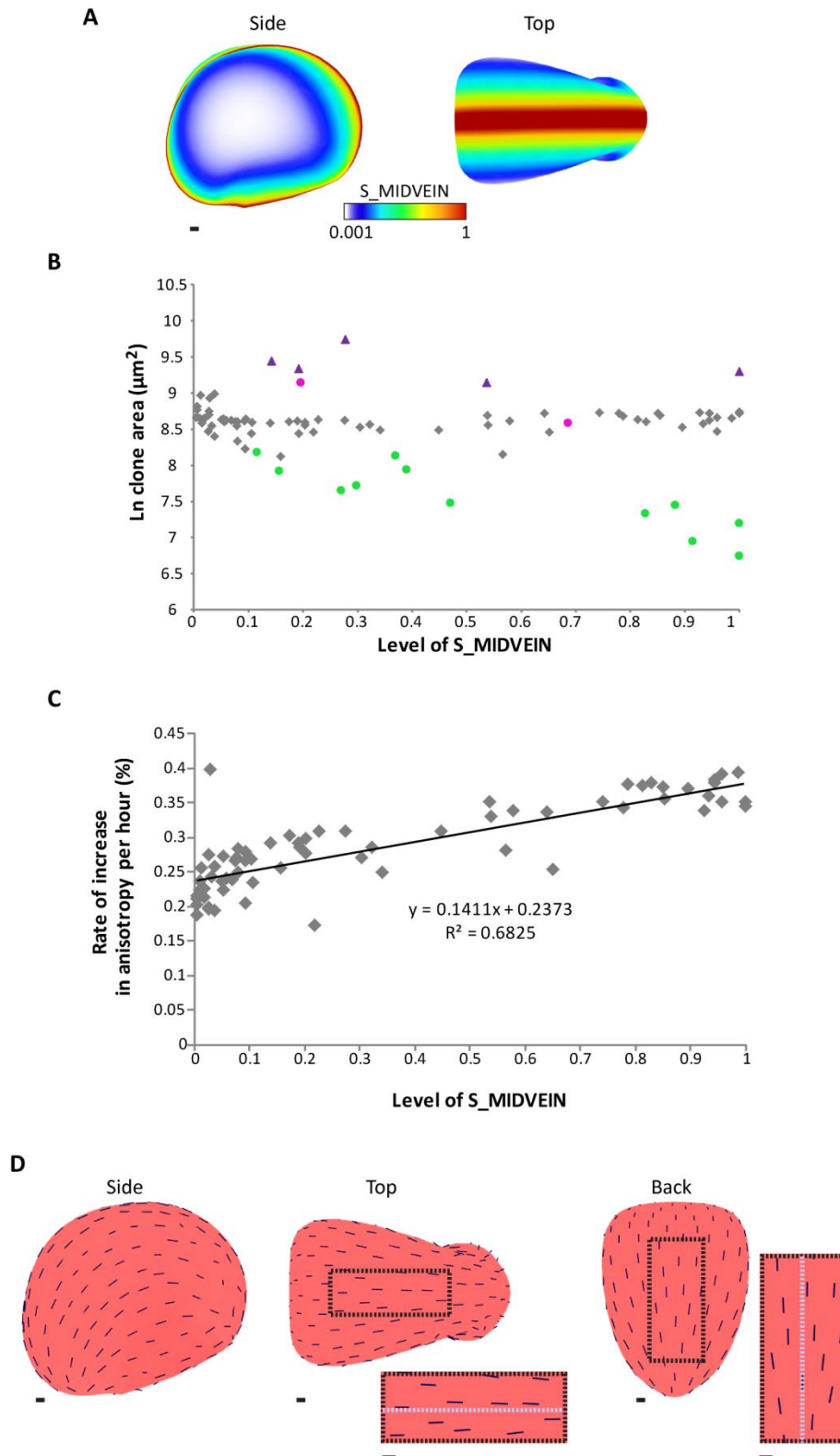
Figure 2.25: Clone area and rate of increase in anisotropy per hour in regions of the canvas at different distances from MIDVEIN (model 6). (A) Model end shape shown from the side and top with S_MIDVEIN plot. S-MIDVEIN diffuses from MIDVEIN and creates a gradient across the canvas. This gives a proxy for clone position on the canvas according to the local level of S_MIDVEIN (higher at the MIDVEIN- red region, lover near the sides of the canvas- white region). (B) Natural logarithm of clone area against the level of S_MIDVEIN.

Data points are coloured to indicate their position on the canvas: main body of the canvas (grey), CHIN (purple triangles), MOUTH (pink circles), and STALK (green circles). (C) Rate of increase in anisotropy per hour plotted against the level of S_MIDVEIN. All data is from the main body of the bladder. Fitted line is shown along with the equation of the line where 0.1411 is the gradient of the line. The R^2 value is given (where 1 indicates a perfect fit of the line to the data). (D) End shape of the canvas shown from the side, top, and back with the major axis of growth marked (black lines). Boxes show zoomed in regions from the top and back. Orientation of the MIDVEIN is indicated (pale lilac dotted line) for reference. All scale bars are 50 μm.

I found no correlation between the clone area and the level of S_MIDVEIN, indicating that clones are roughly equal in area across the main body of the canvas (Figure 2.25, B, grey). Clones in the CHIN region (Figure 2.25, purple) are larger due to the promotion in K_{par} in this region, while clones at STALK are smaller (Figure 2.25, green) due to the restriction in K_{par} and K_{per} in this region.

When I plotted the rate of increase in anisotropy per hour against the level of S_MIDVEIN, I found that clones in regions closer to MIDVEIN had a slightly higher rate of increase in anisotropy per hour than those further from the MIDVEIN (Figure 2.25, C). This may indicate that there are different levels of conflict across the canvas (possibly due to local polarities nearest MIDVEIN being more parallel to MIDVEIN). The lowest value here is about 0.2 % per hour going up to about 0.4 % per hour.

To visualise the orientation of growth across the model I plotted the major axis of growth on the canvas. I found that the orientation of the major axis of growth followed the polarity pattern across the canvas and was therefore parallel to the MIDVEIN at the top and back (Figure 2.25, D).

In summary, model 6 makes a number of predictions about bladder growth:

1.) A polarity field propagating from stalk to mouth is present and orients growth across the bladder.
2.) Specified growth in the chin region is higher than the rest of the tissue and is anisotropic (same as model 3)
3.) Growth orientations across the canvas are parallel with the polarity field.

Although the model captures bladder shape changes well, there are two problems with the final shape of the canvas. First, the back of the canvas has a sharp curve, where in the mature bladder, a much smoother curve is present (Figure 2.26, Ai, red arrow). The model is also concave at the midvein, generating a saddle-like shape at the top (Figure 2.26, Aii, red arrow).

To address these issues I tried introducing a gradient of anisotropy from the midvein to see if this could generate a more rounded back and remove the saddle shape at the top of the canvas. I used the diffusible factor S_MIDVEIN to generate a gradient from the midvein out (Figure 2.26, B). I then promoted K_{par} by the local level of S_MIDVEIN (which spans across CHIN) to generate a gradient of anisotropy. Areal growth in the main body of the canvas (excluding CHIN and STALK) was maintained by normalising areal growth rate so that, in effect S_MIDVEIN was also inhibiting K_{per}.

Side   Top   Front

Ai   **Aii**   **Aiii**

B   Side (oblique)   Front   **C**

STALK → POL ⊢— MOUTH

D

S_MIDVEIN → K_{par}
S_MIDVEIN ↛ K_{per}

Ei   **Eii**   **Eiii**

Fi   **Fii**   **Fiii**

K_{aniso}
-1   1

G   Front section   Top section
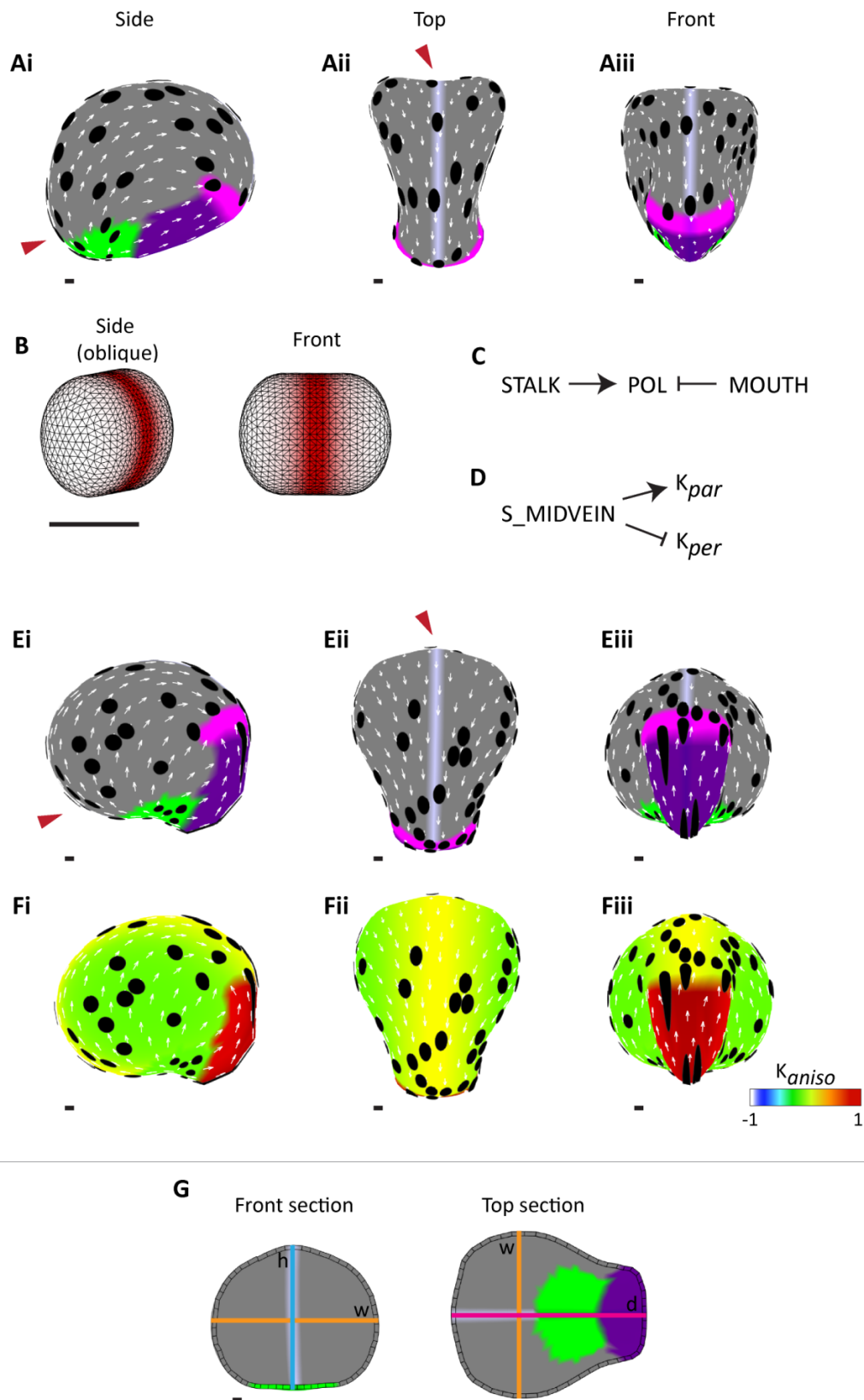
Figure 2.26: Model 7- exploring a gradient of anisotropy from MIDVEIN to generate bladder shape. (A) Original anisotropic model (model 6) viewed from the side (Ai), top (Aii), and front (Aiii). Sharp curve at the back (Ai, red arrow) and the saddle along the

midvein (Aii, red arrow) are indicated. (B) Caplet start shape canvas with diffusible factor S_MIDVEIN (red gradient). (C) Polarity regulatory network (PRN) where POLARISER propagates from the + organiser (STALK) and is absorbed by the − organiser (MOUTH). (D) Growth regulatory network (KRN) where S_MIDVEIN promotes K_{par} and inhibits K_{per} so that areal growth rate is not affected. (Ei-Eiii) Canvas end shape with regions plotted. Red arrows for comparison with (A). (Fi-Fiii) canvas end shape with K_{aniso} plot. (G) Front and top sections of the model with lines indicating how height (blue line), width (orange lines), and depth (pink line) measurements were made. Black clones are induced at the start as circles and deform with the canvas. All scale bars are 50 μm.

This generated a canvas with a much smoother back (Figure 2.26, Ei, red arrow) and the saddle shape at the top of the canvas was also remedied (Figure 2.26, Eii, red arrow). However, the CHIN region now protrudes more and the MOUTH region is much higher than before. This can be explained by anisotropy being boosted at the CHIN region even more by S_MIDVEIN (Figure 2.26, F). When I analysed cross sections of the model, I found that this model is still wider than it is tall (by about 8 %), meaning that it has not achieved the shape transition in height versus width observed in the mature bladder. The model does increase more in depth relative to width, but only becomes approximately 14 % deeper than it is wide.

In summary, this model achieves a smoother back and does not have a saddle shape at the top of the canvas. However, it does not easily achieve the transitions in shape seen in the bladder. To compare this model to previous models presented, I looked at the resultant clone anisotropy and area across the canvas, as well as growth orientations (Figure 2.27).
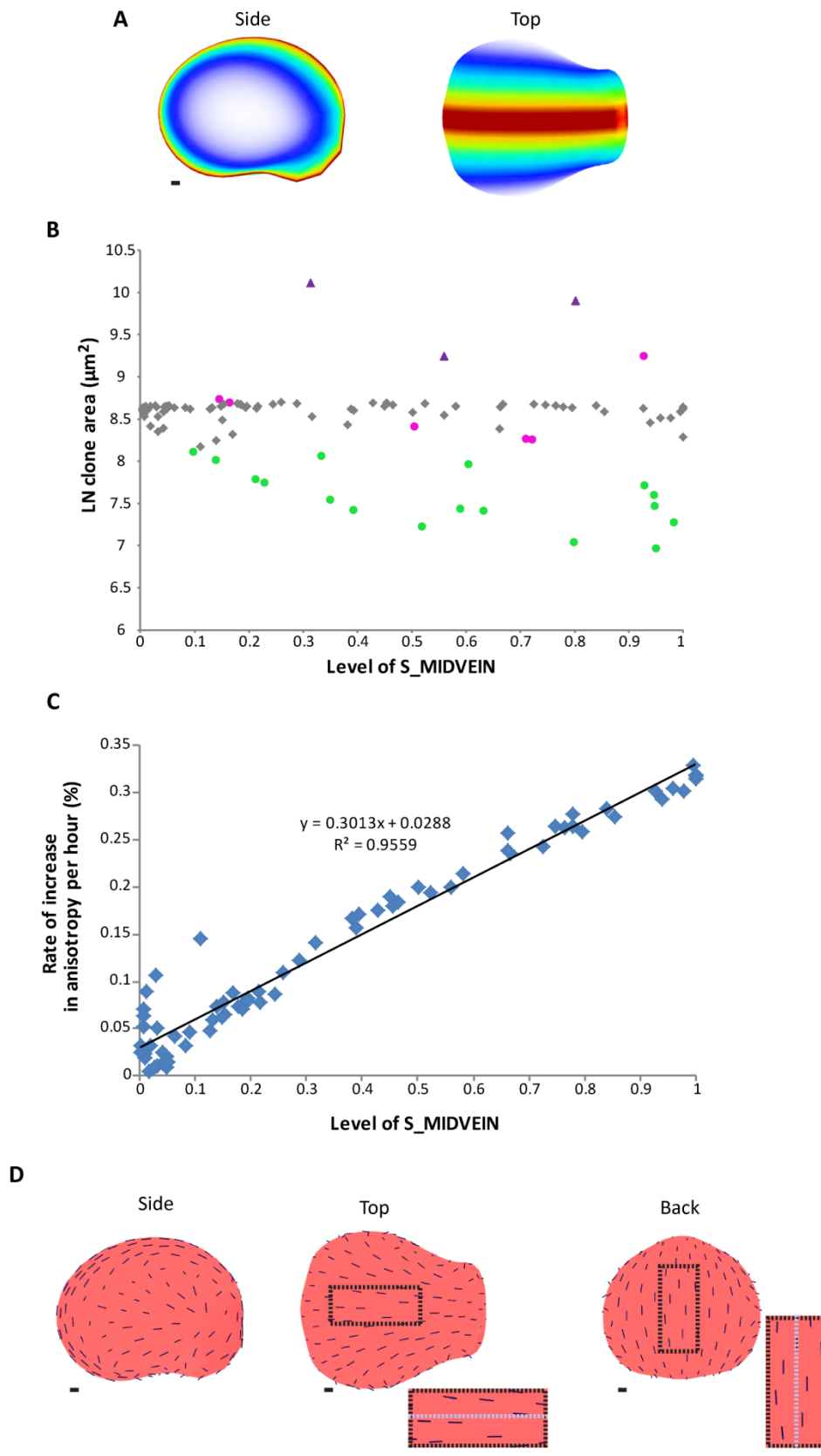
Figure 2.27: Analysing clone area and rate of increase in anisotropy per hour in regions of the canvas at different distances from MIDVEIN (model 7). (A) Model end shape shown from the side and top with S_MIDVEIN plot. S-MIDVEIN diffuses from MIDVEIN and creates a gradient across the canvas. This gives a proxy for clone position on the canvas according

to the local level of S_MIDVEIN (higher at the MIDVEIN- red region, lover near the sides of the canvas- white region). (B) Natural logarithm of clone area against the level of S_MIDVEIN. Data points are coloured to indicate their position on the canvas; main body of the canvas (grey), CHIN (purple triangles), MOUTH (pink circles), and STALK (green circles). (C) Rate of increase in anisotropy per hour plotted against the level of S_MIDVEIN. All data is from the main body of the bladder. Fitted line is shown along with the equation of the line where 0.3013 is the gradient of the line. The R^2 value is given (where 1 indicates a perfect fit of the line to the data). (D) End shape of the canvas shown from the side, top, and back with the major axis of growth marked (black lines). Boxes show zoomed in regions from the top and back. Orientation of the MIDVEIN is indicated (pale lilac dotted line) for reference. All scale bars are 50 μm.

I found no correlation between clone area and position relative to S_MIDVEIN (Figure 2.27, B). However, the rate of increase in anisotropy per hour is lower at regions furthest from the MIDVEIN and increases closer to the MIDVEIN (Figure 2.27, C). The rate of increase in anisotropy per hour furthest from the MIDVEIN is between 0- 0.05 % per hour, increasing to a rate of around 0.35 % per hour in regions closest to the MIDVEIN. This is because specified anisotropy is proportional to the level of S_MIDVEIN. The orientation of this anisotropy is parallel with the polarity field across the canvas and is therefore parallel with MIDVEIN (Figure 2.27, D).

In summary, through specified anisotropic growth modelling, I have found that specified anisotropic growth can capture the shape changes that occur in the main body of the bladder. Areal conflict through differential growth rates is required on top of this anisotropy to generate the elongation of the CHIN region. A gradient in specified anisotropy from the MIDVEIN region out was able to generate a smoother shape but caused the canvas to bulge in the CHIN region due to conflict of neighbouring isotropic regions and was not able to easily generate all shape transitions seen in the bladder.

2.2.3.6 Summary of bladder shape transition models

Through modelling with specified isotropic and specified anisotropic growth, I found that there are two broad ways in which bladder shape change can be captured. In each case, specified anisotropy is required for the elongation of the CHIN region. Model 3 (Figure 2.16) uses specified isotropy with increased areal growth rate at MIDVEIN to capture shape transitions in the main body of the bladder, while model 6 (Figure 2.22) uses specified anisotropy to capture shape transitions in the main body of the bladder. It will therefore be necessary to consider the different predictions made by each model and test these predictions in order to arrive at an understanding of the specified growth patterns underlying shape transitions during bladder development. Table 2-1 provides a summary of the predictions made by each model and highlights those predictions which allow a distinction to be made between models when studying resultant growth patterns experimentally in the biological system.

Table 2-1: Summary of predictions made by model 3 and model 6. Predictions that allow a distinction to be made between models experimentally are indicated in green.

	Model 3 (Figure 2.16) Isotropic specified growth model with anisotropic specified growth in the CHIN region alone	**Model 6** (Figure 2.22) Anisotropic specified growth model
Polarity pattern	Propagates stalk-mouth	Propagates stalk-mouth
Clone area across the main body	Larger near the midvein, smaller at the sides	Approximately equal
Resultant clone anisotropy at chin versus the main body	Higher anisotropy at chin compared to the main body	Higher anisotropy at chin compared to the main body
Clone anisotropy across the main body	Low resultant anisotropy	Low resultant anisotropy
Clone orientations across the main body of the bladder.	Perpendicular to the midvein near the midvein, more parallel to the midvein at the sides of the canvas	Parallel to the midvein and polarity field across the canvas
Clone orientations at chin	Parallel with the midvein (stalk-mouth)	Parallel with the midvein (stalk-mouth)

2.3 Discussion

2.3.1 Characterising bladder shape changes through development

I have generated a resource of 3D bladder images using a combination of confocal microscopy with fixed samples stained with propidium iodide for the youngest bladder stages and OPT (in collaboration with Karen Lee) for the later stages. The use confocal microscopy coupled with the 3D volume software VolViewer has enabled me to study bladder stages and shape changes through development which were not previously characterised and I confirmed that the early stages of *U. gibba* bladder development are morphologically similar to those reported for *U. vulgaris* by Meierhofer (1902). A time course of bladder development with bladder staging has also not previously been available. This is possibly due to the early stages of bladder development being masked by the tissue of the circinnate apex. To overcome this, I tracked bladders from stages outside of the circinnate apex and then extrapolated back. I also set up a staging system to enable characterisation through development based on bladder length rather than time after initiation. I showed that that the main body of the bladder grows at a rate of 1.6 % per hour and bladder development from around the 82 μm stage to maturity takes approximately 170 hours (assuming that growth rate is constant). Using this information, I was able to characterise three main changes through bladder development: a greater increase in height versus width, a greater increase in depth versus width, and an elongation in the chin region. I found that the chin region grows at approximately 2 % per hour, becoming around 25 times longer from the 82 μm stage to maturity. These studies provided me with key information that allowed me to consider different models of growth.

2.3.2 Modelling bladder development

I explored the transition from an 82 μm stage caplet shaped bladder to a mature bladder by modelling growth using GFtbox. Here I explored specified isotropic and specified anisotropic growth. GFtbox was especially useful for considering shape changes in 3D due to the fact that the canvas is mechanically interconnected and can deform out of the plane. This was important when considering 3D bladder shape changes since 2D models have free edges and therefore cannot represent shape transitions occurring in a 3D connected tissue. Therefore, considering bladder shape changes in one 3D canvas was important to

understand how a connected tissue may behave and to make predictions on bladder growth while considering the whole organ.

2.3.2.1   The chin region of the bladder requires specified anisotropy

Through modelling bladder shape change, I found that a purely isotropic specified growth model is unable to generate an elongation at the chin region of the bladder without generating a bulge in the tissue. This is an example of where areal conflict in tissue leads to a 3D deformation due to the interaction of connected tissue where one region is specified to grow faster than neighbouring regions (Kennaway *et al.*, 2011; Rebocho *et al.*, 2016 submitted).

Adding specified anisotropy at the chin region was sufficient to generate elongation in biological proportions and avoid generating a bulge. Furthermore, I found that pure anisotropy with no increased areal growth caused the chin to be pinched in: to keep areal growth even across the canvas, K_{per} must be lowered to allow for the increase in K_{par}. This suggests that both areal conflict and specified anisotropic growth are required for the elongation of the chin. This also indicates that tissue axiality is required so that specified growth oriented parallel with the axis between the stalk and mouth may be higher at the chin.

2.3.2.2   Shape changes in the main body of the bladder can be accounted for with either specified isotropic or anisotropic growth

A greater increase in height versus width in the main body of the bladder can be captured by models in which specified growth is either isotropic or anisotropic. The key to generating such directional growth in a specified isotropic growth model is the presence of differential areal growth rates across the canvas where growth rate is highest around the midvein of the bladder. A greater increase in depth versus width is achieved with higher areal growth in the chin region which drives further elongation of the canvas. These shape changes occur as a result of areal conflict generated by differential growth rates in neighbouring regions of tissue. In the specified anisotropic model, shape change in the main body of the bladder relies on tissue axiality (generated using tissue polarity in the model) oriented from stalk to mouth, and increased growth parallel with this axiality. Increased height and depth here

are driven by local anisotropic growth which is parallel with the MIDVEIN across the canvas. These principles are comparable to the single cell examples from Green (1965) and 3D tissue examples reviewed in Coen & Rebocho (2016 in press) where similar deformations in shape may be achieved using either combinations of specified isotropic growth with differential areal growth rates, or anisotropic specified growth with uniform areal growth rate.

2.3.3 Summary of predictions made by the models and future work

The models presented in this chapter make a number of predictions about bladder development, some of which will help to distinguish between specified isotropic and anisotropic growth when studying the *U. gibba* bladder experimentally. Since a pure isotropic specified growth model (model 2) was unable to generate elongation of the chin region successfully, and the gradient of anisotropy model (model 7) was unable to increase more in height relative to width, I will focus on comparing two models:

1.) **Model 3**- (Figure 2.16) Isotropic specified growth model with anisotropic specified growth in the CHIN region alone.

2.) **Model 6-** (Figure 2.22) Anisotropic specified growth model.

Predictions made by these models are outlined in Table 2-1. Since specified isotropic (model 3) or anisotropic (model 6) growth could account for the shape changes observed in the main body of the bladder, it is important to make predictions that can distinguish between the two. Both models predict low levels of resultant anisotropy across the main body of the bladder. In the specified isotropic growth model the resultant anisotropy near the midvein is perpendicular to the midvein while in the specified anisotropic growth model it is parallel with the midvein. This provides one potential method for distinguishing the models through observing local growth orientation.

Another means to distinguish the models is by predictions made regarding clone size. In the specified isotropic model (model 3), clones near the midvein are larger where areal growth rates are higher, and smaller at the sides of the canvas where areal growth rates are lower. In the specified anisotropic growth model (model 6), clones are of approximately equal area across the main body of the canvas.

These predictions may be tested by looking for biological evidence in the developing *U. gibba* bladder. Growth dynamics may be examined by tracking bladder growth and cell division patterns and by performing sector analysis (Kuchen *et al.,* 2012; Sauret-Güeto *et al.*, 2013). The presence of a polarity field may be investigated by looking at molecular markers of polarity such as PIN1 (Kuchen *et al.*,2012; Kennaway *et al.*, 2011).

3 Testing model predictions

3.1 Introduction

Models presented in the previous chapter make a number of predictions about bladder development. Some predictions (such as the requirement for axiality) are made by each model. Other predictions allow a distinction to be made between models where either specified isotropic growth or specified anisotropic growth underlies the development of the main body of the bladder. In this chapter, I will test these predictions in the biological system.

3.1.1 Markers of polarity

Models 3 and 6 presented in the previous chapter both predict the requirement of axiality to specify anisotropy for development of the bladder chin region. These models assume that axiality is based on a polarity system, using a diffusible factor (POLARISER) to set up a polarity field across the canvas, against which growth orientations may be specified (Kennaway *et al.*, 2011). There is evidence global axes exist in tissues (Bouyer *et al.*, 2001; Strutt, 2001, 2002; Grebe, 2004) and we can assess the orientation of this axiality by studying markers of cellular polarities.

3.1.1.1 External markers of polarity

A number of these markers are visible on the epidermal surface of cells. This has enabled the study of tissue polarisation (the ability of cells to polarize within a plane of a tissue layer), also known as planar polarity (or tissue-cell polarity).

There is extensive evidence for planar polarity in animals including the coordinated bristles and hairs across the body of *Drosophila* (Adler, 2002), and on the body of the milkweed bug *Oncopeltus* (Lawrence, 1966). Many studies have been done to understand the set up and maintenance of this tissue polarity in the *Drosophila* wing and gene products controlling planar cell polarity (PCP) signalling have been characterised including those encoded by approximately ten core PCP genes (Wang & Nathans, 2007). The system involves the Fat/

Dachsous/ Four-jointed (Ft/ Ds/ Fj) signalling system which aligns an apical non-centrosomal microtubule (MT) network (Harumoto *et al*., 2010). This is achieved by gradients of Fj and Ds expression which lead to an excess of Ft activity on the proximal side of each cell and Ds activity on the distal side of each cell. This polarisation of Ft and Ds activity in the cell leads to the organisation of proximal-distal MT tracks. Plus-ends of MTs are biased towards the end of cell with either high Fj or high Ds expression depending on the predominant Pk-Sple protein isoform, Prickle[pk] (Pk) or Prickle[spiny-legs] (Sple), present: MT plus-ends are biased towards areas of high Fj expression in the presence of PK, and high levels of Ds expression in the presence of Sple (Olofsson *et al*., 2014) This allows the system to function in cells of the eye, wing and abdomen where Ft and Ds gradients differ and provides a continual directional bias for polarisation. These MT alignments then lead to polarised, plus-end directed trafficking of vesicles containing Dishevelled (Dsh) and Frizzled (Fz) to the distal side of the cell where Fz signalling eventually leads to the specification of prehair formation (Adler, 2002).

In *Arabidopsis* roots a similar phenomenon can be observed in the planar polarity of root hair cells which initiate close to the basal ends of hair-forming cells and point towards the peak of auxin at the root tip (Grebe, 2004). ROP GTPases have been suggested to be involved in the polarising mechanism since they exhibit polar localisation close to the basal end of epidermal cells (Grebe, 2004). Experiments have also shown that planar polarity of root cell hairs requires the combined activity of *AUX1, EIN2*, and *GNOM* genes: the *Arabidopsis aux1;ein2;gnom^{eb}* triple mutant has loss of polarity and mis-localisation of ROP (Fischer *et al*., 2006). This mutant lacks the auxin influx carrier (AUX1), the ethylene signalling protein (EIN2), and the GNOM protein which is required for polar plasma-membrane localisation of PIN1 and PIN2 auxin efflux carriers. Auxin is thought to play a key role in the planar polarity of root hair positioning since the local application of auxin coordinates polar hair positioning towards the source in the *aux;ein2;gnom^{eb}* triple mutant (Fischer *et al*., 2006). In barley, hairs on the adaxial surface of the lemma point distally towards the lemma tip, and this polarity is disrupted in the *Hooded* mutant where hairs point proximally below the first ectopic flower. These orientations correlate with the pattern of SISTER of PIN1 (SoPIN1) localisation observed in the tissue (Richardson *et al.*, 2016).

The trichomes of *Arabidopsis* also display polarity, with branching events closely related to the leaf axis: the first branching event occurs in the proximal-distal leaf axis and the second branching event takes place only at the distal end. This means that the trichome has a single branch pointing towards the leaf base and two branches pointing towards the leaf tip (Bouyer *et al*., 2001). A number of trichome mutants, some of which exhibit trichomes which are randomly oriented have been characterised (Bouyer *et al*., 2001). However, the mechanisms underlying trichome polarity are poorly understood.

3.1.1.2 PIN proteins as markers of polarity

The polar localisation of PINs (auxin efflux carriers) within a tissue may provide a readout of axiality if this axiality is determined by a polarity based system coordinated by auxin. This marker of polarity is especially useful when studying young tissue when epidermal *PIN* expression is high. The coordinated polar localisation of PIN proteins has been used to study plant tissue-cell polarity in embryonic tissue, roots (Grebe, 2004) and developing leaves and petals (Kuchen *et al*., 2012; Sauret-Güeto *et al*., 2013).

3.1.2 Evidence for resultant anisotropy in the cells of developing tissues.

The models also make predictions on resultant anisotropy, the most striking of which was in the chin region of the bladder where clones appeared much more elongated and the rate of increase in anisotropy per hour was predicted to be much higher than the rest of the tissue and oriented parallel with the axis between stalk and mouth.

Evidence of resultant anisotropy can be explored in developing tissues by studying resultant anisotropy at the cell shape and cell division level. Cells may grow anisotropically, becoming long and thin (Figure 3.1, A). In this case anisotropic growth may be inferred in regions of tissue where individual cells have higher levels of anisotropy. However, if division occurs following the shortest wall algorithm reviewed by Prusinkiewicz & Runions (2012), then isotropy of individual cells will be maintained in regions of tissue growing anisotropically (Figure 3.1, B). This means that anisotropy cannot be assessed by cell shape alone but by patterns of division too.
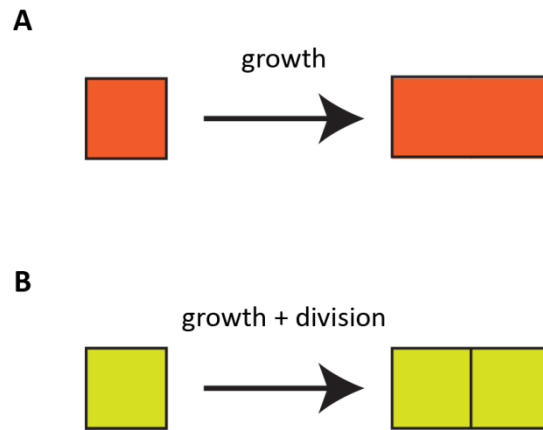
Figure 3.1: Resultant anisotropy at the cell shape and cell division level. (A) Diagram illustrating anisotropic growth of a cell in the absence of division where the final cell shape is anisotropic. (B) Diagram illustrating anisotropic growth of a cell in the presence of division along the shortest wall where isotropy of individual cells is maintained.

Resultant anisotropy can be studied in developing tissue in a number of ways. These include image segmentation of cells (Federici *et al*., 2012) which can give information on cell shape anisotropy across a tissue when individual samples are studied or give information on cell division patterns too if used in conjunction with a time course data set. This method of analysis requires the ability to image structures in such a way that cell outlines are clear, and the ability to computationally fit a surface to the structure and segment it. Tracking also requires good cell definition for microscopy as well as the need for keeping the tissue alive while growing in an imaging chamber.

Another method used to study cell lineages is sector analysis. Sectors may be heat shock induced fluorescent sectors (Kuchen *et al.*, 2012; Sauret-Güeto *et al.*, 2013; Eldridge *et al.*, 2016). This method of sector generation uses Cre-lox*P* recombinase which was identified in bacteriophage P1 (Sternberg & Hamilton, 1981). In this system, site specific recombination requires two components; the 34 bp *loxP* sequence at which recombination occurs and the *Cre* recombinase protein which recognises and binds *loxP* sites, catalysing the recombination of DNA (Sternberg & Hamilton 1981; Hoess *et al*., 1982; Abremski & Hoess 1984). This system has been developed and successfully used in *Arabidopsis* (Gallois *et al.,* 2002; Kuchen *et al.,* 2012; Sauret-Güeto *et al*., 2013). The system used in *Arabidopsis* is based on the transformation of two separate constructs. One construct consists of a *uidA* gene which is flanked by *loxP* sites and inserted between a 35S promoter and *GFP* (*35S:lox-uidA-lox-GFP*). The second construct is Cre recombinase under the control of the promoter

of a Heat Shock Protein 18.2 (Sieburth *et al.*, 1998) (*hsp18.2::Cre*). Before heat shock, only the first marker gene (*uidA*) is expressed. Induction of Cre recombinase by a 38 °C heat shock leads to recombination of the lox sites which are in the same orientation. This causes the excision of *uidA* as a circular piece of DNA and therefore the activation of GFP in random cells. The daughter cells of these cells inherit GFP expression under the control of the 35S promoter, leading to sectors of GFP expressing cells across the tissue. This system can be altered so that marker genes of choice can be used in place of *uidA* and *GFP* (Figure 3.2).
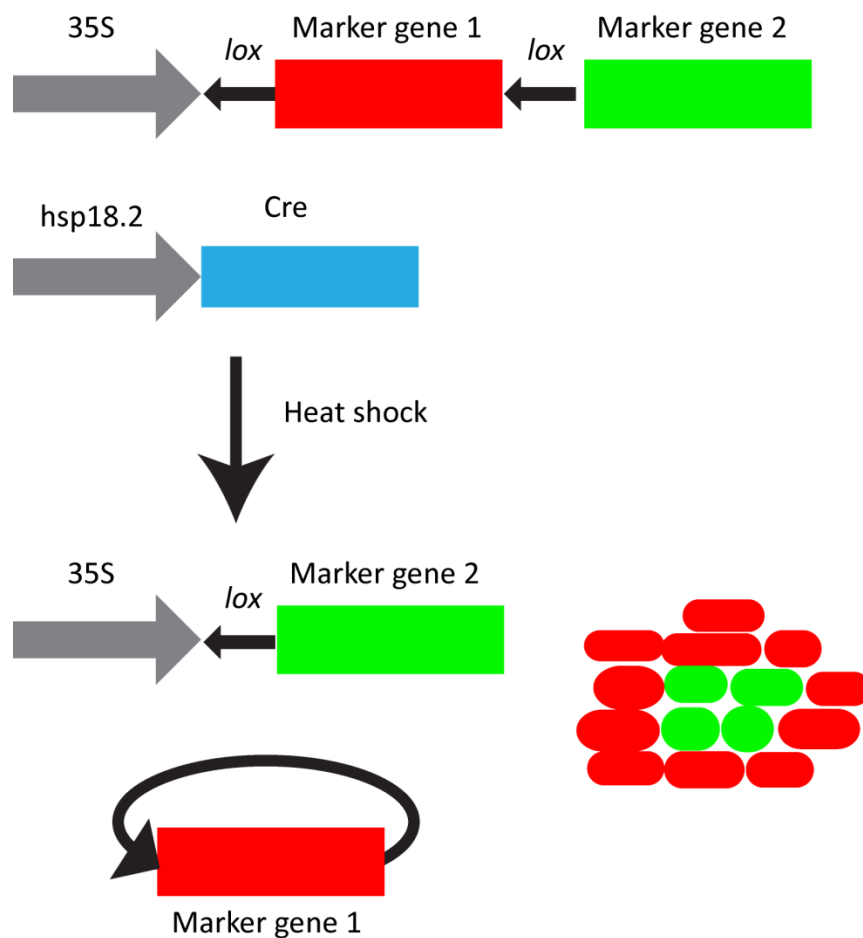
Figure 3.2: Diagram illustrating the cre-loxP based system for the generation of sectors in plant tissue. Transgenic plants contain a reporter construct consisting of the lox-flanked marker gene 1 inserted between the 35S promoter and marker gene 2, and a heat shock inducible Cre recombinase. After heat shock, Cre recombinase is activated which catalyses the recombination of the *loxP* sites flanking marker gene 1. This causes the excision of this marker gene because the *lox* sites are in the same orientation. Marker gene 2 is then activated in random cells and their descendants, forming a sector.

Since sectors are generated from a single cell, they provide information on growth orientations and anisotropy at both the cell shape and division level. The extent of cell shape anisotropy can be inferred by comparing cell number anisotropy (by calculating anisotropy based on the cell number in the major and minor axis of each sector) to anisotropy in length in the major and minor axis of each sector.

3.1.3 Aim of this work

The aim of this work is to test the hypotheses made by isotropic and anisotropic growth models described in the previous chapter by exploring polarity and growth dynamics of developing *U. gibba* bladders.

3.2 Results

3.2.1 Sector analysis

3.2.1.1   Generating a heat shock inducible sector line in *U. gibba*

Sector lines which use the heat shock inducible system are normally generated by transforming separate plants with either the marker genes or the inducible Cre construct and then crossing these plants. This is suited to plants such as *Arabidopsis* which has a short life cycle and can be crossed readily. However, the life cycle of *U. gibba* is more unreliable and flowering was limited to the summer months when plants flowered successfully in the glasshouse. Because of this, a slightly different system is more appealing whereby a single construct can be generated through modular Golden Gate cloning. This technique allows for flexible creation of single binary transformation vectors through progressive cloning. This involves the generation of level 0 (L0) modules (synthesised components) which are combined to make level 1 (L1) components (transcriptional units), which in turn are combined to make L2 constructs (multigene units) (Weber *et al*., 2011). The Golden Gate cloning system is based upon the bacterial type IIS endonuclease restriction enzymes Bsal, Bpil, and ESp3I which cut downstream of a specific recognition site. Specific 3' and 5' overhangs (termed fusion sites) are designed in such a way that fragments cut by the same type IIS endonuclease can be linearly ligated by T4 ligase in a specific order (Weber *et al*., 2011).

I collaborated with Annis Richardson and Samantha Fox who together designed a heat shock Cre construct for the lab using Golden Gate cloning (see materials and methods for details). Christopher Whitewoods performed Golden Gate reactions to generate the construct for *U. gibba*. I also collaborated with Minlong Cui who successfully developed a transformation protocol for *U. gibba* and performed all transformations.

3.2.1.2 Generating a sector data set

I heat shocked *U. gibba* tissue containing a range of bladder sizes at 45 °C for 6-8 minutes. I then imaged bladders at the 622 μm and 933 μm stage, two or four days after heat shock (2 DAHS, 4 DAHS). Based on growth analysis presented in chapter 1, I inferred the sizes of observed bladders at the time of heat shock (Figure 3.3).
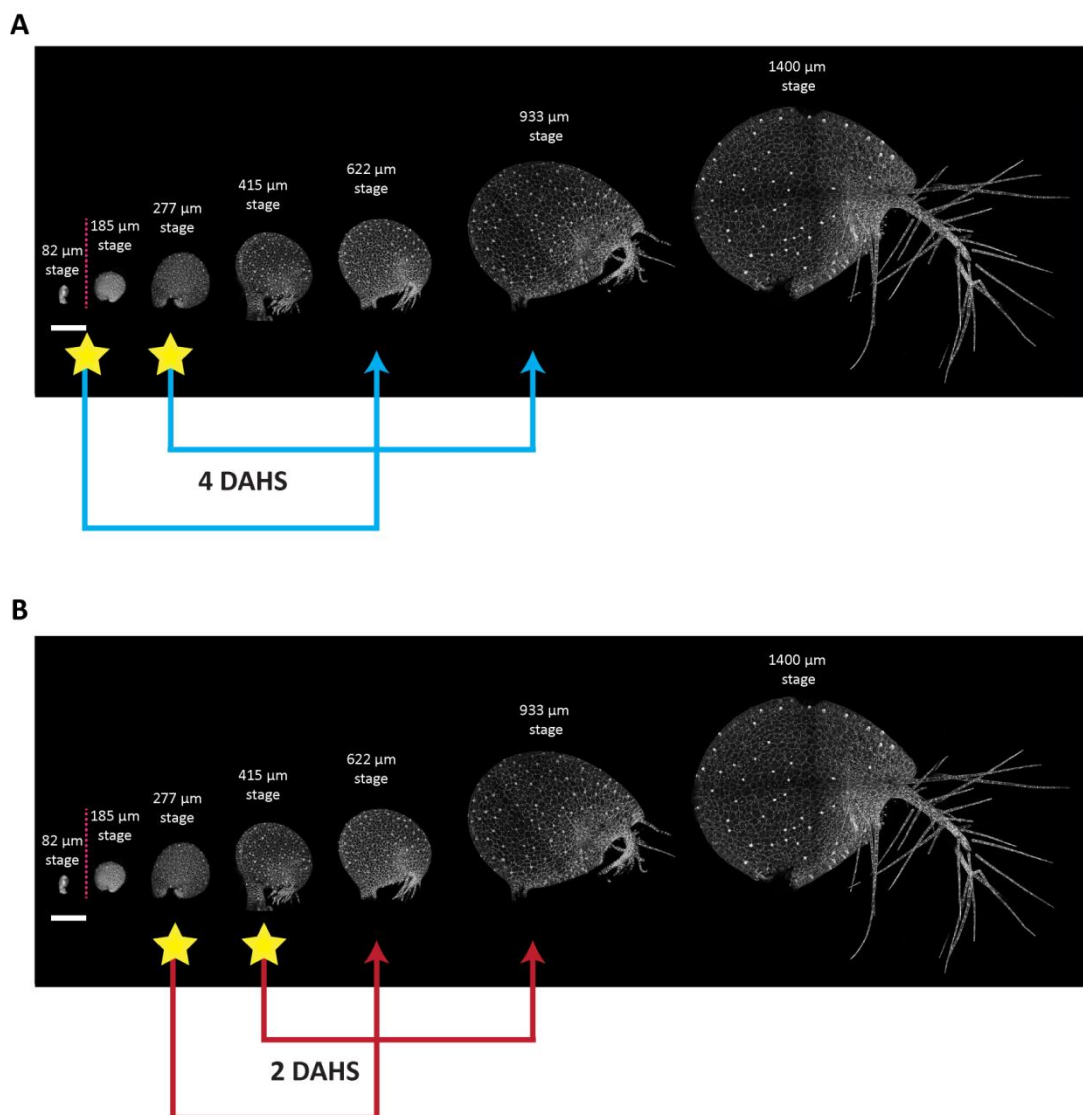
Figure 3.3: Heat shock timings based on bladder stage. Bladder developmental series (stages 82 μm- 1400 μm). (A) Stages heat shocked (yellow star) and imaged 4 days after heat sock (DAHS) (blue arrow). (B) Stages heat shocked (yellow star) and imaged 2 DAHS (Red arrow). Scale bar is 200 μm.

I imaged bladders from the side to capture any sectors in view and so that a length measurement could be made for staging purposes. I then manually turned the bladder to the appropriate view to image any sectors that were near the midvein or in the chin region.
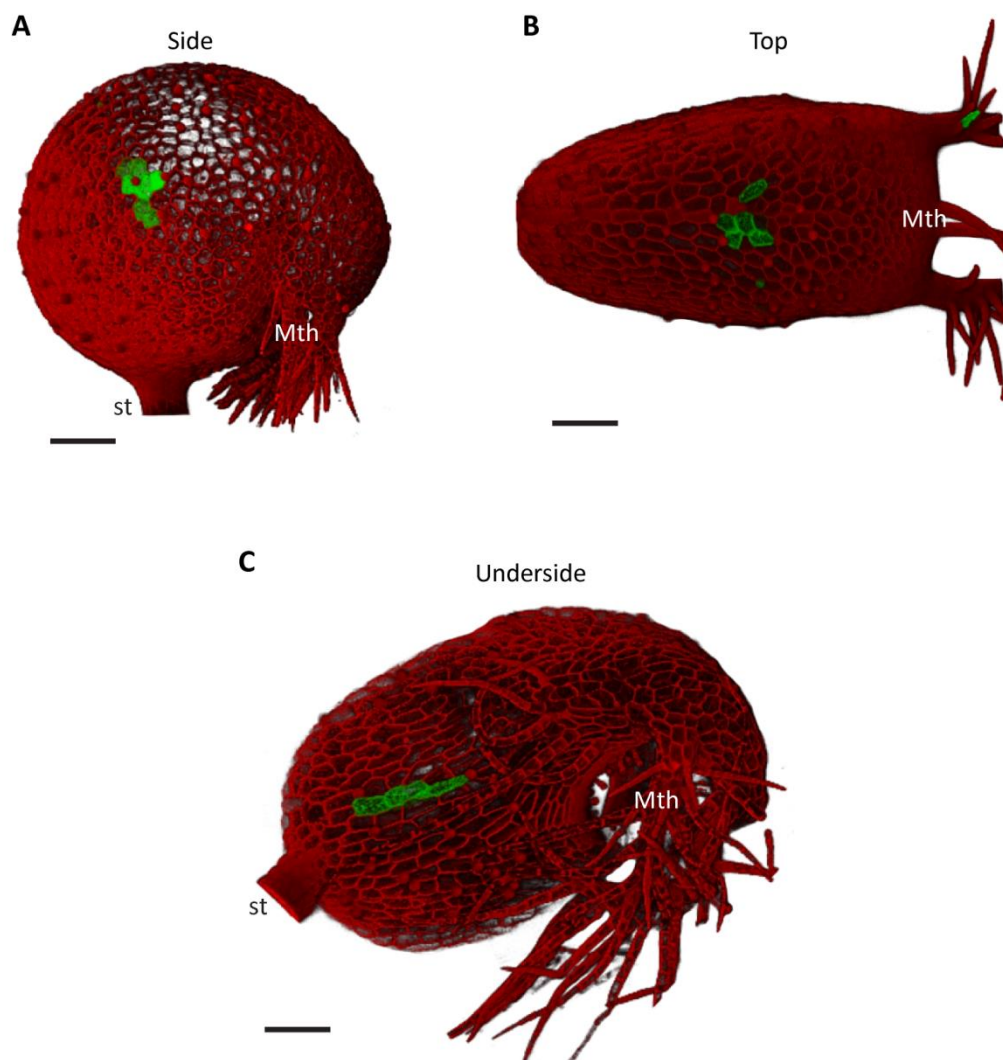
Figure 3.4: Imaging bladders in multiple views to capture sectors on a 3D structure. Heat shock inducible bladders imaged from the side (A), top (B), and underside (C). Tissue was heat shocked at 45 °C for 6-8 minutes and then imaged 2 or 4 DAHS by confocal microscopy.

3.2.1.3   Sector overview

I first looked at this data to gain some broad information on cell division and cell growth in the bladder.

Cell division

To look at cell division, I separated sectors from bladders in the 622 μm and 933 μm categories and plotted the mean number of cells in these sectors at 2 and 4 days after heat shock (Figure 3.5).
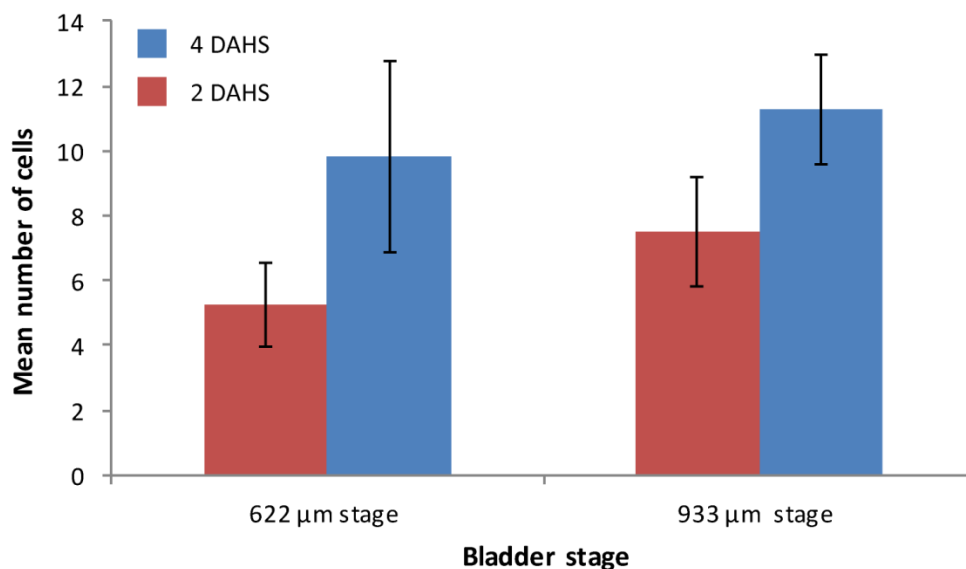
Figure 3.5: Mean number of cells per sector at 2 DAHS and 4 DAHS. Red shows data from bladders imaged 2 DAHS. Blue shows data from bladder imaged 4 DAHS. Bars show standard error of the mean, taking sample size into account.

In each case, there are more cells in sectors imaged 4 DAHS than in sectors images 2 DAHS (Figure 3.6). Division rates inferred by this data are of the order of ~1 division every 2-3 days.

Visual evidence suggests that cell division rate at earlier stages may be higher than at later stages. For example, bladders imaged at 5 DAHS show a 933 μm bladder compared to a 415 μm bladder (Figure 3.6). Here, the 415 μm stage bladder would have been heat

shocked at around the 54 µm stage, while the 933 µm bladder would have been heat shocked around the 123 µm stage. The 415 µm bladder (Figure 3.6, white arrowhead) has a much larger region of GFP which contains many more cells than the sectors on the 933 µm bladder. This patch of GFP covers more than 50 % of the side of the 415 µm bladder. Assuming this region is one sector, this suggests that division rates at very early stages (before the 82 µm caplet stage) are much higher. More analysis of early stages would need to be done to be conclusive.
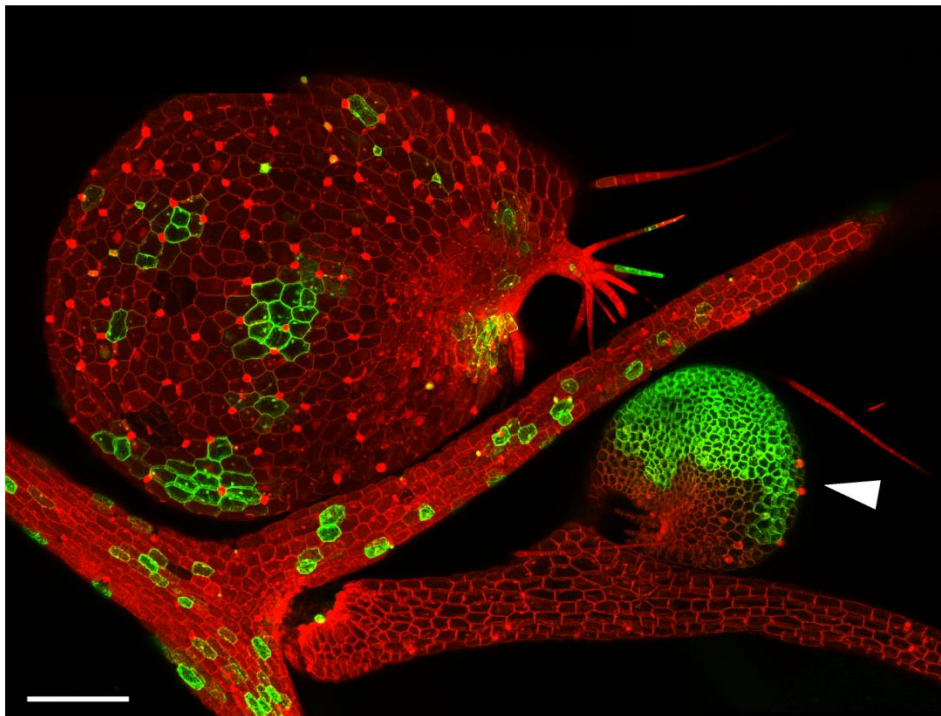
Figure 3.6: Sector cell numbers 5 DAHS on bladders imaged at the 933 µm and 415 µm stage. (Left) bladder imaged at the 933 µm stage 5 DAHS (heat shocked after the 82 µm caplet stage at approximately the 123 µm stage). (Right) Bladder imaged at the 415 µm stage 5 DAHS (heat shocked before the 82 µm stage at approximately the 54 µm stage). Scale bar is 200 µm.

Cell expansion

To study cell expansion in the bladders, I calculated the average cell area per sector by dividing the sector area by the number of cells in the sector. I measured sector area in VolViewer by clicking round the sector using the 'magnetic lines' tool in the VolViewer

measure panel. I then used the 'faces' tool to fill the outline with triangles and obtained sector area information by taking the sum of these triangle faces (Figure 3.7).
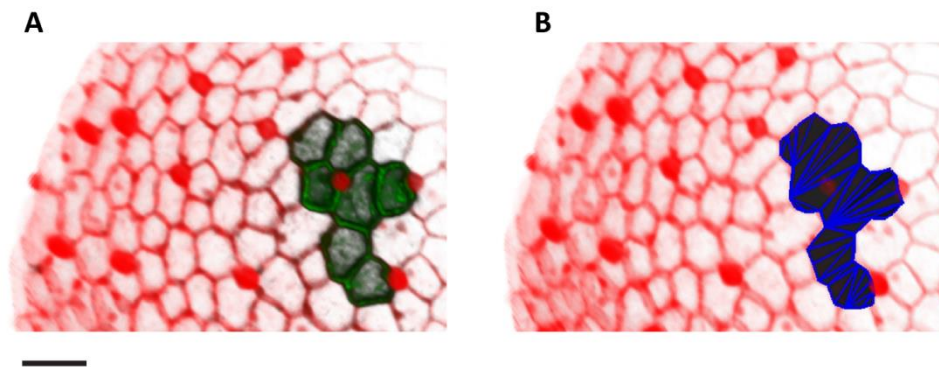
Figure 3.7: Calculating sector area on a 3D volume. (A) GFP sector on the side a bladder imaged 2 DAHS. (B) Sector in (A) after an outline has been attached to the 3D volume and filled with triangles (blue). Sector area is given from the sum of the area of these triangles. Scale bar is 40 μm.

I then plotted the natural logarithm of the average cell area in a sector against the natural logarithm of the bladder length (Figure 3.8). I found that as bladder length increases, the average cell area also increases.

$$y = 1.7571x - 5.0043$$
$$R^2 = 0.7302$$
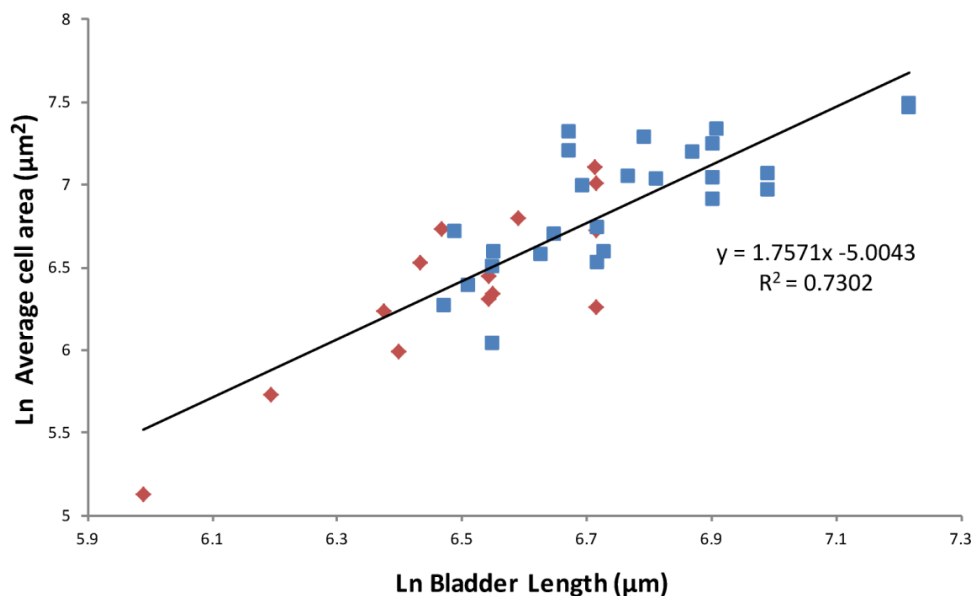
Figure 3.8: Average cell area versus bladder length. Natural logarithm of the average cell area (sector area/ cell number) against the natural log of the bladder length and fitted line. Red diamonds are data collected 2 DAHS. Blue squares are data collected 4 DAHS.

These preliminary results indicate that cell division rate is in the order of ~ 1 division per 1-2 days, and that cell division rate may decrease through development. Cell size increases exponentially between the 622 μm and 933 μm stages. More data is required to validate results and to look at earlier stages where bladders have been heat shocked younger and imaged at younger stages. This would give more information on cell division rates and cell expansion through earlier developmental stages.

3.2.1.4 Testing predictions made by the models

I set out to test a number of predictions made by model 3 (specified isotropic growth in the main body of the bladder) and model 6 (specified anisotropic growth in the main body of the bladder) presented in chapter 2. These predictions include:

1.) A higher level of anisotropy in the chin region of the bladder compared to the main body of the bladder, with clones at the chin region oriented parallel with the axis between the stalk and mouth (predicted by both models).

2.) Larger sectors near the midvein and smaller sectors at the sides of the bladder (predicted by model 3) **or** approximately equal sized sectors (predicted by model 6).

3.) Sectors oriented perpendicular to the midvein near the midvein, and parallel to the midvein at the sides of the bladder (predicted by model 3) **or** sectors oriented parallel to the midvein across the bladder (predicted by model 6).

3.2.1.4.1 Studying sector anisotropy at the chin region

To test predictions made by the models in chapter 2, I first considered growth in the chin region. To achieve elongation of this region without causing the canvas to bulge, the models required increased areal growth and higher specified anisotropy at CHIN. This led to higher levels of resultant anisotropy in the CHIN region compared to the rest of the canvas. If this is the case in the bladder, I would expect sectors in the chin region to also have higher levels of resultant anisotropy than the main body of the bladder.

To study resultant anisotropy in the chin region versus the main body of the bladder, I first compared the shapes of sectors found in these regions. At first glance, sectors in the chin region appear more elongated when compared to sectors across the main body of the bladder (Figure 3.9, C and D). To study this more quantitatively, I calculated the rate of increase in anisotropy per hour of sectors across the bladder. I opened the PNG image stacks in VolViewer and rotated the volume so that the sector of interest was flat to view and took a snapshot of the sector face on with a scale bar present. I then opened sector images in Image J and set the scale based on the known length of the scale bar. I used the polygon selection tool to draw around the sector and fitted the best fitting ellipse to the sector using the Fit Ellipse tool (Figure 3.9, E and F). I then extracted the major and minor measurements which are the primary and secondary axis of the ellipse. To calculate anisotropy, I took the natural logarithm of major/minor. This gave me anisotropy measurements based on the length of the major and minor axes. I also counted the number of cells that the major and minor lines crossed to give me an anisotropy value based on cell number. For this calculation I took the natural logarithm of the major cell number/minor cell number. To allow me to compare this data directly to the model, I calculated the rate of increase in anisotropy per hour:

$$\frac{(Ln(major/minor))}{h}$$

Where h is the number of hours since heat shock and it is assumed that the rate of increase in anisotropy is exponential (as growth is exponential).
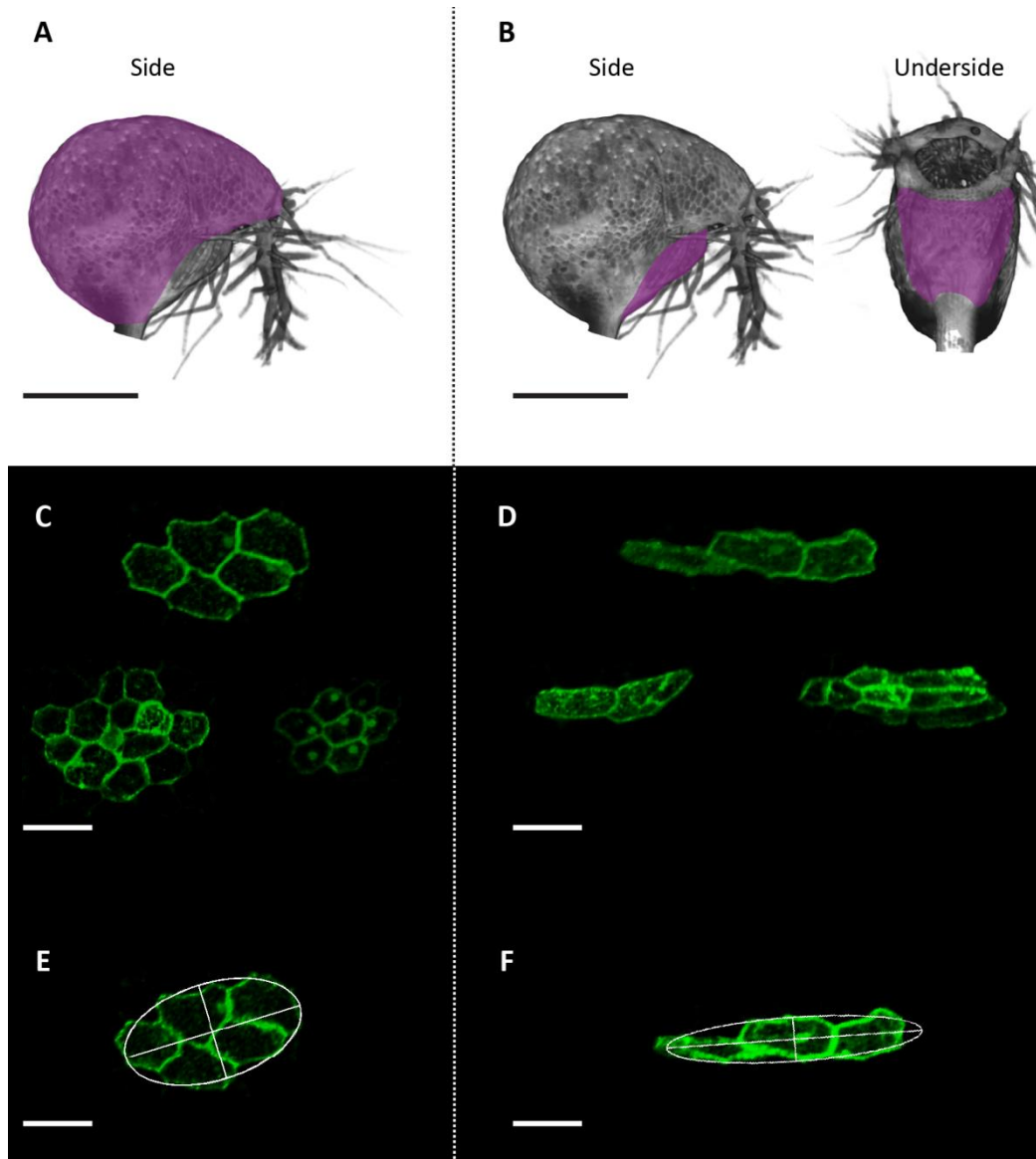
Figure 3.9: Sectors in the main body of the bladder and at the chin region. (A) Bladder with the main body region defined (purple). (B) Bladder viewed from the side and underside with the chin region defined (purple). (C) Example sectors from the main body of the bladder. (D) Example sectors from the chin region. (E) Example sector from the main body with fitted ellipse and major and minor axes marked. (F) Example sector from the chin with fitted ellipse and major and minor axes marked. (A-B) Scale bars are 550 μm. (C-F) Scale bars are 50 μm.

Anisotropy of sectors: limitations

Measurements made here are approximate measurements of the flattened image and do not take bladder curvature into account. Calculations may overestimate the rate of increase in anisotropy per hour for the following reasons; the anisotropy calculation assumes that the initial cell that was heat shocked was isotropic (equivalent to a circular clone in the model). However, it is likely that cells across the bladder had some level of anisotropy at the time of heat shock. There may also be artificial anisotropy due to the irregularity of cell shapes. Since cells are not perfect circles, there is always a long axis. There may also be a level of noise due to cell divisions giving a bias, for example, after one division there will be a 2:1 ratio of cells in the major: minor axis. Therefore, sectors with fewer cells offer more bias.

3.2.1.4.2   Anisotropy in the main body of the bladder compared to the chin region

To study sector anisotropy across the main body of the bladder versus the chin region, I plotted the mean rate of increase in anisotropy per hour for these regions. These calculations are based on the length and cell count of the major/ minor lines of each fitted ellipse (Figure 3.10).

A

B

C
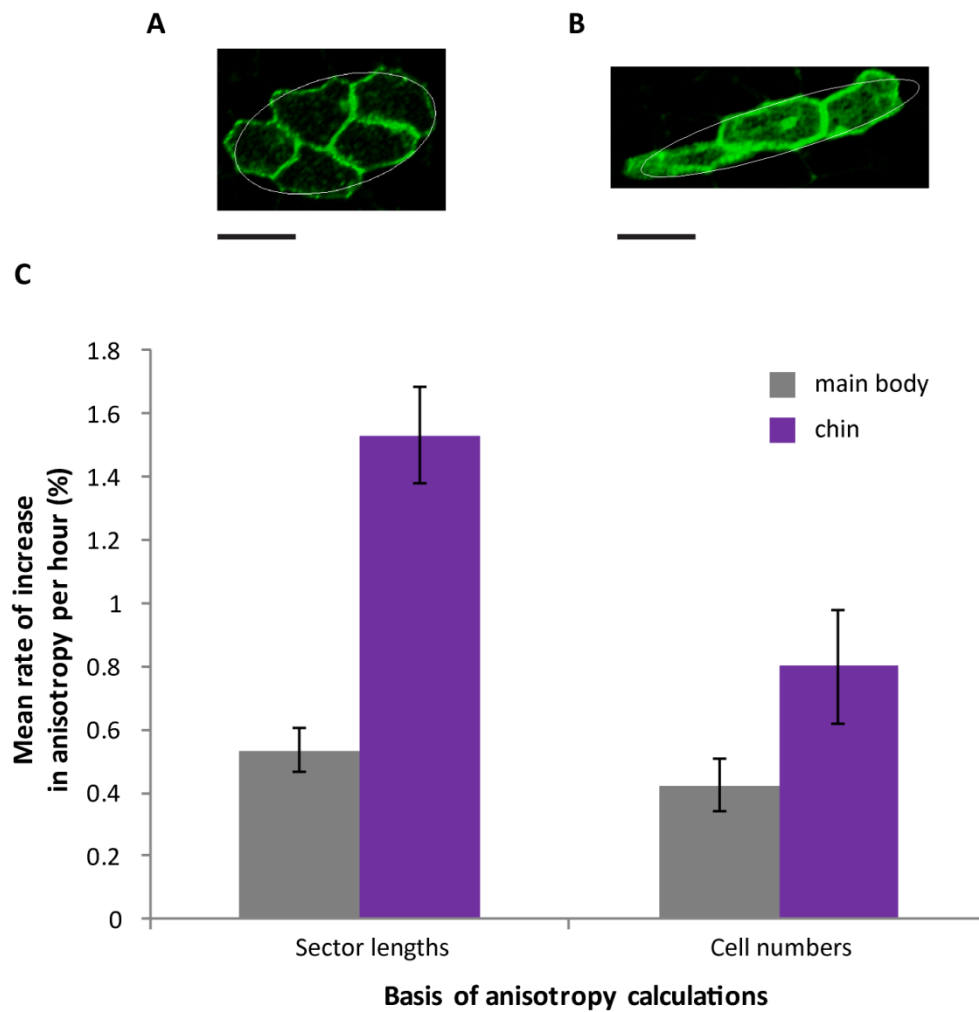
Figure 3.10: Average rate of increase in anisotropy per hour in the main body of the bladder and at the chin region. (A) Example sector from the main body of the bladder with fitted ellipse in white. (B) Example sector from the chin region of the bladder with fitted ellipse in white. (C) Bar graph showing the mean rate of increase in sector anisotropy per hour of sectors across the main body of the bladder (grey) and at the chin region (purple). Sector anisotropy is calculated in terms of major and minor lengths and in terms of cell number in the major and minor axis of each sector. All sectors in this graph were imaged 4 DAHS on 933 μm bladders. Bars show standard error of the mean, taking into account sample size. Scale bars are 50 μm.

The mean rate of increase in anisotropy per hour based on sector length measurements and cell number is greater at the chin region than in the main body of the bladder (Figure 3.10, purple compared to grey bars). Calculations based on sector length measurements show that the mean rate of increase in anisotropy per hour is almost 3 times greater in the chin region compared to the main body of the bladder (approximately 0.5 % per hour in the main body of the bladder, and approximately 1.5 % per hour in the chin region). When I compare these values to those predicted by the model (Table 3-1) I find that the mean rate of increase in anisotropy per hour in the main body of the bladder and the chin region are higher than predicted by either model (models 3 and 6). Values obtained from the bladder data are closer to those predicted by model 6 (the anisotropic specified growth model) where the average rate of increase in anisotropy per hour was also about 3 times greater in the chin region compared to the rest of the canvas. Model 3 (the isotropic specified growth model with anisotropic specified growth at CHIN alone) predicted that the rate of increase in anisotropy in the chin region would be more than 8 times that in the main body of the bladder. As mentioned above, calculations in the bladder assume that cells are isotropic when heat shocked (at the 277 μm stage in this case). If the cells in each region have some anisotropy at this stage then the calculations will overestimate the rate of increase in anisotropy per hour.

Table 3-1: Comparing predictions made by the models to sector data. Values for the rate of increase in anisotropy per hour are shown and are calculated using: (Ln (major/minor))/ h (where h is the model run time or the time since heat shock).

Model/ data	Main body	Chin
Model 3	0.08 % per hour	0.67 % per hour
Model 6	0.3 % per hour	0.8 % per hour
Bladder data	<u>0.5 % per hour</u>	<u>1.5 % per hour</u>

To study the contribution of cell shape, I looked at the resultant anisotropy based on cell number (Figure 3.10). In the main body of the bladder there is little difference between the rate of increase in anisotropy per hour based on sector length or cell number (around 0.5 % per hour and 0.4 % per hour respectively). However, in the chin region the rate of increase in anisotropy per hour based on sector lengths is approximately 2 times greater than that calculated based on the number of cells along the major and minor axis of the sector

(approximately 1.5 % per hour and 0.8 % per hour respectively) (Figure 3.10). This suggests that cell shape heavily contributes to anisotropy in the chin region. It is not clear from this data when cells become longer and thinner. This may also indicate that division rate at the chin region is lower than the rest of the bladder, since division following a shortest wall algorithm would lead to less anisotropic cells. More data is required to explore these ideas.

This analysis of sectors in the chin region versus the main body of the bladder suggests that resultant growth at the chin is more anisotropic than the rest of the bladder. Since a pure isotropic model cannot account for such resultant anisotropy, this supports a model where growth is specified to be anisotropic at chin. Values of the rate of increase in anisotropy per hour obtained from sector data were closer to that predicted by the specified anisotropic model (model 6). However, it is unclear from this analysis, the extent to which specified isotropy/ anisotropy may play a role in the generation of the main body of the bladder.

3.2.1.4.3 Sector area across the bladder

As discussed in chapter 2, models with specified isotropic (model 3) or specified anisotropic (model 6) growth make a number of predictions on resultant growth across the main body of the bladder. The first prediction considers sector area across the main body of the bladder. A specified isotropic growth model predicts that sectors are larger nearer the midvein and become progressively smaller towards the sides of the bladder since greater areal growth rate at the midvein is required. While for specified anisotropic growth models, sector area across the bladder can be roughly even (assuming even areal growth rate across the canvas).

To enable me to test these predictions and study sectors in the bladders from the sides of the bladder to the midvein, I defined a number of bladder zones for analysis which I numbered 1-4 (where 1 is at the centre of the side, and 4 is closest to the midvein). I made a template ellipse with these zones marked. I then resized the template for each individual bladder and assigned each sector with a position from 1-4. In cases where a sector crossed two zones, I labelled it based on the zone in which the majority of the sector area sat (Figure 3.11).
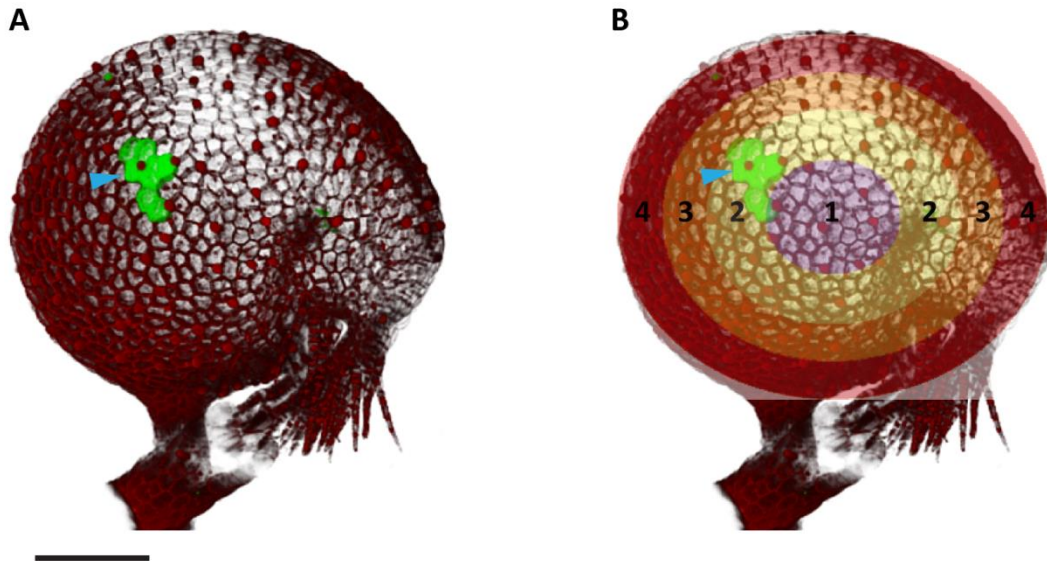
Figure 3.11: Bladder zones 1 to 4 from the centre side to the midvein. (A) Bladder imaged 2 DAHS with a GFP sector indicated (blue arrow). (B) Bladder with zone template overlaid showing zones 1-4 which run around the circumference of the bladder from the centre of the bladder side to the midvein. The same sector as in (A) is indicated (blue arrow) and falls into zone 2. Scale bar is 150 μm.

I looked at the average sector area in each zone at 2 and 4 DAHS. To overcome having a small data set, I normalised the data for bladder size by dividing sector area by bladder length^2 (as a proxy for bladder area) so that I could combine my data across different bladder sizes. I did this because I did not have a way to take the curvature of the bladder into account for a bladder area calculation. This gave me a sector area normalised for bladder size and a series of zones across the bladder which I could compare to data from the models where clone position was given by the level of S_MIDVEIN diffusing from MIDVEIN. Therefore, zone 1 is equivalent to areas with lower levels of S_MIDVEIN in the model, and zone 4 is equivalent to areas with higher levels of S_MIDVEIN in the model.

To test predictions on sector area made by the models I plotted the normalised sector area against the bladder zone. If specified growth is isotropic with areal conflict driving the transition in shape, I would expect there to be an increase in sector size from zone 1 to 4. This is because a greater areal growth rate is required at MIDVEIN to drive the transitions in shape in an isotropic growth model (model 3). If growth is anisotropic with no areal conflict (equal growth rates across the main body of the bladder), I would expect sector area to be approximately equal across the bladder.

A

B
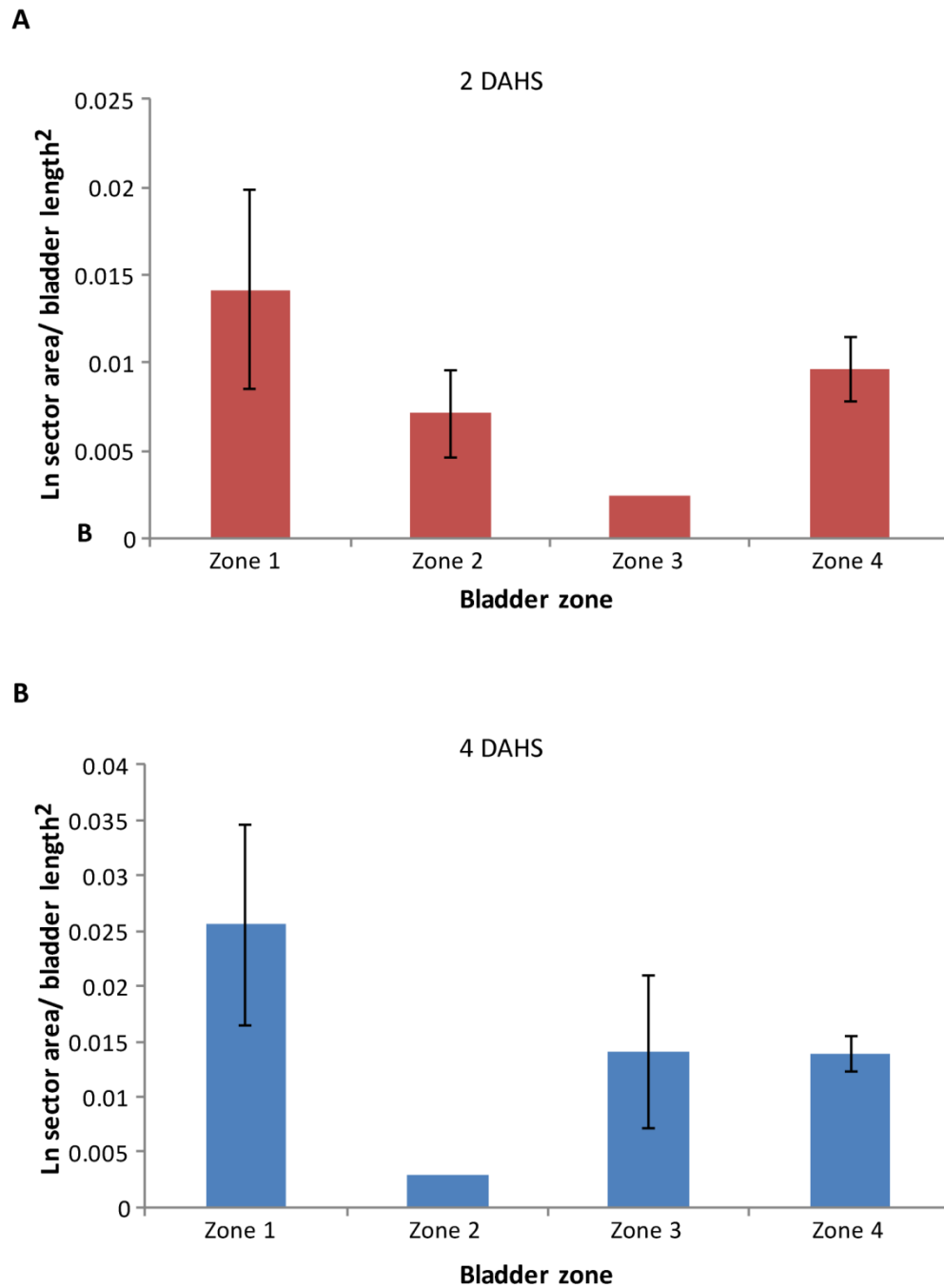
Figure 3.12: Sector area against bladder zone. Sector area normalised for bladder size against bladder zone. (A) Sectors on bladders images 2 DAHS. (B) Sectors on bladders imaged 4 DAHS. Bars show standard error of the mean.

Sector area does not increase from zone 1 to zone 4 at 2 or 4 DAHS (Figure 3.12). Therefore, this data does not support the specified isotropic growth model. Sectors in zone 1 may be larger compared to zones 2 to 4. However, more data is required here to make stronger conclusions and to test for statistical significance.

3.2.1.4.4 Sector anisotropy across the bladder

The models also make a number of predictions on sector anisotropy across the main body of the bladder. The specified isotropic growth model (model 3) predicts low levels of even resultant anisotropy across the main body of the bladder with a rate of increase in anisotropy per hour less than 0.2 % per hour. The specified anisotropic model (model 6) predicts that the rate of increase in anisotropy per hour ranges from around 0.2 % per hour closest to the midvein to around 0.4 % per hour at the sides of the bladder furthest from the midvein.

To test these predictions, I used the same method described above for calculating the rate of increase in anisotropy per hour of each sector. I then plotted the rate of increase in anisotropy per hour against the bladder zone. I pooled my data and made calculations based the measured length of the major and minor axis and in terms of the number of cells in the major and minor axis (Figure 3.13).

A
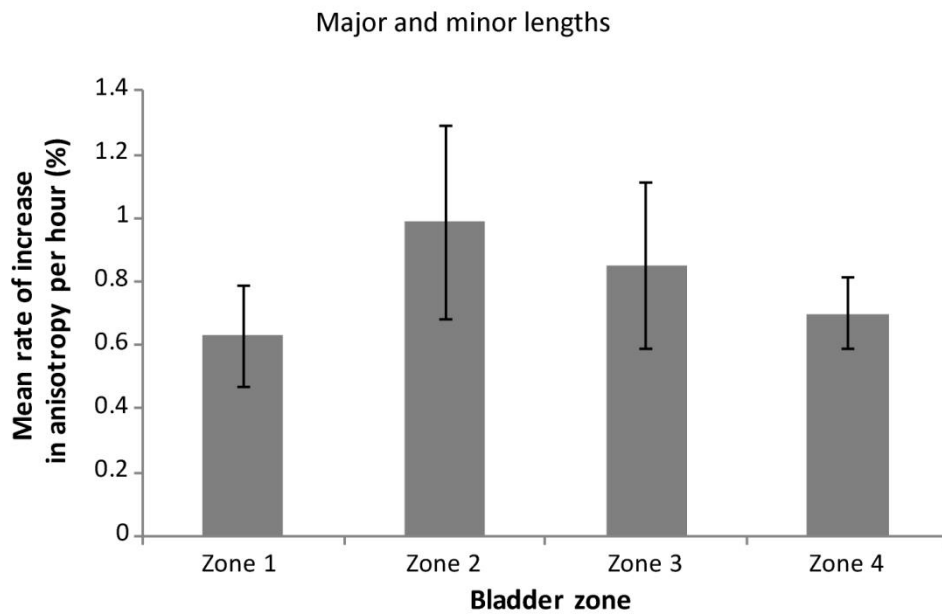
B
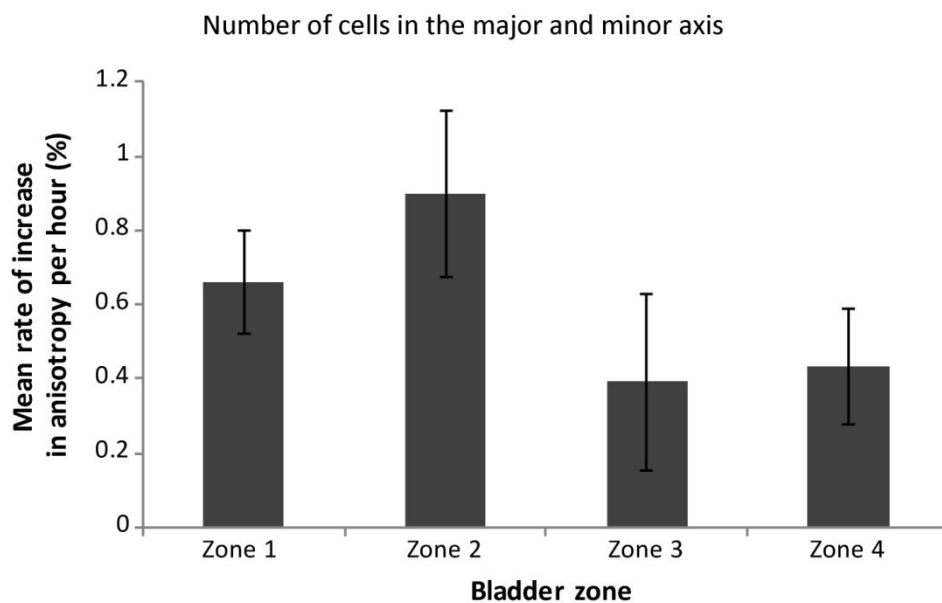
Figure 3.13: Mean rate of increase in anisotropy per hour across the main body of the bladder. (A) Mean rate of increase in sector anisotropy at bladder zones 1-4 where the major and minor lengths were measured. (B) Mean rate of increase in sector anisotropy at bladder zones 1-4 where the number of cells along the major and minor axes were counted. Calculations were based on the major and minor axes of a fitted ellipse on each sector. Error bars show standard error of the mean.

I found no correlation between bladder zone and the mean rate of increase in sector anisotropy per hour in terms of sector length or cell count in the major and minor axes of the sectors (Figure 3.13, A & B). Values based on length measurements of the major and minor axis range between around 0.6 % per hour and about 1 % per hour. This is greater than that predicted by either model where values ranged from < 0.2 % per hour to around 0.4 % per hour. This could mean that the rate of increase in anisotropy per hour across the main body of the bladder is higher than that predicted by the model. However, this higher level could partly be due to cells being anisotropic at the time of heat shock and therefore an overestimation of the rate of increase in anisotropy per hour. Data on cell shape at the time of heat shock is necessary to investigate this further.

This data suggests that there is a level of anisotropy which is roughly even across the main body of the bladder. Although more data would need to be collected to confirm this. I found no evidence for a gradient of anisotropy from the midvein, and therefore no support for a gradient of specified anisotropy model (model 7). Since the level of anisotropy in the data is higher than that predicted by either the isotropic (model 3) or anisotropic (model 6) specified growth models, it is not clear from this analysis alone which is more likely. However, the models also make a clear prediction on the orientation of this anisotropy which I can test.

3.2.1.4.5 Growth orientations

The specified isotropic growth model (model 3) predicts that the major axis of growth in regions closest to the midvein is perpendicular to the midvein, and on the sides of the bladder is more parallel to the midvein. The specified anisotropic growth model (model 6) predicts that the major axis of growth across the bladder is parallel with the midvein, and parallel with the local polarity. In all models which achieve an elongated CHIN region, the major axis of growth at the chin is predicted to be parallel with the midvein and the axis between the stalk and mouth.

To explore growth orientations in the bladder, I fitted each bladder confocal image to an outline of a bladder back, top, side, or chin and marked the fitted ellipse of each sector along with its major axis. I used landmarks such as the mouth, stalk, and midvein to position the sector and compared multiple views of the bladder where possible. This gave

me a rough sector map where I could look at sector orientations globally across the bladder (Figure 3.14). I marked the midvein (Figure 3.14, black dotted line) for reference of orientation to compare to the models.
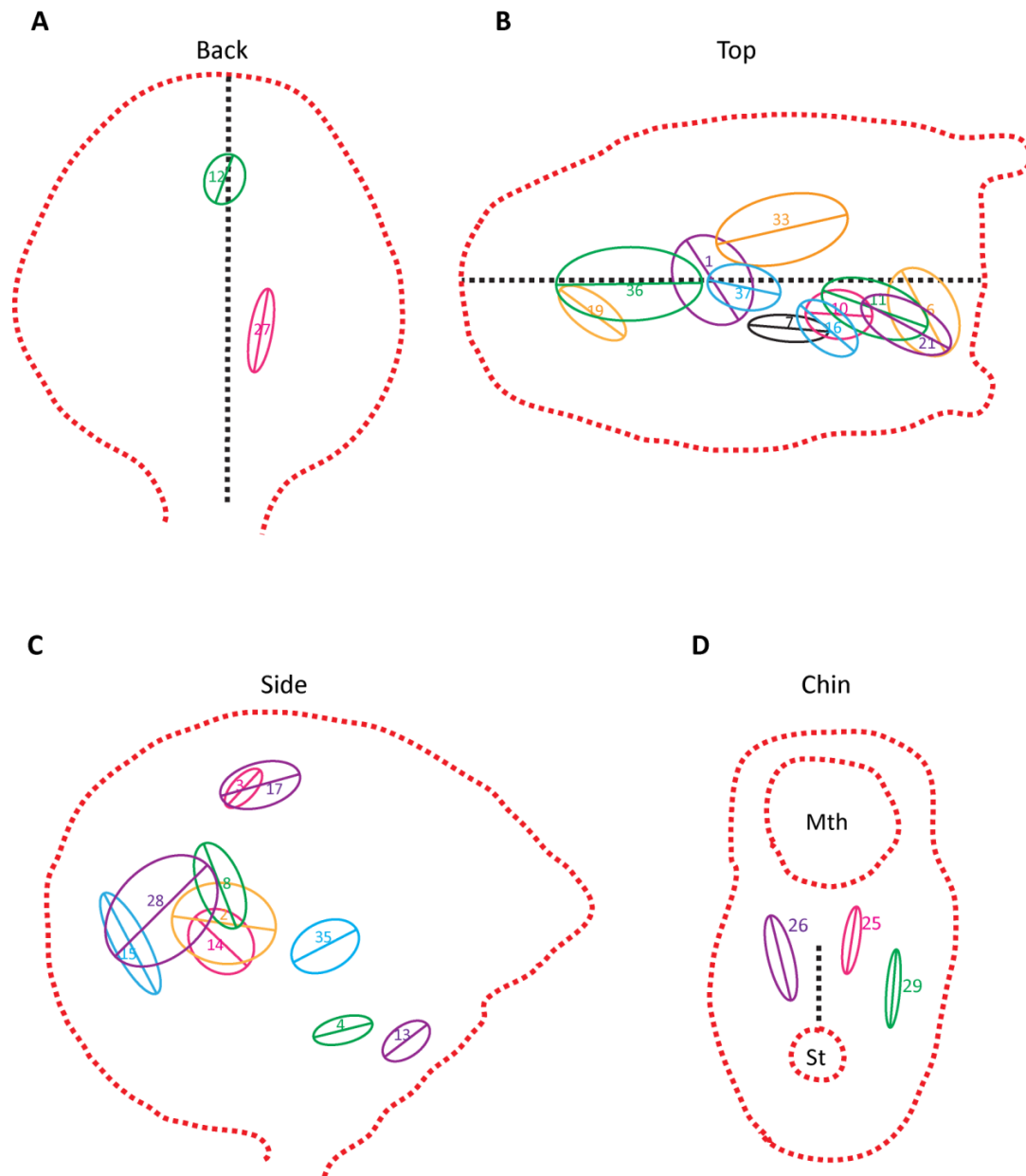
Figure 3.14: Exploring the major axis of growth based on the anisotropy of sectors. Outline of a bladder (red dotted line) viewed from the back (A), top (B), side (C), and chin (D) where St = stalk, Mth = mouth. The orientation of the midvein is indicated (black dotted line). Fitted ellipses of each sector are shown along with their major axis (coloured ellipses and lines). Numbers are a reference for each sector analysed. Ellipses and bladder outlines are not to scale and show the approximate position based on landmarks. Data is a pooled from heat shocked plants images 2 and 4 DAHS and on a range of bladder sizes (622 μm – 933 μm stages).

On the back and top (Figure 3.14, A-B), sectors appear to be oriented approximately parallel with the midvein in general. This supports a specified anisotropic model. Sectors on the side generally appear to be parallel with the midvein across the tissue, also supporting a specified anisotropic model. Some sectors in Figure 3.14, C appear to overlap at orthogonal angles. This is a product of the data analysis method whereby bladders of different sizes were overlaid and resized for analysis. The precise location of sectors relative to one another is therefore not accurate. However, each sector aligns parallel with the proposed local polarity pattern. More data would confirm the patters observed here and remove any cell division bias. At the chin region, sectors are oriented parallel to the midvein, as predicted by models with specified anisotropy in this region and a polarity field pointing from stalk to mouth.

This data suggests that there is a pattern of orientations associated with the anisotropy of the sectors. This suggests that the anisotropy that we see is not entirely artificial due to cell division or shape bias (which one would expect to give rise to a random pattern of orientations based on the major axis). The major axis of the sectors is generally parallel with the midvein, supporting a specified anisotropic model. Sectors in the chin region are oriented parallel with the axis between stalk and mouth, supporting specified anisotropy in this region based on an axis parallel with the midvein.

3.2.1.4.6   Summary of sector analysis data

A key prediction made by the models was that, for elongation of the chin region to occur, specified growth in this region must be anisotropic with the major axis of growth parallel with the midvein. The models predict higher rate of increase in anisotropy per hour in the chin region. I found that clones in the chin region of the bladder had a rate of increase in anisotropy per hour of 1.5 %, compared to 0.5 % per hour in the main body of the bladder. This supports the hypothesis that the chin region has higher anisotropic growth than the rest of the bladder.

A defining feature of the specified isotropic growth model is that clones nearer the centre of the side are smaller and clones closer to the midvein are larger. This is due to the differential areal growth rate across the canvas which drives the shape transition in the

model and is highest near the midvein. In contrast, the specified anisotropic model predicts clones which are approximately even in area across the main body of the bladder. I found no correlation between sector area and position relative to the midvein, suggesting that specified anisotropic growth across the bladder (as in model 6) is more likely. However, more data is required to be more conclusive.

I also found a low level of sector anisotropy across the bladder which was approximately even across zones. This makes model 7 with a gradient of specified anisotropy from the midvein an unlikely solution. It is not clear how much of this anisotropy derives from cells being anisotropic at the time of heat shock. However, a plot of growth orientations studying the major axis of the fitted ellipse for each sector, suggests that there is a consistent pattern across the tissue. Growth appears to be oriented parallel to the midvein across the tissue as predicted by a specified anisotropic growth model (model 6), opposed to an isotropic specified growth model (model 3) which predicts clones at the midvein to be perpendicular to the midvein.

This data supports a model where specified growth is uniformly anisotropic across the main body of the bladder, with higher levels of anisotropy at the chin region. For specified anisotropy to drive growth, axiality is required. Therefore, to test the hypothesis that growth is through specified anisotropy, I will consider how this axiality may be generated.

3.2.2 Axiality via tissue polarity

In the models, axiality is provided by a polarity field that is set up using diffusible POLARISER which diffuses across the canvas from a plus organiser and is absorbed by a minus organiser. Models with specified anisotropic growth in any region of the canvas make the prediction that the polarity field propagates from stalk to mouth (or *vice versa*) and is present from at least the 82 µm stage. Since the model makes key predictions on a polarity based axiality system, I decided to explore these predictions first as a means of generating axiality. To explore axiality during development, I looked for markers of cellular polarities.

3.2.2.1 Quadrifid glands as external markers of tissue polarity in *U. gibba*

One marker that I explored was the quadrifid glands that line the inner surface of the bladder (Figure 3.15, A). These glands consist of a basal cell, a pedestal cell, and 4 terminal cells which from a cross-like arrangement. At later stages of bladder development, the terminal cells of quadrifid glands have a clear direction and orientation which can be defined through the angles between each of the cells. Two opposite obtuse angles and two opposite acute angles allow an orientation to be assigned (parallel with the obtuse angles) to each quadrifid gland (Figure 3.15, Bi). Then each of the acute angles can be studied, and in most cases, a direction can be assigned with an arrow pointing towards the widest of the acute angles (Figure 3.15, Bii).
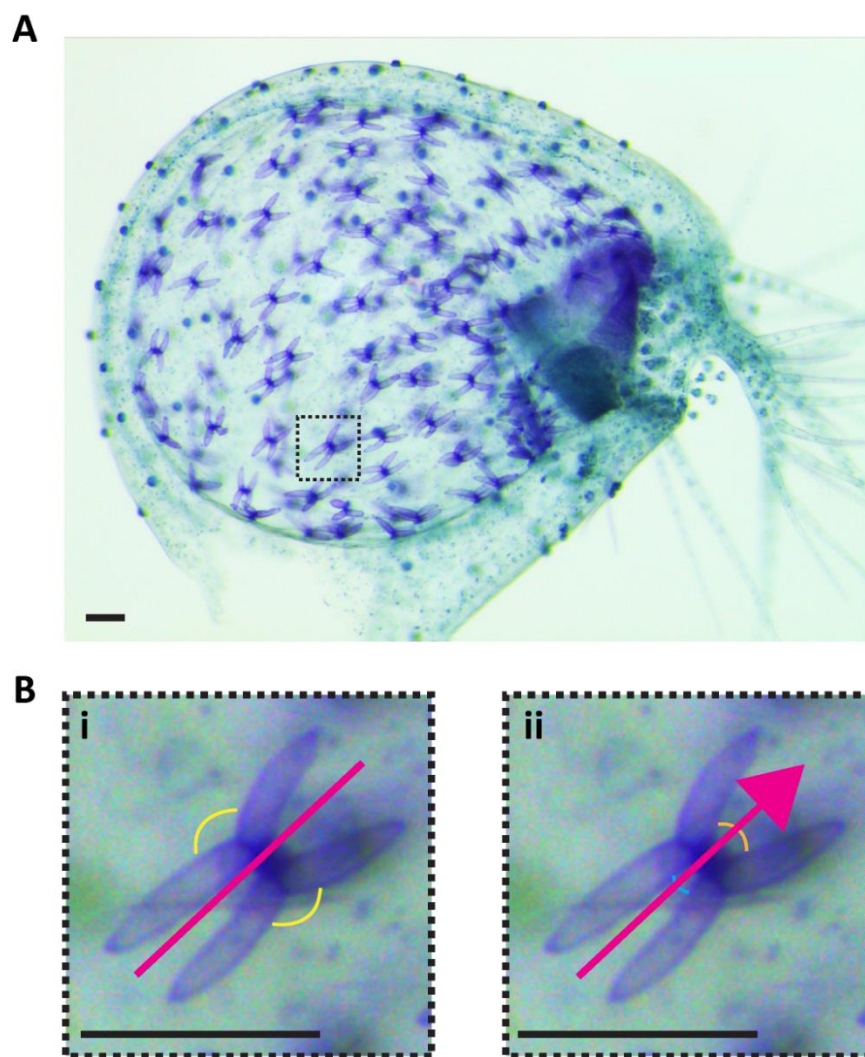
Figure 3.15: Quadrifid glands on the inner surface of the bladder can be assigned an orientation and a direction. (A) Bladder stained with toluidine blue with quadrifid glands visible on the inner surface (blue cross shaped structures). (B) A single quadrifid gland from (A). (Bi) An orientation can be assigned (pink line) parallel with the two widest angles of the quadrifid cells (yellow). (Bii) Direction can be assigned by comparing the remaining two

angles (blue and orange) and placing an arrow head at the wider of the two (orange) for consistency. Bladder image taken by Karen Lee on a light microscope. Scale bars are 50 μm.

To get an overall picture of quadrifid gland polarity across the bladder, I used OPT 3D imaging in collaboration with Karen Lee. To remove any bias in selecting the direction of the arrows, I collaborated with Jake Newman who wrote a MATLAB function which automatically assigns a direction based on comparing the distances between points at the tips of each cell (see materials and methods for more details). This allowed me to generate a map of arrows across a bladder.

The models predict a polarity field which propagates from the bladder stalk and points towards the bladder mouth (or *vice versa*) in arching patterns across the bladder side (see chapter 2). If a polarity field propagating from the stalk exists in the bladder, I would therefore expect to see a similar pattern in the polarity of the quadrifid glands across the bladder side. To test this, I explored the polarity of the quadrifid glands at the sides of the bladder (Figure 3.16). I looked at a 933 μm and 622 μm stage bladder on both sides to see if patterns were consistent.

I found that the quadrifid glands lining the sides of the bladder had a coordinated pattern of orientation and direction, with the majority of arrows pointing away from the stalk region and towards the mouth region in a similar arching pattern as predicted by the model (Figure 3.16). The polarity pattern of the quadrifid glands appears to be consistent across each side of the bladders analysed when the 933 μm and 622 μm stage bladders are compared. The occasional arrow points in the opposite direction to those surrounding it. There doesn't appear to be a pattern associated with these arrows that would suggest a convergence or divergence point in the tissue since they are dispersed across the bladder. These could be errors in the analysis due to the 3D nature of the quadrifid glands. A more detailed analysis would be able to clarify the finer details of the pattern. In all cases, the orientation of the glands is consistent.
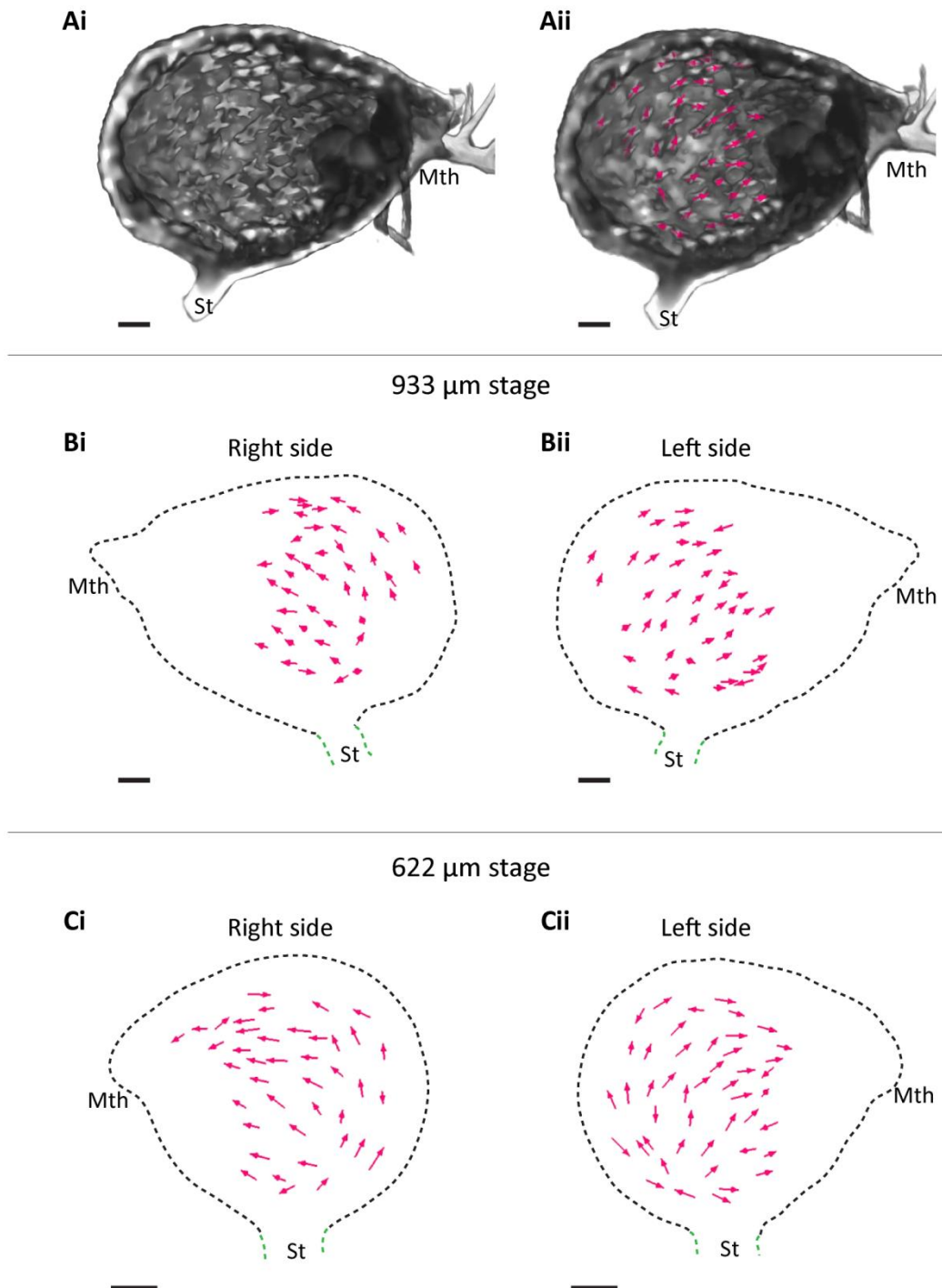
Figure 3.16: Quadrifid gland polarity at the sides of bladders. (Ai) Side section of a 933 µm stage bladder imaged using OPT. Quadrifid glands are visible on the inner surface. (Aii) Arrows indicating the polarity of the quadrifid glands. (B) Outlines of a 933 µm stage bladder viewed from the right (Bi) and left (Bii) sides. (C) Outlines of a 622 µm stage bladder viewed from the right (Ci) and left (Cii) sides. Arrows show quadrifid gland polarity. Bladder stalk (St), mouth (Mth), and antennae (a) are labelled. Scale bars are 100 µm.

I next looked at the top surface of the bladder. The models predict that the polarity field runs parallel to the midvein at the top, pointing towards the mouth of the bladder. To test this I studied the quadrifid glands in this region of a 933 μm and 622 μm stage bladder (Figure 3.17).

A

Bottom section

a

Mth

a

B

933 μm stage

Top

a

Mth

a

C

622 μm stage

Top

a

Mth

a
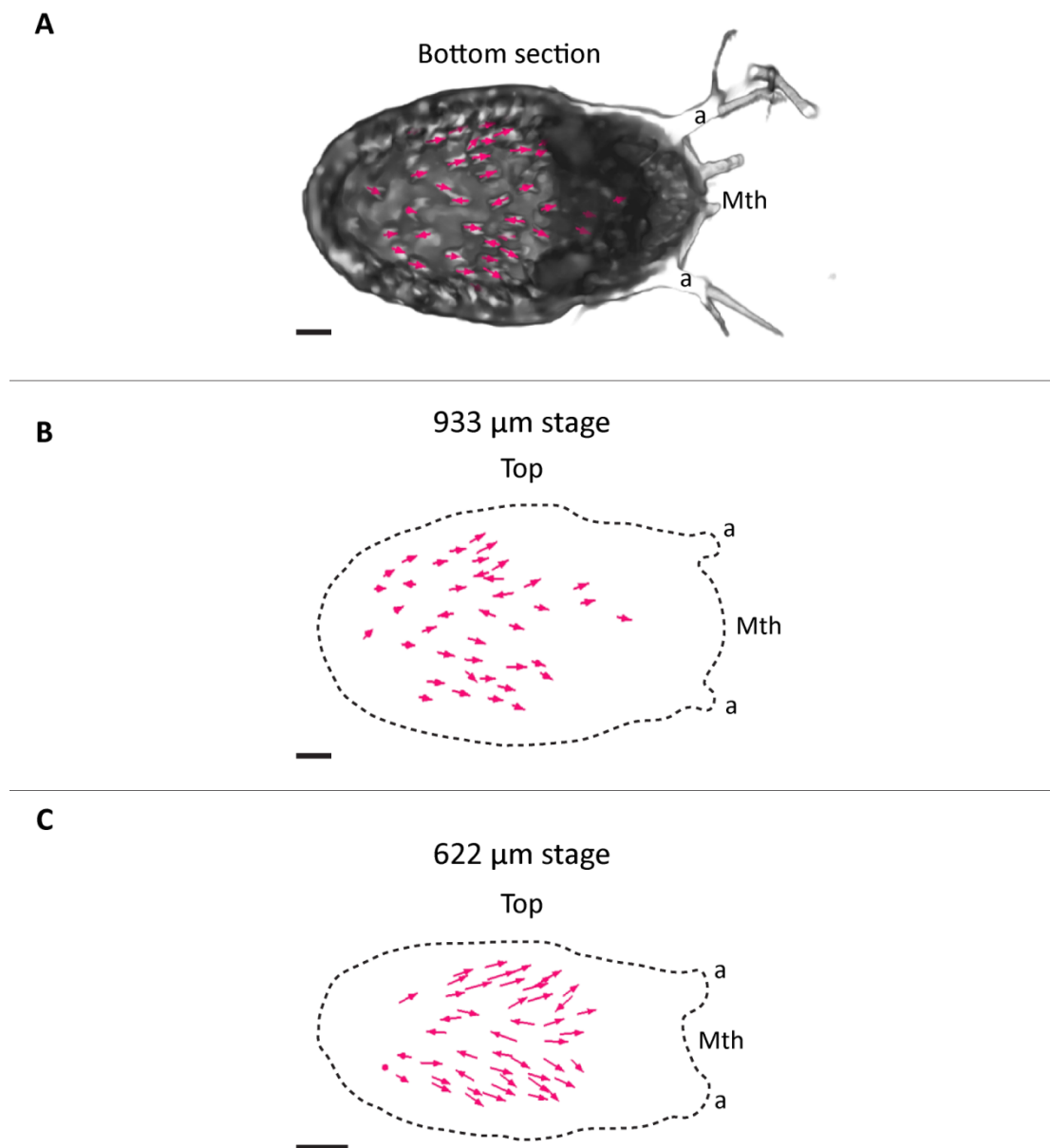
Figure 3.17: Quadrifid gland polarity at the top of bladders. (Ai) Bottom section of a 933 μm stage bladder imaged using OPT showing the top surface of the bladder with quadrifid glands and associated arrows marking their polarity. (B) Outline of a 933 μm stage bladder viewed from the top. (C) Outline of a 622 μm stage bladder viewed from the top. Arrows show quadrifid gland polarity. Bladder stalk (St), mouth (Mth), and antennae (a) are labelled. Scale bars are 100 μm.

Arrows marked on the inner surface of the top of the bladder show that quadrifid glands are oriented parallel with the midvein and then appear to diverge towards the antennae at the front (clearest in Figure 3.17, C). The direction of the arrows in this region is generally towards the mouth (or antennae) and away from the back. However, there are a few arrows nearer the midvein which point backwards (away from the mouth). I see these arrows in both samples. This could suggest that polarity at the midvein points in the opposite direction to the rest of the tissue.

A key prediction in the model is that polarity propagates from the stalk of the bladder. I would therefore expect the polarity of the quadrifid glands around the stalk region to point away from the stalk in a radial fashion. Unfortunately, this region was very blurred in the scans so I was only able to look at the 622 μm stage (Figure 3.18).
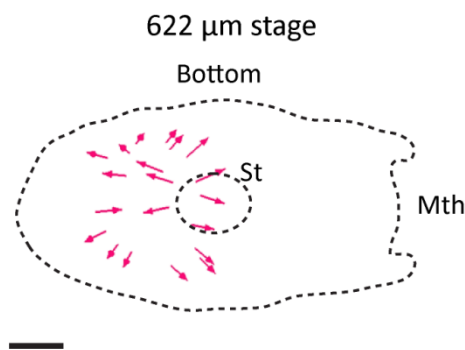
Figure 3.18: Quadrifid polarity at the stalk of the bladder. Outline of the bottom of a 622 μm stage. Arrows show quadrifid gland polarity. Bladder stalk (St) and mouth (Mth) are labelled. Scale bars are 100 μm.

Quadrifid glands across the stalk region appear to point in all directions away from the stalk (Figure 3.18). Quadrifid glands behind the stalk, generally point towards the back of the bladder, while those on the stalk region point towards the mouth. Analysis of more samples is required here to confirm this pattern and to capture more regions, such as the chin region, which were too blurred in the scans to analyse.

3.2.2.1.1 Summary of quadrifid gland analysis

Analysis of quadrifid gland polarity across the bladder suggests that the broad pattern of polarity (from stalk to mouth) is consistent with model predictions. Polarity at the top of the bladder is parallel with the midvein, as predicted by the model, and then diverges towards the antennae at the front. This, suggests that there may be two minus organisers for the generation of the antennae. Quadrifid glands at the stalk appear to point away from the stalk, consistent with a model where the stalk acts as the plus organiser for polarity. However, more data in this region is needed.

The orientation of the quadrifid glands is coordinated across the bladder (when we consider the lines alone) and is also consistent with the model. However, the direction (arrow heads) shows some quadrifid glands pointing in the opposite direction (away from the mouth). It is not clear whether this is patterned or if there are errors in the analysis which could be due to the 3D spacing of the cells. More analysis is needed to look into this. Not all quadrifid glands have a clear direction, since the two acute angles can be very similar to each other. This method of studying tissue polarity is therefore limited.

The model also predicts that this polarity pattern is set up from an early stage. However, quadrifid glands are not visible at very early stages and are therefore not useful as markers of axiality in younger stages of development. To study earlier stages, I looked at a marker for polarity that is present at earlier stages such as the polar localisation of PIN proteins.

3.2.2.2 PIN polarity

Assuming that a polarity based axiality system is present in the developing bladder, PIN1 auxin transporters may be used as markers of cell polarity. The coordination of these cell polarities across the tissue (tissue cell polarity) may therefore indicate the orientation of axiality.

3.2.2.2.1 PIN protein phylogeny in U. gibba

In order to use PIN1 localisation as a tissue cell polarity marker, I first looked for candidate PIN proteins in *U. gibba.* I performed blast searches within the published *U. gibba* genome (Ibarra-Laclette *et al.*, 2013) and the genome of the *U. gibba* Bergh Apton (BA) line

sequenced by our lab. I then performed a protein sequence alignment (ClustalW), and compared all *U. gibba* PIN homologous with known PIN sequences from *Arabidopsis thaliana* and *Antirrhinum majus,* as well as candidate PIN sequences from asterid angiosperms; *Solanum lycopersicum* and *Mimulus guttatus*. I then identified the intracellular domain sequence (between amino acids 'EYRGA' to 'PNTYSS') based on published sequence information (Křeček *et al.*, 2009) and removed it so that I was left with the conserved sequence for each protein. I aligned these sequences and generated a guide phylogenetic tree to identify *U. gibba* PIN1 homologues (Figure 3.19). I found three homologous of PIN1 in *U. gibba* which I termed UgPIN1a, UgPIN1b, and UgPIN1c. In each case, the protein homolog was found in both the published (Ug_lcl) genome and the genome sequenced by our lab (Ug_TG). I confirmed the sequence of each *U. gibba* PIN1 homolog by PCR before proceeding.
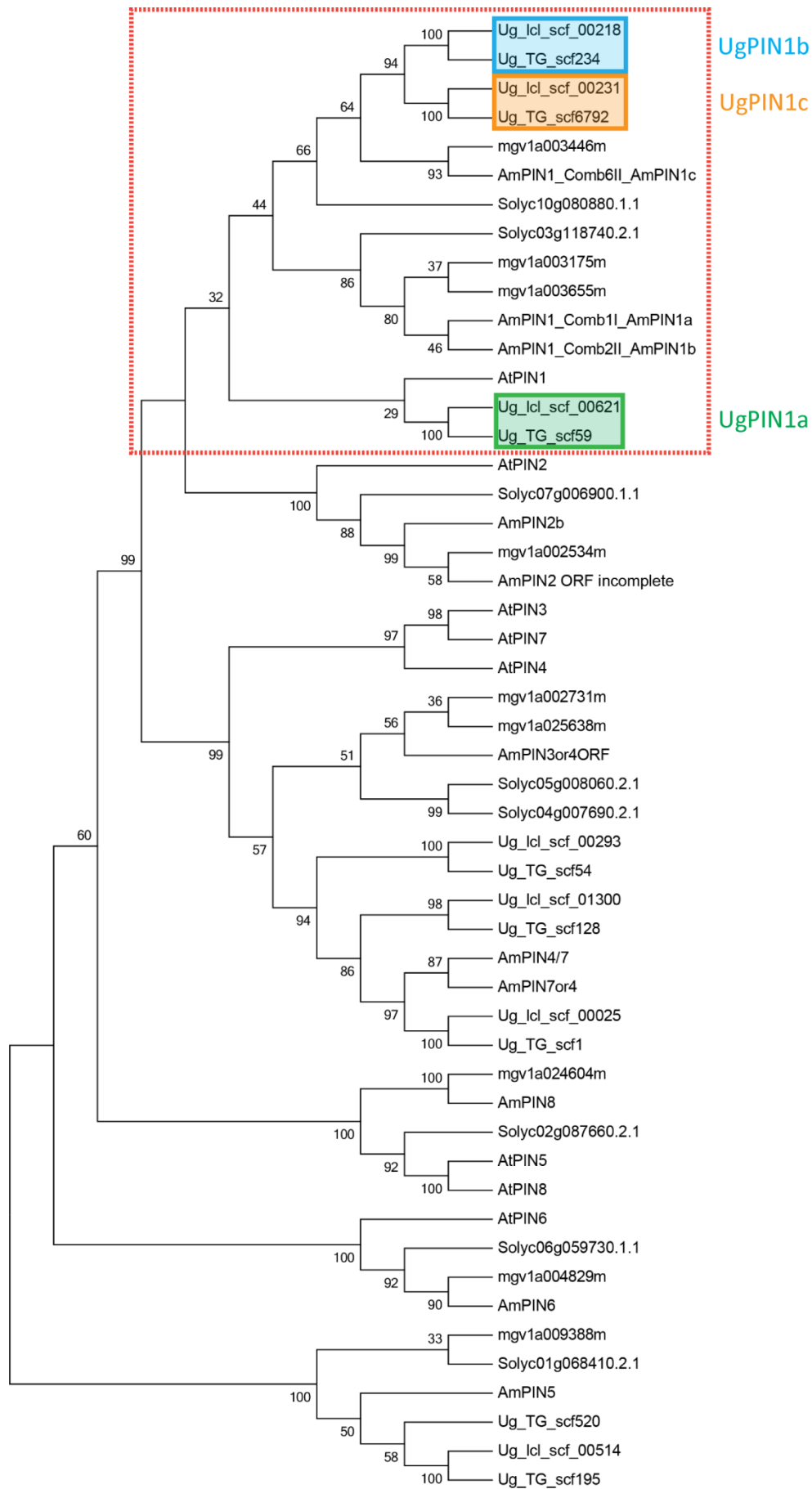
Figure 3.19: Guide phylogenetic tree of PIN proteins. Tree was constructed using Mega5. Conserved regions of protein sequence were aligned and a Neighbour-Joining tree was constructed using 500 bootstrap replicas, Jones-Taylor-Thornton (JTT) model, and pairwise deletion. Abbreviations are as follows: Ug, *Utricularia gibba*; Am, *Antirrhinum majus*; At; *Arabidopsis thaliana*; Solyc, *Solanum lycopersicum*; mgv, *Mimulus guttatus*. Red dotted box indicates the PIN1 family.

A further PIN clade, termed Sister-of-PIN1 (SoPIN1) has been identified and is present in all angiosperms except for Brassicaceae. In *Brachypodium* SoPIN1 has been found to be highly expressed in the epidermis and polarised towards regions of high auxin concentration while the other PIN1 homologues are implicated in vascular patterning and were more highly expressed in internal tissues (O'Connor *et al.*, 2014). To see if any of the UgPIN1 homologues were more closely related to SoPIN1, I collaborated with Devin O'Connor to extend my initial phylogenetic analysis to other species. This analysis suggests that UgPIN1a is in the PIN1 clade, while both UgPIN1b and UgPIN1c are in the SoPIN1 clade (Figure 3.20). This possible duplication in *SoPIN1* genes is not uncommon: *Solanum lycopersicum* also has *SoPIN1* duplication (Martinez *et al.*, 2016). Based on SoPIN1 localisation observed in *Brachypodium,* UgPIN1c and UgPIN1b may be localised to the epidermis and therefore be more useful markers of tissue polarity that UgPIN1a which may be more vascular.
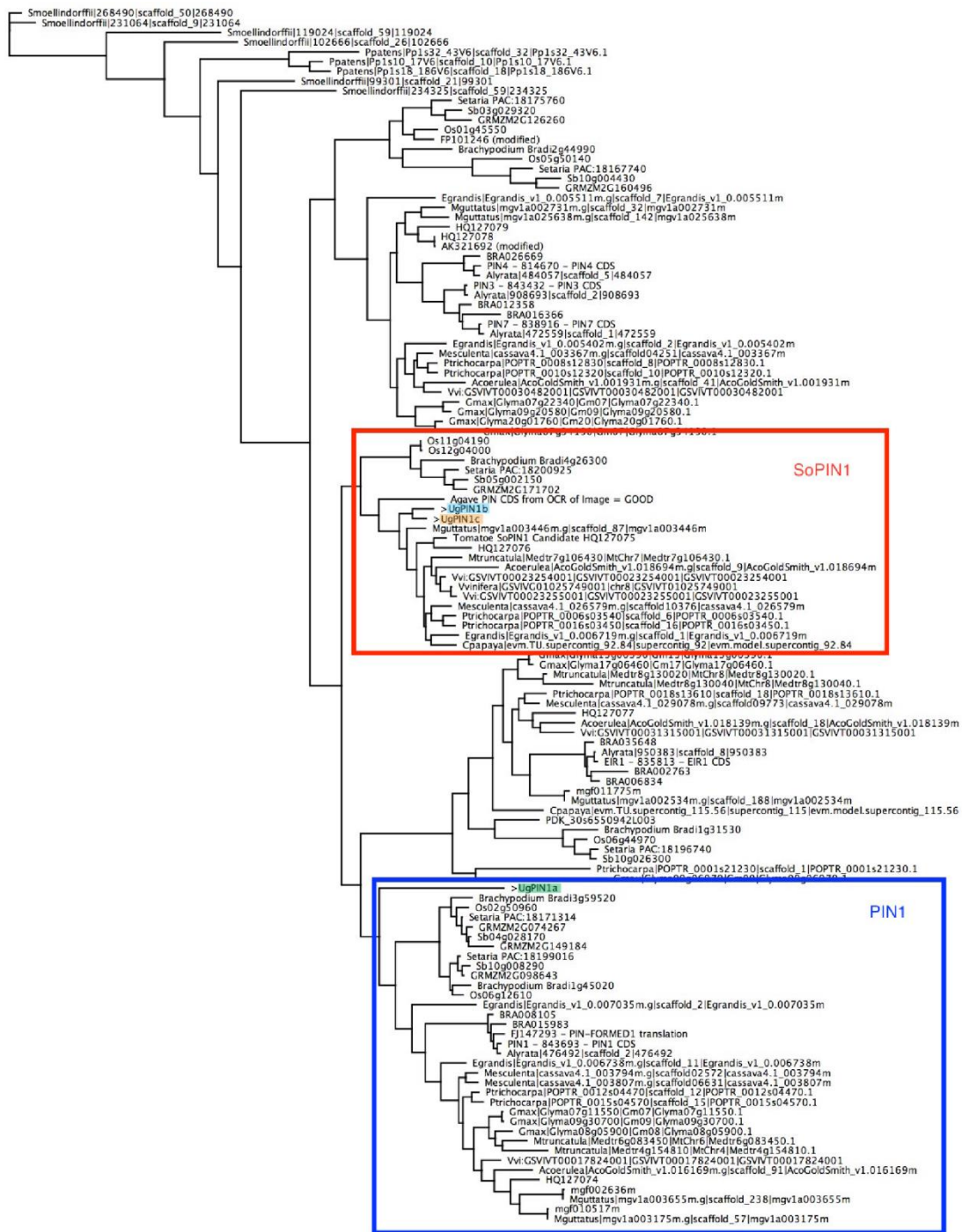
Figure 3.20: Analysing the relationship of the three UgPIN1 proteins to the PIN1 clade and the Sister-of-PIN1 (SoPIN1) clade. Guide phylogenetic tree generated by Devin O'Connor showing the placement of UgPIN1a (green), UgPIN1b (blue), and UgPIN1c (orange) in either the PIN1 or the SoPIN clade.

3.2.2.2.2 U. gibba PIN antibody production

Antibodies against UgPIN1a, b, and c were raised against potentially antigenic peptide sequences derived from the sequence of each UgPIN1 protein. Peptide sequences were selected based on their surface probability and antigenicity. A number of potential peptides were found that combined the right requirements: epitope accessibility in the native protein, high antigenicity, and a good hydrophilic/ hydrophobic residue ratio. I chose peptide sequences found in the intracytosolic loop domain of PIN1 (Wang *et al.*, 2014). This is important since hydrophilic regions located outside of the membrane, are exposed in aqueous solution, and are therefore more accessible to the antibody. I also chose regions of the protein which aligned with other successful PIN1 antibodies from *Arabidopsis* and *Antirrhinum* (Figure 3.21). Antibodies were produced by Cambridge Research Biochemicals (CRB).

```
              ....|....| ....|....| ....|....| ....|....| ....|....| ....|....| ....|....| ....|....| ....|....| ....|....|
                  305        315        325        335        345        355        365        375        385        395
AtPIN1        PTPRGSSFNH TDFYSMMASG -----GGRNS NFGPGEAVFG ---SKGPTPR PSNYEEDGGP AKPTAAGTAA GAGRFHYQSG GSG--GGGGA HYPAPN-PGM
UgPIN1a       PTPRGSSARS TSPIRKLDAG ---------- ---------- -----GPEAD PVFLGSSTGS S--------- VSGRVF---- ---------- --------V
UgPIN1b       PTPRGSSFNH ADFYTMVNGK ---------- ---------- --NAISHSPR QSSYANPGLD E--------E NQSRVNT--- ------NAGG GYAPPATTGI
UgPIN1c       PTPRGSSFNH TDFYSMVNGK ---------- ---------- --SALSASPR HSNFGNSGFD E--------E NQVRVT---- --------G GYGGSAAAGI
AmPIN1a       PTPRGSSFNH TDFYSMMQGG -----APRNS NVG-ANDVYG FSASRGPTPR PSNFEEETGN INNANN---N NKSRFYHGGS NNNNNSAANG NYPAPN-AGM
AmPIN1b       PTPRGSSFNH TDFYSMMQGG GGGGGGARNS NFG-ANDVFG LSTSRGPTPR SSNFEEESG- ---------- NKSRFYHGSS N------INA HYPAPNNTGM
AmPIN1c       PTPRGSNFSH TDFYSMVNG- ---------- ---------- ---GKNVSPR QSNF-DEEIG Y--------G NQSRAH---- ---------- -------GI

              ....|....| ....|....| ....|....| ....|....| ....|....| ....|....| ....|....| ....|....| ....|....| ....|....|
                  435        445        455        465        475        485        495        505        515        525
AtPIN1        DLHMFVWSSS ASPVSD---- VFGGGGGNHH ADYSTATNDH QKDVKISVP- ------QGNS NDNQYVEREE FSF----GNK DDDSKVLATD GGNNISNKTT
UgPIN1a       EIRFVSPIRT RSPEGE---- ---------- ---------- ---------- ------E MEVEMES EKS----PTD DLAE------ --------K
UgPIN1b       DLHMFVWSSS ASPVSERGIH VFRGGEYGNE LNLGPHPKEY DEFGRDDFSF GNKQG----- ----ADPLKL GSS----SKA ELR------- --TKSGNDDT
UgPIN1c       DLHMFVWSSS ASPVSEGGIH VFRGGEYGNE VTVGPHPKEY DDFGREEFSF GNKHGPN--- ---GPDASKL ASS----STA ELR------- --TKSGGD-A
AmPIN1a       DVHMFVWSSS ASPVSD---- VFGGGG--HH DQYG-ALDQH GKEVKAAVSP TKVEGQRDNH GEDYNLERDE FSF----GNK ENN------- EGE-------
AmPIN1b       DLHMFVWSSS ASPVSD---- VFGGGA--AQ HDYG-DLHR- --EVRVAVSP TKGDGHRGNN -EDGYLERDE LSFGIRDGNR ENN------- NNEEAKVGEN
AmPIN1c       DVHMFVWSSS ASPVSEGGIH VFR------- ------ADY DDFGRDEFSF GNKQGGSNGT EREGPVLSKL GSS----STA ELN------- --PKTAID-T
```

Figure 3.21: Peptide sequences for antibodies against PIN1 in *Utricularia gibba, Arabidopsis thaliana,* and *Antirrhinum majus*. Protein sequence alignment for PIN1 proteins focussing on the intracytosolic loop sequence marked for the various peptide sequences. (Red) peptide sequence successfully used in the generation of an antibody against AtPIN1 (Barbier De Reuille *et al.*, 2006). (Blue) Peptide sequence used to raise antibodies against UgPIN1b. (Orange) Peptide sequence used to raise antibodies against UgPIN1c. (Pink) Peptide sequence used to raise successful antibodies for the immunolocalisation of AmPIN1 (Xana Rebocho). (Purple) Peptide sequence used to raise the commercial Arabidopsis AP-20 antibody. (Green) Peptide sequence used to raise antibodies against UgPIN1a. Guide protein alignment was generated in BioEdit by performing a ClustalW multiple alignment.

3.2.2.2.3 Setting up immunolocalisations in U. gibba

Several factors are important for successful immunolocalisation of proteins. These include fixation of the tissue, tissue integrity, tissue permeabilization, antibody specificity, antibody hybridisation efficiency, and signal/ background ratio. From work in our lab with *Antirrhinum*, we found that permeabilization of the tissue can be one of the most limiting steps. I decided to start by addressing this in *U. gibba.*

Permeabilization treatments

To set up an immunolocalisation protocol for *Utricularia gibba*, I first tested different permeabilization treatments using a HISTONE 3 (H3) commercial antibody. I used an Alexa 647 secondary antibody as I found that excitation around 633 nm produced the least auto fluorescence in fixed *U. gibba* tissue. I first tested tissue fixed in FAA (Formalin Acetic Alcohol) plus triton which is a popular fixative for immunolocalisations. For tissue permeabilization, I treated sectioned tissue with either Proteinase K or boiled slides in an antigen retrieval solution (Figure 3.22). The full protocol can be found in the materials and methods of this thesis.

I found that the Alexa 647 secondary antibody gave a clear signal that was above any background fluorescence, producing clear rings of H3 signal. Both Proteinase K treatment and boiling in antigen retrieval solution were successful. However, I found results from boiling more consistent, which is also the case for *Antirrhinum* tissue (Xana Rebocho, personal communication). No signal was observed in controls where either no primary or no secondary antibody was used. These results indicate that fixation in FAA is suitable for *U. gibba* and that the tissue is permeable and is capable of hybridisation for nuclear proteins.
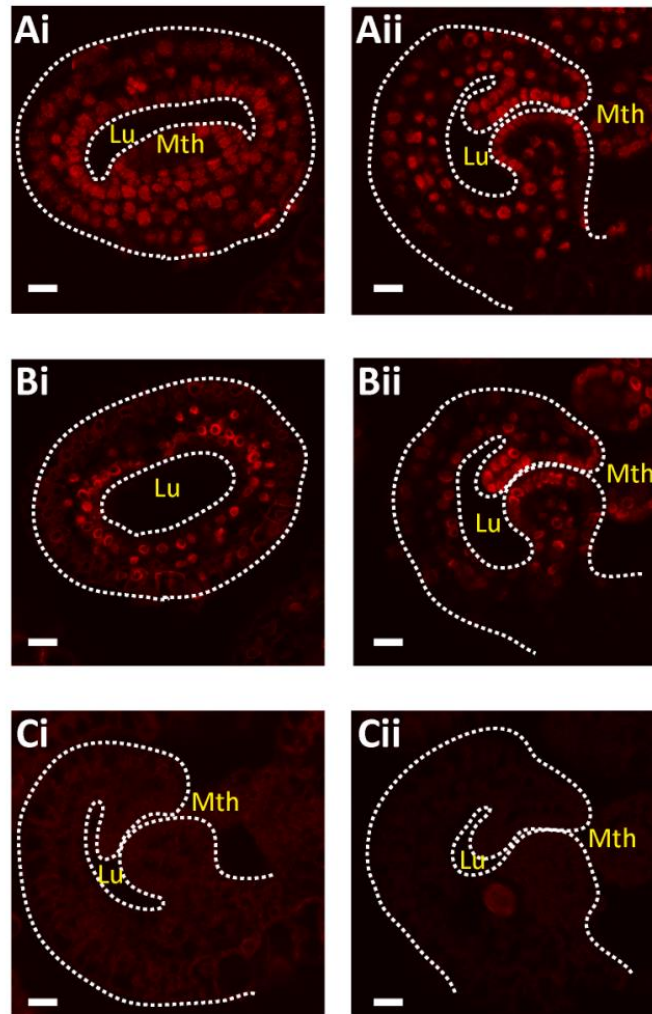
Figure 3.22: Optimising the immunolocalisation protocol in *U. gibba* using a H3 antibody. (A) Bladder sections from the front (Ai) and side (Aii) treated with Proteinase K. Signal is H3. (B) Bladder sections from the front (Bi) and side (Bii) boiled in an antigen retrieval solution. (C) Negative controls where (Ci) no primary antibody was used, and (Cii) no secondary antibody was used. The mouth (Mth) and lumen (Lu) of the bladder are marked. Secondary antibody is Alexa 647. Scale bars are 10 µm.

Tissue fixation

The next limiting step to consider is the fixation of the tissue. I found that FAA plus triton was a good fixative for the localisation of the nuclear protein H3 but it is not clear whether this will be suitable for the cross linking of membrane proteins such as PIN1 in *U. gibba*. I therefore tested the UgPIN1 antibodies on *U. gibba* tissue fixed in either, FAA with triton and DMSO, a pre fixation in methanol acetic acid followed by FAA with triton and DMSO,

zinc formalin fixative, or paraformaldehyde (Figure 3.23). I used a 1:200 dilution of each antibody (combining the 2 antibodies from the different rabbits for each UgPIN1).
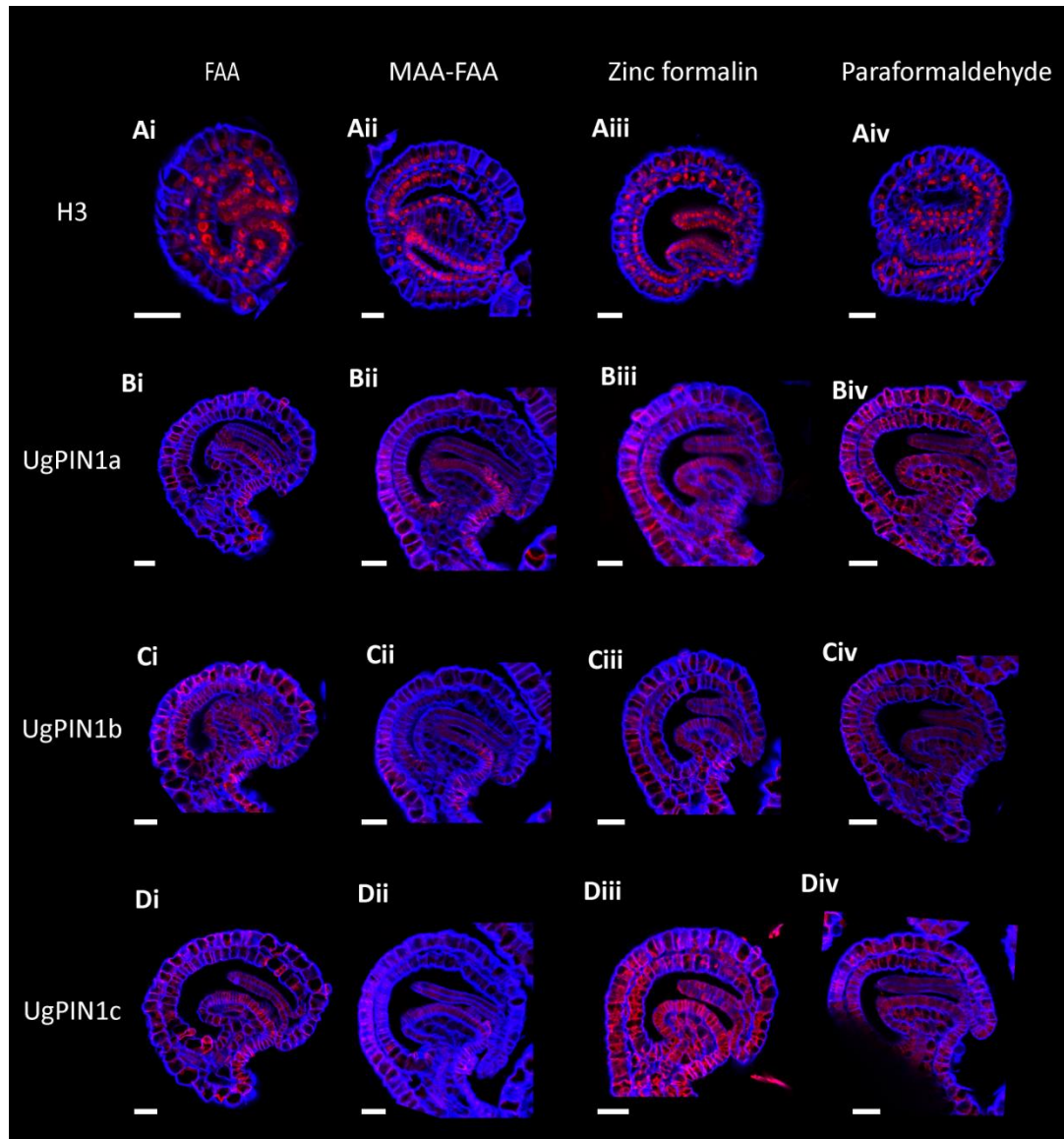
Figure 3.23: Testing different fixatives with *U. gibba* bladder tissue for the immunolocalisation of UgPIN1. *U. gibba* bladder tissue fixed in FAA, MAA into FAA, zinc formalin, or paraformaldehyde (i-iv respectively). Immunolocalisation performed with antibodies against (A) H3, (B) UgPIN1a, (C) UgPIN1b, or (D) UgPIN1c. Signal is shown in red. Blue is calcofluor staining of the cell wall. Scale bars are 20 μm.

H3 signal is good in each case, indicating that all the fixatives explored are suitable for immunolocalisation of nuclear proteins. However, UgPIN1 signal is more variable. Tissue fixed with FAA plus triton and DMSO or with a pre fixation in methanol acetic acid gave the

Chapter 3

clearest UgPIN1 signal (Figure 3.23). Tissue fixed in paraformaldehyde or zinc formalin had messy signal for each of the three UgPIN1s and I had to use a higher laser power to observe anything here (Figure 3.23). Overall, I found that alcohol based fixatives worked best for immunolocalisation of UgPIN1.

In all cases there is some non-specific signal, especially in the L1 layer of the bladder where it is not clear if the signal is real. To check if the antibodies are recognising the PIN1 protein and are not just binding to other cell membrane proteins, I performed an immunolocalisation of each of the UgPIN1 antibodies against *Antirrhinum majus* floral tissue (since we know that this tissue is very successful in AmPIN1 immunolocalisation by Xana Rebocho) (Figure 3.24). I found that each of the UgPIN1 antibodies gave a similar pattern in *Antirrhinum* tissue to the AmPIN1 antibody (Figure 3.24). This suggests that the antibodies are binding to PIN1 protein and are therefore promising. This indicates that the background seen in the *U. gibba* tissue may be due to other factors which I was unable to identify.
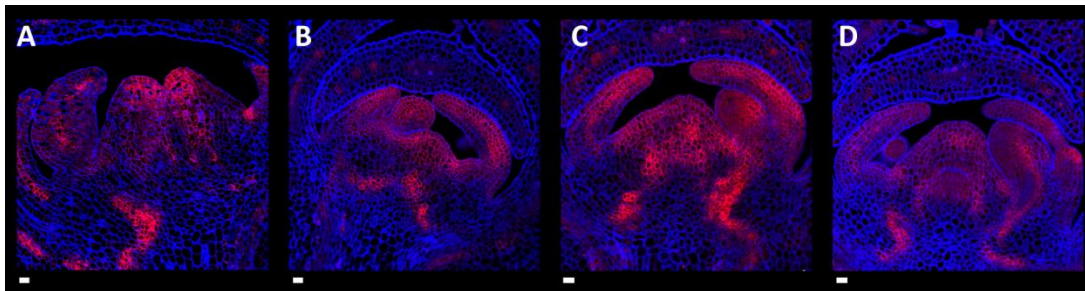
Figure 3.24: Immunolocalisation of UgPIN1a, b, c on *Antirrhinum majus* floral tissue. (A) AmPIN1a, (B) UgPIN1a, (C) UgPIN1b, (D) UgPIN1c. PIN1 signal is shown in red. Blue is calcofluor staining of the cell wall. Scale bars are 20 µm.

To see if I could get a better signal to background ratio I performed titrations of the antibodies for each UgPIN1 in tissue fixed in FAA plus triton and tissue fixed with a pre fixation in methanol acetic acid and transferred to FAA plus triton (Figure 3.25 and Figure 3.26).
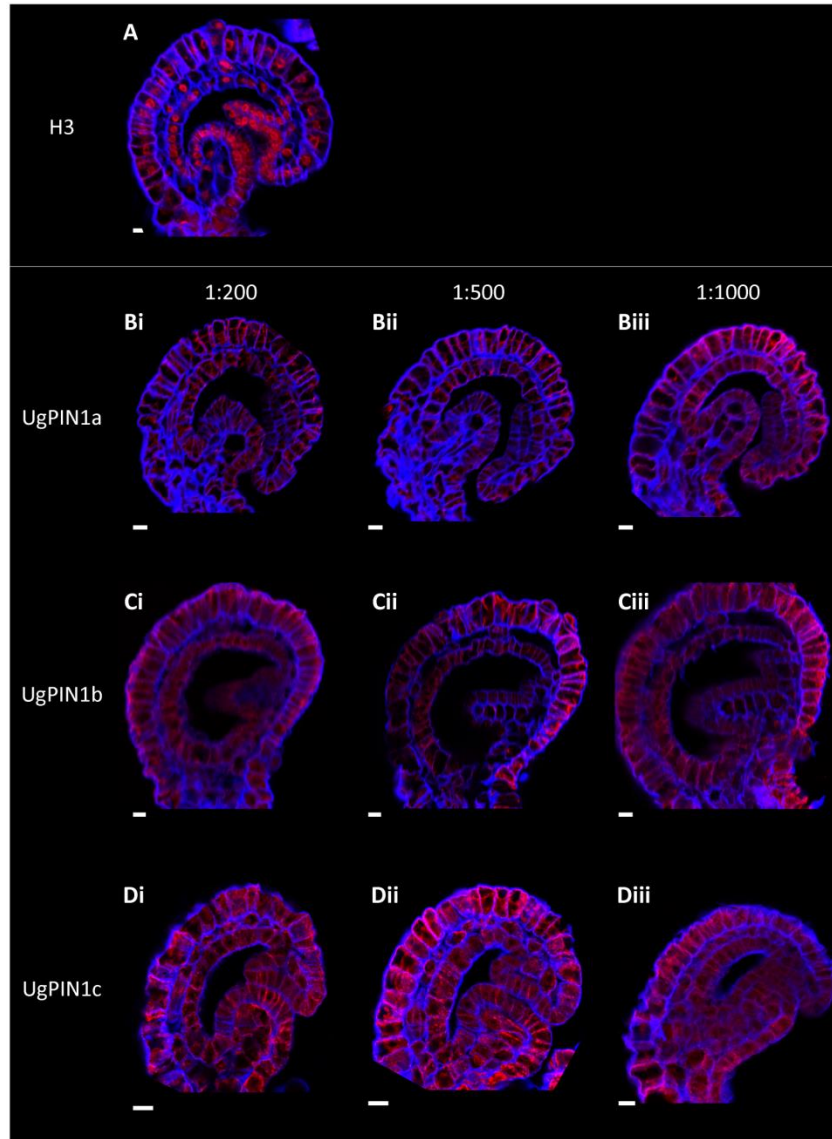
Figure 3.25: Titrations for UgPIN1 antibodies in *U. gibba* bladder tissue fixed in FAA plus triton plus DMSO. All tissue was fixed in FAA + triton. (A) Immunolocalisation of H3. (Bi-Biii) Immunolocalisation of UgPIN1a, titrations of 1:200, 1:500, 1:1000. (Ci-Ciii) Immunolocalisation of UgPIN1b, titrations of 1:200, 1:500, 1:1000. (Di-Diii) Immunolocalisation of UgPIN1c, titrations of 1:200, 1:500, 1:1000. H3 and UgPIN1a, b, c signal shown in red. Blue is calcofluor staining of the cell wall. Scale bars are 10 μm
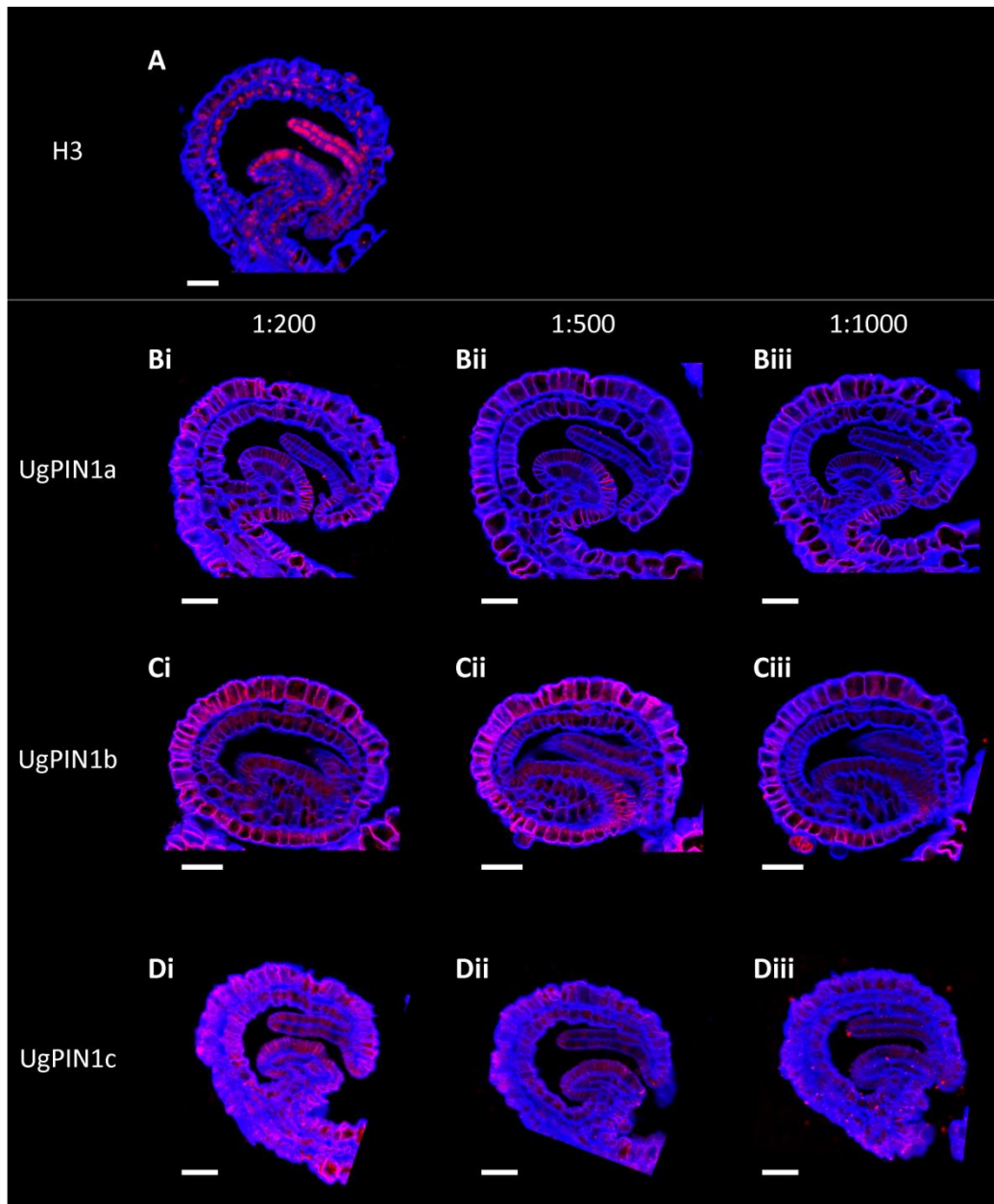
Figure 3.26: Titrations for UgPIN1 antibodies on tissue fixed in methanol acetic acid and transferred to FAA plus triton and DMSO. All tissue was pre fixed in MAA and then transferred to FAA + triton. (A) Immunolocalisation of H3. (Bi-Biii) Immunolocalisation of UgPIN1a, titrations of 1:200, 1:500, 1:1000. (Ci-Ciii) Immunolocalisation of UgPIN1b, titrations of 1:200, 1:500, 1:1000. (Di-Diii) Immunolocalisation of UgPIN1c, titrations of 1:200, 1:500, 1:1000. H3 and UgPIN1a, b, c signal shown in red. Blue is calcofluor staining of the cell wall. Scale bars are 10 μm.

The positive control worked well in each case with strong H3 signal. There is also PIN1 signal visible in tissue fixed with either FAA or with a pre fixation in MAA. Overall, the tissue appears to have been preserved better with a pre fixation in MAA, indicating that this method of fixation may be better for preserving bladder structure. The results are not consistent across UgPIN1a, b and c between experiments; sometimes UgPIN1c appears to give the most promising signal, other times UgPIN1a and b give the most promising signal. This suggests that the success or failure of the immunolocalisation may be due to tissue variability rather than the antibody. There are also some regions of tissue in which I see more PIN1 signal, such as the cells in the mouth region of the bladder. Cells in the L1 layer of the bladder also tend to have PIN1 signal, although it is not clear whether this is specific signal. A concentration of 1:500 looked best for UgPIN1a and UgPIN1b, while a concentration of 1:200 looked most promising for UgPIN1c. However, there is still background present.

To see if I could reduce the background fluorescence I tried testing the antibodies produced in different rabbits separately, as one may be giving cleaner signal that the other in each case.
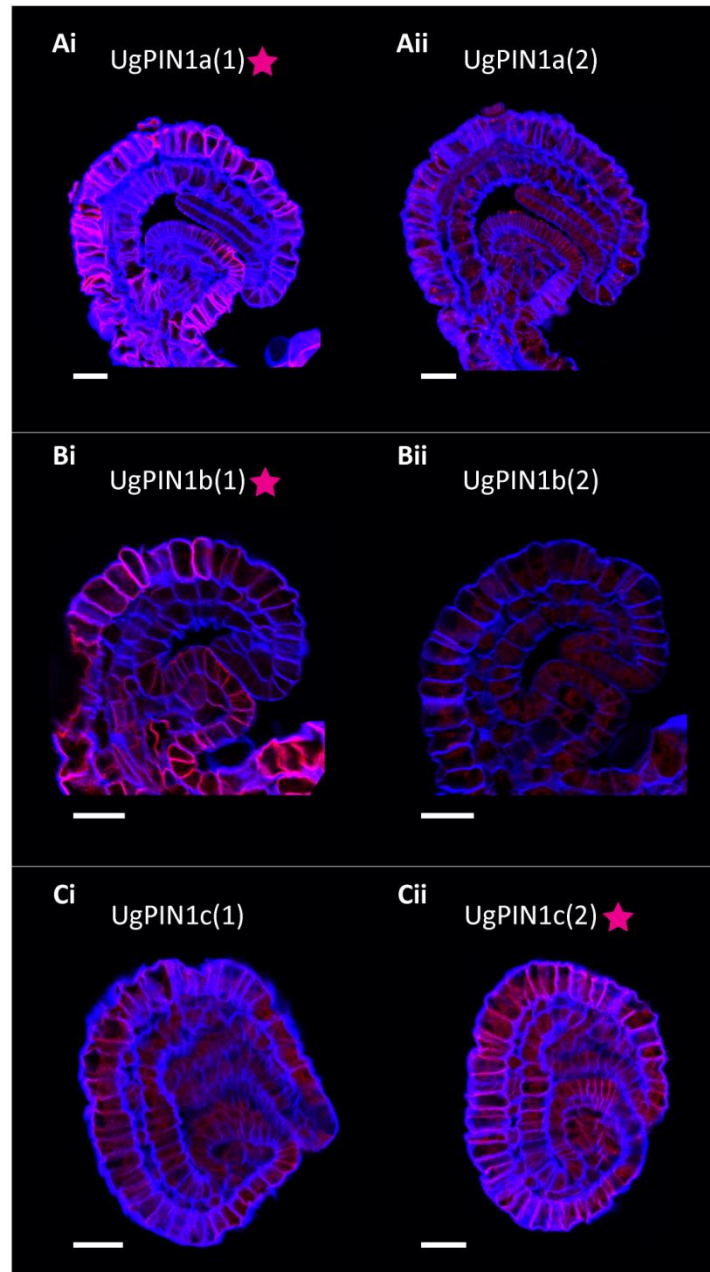
Figure 3.27: Comparing antibodies for each UgPIN1 raised in different rabbits. (Ai-Aii) Immunolocalisation of UgPIN1a using antibodies raised in two different rabbits (1 and 2). (Bi-Bii) Immunolocalisation of UgPIN1b using antibodies raised in two different rabbits (1 and 2). (i-Cii) Immunolocalisation of UgPIN1c using antibodies raised in two different rabbits (1 and 2). Pink stars indicate which antibody gave the best signal between those raised in different rabbits. UgPIN1 signal is shown in red. Blue is calcofluor staining of the cell wall. Scale bars are 20 μm.

For each UgPIN1 (a, b, c) one antibody gave better results across multiple bladder sections (Figure 3.27, pink stars). The pattern observed was very similar to that when the antibodies from two rabbits were combined, but the background was reduced slightly. I also tried goat serum in place of BSA as a blocking agent before adding the secondary (as the secondary antibody was raised in goat) but this made no difference to the signal/background ratio. To improve tissue structure further I tried fixing tissue with no vacuum treatment. The immunos were still successful but the tissue structure was not further improved. I next tested the best antibody against each UgPIN1 against a negative control (the pre immune bleed before the antigenic peptide is injected in the rabbit) (Figure 3.28). I found no signal in the control tissue treated with the pre-immune in place of the primary PIN1 antibody. This indicates that the signal observed is real in each case. Again, the signal was very variable in quality across samples.
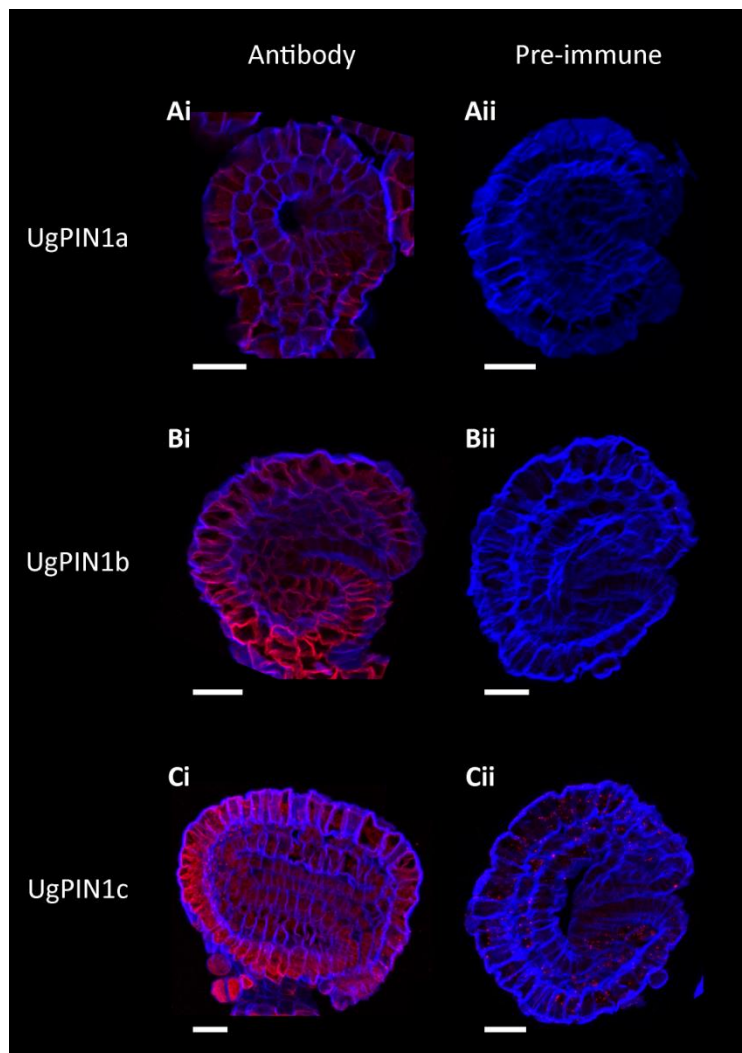
Figure 3.28: UgPIN1 antibodies and pre-immune negative control. Immunolocalisations with the following: (Ai) UgPIN1a primary antibody; (Aii) UgPIN1a pre-immune negative control; (Bi) UgPIN1b primary antibody; (Bii) UgPIN1b pre-immune negative control; (Ci) UgPIN1c primary antibody; (Cii) UgPIN1c pre-immune negative control. UgPIN1 signal is shown in red. Blue is calcofluor staining of the cell wall. Microscope and laser settings used were the same for each antibody and its corresponding pre-immune control. The pre-immune samples were also checked with higher laser power and no signal was seen (not shown). Scale bars are 20 μm.

3.2.2.2.4 Summary of immunolocalisation progress in U. gibba

I found that immunolocalisation of nuclear proteins such as histone H3 worked well in *U. gibba* tissue. However, I found it more difficult to obtain good, clear signal using the UgPIN1 antibodies. Each of the three UgPIN1 antibodies gave some signal but the quality of signal was variable across samples (although any general patterns appeared to be consistent). This difficulty could be due to tissue preservation issues. Since UgPIN1 is a membrane protein, it is possible that tissue fixation was not homogenous across the bladder tissue. The L1 layer of the bladder often appeared collapsed and in some cases the cell membrane appeared to be detached from the cell wall. I tested a number of fixatives and found that alcohol-based fixatives were most successful for UgPIN1 immunolocalisation, despite the fact that ethanol-based fixatives can lead to plasmolysis of cells. A pre fixation in methanol acetic acid followed by fixation in FAA + triton + DMSO worked best, although with room for improvement.

Evidence suggests that the signal observed is real and that the UgPIN1 antibodies are specific to the PIN1 protein: the pattern observed in *Antirrhinum* tissue is as expected for PIN1 with each of the UgPIN1 antibodies. The pre-immune controls gave no signal, suggesting that the signal from the UgPIN1 antibodies is real. Some areas of tissue seem to give clearer signal than others. I consistently see patterns of PIN1 in the chin and threshold cells (just below the mouth). The L1 layer is often bright but appears much less specific. Older tissue also appears bright and not as specific.

In conclusion, there is more work to be done, perhaps testing different methods of fixation such as cryofixation where samples are frozen and therefore fixation does not rely on the fixative entering the membrane of the cells. Since I have promising and consistent signal in the chin and threshold cells I decided to analyse some of the clearest images to see what patterns of PIN1 I could observe.

3.2.2.2.5 UgPIN1 patterns in developing bladders

I took some of the clearest images generated from all of the above UgPIN1 immunolocalisation experiments to look at PIN1 patterns, and tried to infer the cellular PIN1 polarity or axiality in developing *U. gibba* bladders. The most consistent region where I saw clear signal was at the chin and threshold cells (just below the mouth) of the bladder. The models predicted that a polarity field in this region would point from stalk to mouth with an axiality parallel to the midvein. To look at this, I used calcofluor staining of the cell wall to assign polarity to the PIN1 patterns (with the arrow head pointing towards the cell membrane where PIN1 is localised). Where this was not clear, I assigned axiality based on the localisation of PIN1.

I first looked at side sections of bladders (most of them in the 123 μm stage which is one stage after the model begins) (Figure 3.29).
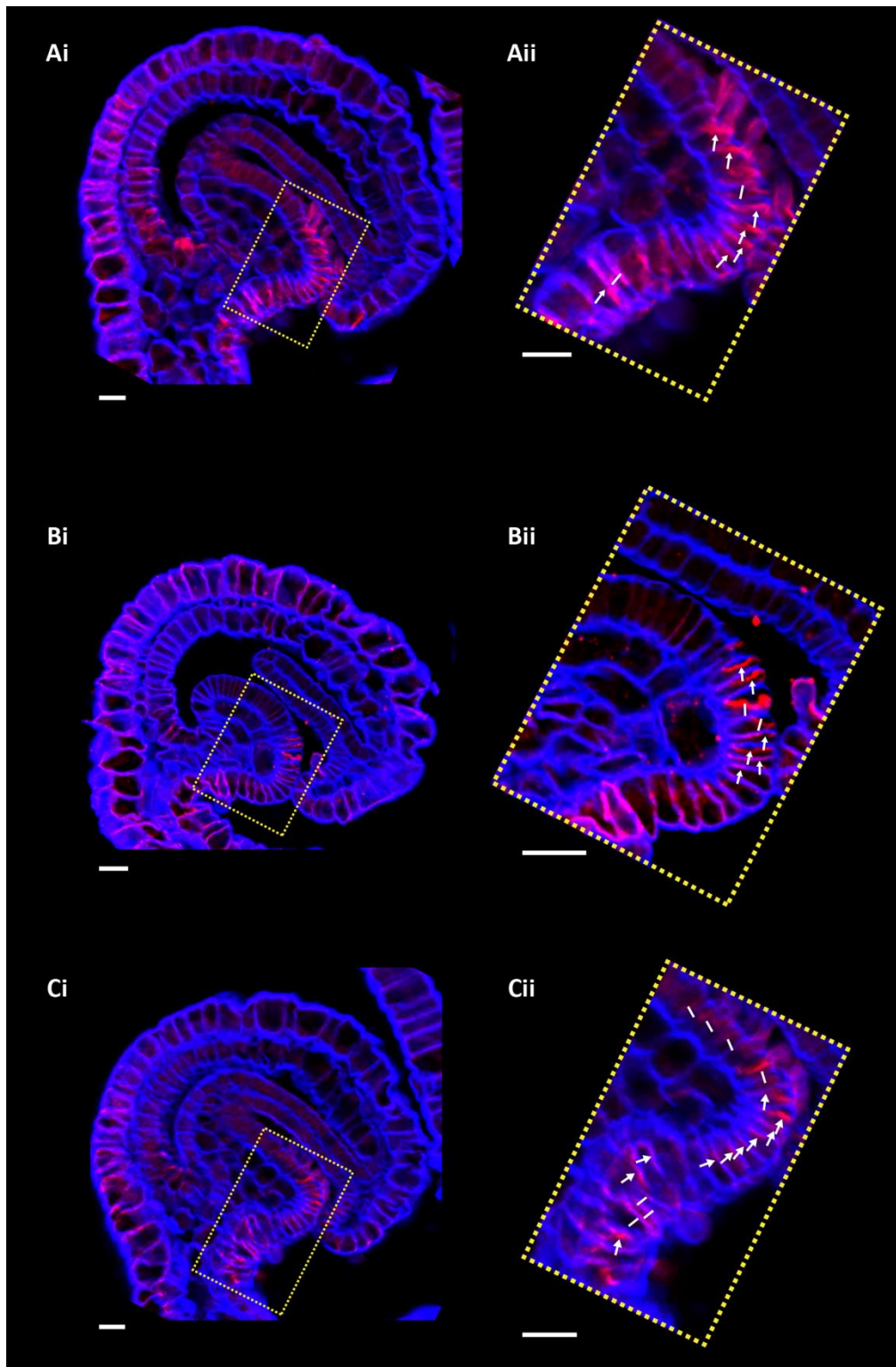
Figure 3.29: UgPIN1 patterns at the bladder chin and threshold in side section. Side sections of *U. gibba* bladder (approx. 123 μm stage). (Ai-Aii) UgPIN1a immunolocalisation. (Bi-Bii) UgPIN1a immunolocalisation. (Ci-Cii) UgPIN1b immunolocalisation. White lines indicate the inferred axiality of the UgPIN1 signal. White arrows show the inferred polarity. Scale bars are 10 μm.

PIN1 polarity in the chin and threshold regions points away from stalk and towards the mouth opening (Figure 3.29). Where polarity could not be assigned in these regions, axiality was parallel with the midvein. To confirm this data, I looked for more evidence of PIN1 localisation in the threshold region (Figure 3.30, purple) in front section (Figure 3.30).
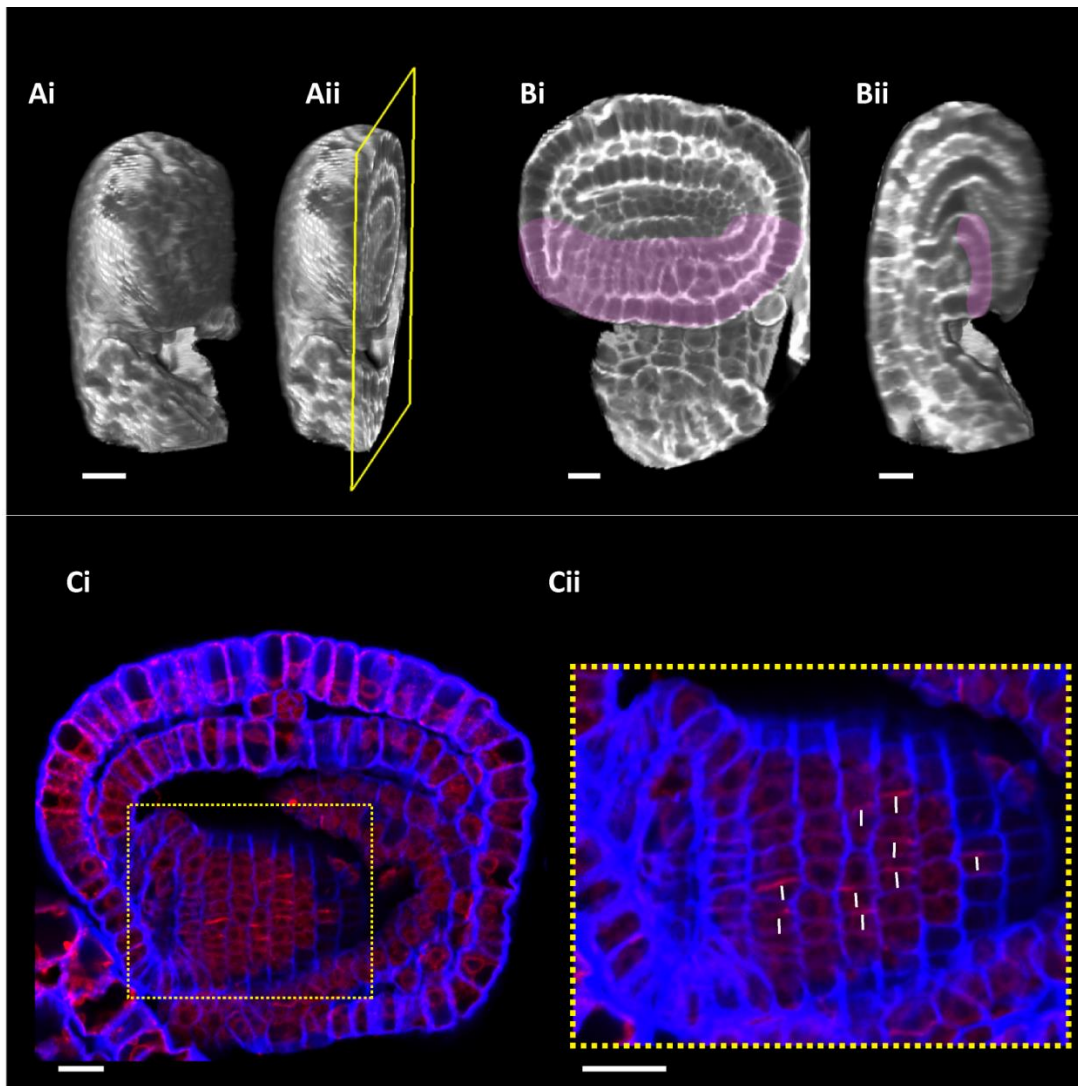
Figure 3.30: UgPIN1 patterns at the bladder threshold in front section. (A-B) *U. gibba* bladder fixed and stained with propidium iodide. Views indicate where the section in (C) was made. (Ai) *U. gibba* bladder viewed from the side (oblique). (Aii) *U. gibba* bladder cropped from the front, viewed from the side. (Bi) Front section generated in (Aii) viewed from the front. Bladder threshold is marked in pink. (Bii) Bladder side section with threshold cells marked in pink. (Ci) *U. gibba* bladder sections from the front (approx. 123 µm stage) with UgPIN1c signal shown (red) and calcofluor staining of the cell wall (blue). (Cii) Close up of the threshold cells from (Ci). White lines indicate the inferred axiality of the UgPIN1c distribution. Scale bars are 10 µm.

I also found some PIN1 signal in the threshold region viewed in front section. I was unable to assign any polarity to my images in this view since the calcofluor staining of the cell wall was not bright enough in the tiny cells of the threshold. However, the inferred axiality in this region is consistent with that found in side section. The axiality is parallel with the midvein and runs between stalk and mouth.

3.2.2.2.6 Summary of PIN1 exploration in U. gibba

There are three PIN1 proteins in *U gibba*, UgPIN1a, UgPIN1b, and UgPIN1c. I designed antigens from within the intracytosolic loop of each UgPIN1 from which antibodies were raised in rabbit. I found that each UgPIN1 antibody produced signal in *U. gibba* tissue, although this was sometimes messy and the quality of signal varied between samples. More work will need to be done to further optimise conditions for tissue fixation to better suit *U. gibba* bladder tissue.

The signal that I observed in the chin and threshold of the bladder was consistent throughout samples with good signal and the inferred axiality and polarity at these regions runs from stalk to mouth, parallel with the midvein. These results agree with models where axiality in the chin region is required to generate the elongation at the chin without causing a bulge in the tissue. More experiments would need to be performed to study PIN1 polarity in other regions of the bladder, and to confirm the patterns at the chin and threshold.

3.3 Discussion

3.3.1 Evidence for axiality in mature and developing bladders

The models predict that anisotropic growth and therefore axial information are required for the elongation of the chin region of the bladder. In the models, this axiality was provided by a polarity field propagating from stalk to mouth. I found that the quadrifid glands on the inner surface of bladders have a patterned orientation across the bladder which is parallel to the midvein on the sides and top of the bladder, and appears to radiate around the bladder stalk intersect These quadrifid glands also have a coordinated polarity between the stalk and mouth of the bladder. Since the quadrifid glands are only visible at later stages of development (from just before the 622 μm stage) this pattern of inferred

axiality and polarity gives possible evidence of a readout of an underlying polarity based system much like that seen with hairs in *Drosophila* (Adler, 2002) and root hairs in *Arabidopsis* (Grebe, 2004). Although the overall pattern agrees with that predicted by the model, I was not able to obtain good enough resolution to study the quadrifid glands lining the chin region. This region is of particular interest, since the models predict that axiality in this region is essential.

Axiality was also predicted to be set up early in bladder development. Preliminary results on the localisation of UgPIN1 proteins as an earlier readout of axial information suggest that polarity at the chin and threshold region of young *U. gibba* bladders is oriented away from the stalk region and towards the mouth. This is consistent with models where specified anisotropic growth at CHIN drives the elongation of the CHIN region and prevents it bulging during growth. More bladder stages need to be studied to confirm these results.

3.3.2 Anisotropic growth in bladder development

3.3.2.1 Anisotropy at the chin region

In concurrence with model predictions, analysis of growth at the chin region compared to the main body of the bladder indicates that growth in the chin is more anisotropic. If we assume that cells were approximately isometric at the time of heat shock then the rate of increase in anisotropy per hour of sectors in the chin region is 3 times higher than that in the main body of the bladder (1.5 % per hour compared to 0.5 % per hour respectively). This is more similar to the difference predicted in the specified anisotropic growth model (model 6) where the rate of increase in anisotropy per hour was also 3 times higher in the CHIN region compared to the main body of the canvas. In contrast, the isotropic specified growth model (model 3) predicted the rate of increase in anisotropy in the chin region to be 8 times greater than the main body of the bladder.

The rate of increase in anisotropy per hour calculated based on sector length at the chin is almost twice as much as that calculated based on cell count along the major and minor axes, indicating that cell shape in this region contributes to anisotropy. Sectors in the chin region also appear to be made up of files of cells with more cells in one orientation than

the other. This suggests that anisotropy in the chin region is at both the cell shape level and at the cell division level, although more data is required to draw stronger conclusions. The orientation of sectors at the chin region is parallel with the midvein and the pattern of UgPIN1 polarity observed in younger bladders. This concurs with models where specified growth in the CHIN region is anisotropic and growth rates are highest parallel to a polarity field propagating from stalk to mouth.

3.3.2.2 Anisotropy across the main body of the bladder

There is evidence for weak anisotropy across the main body of the bladder which appears to be oriented parallel with both the midvein, and the implied polarity given by quadrifid gland analysis. The fact that sectors near the midvein are oriented parallel with the midvein rather than perpendicular to the midvein lends support to model 6 where specified growth in the main body of the bladder is anisotropic. Specified isotropic growth is also unlikely to drive growth in the main body of the bladder, since there was no correlation between sector area and distance from the midvein. This does not support model 3 where specified growth in the main body of the bladder is isotropic, since clones near the midvein are predicted to be larger than those at the sides of the bladder in this case. Specified anisotropy across the bladder is therefore a more likely explanation for the growth patterns observed. Tracking experiments would also provide data on growth rates in specific regions of tissue, allowing this to be explored in more detail.

3.3.3 Axiality and growth orientations beyond the model

Analysis of quadrifid gland polarity indicates a divergence of polarity towards the antennae at the top front of the bladder. This was not predicted by the models and suggests that there may be two minus organisers (one at each antenna). This may be important for the formation of auxin maxima prior to the initiation of antenna outgrowths at the front of the bladder. It would therefore be interesting to study UgPIN1 localisation at the time of antennae initiation to see if there are observable convergence points.

3.3.4 Conclusions and future work

This work aimed to test hypotheses made by specified isotropic and anisotropic growth models described in the previous chapter to see if axiality was important for the generation of bladder shape and to what extent specified anisotropic growth may play in bladder development. The models provided clear predictions on axiality, growth rate, and growth orientation. The data presented in this chapter supports models where specified growth at the chin region is anisotropic. Since this relies on the presence of tissue axiality it will be important to confirm the preliminary data provided by analysis of UgPIN1 localisation. I found that UgPIN1 immunolocalisation was not always successful and that the structural preservation of young bladders was problematic. Other fixation methods such as cryofixation may therefore be useful in future work. Another option is to study transgenic transcriptional UgPIN1 reporter lines to see if PIN patterns are clearer. This may have other complications, since it would be necessary to view whole bladders rather than sections, and at young stages bladders are wrapped up in the tissue of the circinnate apex and are difficult to view live.

This work has provided some evidence that a polarity-based axiality system may be involved in bladder development. Axial patterns and inferred polarities concur with polarity patterns predicted by models where axiality is implemented through a polarity system. The models predict that polarity is set up using a plus organiser (which promotes production of POLARISER) found at the stalk of the bladder, and a minus organiser (which promotes degradation of POLARISER) found at the mouth region. Evidence of these regions would therefore further support a polarity based axiality model. Assuming polarity is set up by auxin, plus organisers could be auxin biosynthesis genes such as *YUCCA*s (Cheng *et al*., 2006). Minus organisers may be composed of auxin importers such as *AUX* and *LAX* genes which encode proteins that actively transport auxin from the extracellular space into the cytoplasm (Parry *et al*., 2001; Yang *et al*., 2006; Péret *et al*., 2012). Future work investigating the expression patterns of these genes would therefore provide useful information.

Since the levels of resultant anisotropy across the main body of the bladder are low, it is difficult to distinguish between a model where specified growth in the main body of the bladder is either isotropic or anisotropic. Sector analysis also has limitations concerned with not knowing the shape of cells at the time of heat shock. These issues could be dealt

with by tracking bladder growth live. One option is to use a tracking chamber which has been used by the lab in the past (Kuchen *et al.*, 2012). Again this may prove complicated due to the problems associated with imaging young bladders while they are developing inside the circinnate apex tissue. However, later stages may be traceable in this way.

To carry out my investigations I set up a number of techniques and tools for *U. gibba* including immunolocalisation and the generation of transgenic lines using Golden Gate cloning (the latter of which was done in collaboration with Minlong Cui, Annis Richardson, Samantha Fox, and Christopher Whitewoods). In order to explore the genetic basis of some of the ideas presented above, there are a number of other techniques and resources that will be useful, particularly concerning forward and reverse genetics. For example, *in situ* hybridisation would be useful to study the expression patterns of candidate genes. Mutagenesis experiments may also help to identify new candidate genes involved in bladder development.

4 Developing *Utricularia gibba* as a model system

4.1 Introduction

In the previous chapters, models for *Utricularia gibba* bladder development have been explored and hypotheses generated by these models tested. These models make several predictions about potential factors which may control growth. For example, plus and minus organisers of polarity, and a factor in the chin region of the bladder where anisotropic growth is specified. There are also a number of hypotheses about the genes involved in the generation of epiascidiate bladder shape from the primordium. To investigate the identity of such genes and to study their expression patterns spatially, a number of techniques need to be developed in *U. gibba*. These include the ability to use forward and reverse genetics to identify novel genes and explore candidates based on knowledge from other systems.

4.1.1 Genomic and transcriptomic resources

A reference genome is a key requirement when setting up a new model system. *U. gibba* has been reported to have a small genome which is predicted to be around 88 Mbp (Greilhuber *et al.*, 2006), even smaller than *Arabidopsis* at 157 Mbp (Bennett *et al.*, 2003). The chromosome number of *U. gibba* has also previously been reported (n=14) which is one of the lowest number of chromosomes known in *Utricularia* species (Rahman *et al.*, 2001). A transcriptome of *U. gibba* has been published (Ibarra-Laclette *et al.*, 2011) which is useful for predicting genes.

This work aims to sequence the whole genome of *U. gibba.* Our lab has five different *U. gibba* accessions avaliable. Since we do not know the history of these accessions, we do not know which one is most likely to be homozygous (and therefore which is best for the generation of a haploid reference genome). We could therefore sequence each line and choose the most homozygous by comparing the assemblies. Illumina next-generation sequencing (NGS) platforms generate sequencing data which consists of several millions of short sequences (reads) which are between 50-150 bp long. Sequencing is carried out by

SBS (sequencing by synthesis) whereby DNA bases are identified as they are incorporated into a nucleic acid chain by their unique fluorescent signal. This method is high throughput. During this work a genome of *U. gibba* was published with some annotation which provided us with a useful comparison (Ibarra-Laclette *et al.*, 2013).

4.1.2 Forward and reverse genetics

Forward genetics involves the identification of a given phenotype, followed by the study of the genetic basis of this phenotype. In contrast, a reverse genetic study begins with a candidate gene/ multiple candidate genes and the phenotypic effect of these genes is investigated.

4.1.2.1 Identifying candidate genes using mutagenesis

Forward genetic screens are useful for identifying novel genes involved in a biological process. This approach begins with a random mutagenesis. Different mutagens can be used according to the experimental requirements and may be physical, biological, or chemical (Koornneef, 2002). X-rays cause mutations by introducing breaks in double-stranded DNA, causing large deletions of pieces of chromosome, or chromosomal rearrangements (Vrieling *et al.*, 1985). Transposon (insertional) mutagenesis involves the use of transposable elements (TEs) which are mobilized in the genome and insert randomly within coding regions, or in non-coding DNA where they may affect intron splicing or gene expression (Alonso *et al.*, 2003). This technique has the benefit that genes are likely to be knocked out and the position of the TE insertion can be easily detected by PCR and the region of genome can then be cloned. A popular chemical mutagen is ethyl methanesulfonate (EMS) which introduces random single point mutations in the genome. Most substitutions (99 %) are G/C to A/T substitutions (Greene *et al.*, 2003) caused by a biased alkylation of guanine residues which leads to the production of the unusual base O^6-ethylguanine which pairs with T instead of C (Jansen *et al.*, 1995). This therefore leads to base changes following replication. About 50 % of mutations are expected to be missense mutations where incorrect amino acids are incorporated into the protein sequence as a result. This may or may not alter protein function (Greene *et al.*, 2003; Kurowska *et al.*, 2011). Approximately 5 % of mutations caused will produce truncated proteins due to the

introduction of a premature stop codon or splice site mutation. This is more likely to generate a severe phenotype which is more readily selected for in forward genetic screens (Greene *et al.*, 2003; Kurowska *et al.*, 2011).

Reverse-screening may also be carried out following EMS mutagenesis using TILLING (targeting induced local lesions in genomics) which involves screening for point mutations in a gene of interest (Colbert *et al.*, 2001; McCallum *et al.*, 2000). TILLING populations have been set up in a number of plant species, including wheat, *Brassica rapa, Arabidopsis*, and maize (Till *et al.*, 2004; Uauy *et al.*, 2009; Stephenson *et al.*, 2010).

4.1.3 Life cycle of a model plant

For genetic studies such as mutagenesis to be performed, a relatively short life cycle is advantageous. In an ideal situation, the seed to flowering time of an individual is as short as possible. In *U. gibba*, this is limited by very low germination efficiency.

4.1.3.1 Improving germination efficiency

A number of treatments and conditions have been reported to improve the germination of seeds from different species. These often work by breaking different types of seed dormancy which prevents germination during periods of unfavourable seedling growth. A number of different types of dormancy exist, including physiological, morphological, physical, and chemical (Baskin & Baskin, 1998). Methods to break dormancy and improve germination may be related to the natural environment in which the plant grows. For example, physical dormancy may be broken by heat, smoke and darkness treatment, in species living in fire-prone ecosystems (Keith, 1997; Moreira & Pausas, 2012). The germination of other plants including pines and milkweed may be improved by stratification (cold treatment) which simulates natural conditions before germination (Oegema & Fletcher, 1972; Skordilis & Thanos, 1995; Bratcher *et al.*, 1993). A number of plant hormones have also been shown to improve germination. For example, gibberellic acid (GA) can overcome a germination requirement for far-red wavelength light in species of *Asteraceae* (Plummer & Bell, 1995). GA has also been shown to weaken a mechanical restraint of endosperm cells in tomato to permit germination (Groot & Karssen, 1987).

Cytokinins have also been found to improve germination, possibly due to the alleviation of stress factors (Nikolić *et al*., 2006) and have been found to reverse the inhibition of GA induced germination by abscisic acid (Khan, 1968). Ethephon (an ethylene releasing compound) has been found to improve germination efficiency in species such as *Echinacea* (Sari *et al*., 2001). It is thought that ethylene is involved in seed maturation (Matilla, 2000). This work will involve testing some of these treatments with the aim to improve the germination efficiency of *U. gibba* seeds in culture.

4.1.4 *In situ* hybridisation

Once candidate genes are identified, we need to study their biological relevance in the system of interest. The spatial expression of genes is of particular relevance when testing predictions of gene activity made by developmental models. One method to look at spatial expression patterns of genes is RNA *in situ* hybridisation. This method uses a complementary RNA probe to localise a specific mRNA sequence in a section (or whole piece) of tissue. A detection label is added to the probe so that signal can be observed under the microscope. This label is often digoxigenin (Dig) (Farquharson *et al*., 1990) which can be detected by incubation with an alkaline phosphatase- conjugated anti-digoxigenin antibody followed by an alkaline phosphatase NBT/BCIP chromogenic reaction. The hydrolysis of BCIP by alkaline phosphatase leads to the production of indoxyl which dimerises to form lucoindigo which is then oxidised by NBT to form insoluble, blue BCI (5,5'-dibromo-4,4'-dichloro indigo). NBT is reduced to form insoluble purple DF (diformazan), forming NBT-DF. Therefore, a dark purple precipitate is made (a mixture of NBT-DF and BCI) (Wolf *et al.,* 1968; Trinh *et al.*, 2007). This stain can be visualised easily by light microscopy.

4.1.5 Aim of this work

The aim of this work is to set up a number of resources and techniques in *U. gibba* to further the development of this plant as a new model system and to continue investigating predictions made by modelling in previous chapters. This will involve the following:

1.) Whole genome sequencing of the *U. gibba* lines in the lab.

2.) Setting up an EMS mutagenesis experiment for *U. gibba.*

3.) Improving the germination efficiency of *U. gibba* seeds (to shorten the life cycle of *U. gibba* in the lab).

4.) Optimising an RNA *in situ* hybridization protocol for *U. gibba* to allow the spatial expression of genes of interest to be studied.

The results presented in this chapter are part of a work in progress and many of the experiments started are beyond the scope of this thesis.

4.2 Results

4.2.1 Sequencing and assembly of the *U. gibba* genome

We had five different *U. gibba* accessions available: Burgh Apton (BA), Carnivorous Plant Society (CPS), Morley, Bonn, and Czech. In order to obtain genomic sequence information and to establish the best accession to work with, I sent DNA isolated from each line to TGAC, Norwich for sequencing. Sequencing of a single library for each line was performed using Illumina HiSeq (100 bp paired end reads). A summary of the data is below (Table 4-1).

Table 4-1: Summary of *U. gibba* accession sequencing. The average coverage assumes an 88 Mbp genome based on (Greilhuber *et al.*, 2006).

Sample/ accession	Library ref. name	Mean library insert size	No. of read pairs (2x100 bp)	Average coverage	Size of assembly (Mbp)	No. of scaffolds	N50 length
BA	LIB2632	466 bp	56,776,681	130x	154	66,189	15,336
CPS	LIB2633	624 bp	49,512,928	114x	166	110,611	16,524
MORLEY	LIB2634	537 bp	65,682,078	150x	166	54,168	14,731
BONN	LIB2980	531 bp	83,487,071	189x	225	106,532	7,704
CZECH	LIB2981	532 bp	76,016,915	173x	174	83,772	11,341

4.2.1.1 Choosing a *U. gibba* accession reference genome

To set up *U. gibba* as a model system, we required a single reference genome. When studying assemblies there are a number of genome properties to consider when selecting an assembly for use. These include: the level of heterozygosity, completeness of the genome, and the quality of the assembly (the extent to which the genome is subdivided into scaffolds). Once data had been generated for the *de novo* assembly of each of the five accessions, choosing a *U. gibba* genome was a compromise between these metrics.

Heterozygosity is a confounding factor in reference generation, particularly in non-inbred lines, as the ultimate goal is typically to reduce a diploid individual to a haploid reference genome. The presence of heterozygous polymorphism can interfere with this process. To study the heterozygosity of the assemblies, the k-mer profile of each library was assessed. K-mers are sub-sequences of length k and can be used to explore properties of uniqueness and coverage within a read set. Using a k-mer size of 31 bp, Figure 4.1 shows a plot of the number of distinct k-mer sequences that align to the reference genome (coverage). Different colours indicate the different lines sequenced. For each line, a peak close to 0 consists of rare k-mers that reflect sequencing error. The first peak of the graph after this error peak indicates the heterozygous content while the second peak, which has approximately double the coverage, indicates the homozygous content. This is due to the fact that at a heterozygous site where there are two alleles, there will be two different k-mers, whereas for homozygous content, there will be two identical k-mers, producing

double the coverage. In selecting the best assembly, there were two key concerns: the overall coverage level and the balance between haploid (homozygous) and diploid (heterozygous) scaffolds. When sequence coverage is low, it can be difficult to make a clear distinction between error (rare k-mers) and the peaks of homozygous and heterozygous signal are less well separated. This situation is illustrated by the CPS accession, where coverage is low and it is difficult to distinguish between the two peaks (Figure 4.1, yellow). Coverage is better in the BONN and CZECH accessions but both have a skewed profile where the heterozygous peak is considerably higher than the homozygous peak (Figure 4.1, blue and purple). During sequence assembly, reads are assembled into scaffolds, which are eventually merged to form larger scaffold assemblies. In the case of BONN and CZECH, there are multiple scaffolds which contain the same sequences (redundancy), but are yet to be assembled. This means that k-mers appear to map multiple times more than compared to how they would map against a fully assembled genome sequence. This gives a falsely high impression of the heterozygosity of the genome based on k-mer analysis. The BA and MORLEY assemblies have approximately equal heterozygous and homozygous content peaks, although this profile does suggest that substantial redundancy persists and that overall genome size is likely over-estimated (Figure 4.1, red and green).
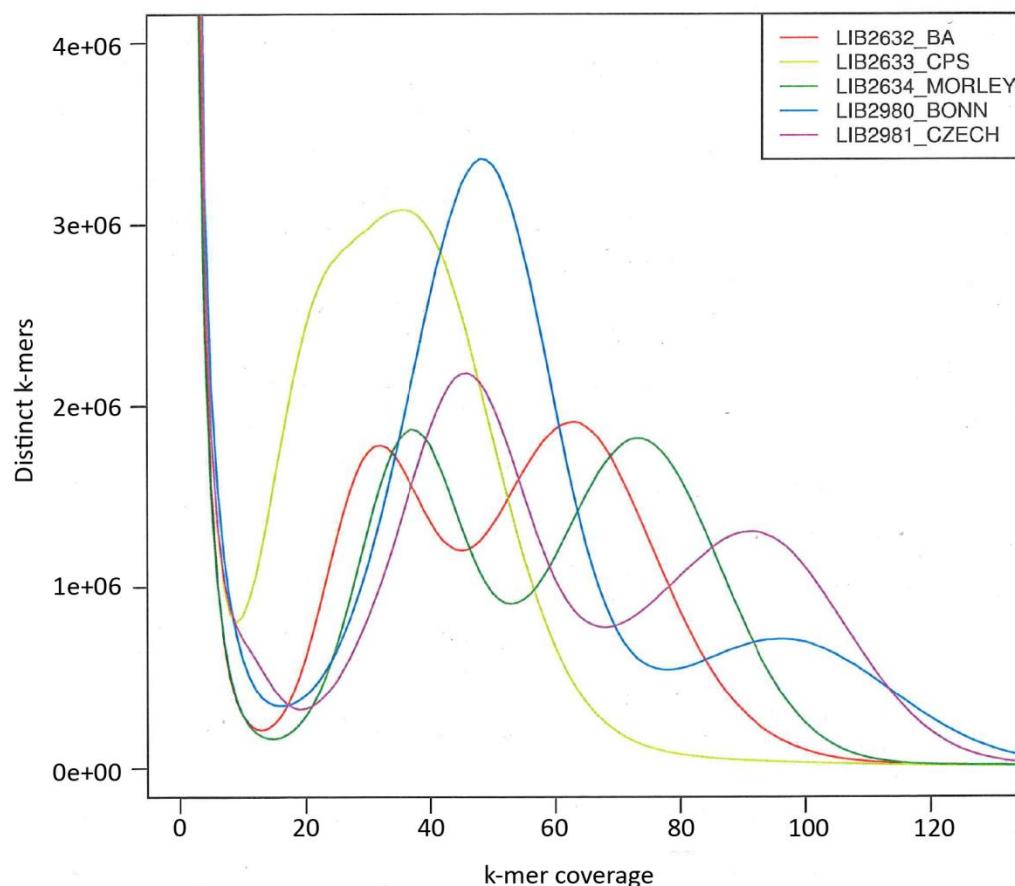
Figure 4.1: k-mer profiles for each *U. gibba* accession. k= 31. Plot was generated by Daniel Mapleson at TGAC.

Further considerations in selecting the optimal reference are the fragmentation level and completeness of the assembly. The fragmentation level can be assessed by looking at the total number of scaffolds and the N50 value. The scaffold N50 length is a weighted median statistic where 50 % of the entire assembly is contained in scaffolds equal to or larger than this value. When comparing assemblies of similar sizes, a large N50 value and a low number of scaffolds, relative to the expected chromosome level is preferable. The assemblies with the highest N50 values are CPS (16,527) and BA (15,336) (Table 4-1). The assemblies with the least scaffolds are Morley (54,168) and BA (66,189) (Table 4-1). In this sense, BA may the most favourable line. However, these are still preliminary assemblies based on low depth sequencing.

Based on this analysis the BA accession was chosen. The assembly of BA has one of the higher N50 values, and lower number of scaffolds indicating that the genome is spread across fewer and larger scaffolds (Table 4-1). It is also one of the lines which showed fairly even homozygous and heterozygous content as opposed to mostly heterozygous content (Figure 4.1).

4.2.1.2   Comparing the BA assembly to the published LangeBio genome

During this work, another group published a *U. gibba* genome (LangeBio) (Ibarra-Laclette *et al.*, 2013). This was a useful comparison to our BA assembly and enabled us to check that we had captured similar information from the genome.

4.2.1.2.1   Completeness of the BA and LangeBio genomes

To study the completeness of the BA genome in comparison to the published LangeBio genome, CEGMA (core eukaryotic genes mapping approach) analysis was performed by TGAC. This analysis identifies the presence/ absence of a set of few hundred eukaryotic proteins that would be expected in the genome. The table below summarises the data for each genome (Table 4-2). This provides a rough indication that the BA and LangeBio genomes are comparable and are not missing a large extent of gene content.

Table 4-2: CEGMA completeness analysis of the BA genome and published genome.

Genome	Genes with complete presence (%)	Genes with partial presence (%)
LangeBio (published)	96	98
BA accession (TGAC)	95	98

4.2.1.2.2   Exploring the larger size of the BA assembly

The size of the assembly for all accessions was larger than the published genome size (82 Mbp) (Ibarra-Laclette *et al.*, 2013). In the case of BA, the assembly size was 154 Mbp. To

investigate possible causes of this discrepancy, TGAC mapped the BA assembly to the published *U. gibba* genome. They found that 40 % of the BA genome did not map to the published assembly. This might reflect extensive divergence between the accessions used for genome assembly (such that reads from BA contained too many sequence differences from the reference to be mapped to their homologous alleles). It might also reflect a contribution of symbiont or other contaminant genomes in the BA read set. Read pairs that could not be mapped to the LangeBio reference genome were run through a *de novo* assembly pipeline at TGAC and a putative origin of any large contigs was assessed by BLAST. No major contribution of any specific microbial or other non-*Utricularia* lineage was detected.

K-mer profiles were also used by TGAC to explore the relationship between the BA and LangeBio assemblies (Figure 4.2) K-mer profiles were produced using the KAT tool which can be found at: https://documentation.tgac.ac.uk/display/KAT/KAT+Home. 31 bp k-mers were generated from the TGAC (BA) reads. The k-mer spectra show the number of specific 31-mers showing a given coverage value within a set of reads. The plot is further decomposed to reveal the number of times each individual k-mer is found within a reference assembly (indicated by the different colours within the profiles) and gives an estimation on the redundancy in the genome. A k-mer with coverage close to zero most likely contains a sequence error, whereas the two major peaks correspond to heterozygous and homozygous coverage. The similarity in size of the two peaks when the k-mers are mapped to each genome highlights the extent of BA heterozygosity (Figure 4.2, A & C, main profile).

LangeBio published genome

TGAC (BA) genome
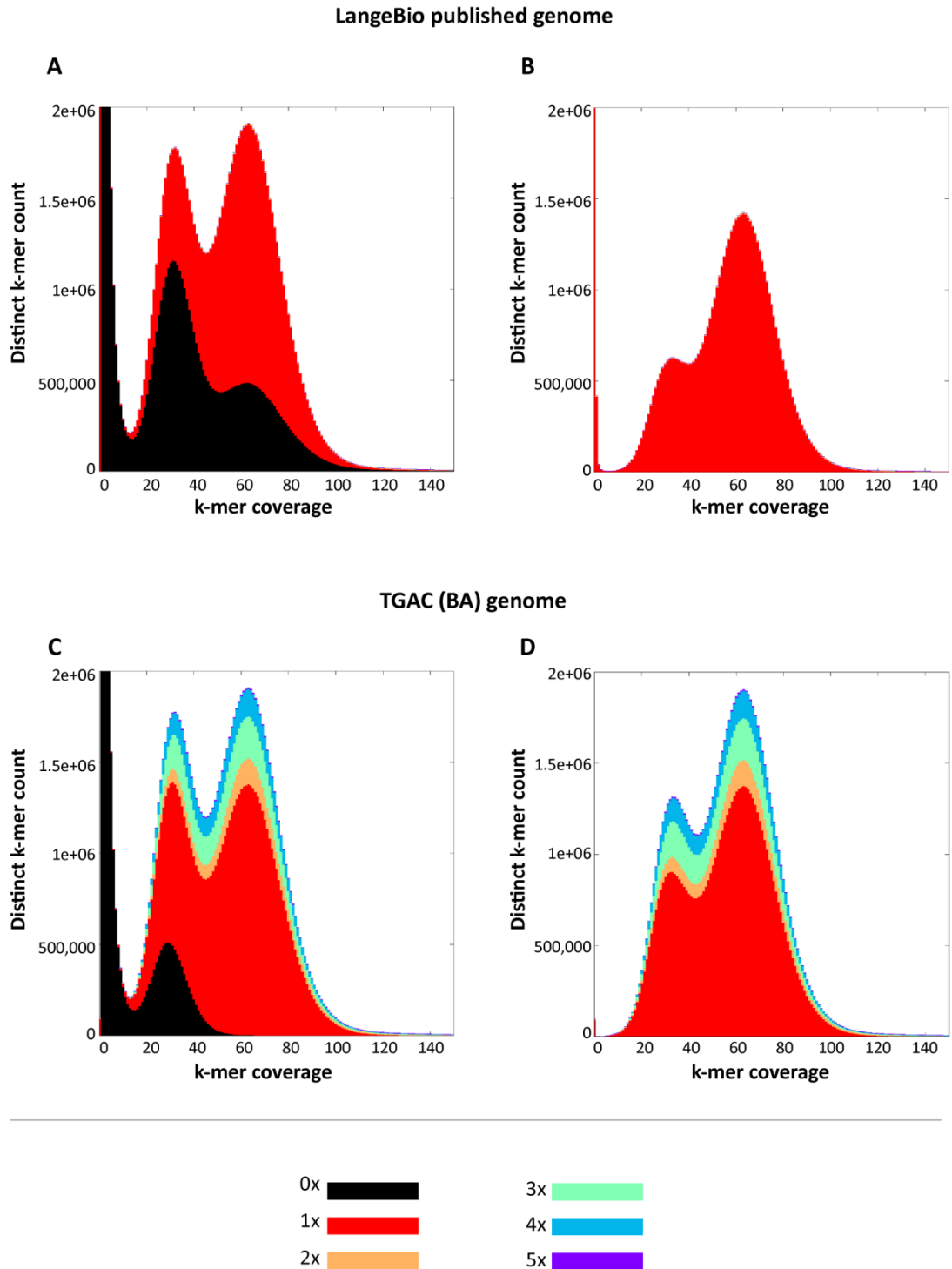
Figure 4.2: Assembly duplication histograms based on k-mers from the BA assembly.
31 bp k-mers are from the TGAC (BA) reads. K-mer count is plotted against k-mer coverage in the LangeBio (published) assembly (A & B) and the TGAC (BA) assembly (C & D). Plots are further decomposed to reveal the number of times each k-mer is found within a reference assembly: 0x (black), 1x (red), 2x (orange), 3x (green), 4x (blue), and 5x (purple). B & D are 'no-absent' plots which do not include those 31-mers not found in the reference assembly. Plots were generated by Daniel Mapleson at TGAC.

The number of BA-derived k-mers that are absent from the reference genome assembly (Figure 4.2, A & C, black) is more substantial in the LangBio assembly (Figure 4.2, A, black) than the BA assembly (Figure 4.2, C, black), consistent with the observation that a sizeable proportion of the BA-derived reads are absent from the LangeBio assembly. Duplication levels are higher in the BA assembly (colours), indicating an increased degree of redundancy in the BA assembly, perhaps not surprising given the greater size of the assembly. This redundancy may be due to different reads not being collapsed together propery in the assembly or due to gene dupliction within the genome. The similarity of the main second (homozygous) peak in the no-absent plots (Figure 4.2, B & D) suggests that both assemblies contain most of the same core content, in line with the CEGMA analysis.

4.2.1.3   Summary

The BA accession assembly was chosen due to its lower heterozygosity compared to the other assemblies and its higher N50 and lower scaffold number. Comparisons were made between the BA assembly and a newly published LangeBio assembly (Ibarra-Laclette *et al.*, 2013) and were comparable in CEGMA analysis, indicating that both have a good level of completeness. The assembly size of the BA genome was larger than that of the published assembly (154 Mbp compared to 82 Mbp). This is partly due to an apparent greater degree of heterozygosity in the BA assembly compared to the LangeBio assembly. Also, more redundancy in the BA genome may contribute to its larger size. This redundancy may indicate gene duplications or may be due to artefacts in the assembly. To improve these data a higher depth sequencing run could be performed on the BA line to generate a higher quality genome assembly.

4.2.2 *U. gibba* EMS mutagenesis

I took a forward genetic screen approach to identify novel genes associated with bladder development. *U. gibba* is particularly amenable to a mutagenesis screen since it is diploid, self-fertile, the bladders appear soon after germination for screening, and it has a small genome which has been sequenced in our lab as well as elsewhere (Ibarra-Laclette *et al.*, 2013). The BA accession was chosen based on the reference assembly discussed above

which will enable us to compare the genome of any mutants generated with that of the wild type. I set up EMS mutagenesis in *U. gibba* in collaboration with Karen Lee.

4.2.2.1   Setting up the mutagenesis

We decided to mutagenize *U. gibba* tissue rather than seed since the germination of *U. gibba* seeds was very low (see 4.2.3). The ability to readily propagate *U. gibba* makes this a suitable technique since tissue can be treated with EMS and then broken up and each piece grown as an individual (M1). Since the plants self-fertilize, seeds from individual pods of M1 can then be collected and sown as families for screening of the M2 generation. The overall process is illustrated below (Figure 4.3). For germination of the M2 generation, I had to improve the germination efficiency of *U. gibba* seeds (see 4.2.3).
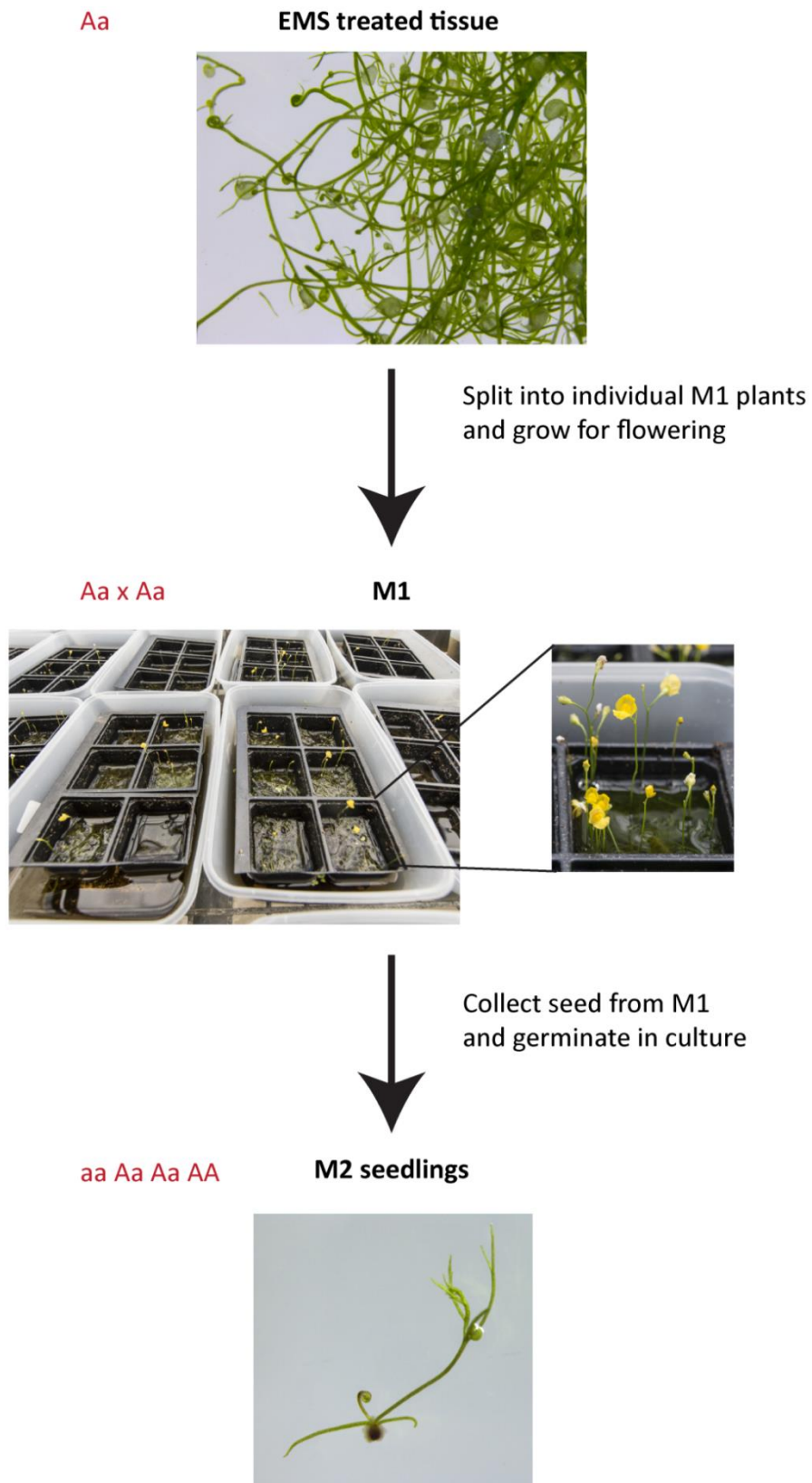
Figure 4.3: Mutagenesis plan. Tissue can be treated with EMS and then propagated to generate multiple M1 plants. The M1 plants self-fertilise and seeds can be collected from these plants and sown (M2 generation). M2 seedlings can be screened for mutant bladder phenotypes. Red text indicates a hypothetical mutation which segregates in M2 plants.

4.2.2.2 Mutagenesis experiment 1

To find a suitable EMS concentration we considered concentrations used in other EMS mutagenesis experiments. In *Arabidopsis*, 0.2 % EMS is optimal (Till *et al.*, 2003), while in *Brassica rapa* 0.3 % EMS is optimal (Stephenson *et al.*, 2010), and in *Capsella rubella* 0.25 % and 0.3 % EMS are optimal (Eldridge, 2014). Since we used tissue rather than seeds it was difficult to predict what dose would be optimal so we started by treating tissue with either: 0.01 % EMS, 0.05 % EMS, 0.1 % EMS, 0.15 % EMS, 0.2 % EMS, or 0.25 % EMS. After propagation we had approximately 4500 M1 plants in total. We observed that EMS treatment had been effective, since plant survival was affected by EMS treatment: higher concentrations of EMS led to lower survival rates of plants, and therefore more plants were discarded (Figure 4.4).
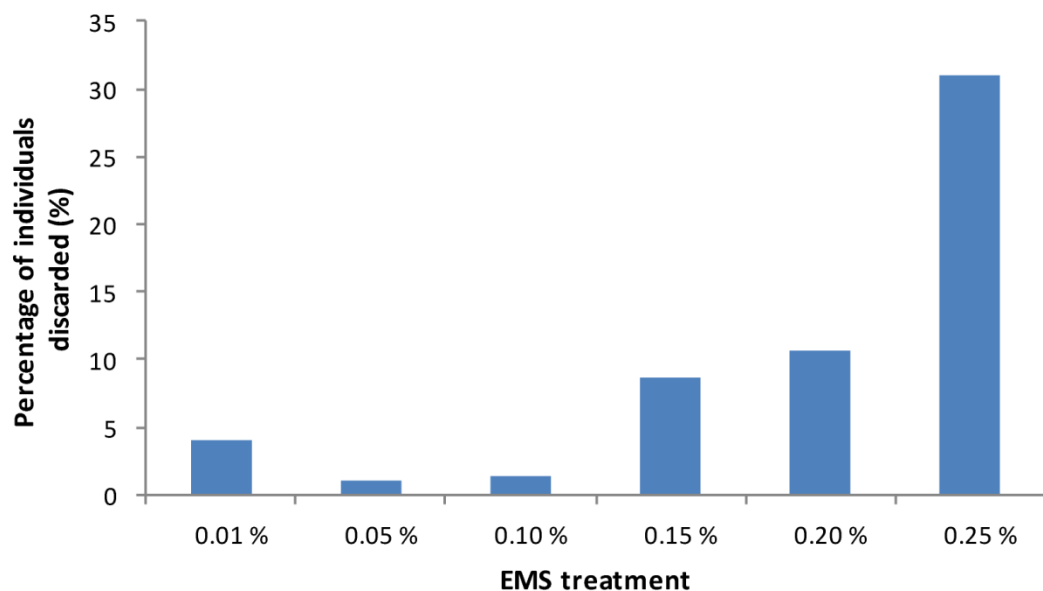
Figure 4.4: Percentage of discarded M1 plants after treatment with different concentrations of EMS.

Plants began to flower after approximately 3 months in the glasshouse, however only 7.5 % of all plants produced seed. This was probably due to the plants taking 3 months to flower, missing the growing season with no supplementary lighting available in the glasshouse, and possibly due to disruption of the flowers during watering. In general, we found that plants in the brighter areas of the glasshouse produced the most flowers and seeds across all EMS concentrations. We tried moving some plants to a lit glasshouse which was heated

between 15 °C and 20 °C for 2 months. This improved the number of plants producing seed to approximately 20 %.

4.2.2.3 Mutagenesis experiment 2

We decided to set up a second mutagenesis so that we could propagate the tissue and transfer the M1 plants to the glasshouse earlier in the year for growth and flowering in the following summer months. We also used a lit, heated glasshouse when available. We focussed on 0.1 %, 0.15 %, and 0.2 % EMS treatments because at 0.15 % and 0.2 % EMS treatment the percentage of unhealthy plants increased to around 10 %, indicating that the EMS treatment had a deleterious effect. Since we could not yet assess the full effect on fertility (because only 7.5 % of plants produced seed), we included a treatment category of 0.1 % EMS in case higher concentrations affected fertility significantly more.

4.2.2.4 Analysis of plant fertility from mutagenesis experiments 1 and 2

Once the M1 treated plants from both mutagenesis experiments had flowered, seed pods were collected and the number of seeds within a pod was scored. To see what effect EMS concentration had on fertility, the number of seeds per pod was studied for those plants which flowered and produced seed (Figure 4.5).
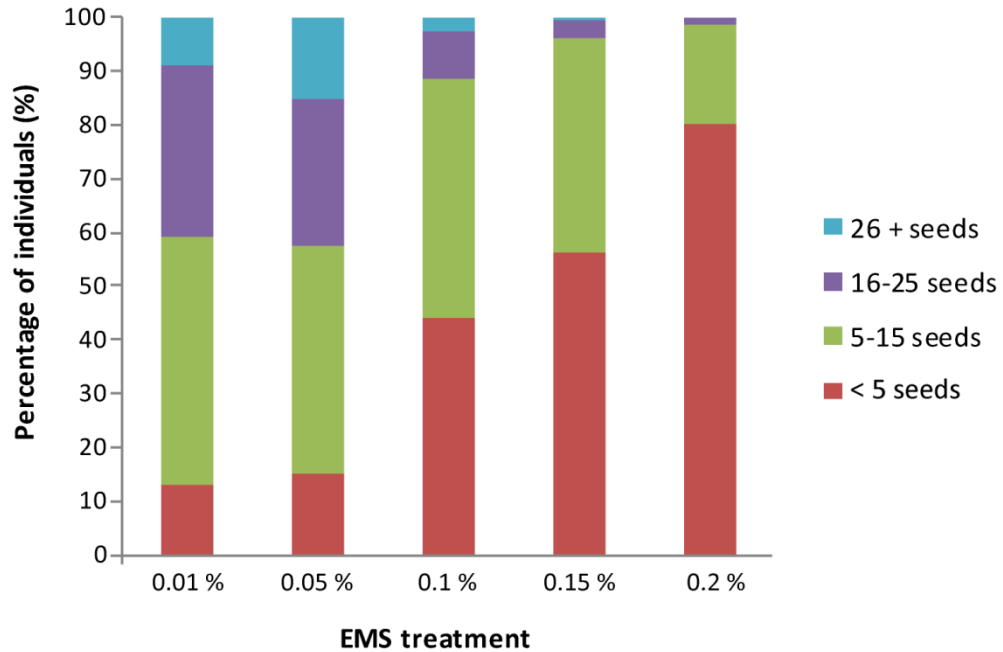
Figure 4.5: Seed production in plants treated with different concentrations of EMS. The number of seeds per pod was counted from plants treated with increasing concentrations of EMS.

No plants treated with 0.25 % EMS in the first experiment produced seed. There is a decrease in fertility of M1 plants as the concentration of EMS increases (Figure 4.5). This indicates that the mutagenesis was successful. Since the total number of seeds was quite low (c. 14,000 across all conditions), we decided to screen all families (individual pods) for mutant phenotypes.

4.2.2.5 Forward screens

M2 seedlings from both mutagenesis experiments were screened for mutant phenotypes. Screens were carried out with Christopher Whitewoods, Karen Lee and Jamie Spooner. Each pod was considered a family, since the plant is likely chimeric and therefore pods from flowers originating from the same plant were considered separate families. Some segregating mutant phenotypes observed are shown below including mutants with long spurs on their flowers, deformed bladders, and mutants completely lacking bladders (Figure 4.6). Other mutant phenotypes included flowers containing multiple carpels and bladders which appeared to be unable to capture prey. Some wt: mutant ratios within a family were low. This is due to the low seed number available.

Long spur mutant   wt flower

M2 wt:mut ratio = 4:2

Deformed bladder mutant   wt bladder

M2 wt:mut ratio = 4:1

No bladders mutant   wt stolons with bladders

M2 wt:mut ratio = 4:1
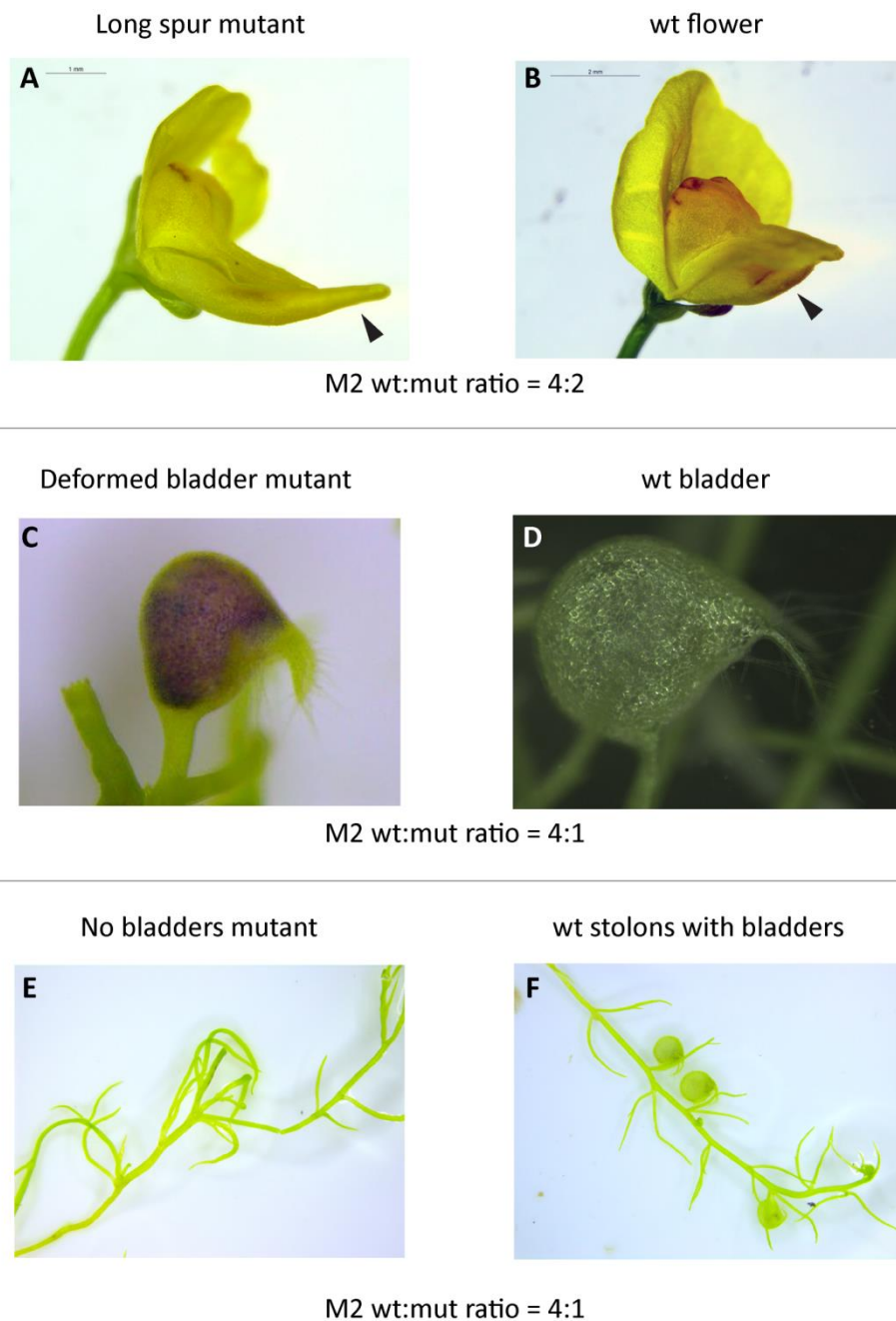
Figure 4.6: Examples of segregating M2 *Utricularia gibba* mutants. (A) Long spur mutant compared to wt flower (B). (C) Deformed bladder mutant compared to a wt bladder (D). Dark colouration in C is sometimes noted in wt bladders and may be due to an increase in anthocyanin production. (E) A mutant which does not make bladders compared to a wt plant with bladders along the stolon (F).

Any families with mutant phenotypes were kept and grown for flowering to study the M3 generation to check for further segregation of the phenotype.

4.2.3 Improving *U. gibba* germination efficiency

Efficient seed germination is important for the success of a model plant since genetic studies rely on the ability to cross plants and study following generations. This was of particular importance for the mutagenesis screen in which an M2 generation was required for screening. The germination efficiency of *U. gibba* seeds in the lab was very low, with only 11 % of all seeds sown germinating (within approximately 6 months). This may be partly due to seed pods not being mature at collection. However, only 20 % of seeds germinated from those pods which showed germination. To improve germination, I first tried storing and germinating seeds at different temperatures and using different culture medium. However, this did not improve germination efficiency.

I then tried a number of hormone treatments which have been reported to improve germination in other species. These included cytokinins (Nikolić *et al*., *2006*), gibberellic acid (GA) (Bell *et al*., 1995; Eghobor *et al.,* 2015), and ethylene (Matilla, 2000; Sari *et al.,* 2001). All seeds were sown onto a layer of solid MS medium and covered with liquid MS medium containing either no hormone (control), 30 µM gibberellic acid, 1.6 µM or 7 µM zeatin (cytokinin), or 1 mM ethephon (which decomposes to ethylene) (Figure 4.7). Each group had between 120 and 200 seeds.
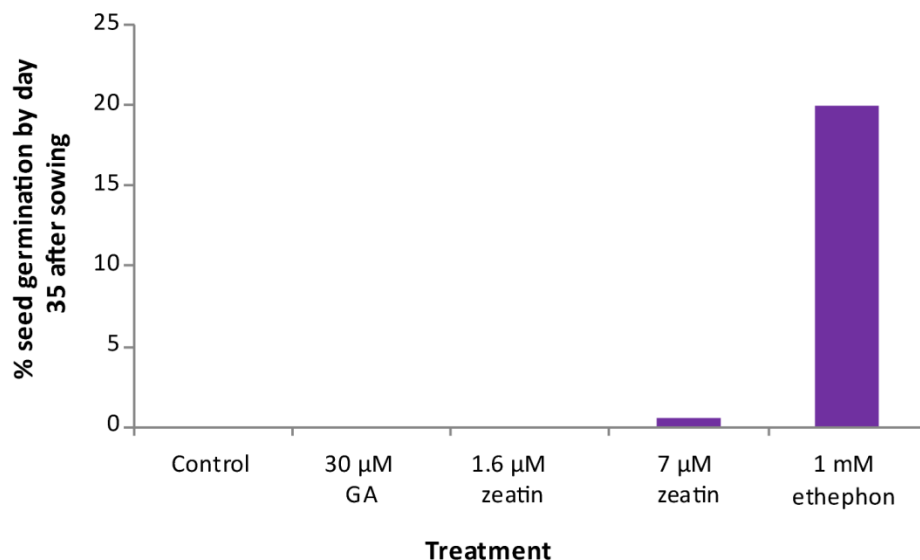
Figure 4.7: Testing different hormone treatments to improve *U. gibba* seed germination efficiency. Seeds were treated with either 30 µm gibberellic acid (GA), 1.6 µM or 7µM zeatin (a cytokinin), or 1 mM ethephon. The percentage of seeds which germinated within 35 days is shown. Each group had between 120 and 200 seeds.

At 35 days after sowing, no seeds had germinated in the control group or from the group treated with GA. Only 0.5 % of seeds germinated in the group treated with 7 µM zeatin. However, 20 % of seeds treated with 1 mM ethephon germinated (Figure 4.7). I decided to test different concentrations of ethephon to see if it could consistently improve germination.

I tested 0.1 mM, 1 mM, and 10 mM ethephon concentrations for the germination of *U. gibba* seeds. Prior to sowing, seeds were kept dry at room temperature. I counted the total number of seeds germinated by day 60 after sowing (Figure 4.8). I found that 75 % of seeds sown in media containing 0.1 mM ethephon and almost 56 % of seeds sown in media containing 1 mM ethephon germinated compared to only 18 % of seeds in control media containing no ethephon. Increasing the ethephon concentration to 10 mM prevented seeds from germinating. There is also a drop from 75 % to 56 % germination between 0.1 mM and 1 mM ethephon, suggesting that higher concentrations are not as effective at promoting germination.
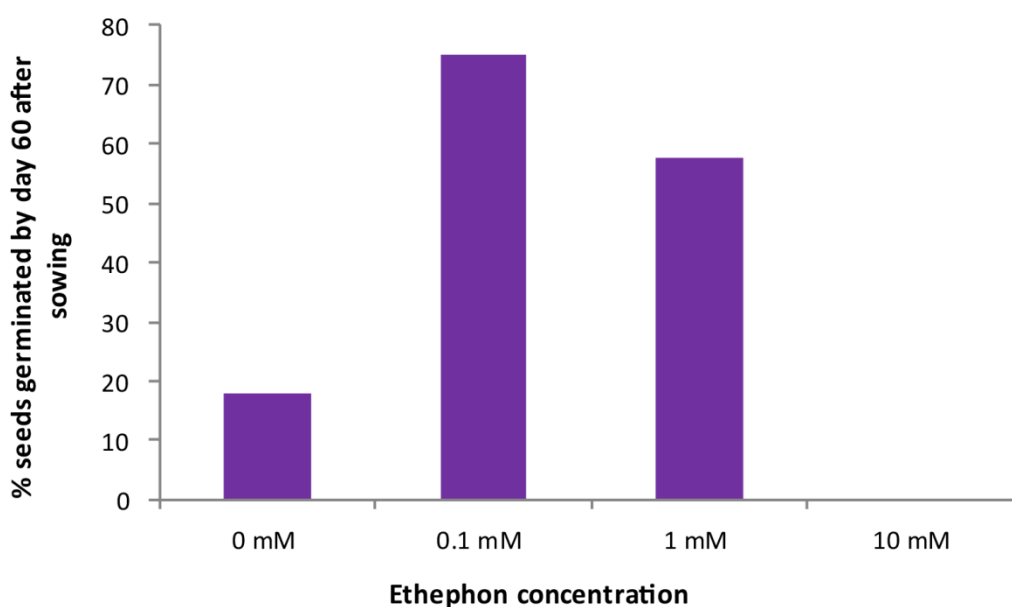
Figure 4.8: Improving the germination efficiency of *U. gibba* seeds with ethephon. 50 seeds were sown on solid MS media and covered with liquid MS media containing different concentrations of the ethylene releaser ethephon. The number of seeds germinated over a 60 day period was recorded.

This initial test was done on seeds from two different lines of *U. gibba* (CPS and BA). I repeated the experiment to check results in the BA line only (since we decided to work on this line as it was less heterozygous). This time I recorded the date of each seed germination so I could compare the germination efficiency at 30 days and 60 days after sowing. I also studied the morphology of the seedlings to assess whether ethephon treatment had any deleterious effect on seedling growth or development (Figure 4.9). The percentage of seeds germinating in the first 30 days after sowing increases from 12 % in the control to around 60 % when sown in 0.1 mM ethephon. At 1 mM ethephon, germination in the first 30 days was around 42 %, and by 10 mM ethephon, no seeds germinated. This indicates that ethephon improves the overall germination of *U. gibba* seeds and also speeds up the time it takes for seeds to germinate. The total percentage germination of the control in this experiment was higher than before (36 % germination by day 60 compared to 18 % in the first experiment). This indicates that there is variability in the germination efficiency of *U. gibba* seeds. This may be due to the conditions that the parent plant was grown in, the time since collection that seeds were sown, the storage conditions of seeds, and the line of *U. gibba* (in the second experiment, only BA seeds were studied, while in the first experiment CPS seeds were also sown). The morphology and growth of seedlings does not appear to be affected by ethephon treatment (Figure 4.9, B).

A

B

Control   0.1 mM ethephon
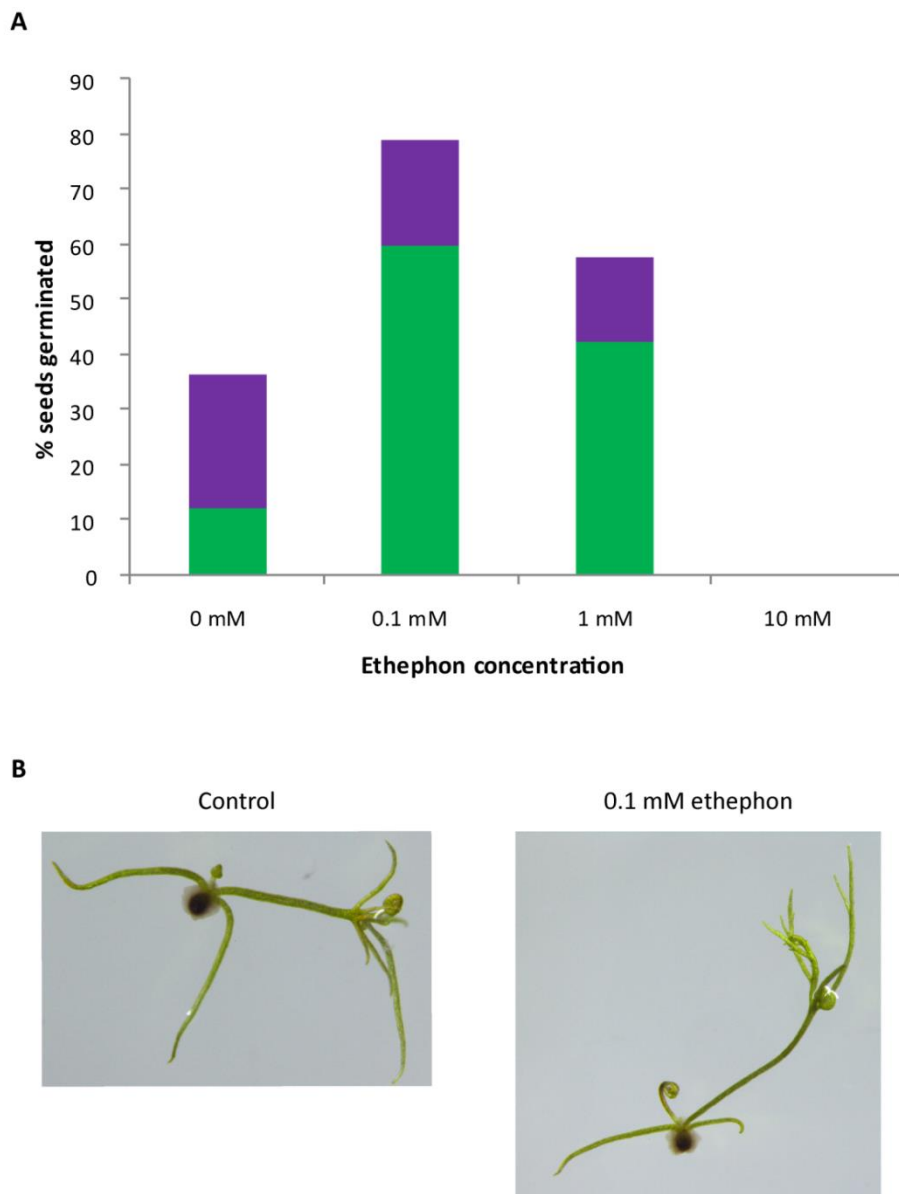
Figure 4.9: Improving germination in the BA *U. gibba* line. (A) Percentage of seeds germinated by day 60 after sowing in media containing different concentrations of ethephon. Green indicates % of seeds germinated by day 30 after sowing. Purple indicates % of seeds germinated between day 30 and day 60 after sowing. (B) Seedlings germinated in the control (0 mM ethephon) and 0.1 mM ethephon, imaged five days after germination.

4.2.3.1 Summary

Overall, these experiments show that the ethylene releasing compound ethephon can improve *U. gibba* germination by up to 500 % in a 30 day period (Figure 4.9). I found that 0.1 mM ethephon was the most successful concentration and that this treatment does not affect the growth or morphology of *U. gibba* seedlings.

4.2.4 Optimising an RNA *in situ* hybridisation protocol in *U. gibba*

RNA *in situ* hybridisation is a useful technique for the study of gene expression patterns in tissue. This technique allows the spatial patterning of candidate gene expression to be studied using RNA probes which bind to specific mRNA sequences in preserved tissue and have an attached label for visualisation.

The success of RNA in situ hybridisation relies on a number of factors. The first is the fixation of the tissue and the preservation of mRNA in the tissue. The second is the design of a probe which must specifically bind to the mRNA sequence of interest. Another important factor is the digestion of proteins in the tissue so that they do not mask the sequence being detected, and increasing the permeabilization of tissue so that the probe has access to the target sequence. I first explored different fixatives: I tried fixing circinnate apex tissue (which contains young bladders) in 4 % paraformaldehyde or Formalin Acetic Alcohol (FAA) plus triton, as both have been successful in a number of species in the lab. I used vacuum infiltration to improve penetration of the fixative.

To test the *in situ* hybridisation protocol, I decided to look at genes with expected patterns of expression. I designed a probe against the YABBY transcription factor *FILAMENTOUS FLOWER* (*FIL*) which is expressed on the abaxial surface of some eudicot leaves (Sawa *et al.*, 1999; Siegfried *et al.*, 1999) and on the abaxial (outer) surface of *Sarracenia* epiascidiate leaves (Fukushima *et al.*, 2015). I would therefore expect *FIL* expression on only one surface of the *U. gibba* bladder. While this provides an expected pattern of expression to test the *in situ* protocol with, it is also interesting to reveal the identity of each surface of *U. gibba* in the context of epiascidiate leaf development (Fukushima & Hasebe, 2014). I first identified two *UgFIL* homologs in *U. gibba* by performing blast searches (tblastn) using the *Arabidopsis* protein sequences against the published *U. gibba* transcriptome (at this time no genome information was available). I checked the hits from the *U. gibba* transcriptome by performing blastx searches using the candidate nucleotide sequence against the NCBI SWISS-PROT protein database and then performing a reciprocal blast search with the top hit. Later genome analysis revealed a further two *FIL* homologs (Figure 4.10).
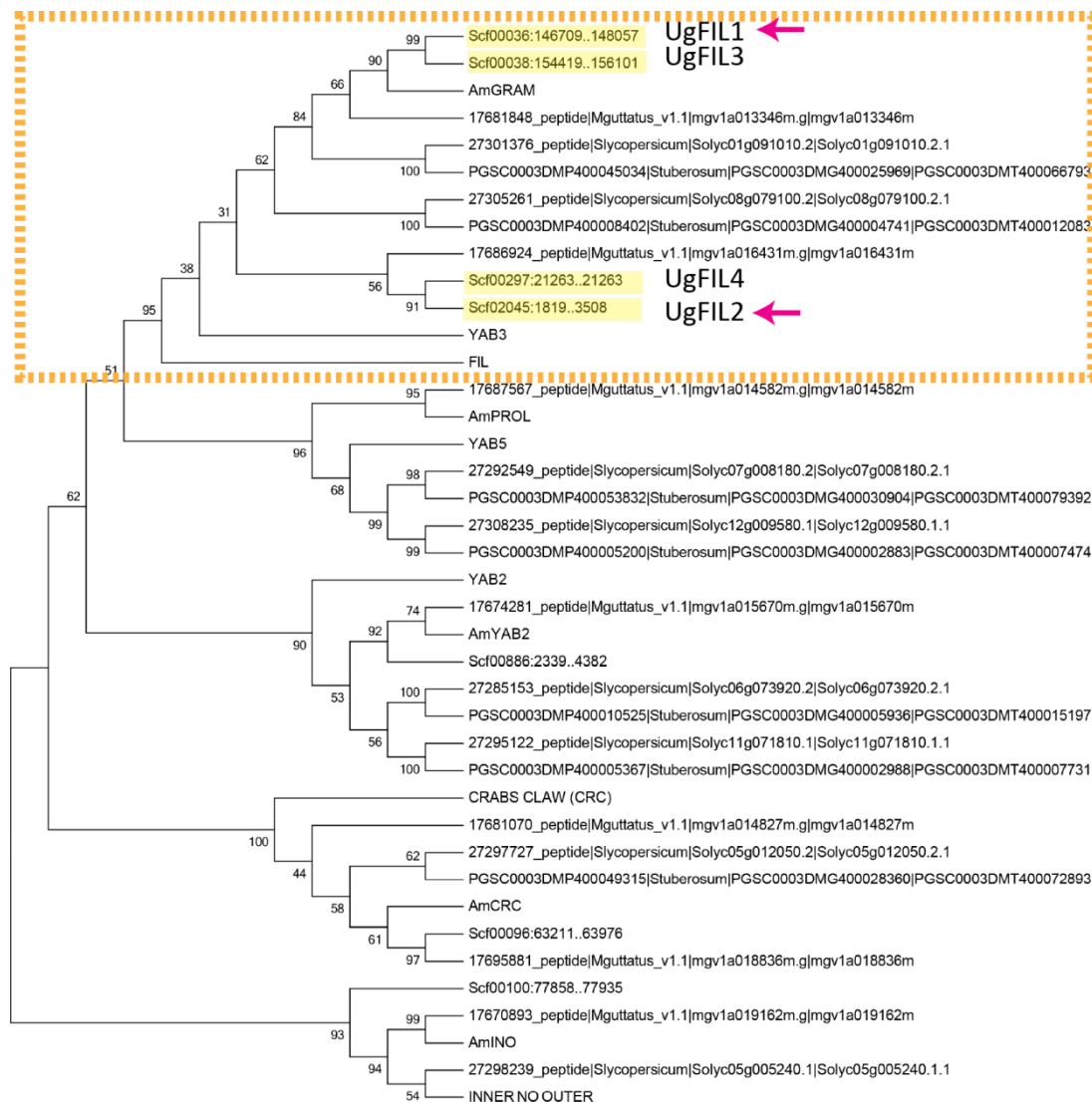
Figure 4.10: Guide phylogenetic tree of YABBY transcription factors. Tree was constructed using Mega5. Conserved regions of protein sequence were aligned and a Neighbour-Joining tree was constructed using 500 bootstrap replicas, the Jones-Taylor-Thornton (JTT) model, and pairwise deletion. Orange box indicates homologues of FIL/YAB3. Four homologs of FIL/ YAB3 are indicated in yellow. Pink arrows indicate those homologs also found in published transcriptome data.

I designed antisense RNA probes against *UgFIL1* and *UgFIL2* based on the transcript sequences I had available at the time. I was successful in making a probe against *UgFIL1*. However, the transcript available for *UgFIL2* was not complete (only 296 bp long) and I was unable to successfully clone *UgFIL2.* I performed an in situ hybridization using the probe for *UgFIL1*. I labelled the probe with an anti-digoxigenin antibody covalently linked with the enzyme alkaline phosphatase (AP). This allows for mRNA detection by the addition of BCIP

and NBT where BCIP is cleaved in the presence of NBT, leading to a blue precipitate where AP is present.

I followed the current protocol from the lab which was modified from Coen *et al.* (1990) and uses pronase to digest proteins in the sliced tissue (see materials and methods for details). Overall, I found the success of the in situ hybridization very variable across both fixations; some sections had signal while others did not, some had high levels of background, and some tissue was preserved better than others. The best examples of signal are shown below (Figure 4.11). The signal was very faint after one overnight incubation in buffer 6 (containing NBT and BCIP). I performed an extra overnight incubation in fresh buffer 6 which improved the signal. There appears to be expression of *UgFIL* on the outer layer of cells (Figure 4.11, pink arrows). *UgFIL* expression is also seen in cells of the threshold (Figure 4.11, white arrow) and on the lower cells of the trapdoor (Figure 4.11, yellow arrow). It is not clear from these images where the expression of *UgFIL* in the threshold and trap door stops and therefore where the ad-ab boundary may be. Based on the approximate location of the cross section (Figure 4.11, C) I can get a rough idea of where I do see *UgFIL* expression in these regions and make a prediction on the boundary (Figure 4.11, D). More sections would need to be studied to confirm this. In general, I found that tissue fixed in FAA had better preservation than that fixed in paraformaldehyde (Figure 4.11, A & B comparison). There is still room for improvement with tissue preservation so that cell layers may be more distinguishable.

FAA

4 % Paraformaldehyde
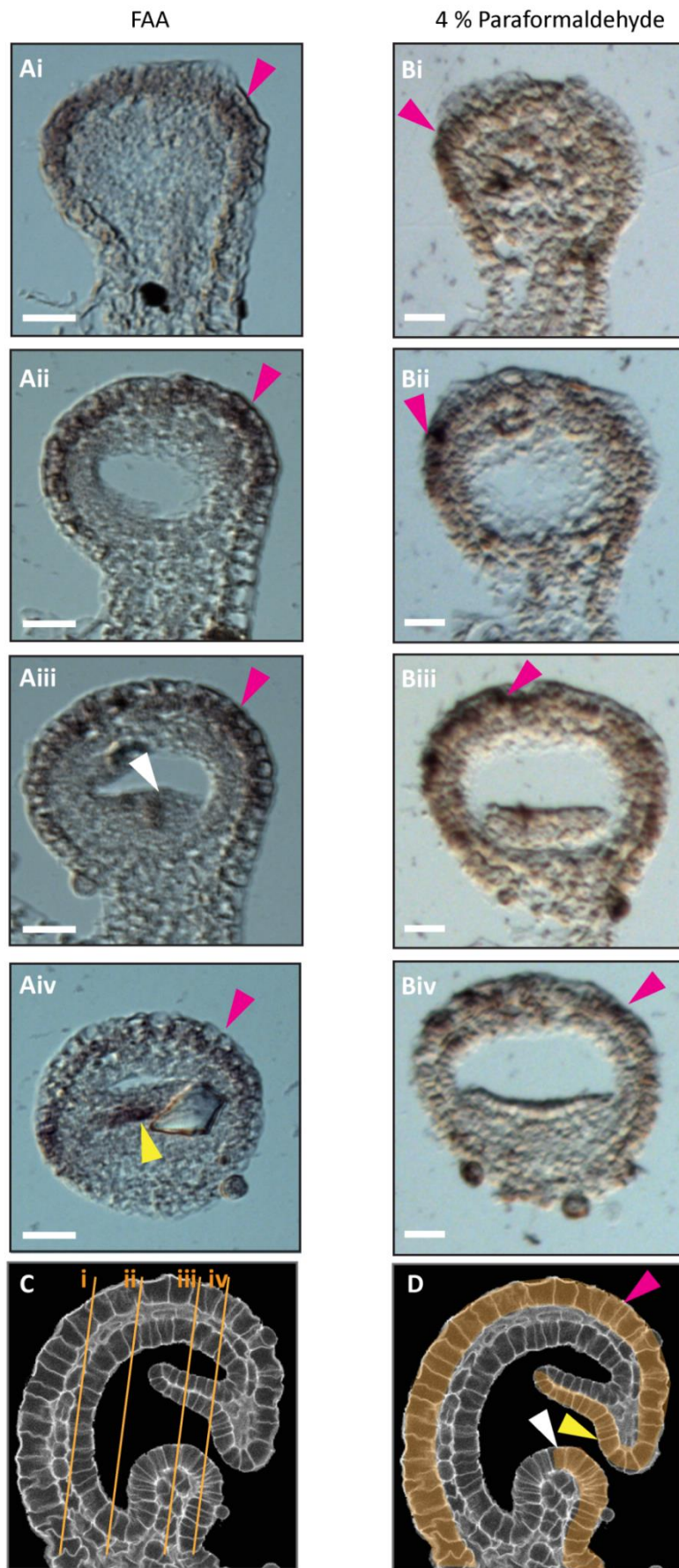
Figure 4.11: Expression of *UgFIL1* in *U. gibba* young bladders fixed in either 4 % paraformaldehyde or FAA. Sections are from the back of a young bladder, towards the mouth. (A) Tissue was fixed in FAA. (B) Tissue was fixed in 4 % paraformaldehyde. (C) Side section of a young bladder indicating the positions of the sections from (Ai-Aiv) (orange lines). (D) Side section of a young bladder indicating the corresponding regions of *UgFIL* expression around the outside layer of the main body of the bladder (pink arrowhead), at the trap door (yellow arrowhead) and at the threshold (white arrowhead). Orange in (D) indicates the proposed region of *FIL* expression based on this data. Scale bars are 20 μm.

To further develop the protocol, I designed a control probe against *U. gibba* HISTONE 4 (*UgH4*) to check a different pattern of expression against *FIL* expression. I found eight homologs for H4 in *U. gibba* I designed probes for the two most closely related to H4 from *Antirrhinum* and *Arabidopsis* (Figure 4.12). I obtained successful PCR products for a fragment of Scf00915:10384..10692 (*UgH4* most homologous to *Arabidopsis H4*) and continued with these products to generate a *UgH4* RNA probe.
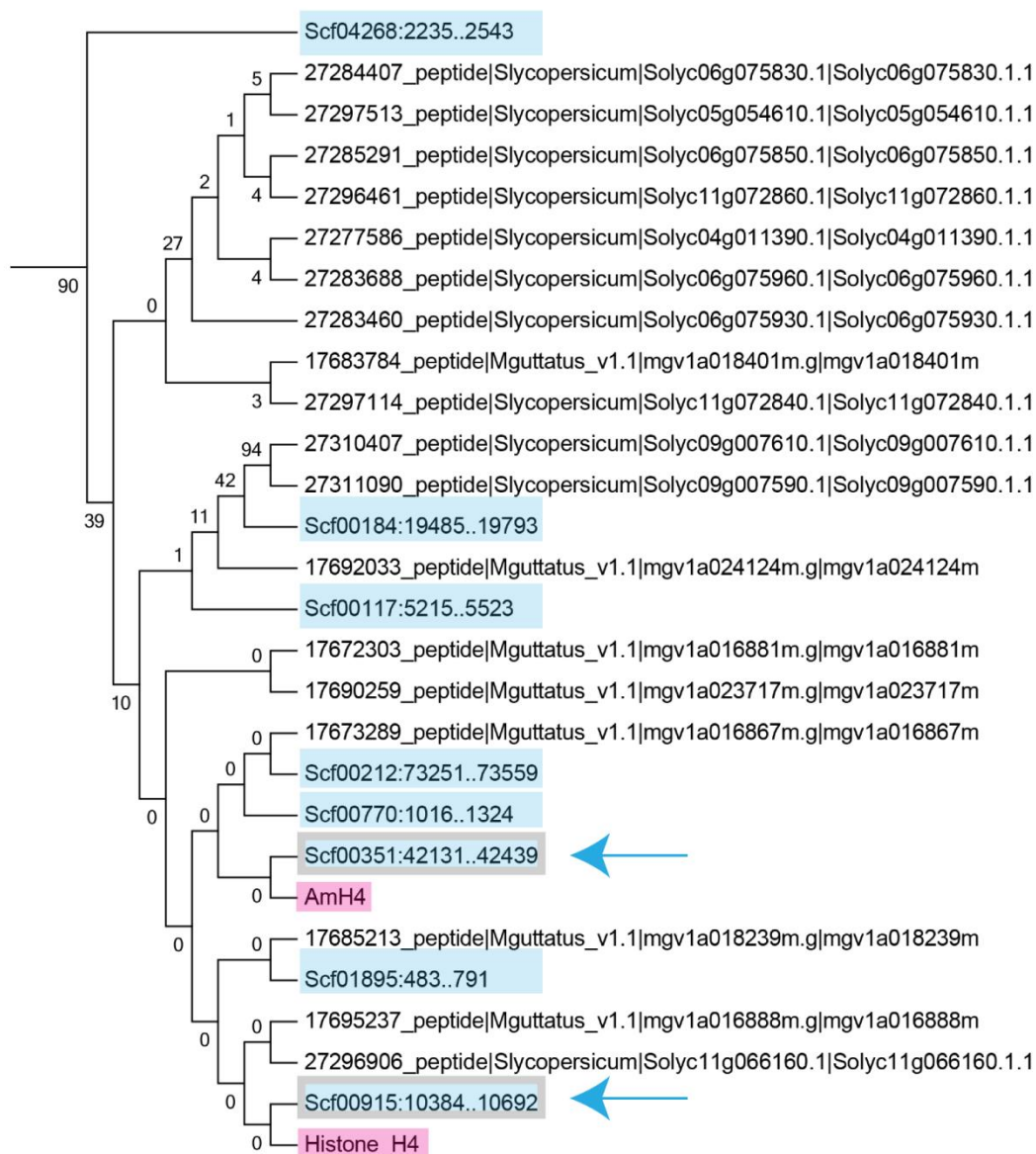
Figure 4.12: Guide phylogenetic tree of H4. Tree was constructed using Mega5. Conserved regions of protein sequence were aligned and a Neighbour-Joining tree was constructed using 500 bootstrap replicas, the Jones-Taylor-Thornton (JTT) model, and pairwise deletion. Eight homologs of H4 are indicated in blue. Blue arrows indicate those homologs used to design probes based on close homology to *Antirrhinum* H4 (AmH4) and *Arabidopsis* H4 (Histone_H4) shown in pink.

Since tissue fixed in FAA gave the most promising results in the first *in situ* experiment, I decided to continue working with this fixative. I tried using longer cycles of vacuum treatment in the vacuum infiltration processor (VIP) machine when embedding samples to see if this would improve the structural preservation of the tissue. I also tried using proteinase K in place of pronase to see if I could obtain a stronger signal and less background. To be sure any signal was real, and to explore where any background may be coming from, I included three separate negative controls; a sense probe which is not complimentary to the target sequence, no probe, and no anti-digoxigenin-AP antibody. The results are shown below (Figure 4.13).

The tissue was more structurally intact than before, indicating that the fixation was more successful. There was very little background signal, with no background observed in any of the negative controls. There is some signal in young bladder tissue and in apex tissue visible (Figure 4.13, Ai & Bi). The expression patterns observed are as expected for H4 which is an S-phase specific marker and is usually expressed in patches similar to that observed (Wu *et al.*, 2005). These results indicate that the tissue is permeable and that protein digestion with proteinase K is successful. Tissue layers also appear more distinct.
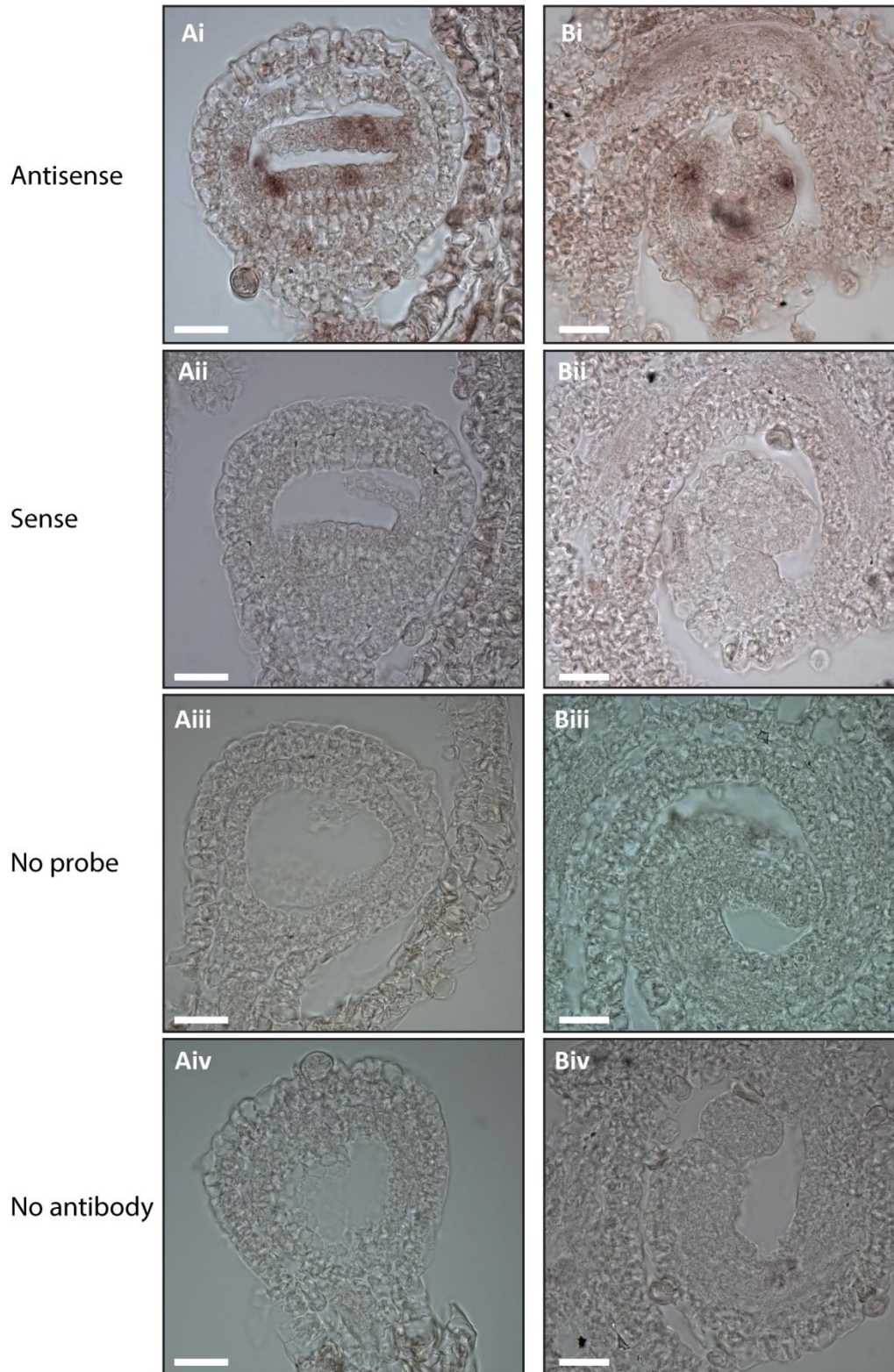
Figure 4.13: Expression of *UgH4* in *U. gibba* bladder and circinnate apex tissue. (A) *U. gibba* bladder sectioned from the back. (B) *U. gibba* circinnate apex tissue. (Ai & Bi) Hybridisation with the *UgH4* antisense probe. (Aii & Bii) Hybridisation with the *UgH4* sense probe (negative control). (Aiii & Biii) Negative control with no probe. (Aiv & Biv) Negative control with no anti-digoxigenin-AP antibody. All scale bars are 20 μm.

4.3 Discussion

4.3.1 Practicalities of *U. gibba* as a model system

4.3.1.1 Propagating *U. gibba* tissue

In this chapter I have presented a number of resources and methods set up for the development of *U. gibba* as a new model system. During this set up, I found the ability to propagate *U. gibba* tissue particularly useful since it allowed me to quickly collect tissue at my convenience for any given experiment. Since bladders of all developmental stages could be found on a single plant at any given time, I was also able to perform large scale tissue collection of bladders for *in situ* hybridisations without the need for mass plant growth.

4.3.1.2 Germination time of U. gibba seeds

One of the main issues with *U. gibba* was the low efficiency at which *U. gibba* seeds would germinate. After exploring a range of treatments and growing conditions, I found that the ethylene releaser, ethephon, could significantly improve *U. gibba* seed germination without affecting seedling morphology. Ethylene has been found to stimulate germination in a number of species, including *Echinacea* (Sari *et al.*, 2001). Endogenous ethylene was found to stimulate or accelerate germination in species such as *Chenopodium album* (Saini *et al.*, 1985), *Amaranthus retroflexus* and aged *Striga lutea* and *Brassica napus* seeds, reviewed by Matilla (2000). The application of ethylene was also found to break heat induced dormancy in lettuce (Stewart & Freebairn, 1969). It has been suggested that ethylene production may be essential for alleviating heat induced dormancy in some seeds. However, the mechanism by which this may work is not understood (Matilla, 2000).

4.3.2 Generating a reference genome for U. gibba

We now have two reference assemblies (the BA assembly sequenced by TGAC, and the LangeBio, published assembly). The published assembly has the advantage that it has a set of predicted genes associated with it. However, the BA assembly is valuable for finding

homologous genes with more sequence similarity to the plant available for tissue collection and experiments. It is useful to use the sequence of the plant we are growing for primer and antibody design to ensure the best sequence match. The BA genome appeared to have a high level of heterozygous content. Future work may therefore include filtering the BA assembly to remove some of this heterozygous content and selfing the BA line through multiple generations to obtain a more homozygous line for sequencing. Furthermore, a higher depth sequencing run could be performed on the BA line to generate a higher quality genome assembly.

4.3.3 *In situ* hybridisations

I made progress with setting up an *in situ* hybridisation protocol that worked in *U. gibba.* I observed promising signal with probes against *UgFIL* and *UgH4.* The use of proteinase K in place of pronase appeared to give cleaner signal, although these have not been tested side by side. I found that fixing tissue in FAA led to better tissue preservation than fixation in paraformaldehyde. This concurs with similar observations made when comparing different fixatives for immunolocalisation in *U. gibba.* However, variability in the success of *in situ* hybridisation suggests that fixation may not always be successful in preserving bladder structure and/or RNA. One possibility for the future is to try alternative fixatives and fixation methods. For example, tissue may be snap frozen and then embedded in a support medium for thin cryosectioning and then rapidly fixed in 4 % paraformaldehyde prior to hybridisation.

Preliminary results indicate that *UgFIL* may be expressed on the outer layer of cells of the *U. gibba* bladder. This agrees with the idea that the outside layer of epiascidiate leaves corresponds to the abaxial surface of a conventional flat leaf, as found in *Nepenthes* and *Sarracenia* (Fukushima & Hasebe, 2014). Future work looking into the expression of surface identity genes in *U. gibba* may also include looking at adaxial specification genes such as *PHABULOSA* (*PHB*) and at abaxial identity genes in the *KANADI* family which are expressed in adaxial domains in both eudicots and monocots, reviewed in (Fukushima & Hasebe, 2014).

4.3.4 Mutagenesis

Mutagenesis of *U. gibba* enabled the setup of the first forward genetic screen in *U. gibba* and this generated some promising, segregating mutants. Since I was able to improve germination over the course of this work, it is also now also possible to perform mutagenesis on seed from *U. gibba* which has the benefit of speeding up the initial process of EMS treatment since thousands of seeds can be readily treated at once without the need to propagate large quantities of tissue afterwards. This high throughput approach should lead to the generation of more mutant phenotypes.

Future work will involve screening the M3 generation (from selfed- M2 plants) to check for segregation of mutant phenotypes in the next generation. One advantage of *U. gibba* is that M2 plants may be kept growing in culture while M3 seedlings are screened. This means that heterozygotes can be identified based on segregation of M3 offspring. Offspring from segregating populations can then be sequenced and the SNPs (single nucleotide polymorphisms) in wild type and mutant plants can be compared. Mapping mutations by sequencing will be made easier by the generation of a linkage map which compiles scaffolds and provides chromosome information.

4.3.5 Summary

Overall, this work provides future researchers working with *U. gibba* with some useful techniques and vital resources for further study of the genetic basis of development in *U. gibba.*

5 Main discussion

5.1 Summary of work

In this work I used an integrative approach to study the development of complex leaf shape in *Utricularia gibba.* I generated models exploring the extent to which specified isotropic and anisotropic growth could account for the shape changes observed in *U. gibba* bladder development. I tested predictions made by these models to arrive at an understanding of the growth mechanisms underlying *U. gibba* bladder development. Overall, I found that specified anisotropic growth, and therefore tissue axiality is required for the development of the *U. gibba* bladder.

5.2 Evidence for specified anisotropy in the *U. gibba* bladder

5.2.1 Evidence for specified anisotropy based on modelling and geometry

In chapter 2, I showed that specified anisotropy is required for the elongation of the chin region of the bladder. A pure specified isotropic growth model could not account for the elongation of the chin region of the bladder: an increase in areal growth rate at chin alone generated a bulbous chin. This bulging of the tissue is caused by the resolution of areal conflict in the canvas, generated by differential areal growth rates in neighbouring regions. When specified anisotropy was included in the model, the chin region was able to elongate without buckling. Not all biological shapes require specified anisotropy to explain their morphogenesis. For example, A model for *Coleochaete scutata* thallus morphogenesis shows how irregularities in shape can be generated through specified isotropic growth when cell wall bending properties are altered, or when cell ablation is used to trigger an outgrowth (Dupuy *et al.*, 2010). Developmental stages of *Marchantia* thallus growth are also captured by a model using isotropic specified growth (Solly, 2015). Models of *U. gibba* bladder development therefore give an important example where specified anisotropy is required for the generation of the final organ shape.

Although development of the bladder chin region required specified anisotropy in the models, I found that using either specified isotropy or specified anisotropy could explain the shape changes observed in the main body of the bladder. This reflects the fact that similar shapes may be generated through specified isotropic or anisotropic growth (Green, 1965) and the resolution of different types of conflicts (Coen & Rebocho, 2016). This is also evident in models exploring embryonic limb bud development where models using specified isotropic growth (Popławski *et al.*, 2007) and specified anisotropic growth (Marcon *et al.*, 2011) have been explored, and only through clonal analysis could local anisotropy be confirmed (Marcon *et al.*, 2011). It was therefore necessary for me to make predictions which could be tested to validate one growth mechanism over another. Through studying clonal patterns on the growing canvas of each model, I found that I could make several predictions that would allow me to distinguish between models based on clone anisotropy, orientation, and size. This highlights a major benefit of modelling to generate hypotheses for biological study with respect to understanding the underlying principles of growth.

5.2.2 Evidence for specified anisotropy based on experimental observations

Sectors in the chin region were anisotropic, with their major axis parallel to the axis between the stalk and mouth. This pattern of anisotropy is consistent with a specified anisotropy model, where sectors are expected to elongate parallel to the orientation of tissue growth. There is anisotropy in the chin region of the bladder at the cellular as well as at the sector level. This is evident when I look at the cell shape in the sectors from the chin region and when I compare the rate of increase in anisotropy per hour in terms of cell number and in terms of the major and minor length (the rate of increase in anisotropy per hour is less in cell number than in sector lengths). At the cell level, this indicates that cells in the chin region are growing and dividing more anisotropically than cells in the rest of the bladder.

When studying the main body of the bladder I found no evidence for increased sector area near the midvein (predicted by the specified isotropic growth model), suggesting that specified anisotropic growth across the bladder is more likely to drive the shape transitions observed. These shape transitions included a greater growth in height relative to width and

a greater growth in depth relative to width. The flattening of the bladder in width is therefore achievable with uniform specified anisotropy and uniform areal growth across the main body of the canvas (excluding the chin region). A similar transition in shape is seen in the fruit of *Capsella rubella* which starts as a cylinder and becomes flattened medially (Eldridge *et al.*, 2016). Modelling suggested a higher relative growth rate parallel to a proximal- distal polarity (K_{par}) at the midvalve regions of the developing *Capsella* gynoecium (Eldridge *et al.*, 2016). The complex 3D transitions in shape of the *U. gibba* bladder and the *C. rubella* gynoecium both require specified anisotropic growth. However, unlike that proposed in the *Capsella* gynoecium, an increase in K_{par} at the midvein of the bladder relative to its sides is not required.

5.3 Polarity as a common mechanism for orienting growth in plants

Specified anisotropic growth requires the presence of tissue axiality so that growth orientations may be specified in relation to a local axis. The model assumes that axiality is based on a polarity system, using a diffusible factor to set up a polarity field across the canvas, against which growth orientations may be specified (Kennaway *et al.*, 2011). I found evidence of tissue polarity in the *U. gibba* bladder through the analysis of the coordinated polarity of quadrifid glands and the localisation of UgPIN1 proteins. This polarity pattern is oriented from the stalk to the mouth of the bladder, concurring with that predicted by bladder models.

The polarity field observed in *U. gibba* may be considered as a proximal-marginal polarity field if we consider the modified peltation theory for the evolution of epiascidiate leaves (Franck, 1976), whereby the mouth of the bladder is equivalent to the margin of a peltate leaf and the petiole is displaced to the centre of the abaxial surface. This proximal-marginal polarity is different form the proximal-distal polarity modelled and experimentally observed in *Arabidopsis thaliana* leaves (Kuchen *et al.*, 2012). This difference may indicate a shift in polarity in the evolution of peltate leaves from conventional flat leaves (proximal-distal to a proximal-marginal polarity) (Figure 5.1). It would therefore be interesting to look for evidence of a proximal-marginal polarity field in peltate leaves and other epiascidiate leaves. The *Arabidopsis* petal also shows some shift in polarity, where there is a divergence

of polarity at the distal end of the petal rather than a convergence point at the tip. This polarity field may be an intermediate case, where a divergent polarity field is thought to arise through a broad minus organiser along the distal margin of the developing petal (Sauret-Güeto *et al.*, 2013).
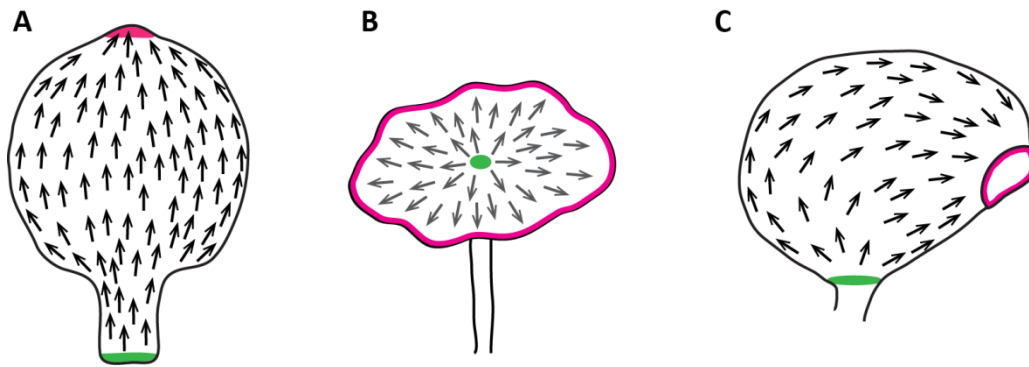
Figure 5.1: Polarity in conventional flat, peltate, and epiascidiate leaves. (A) Proximal-distal polarity in an *Arabidopsis* conventional flat leaf (Kuchen *et al.*, 2012). (B) Hypothesised proximal-marginal polarity of a peltate leaf. (C) Proximal-marginal polarity in a *Utricularia gibba* epiascidiate leaf. A plus (green) and minus (pink) organiser of polarity is shown in each case.

I found evidence of UgPIN1 polarity in the chin and threshold regions of the bladder which was consistent with the stalk-mouth polarity predicted by the model and observed with the quadrifid glands. This observation supports the idea that polarity fields (polarity-based axiality) may be established at the cellular level through the asymmetric cellular localisation of PIN auxin transporters (Abley *et al.*, 2016). Models using the feedback of averaged residual stresses have been able to generate tissue axiality (in an alternative stress-based axiality model). However, the mechanism behind the sensing of average stresses across a tissue is unknown (Hervieux *et al.*, 2016). Another stress-based axiality model treats meristem tissue as a pressurised cylinder which is under tension and inflated by an inner pressure. This model has geometric induced stresses which are higher in the circumferential direction than along the meridian (Hamant *et al.*, 2008). At maturity, the bladder is under negative pressure (is under constriction) (Llorens *et al.*, 2012). It is unclear at which point in development this negative pressure begins to act and what role it may play in generating stresses in the developing tissue. It would be interesting to explore the pressure at early stages of bladder development and implement this pressure in stress-based models and compare resultant models to the observed tissue growth dynamics.

5.4 A means to generate *Utricularia* trap diversity

The traps of different *Utricularia* species show a great degree of variation in their morphology and several features can be used for species identification. One feature is the position of the mouth relative to the stalk (Rutishauser & Brugger, 1992; Taylor, 1994). The mouth position in *Utricularia* species can be either basal (adjacent to the stalk), terminal (opposite to the stalk), or lateral (in an intermediate position) (Taylor, 1994). Examples of *Utricularia* species with these mouth positions are shown in Figure 5.2. Examples of each case are present in both terrestrial and aquatic species (Rutishauser & Brugger, 1992; Taylor, 1994).

Basal mouth

Lateral mouth

Terminal mouth

U. endresii

U. gibba

U. sandersonii

U. nephrophylla

U. minor

U. antennifera

U. reniformis

U. perversa

U. triloba

U. warmingii

U. naviculata

U. cucullata
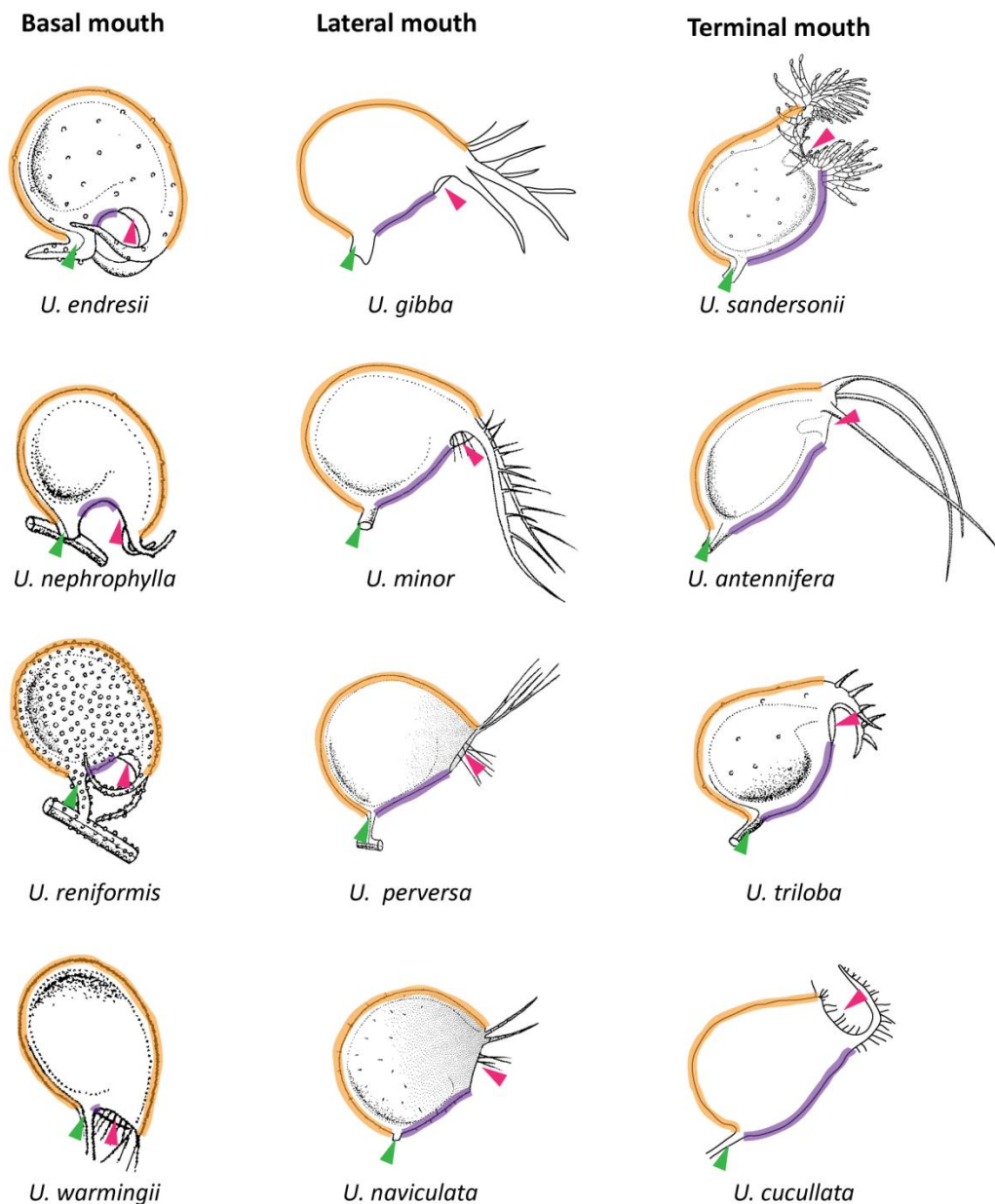
Figure 5.2: Mouth position in different *Utricularia* species. Examples of *Utricularia* species exhibiting different mouth positions where the mouth is either basal (adjacent to the stalk), lateral (intermediate position), or terminal (opposite to the stalk). The stalk (green arrowhead), mouth (pink arrowhead), chin (purple line), and back (orange line) regions of each bladder are shown. Images are not to scale. Images are adapted from drawings from Taylor (1994).

I found that specified anisotropic growth was essential for obtaining elongation of the chin region and therefore the displacement of the mouth relative to the stalk. When modelling, I found that the length of the chin region could easily be altered by changing the degree of specified anisotropy and areal growth rate at chin. Diversity in bladder morphology could

therefore be accounted for by the relative levels of specified anisotropy in the chin and back regions (Figure 5.2, purple and orange lines). At very early stages, the mouth positioning on the primordia of *U. livida* (exhibiting a terminal mouth at maturity) appears to be similar to that observed in *U. gibba* (exhibiting a lateral mouth at maturity) (Rutishauser & Brugger, 1992). Both start with a mouth slit forming at approximately 90 ° to the primordial stalk. This similarity in initial mouth position on two bladders which exhibit different mouth positions at maturity suggests that the initial position of the mouth indentation may be similar for each type of bladder and that differential growth after this controls the final position of the mouth relative to the stalk. This requirement for differential growth indicates that specified anisotropy is required in each case, because differential areal growth alone is not sufficient to displace the mouth and stalk. Some *Utricularia* species are dimorphic*,* exhibiting bladders which differ morphologically in the positioning of the mouth. For example, *U. hydrocarpa* and *U. vulgaris* possess bladders with a lateral mouth and bladders with a basal mouth, indicating that a simple underlying mechanism could account for the control of chin length. It would be interesting to compare the two bladder types from each plant, possibly by using RNA sequencing which may help to identify genetic regulators in chin length.

There are other cases where variations in the final shape of a plant organ are due to differences in relative dimensional growth at later stages of development. For example, shape differences in acutely lobed, roundly lobed, and orbicular peltate leaves of *Tropaeolum* are due to differential growth in the lobes and sinuses and each mature leaf shape begins with the same initial shape (Whaley & Whaley, 1942).

5.5 Other epiascidiate leaves

The primordia of other epiascidiate leaves have a similar structure to that of *Utricularia.* For example, the primordium of *Sarracenia* is a flattened structure which develops a hollow on the adaxial side of the primordium, above the adaxial ridge. Growth in the margin and the adaxial ridge generates a hollow structure in the distal portion of the primordium and continued growth forms the pitcher shape (Fukushima *et al.*, 2015). The formation of a tube in this way is similar to the growth of the chin and back region in *U. gibba*. Similar factors may control the growth of pitcher shapes through specified anisotropic growth. It

would be interesting to model shape transitions in other epiascidiate leaves to see to what extent specified isotropic growth can account for different epiascidiate leaf shapes or whether specified anisotropy is required in each case.

5.6 Future directions

5.6.1 Testing the models further

The work described in this thesis has developed hypotheses for bladder development and evolution through computational modelling and experiments. I found that the development of the bladder shape requires specified anisotropic growth. Future work will include collecting more sector data at the chin region of the bladder to complete the current data set and confirm growth rates and orientations in the live system. Tracking experiments and cell segmentation analysis could also be used to analyse cell shape across the bladder, for a more accurate calculation of the rate of increase in anisotropy per hour (currently, these calculations assume cells are isotropic at the time of heat shock). This is difficult to verify in the chin region, since the bladder is tightly wrapped up. Dissection of the antennae and mouth region may be necessary to study this in more detail.

Future work will also involve confirming the polarity pattern in the chin region by using confocal microscopy to analyse the polarity of quadrifid glands in the chin region, as this region often had bad resolution in the OPT scans. More work looking at the localisation of UgPIN1 across the bladder would also be useful to validate the preliminary results presented here. This may include further optimisation of the immunolocalisation protocol, for example trying cryofixation, purification of antibodies, and the exploration of transgenic lines expressing fluorescent proteins under UgPIN1 promoters. One challenge associated with this work is the fact that young bladder stages are found wrapped up in the circinnate apex of growing stolons. A possible solution is to look into terrestrial species of *Utricularia* such as *U. livida* and *U. bisquamata* in which bladders develop on stolons without a circinnate apex, making them more easily accessible to study.

5.6.2 Elucidating the genetic basis of bladder growth

A key question is how genes control the factors in the model. In the modelling framework, factors that control growth and polarity are generalised, abstracting from specific genetic components. This allowed me to explore the core mechanisms controlling bladder shape without the complication of genetic interactions. There are no published studies on the genetic pathways that control bladder development and so genetic interactions would need to be based on studies done in *Arabidopsis*. A key area of the model is the chin region. Since there are no published gene expression patterns in *U. gibba*, there are no clear candidate genes that could carry out the role of the CHIN factor. Future work may include identifying such genes by comparative RNA sequencing, comparing the chin region of the bladder to the main body of the bladder following microdissection as well as comparative studies between different bladder types on dimorphic species which exhibit bladders with lateral and basal mouths. Mutants with a truncated or elongated chin region may also be identified through further mutant screens and subsequent sequencing could be used to identify candidate genes responsible for controlling increased growth parallel to the polarity field here. Cell wall modifying enzymes such as expansins which loosen the cell wall or pectin methylesterases (PMEs) which alter the rigidity of the cell wall (McQueen-Mason *et al.*, 1992; Cosgrove *et al.*, 2002; Bosch *et al.*, 2005) may be important for the elongation of the chin region at the cellular level where I see longer and thinner cells compared to the rest of the tissue.

Other candidate genes for bladder shape development include homologs of *Arabidopsis ROT3* and *AN* which regulate growth rates in the proximal-distal and mediolateral axis of the *Arabidopsis* leaf respectively (Tsuge *et al.*, 1996; Kim *et al.*, 1999). Generating knock out mutants of these genes in *U. gibba* may produce plants with more or less elongated bladders if these genes play a role in specifying growth rates parallel and perpendicular to the axis of polarity. It is unclear how they may function in the context of a proximal-marginal polarity as opposed to a proximal-distal polarity.

The expression of candidate organiser genes such as *CUC, AUX, LAX* and *YUCCA* may be explored using fluorescent reporter constructs or *in situ* hybridisation. This would give further evidence for a polarity based axiality system where I would expect auxin biosynthesis genes such as *YUCCAs,* and *CUC* which is expressed at the base of the *Arabidopsis* leaf, to be expressed near the stalk intersect, and auxin importers such as *AUX*

and *LAX* to be expressed near the mouth of the bladder. It would also be interesting to explore the expression of these candidates in peltate leaves to test the hypothesis that peltate leaves may have a proximal-marginal polarity.

Broader approaches may also be taken to find candidate genes. For example, it may be interesting to perform comparative RNA sequencing on the bladderless mutant identified in the mutagenesis screen and its wild type sibling. Microdissection of very young bladders may also allow RNA sequencing of a developmental series of younger bladders or of specific regions of bladders, such as the chin.

5.6.3 Exploring the early stages of bladder development

In this work I have focussed on the *U. gibba* bladder shape transitions that occur between the 82 μm stage and maturity. It would be interesting to explore the earlier stages of bladder development to better understand epiascidiate leaf development from the primordium. For this work, it may also be useful to also explore terrestrial species mentioned above, in which the bladders develop on stolons without a circinnate apex, making them more accessible to tracking, whole-mount immunolocalisation and *in situ* studies. However, the genome sizes of these species are larger: 239 Mbp and 308 Mbp for *U. livida* and *U. bisquamata* respectively (Veleba *et al.*, 2014), and protocols for key methods such as transformation would need to be investigated.

5.7 Concluding remarks

I have characterised the main stages of growth in a new model system, *Utricularia gibba,* and have used this information to generate models of bladder growth, exploring the extent to which specified isotropic and specified anisotropic growth can account for bladder shape. I have tested predictions made by these models, by performing sector analysis and by finding evidence of tissue cell polarity in the bladder. Through this analysis I have arrived at a model of bladder development which uses specified anisotropic growth across the bladder. I have developed a number of techniques and resources which support *U. gibba* as a new model system. Using this ground work and further predictions made by the model, it should be possible to identify key genes involved in the development of bladder shape. This work shows how different specified growth patterns can be explored using computational

modelling and how these models are able to make a number of predictions in relation to resultant growth patterns. These resultant growth patterns can be tested in the biological system to distinguish between models and therefore provide an understanding of the specified growth patterns underlying the generation of an organ shape. This allows the exploration of specified growth dynamics within connected tissue which are not intuitive. More generally, this work supports the hypothesis that plant growth and development is based on orienting growth against a polarity field which may have a similar molecular mechanism across plants.

6   Materials and methods

6.1   Plant material and growth

6.1.1   Tissue culture

Plant material was grown in liquid MS plant tissue culture media (0.22 % Murashige and Skoog Medium (Duchefa Biochemie M0233), 2.5 % sucrose, pH 5.8) and maintained (in culture) in a controlled environment room at 25 °C long day conditions (16 hours light/ 8 hours dark cycles).

6.1.2   Glasshouse conditions

Plant material was grown in the glasshouse to induce flowering for seed collection. Plants were grown in containers containing a 2 cm layer of sphagnum moss and sand mix, topped up with reverse osmosis water.

6.1.3   Seed sterilisation

Utricularia gibba seeds were washed for 5 minutes in 70 % ethanol, 0.1 % SDS, followed by a wash in sterile water. Seeds were then transferred to 4 % Parazone bleach, 0.2 % triton 100 for 10 minutes and then washed 3 times with sterile water.

6.1.4   Seed germination

Seeds were sown in pots containing a layer of solid culture medium (0.22 % Murashige and Skoog Medium (Duchefa Biochemie M0233), 2.5 % sucrose, 0.3 % agar, pH 5.8) topped up with liquid MS culture medium containing 0.1 mM ethephon (Sigma C0143). To make ethephon containing media, a concentrated 2.5 M ethephon solution was first made in a

pH 3 buffer (41 mM disodium hydrogen phosphate, 79 mM citric acid) and then diluted in liquid media to a final concentration of 0.1 mM ethephon. Seedlings were germinated at 25 °C long day conditions (16 hours light/8 hours dark cycles). Once seeds had germinated, seedlings were removed from ethephon containing media and grown in MS liquid media as described above.

6.1.5 Time course of *U. gibba* bladder growth

U. gibba stolons were embedded in low melting point agarose and then covered with liquid MS medium. Plants were kept sterile in a closed petri dish sealed with micropore tape and grown at 25 °C long day cycles. Each bladder was imaged every 24 hours by light microscopy, keeping track of the position of each bladder by imaging the whole plate for reference. Growing bladders were imaged until they reached maturity or until they were no longer visible due to other tissue growing over them. Measurements were made from the antennae to the furthest point on the back of the bladder (bladder length). At some time points bladders twisted and turned out of view in the media and so a measurement could not be made. Growth arrest occurred in bladders which were close to the cut edge of a stolon, so only bladders which were near growing tips were included for analysis. Length measurements were used to place each data set on a normalised timescale of development to overcome different starting sizes of bladders.

6.2 General methods

6.2.1 Searching for homologous genes in *U. gibba*

Sequences of candidate genes/proteins from *Arabidopsis thaliana* were found by searching the NCBI database (http://www.ncbi.nlm.nih.gov/). A *tblastn* (protein to translated nucleotide) query was then performed against the published (LangeBio) *U. gibba* genome (Ibarra-Laclette *et al.*, 2013) and the genome of the Bergh Apton (BA) line sequenced in our lab. Browsers with BLAST functionality for each genome were made by TGAC and can be found at:

Langbio: http://tgac-browser.tgac.ac.uk/ugibba_langbio/

BA: http://tgac-browser.tgac.ac.uk/ugibba_tgac/

Sequences were obtained from the published LangeBio genome in the following way: the scaffold position obtained from the above BLAST search the browser above (e.g. Scf00203:12578..15717) was entered into a Jbrowse browser to find the predicted gene number. Sequence information was then obtained by selecting the predicted gene region and selecting 'view details'. The Jbrowse browser can be found at:

http://apollo.tgac.ac.uk/Utricularia_gibba_4_1_19475_browser

Sequence information in the BA line was obtained by searching for the relevant scaffold (based on the scaffold number given in the BLAST search) and performing BLAST searches using the scaffold sequence in general databases such as those found at NCBI. Exons were then predicted based on alignments with relevant hits. This generated a predicted coding sequence which could be confirmed by sequencing.

Sequences from *U. gibba* with good homology were used in a *blastx* (translated nucleotide to protein) against the UniProtKB/Swiss-Prot(swissprot) database within NCBI to check that the hits returned were the protein of interest. Reciprocal blast searches were performed with the best hit.

6.2.2 Propidium iodide staining

6.2.2.1 Propidium iodide staining for optical projection tomography

The propidium iodide staining protocol for whole-mount imaging (Truernit *et al.*, 2008) was followed to stain *U. gibba* bladders and circinnate apexes for Optical Projection Tomography (OPT).

Tissue was fixed in pre-cooled 50 % methanol, 10 % acetic acid and stored at 4 $^{\circ}$C for up to 1 month. Samples were then washed with water twice before being dehydrated to 80 %

ethanol through 40 %, 60 %, 80 % Ethanol (x 2 each). Tissue was then incubated in an 80 °C water bath for 10 minutes, followed by rehydration through 60 %, 40 %, 20 % ethanol, water (x2 each). Samples were incubated for 12 hours in alpha-amylase solution (20mM sodium phosphate buffer, (pH7), 2 mM NaCl, 0.25 mM CaCl$_2$, 0.3mg/ml alpha-amylase from *Bacillus licheniformis* (Sigma Aldrich A4551) at 37°C. Samples were washed with water (x 3) and incubated with 1 % periodic acid (Sigma Aldrich, 3951) for 1 hour at room temperature in the fume hood. Tissue was washed again with water (x 2) and then incubated with Shiff reagent with propidium iodide (100mM sodium metabisulphite and 0.15M HCl; propidium iodide to a final concentration of 100 mg/mL) for 2 hours. Samples were washed with water (x2) and then kept in water at 4 °C overnight.

6.2.2.2 Propidium iodide staining for confocal imaging

Samples were treated as above for OPT with the following extra steps. After the final water wash, tissue was mounted onto glass coverslips with added Frame-Seal Incubation Chambers (BIO-RAD, SLF0601). A drop of ½ chloral hydrate solution was added to cover the tissue and samples were incubated over night at room temperature. Excess chloral hydrate was removed and samples were correctly spaced on the cover slip. Samples were mounted in Hoyer's solution and a slide was placed on top to ensure samples were close to the coverslip for imaging.

6.2.3 Optical projection tomography

 OPT was performed by Karen Lee using the protocol published in (Lee *et al.*, 2006). Visualisation of OPT scans was achieved using a freely available software package VolViewer which enables interaction of volumes in 3D and is available at http://cmpdartsvr3.cmp.uea.ac.uk/wiki/BanghamLab/index.php/VolViewer#Description.

6.2.4 *U. gibba* DNA extraction

6.2.4.1 DNA extraction

gDNA was extracted from *U. gibba* using the DNeasy Plant Mini Kit (Qiagen, 69104) following the manufacturers protocol. Excess liquid media was removed from *U. gibba* tissue using clean paper towels. Tissue was then frozen in liquid nitrogen and ground to a fine powder in liquid nitrogen using a pre-cooled pestle and mortar. A 1.5 ml microfuge tube was then filled to the 0.25 ml mark with ground tissue and 400 μl of Buffer AP1 and 4 μl RNase A was added to the tissue. Samples were vortexed and then incubated at 65 °C for 10 minutes. Next, 130 μl Buffer P3 was added and samples were incubated for 5 minutes on ice, followed by centrifugation at 16, 500 x g for 5 minutes. The lysate was pipetted into a QIAshredder spin column placed in a 2 ml collection tube and samples were then centrifuged for 2 min at 14,000 rpm. The flow-through was transferred to a new tube and 1.5 volumes of Buffer AW1 was added and mixed by pipetting. Next, 650 μl of the mixture was transferred into a DNeasy Mini spin column placed in a 2 ml collection tube and samples were centrifuged for 1 minute at 8000 rpm. The flow through was discarded and this stepwas repeated with the remaining sample. The column was then washed with 500 μl Buffer AW2 and centrifuges at 8000 rpm (this was done twice). DNA was eluted in 100 μl buffer AE which was added to the column followed by incubation at room temperature for 5 minutes and then centrifuged for 1 minute. The elution was passed through the column a second time to obtain higher concentrations of DNA.

6.2.4.2 DNA extraction for whole genome sequencing

gDNA was extracted from *U. gibba* plants for sequencing using the DNeasy Plant Maxi Kit (Qiagen, 68163). Excess liquid media was removed from *U. gibba* tissue using clean paper towels. Tissue was then frozen in liquid nitrogen and ground to a fine powder in liquid nitrogen using a pre-cooled pestle and mortar. A 50 ml centrifuge tube was filled to the 5 ml mark with crushed tissue and 5 ml preheated Buffer AP1 and 10 μl RNase A were added to the tube. Samples were vortexed vigorously until no tissue clumps were visible and then incubated for 10 minutes at 65 °C. During incubation, tubes were inverted several times. The protocol was then followed as per the manufacturer's instructions. DNA was eluted in

500 µl buffer AE which was passed through the column twice. DNA was then precipitated by adding 2 volumes of 100 % EtOH and 1/10 volume 3 M NaAc. Samples were incubated for 30 minutes at -20 °C and then centrifuged at 20,000 x g for 5 minutes at 4 °C. The supernatant was then discarded and the pellet was washed with 800 µl 70 % EtOH by gentle pipetting. Samples were centrifuged again for 5 minutes and the EtOH was removed carefully. Another wash with 70 % EtOH was performed, samples were centrifuged and the EtOH was removed. The pellet was left for the EtOH to evaporate and then resuspended in 100 µl H_2O.

6.2.5 *U. gibba* RNA extraction

U. gibba material was collected from plants grown in culture. Excess liquid media was removed using clean paper towel. Material was then frozen in liquid nitrogen before being crushed to a fine powder in liquid nitrogen using a pre-cooled pestle and mortar. A pre-cooled microcentrifuge tube was filled to the 0.1 ml mark with crushed tissue and RNA was extracted using the RNeasy Plant Mini Kit (Qiagen, 74904) following the manufacturer's instructions. On-column DNase digestion was performed. RNA was eluted in 30 µl RNase-free water which was passed through the column twice.

6.2.6 cDNA synthesis

cDNA was synthesised from *U. gibba* RNA using the SuperScript® III First-Strand Synthesis System kit (Invitrogen, 18080051) as per the manufacturer's instructions. Incubations were carried out on a G-STORM® Thermocycler (GT40361).

 A 10 µl reaction containing 1 µg RNA, 0.5 µl B26 oligo(dT) + adapter primer (100 µM stock), 1 µl 10 mM dNTP mix, and DEPC-treated water up to 10 µl, was incubated at 65 °C for 5 minutes and then transferred to ice for 1 minute. A cDNA synthesis mix was then prepared as stated in the manufacture's protocol. The RNA/primer mix was added to 10 µl of cDNA synthesis mix and incubated at 50 °C for 50 minutes. The reaction was terminated at 85 °C and then chilled on ice. Each tube was then incubated with 1 µl of RNase H at 37 °C for 20 minutes. Once complete, 10 µl of the cDNA synthesis reaction was taken and added to 90

µl H_2O and stored at -20 ^{o}C. The remaining cDNA synthesis reaction was stored at -80 ^{o}C for later use.

6.2.7 Polymerase chain reaction (PCR)

PCR reactions were carried out using the Taq DNA Polymerase kit (Qiagen, 201205). A 20 µl reaction was set up containing 1x PCR buffer, 200 µM of each dNTP, 5 mM of each primer, 1-500 ng template DNA, plasmid or cDNA, 2 units Taq DNA polymerase. A standard PCR program was used as follows; 94 ^{o}C for 3 minutes, followed by 35 cycles of 94 ^{o}C for 1 minute, 58 ^{o}C for 1 minute (annealing temperature), and 72 ^{o}C for 1 minute (extension time). Then a single step of 72 ^{o}C for 10 minutes and a hold step at 12 ^{o}C. The annealing temperature and elongation time were altered according to primer melting point and length of target respectively. Annealing temperature was set to approximately 5 ^{o}C below the T_m of the primers. Extension time was set to 1 minute per kb of DNA. All PCR reactions were carried out on a G-STORM® Thermocycler (GT40361). Amplified products were analysed via 1 % agarose gel electrophoresis.

6.2.7.1 Colony PCR

Single colonies were picked using a sterile p2 tip. The tip was then touched in the bottom of a dry microcentrifuge tube and 10 µl sterile H_2O was added. The sample was then incubated at 99 ^{o}C for 10 minutes. The colony PCR reaction was then set up using the mix as described for PCR above with 1 µl colony/H_2O mix in place of DNA. A PCR program was used as described for PCR above.

6.2.8 Transformation of *E. coli* cells

One Shot® TOP10 chemically competent *E. coli* (Invitrogen, C4040) were used. Cells were thawed on ice and then 2 µl of plasmid was added to 20 µl of cells. The reaction was incubated on ice for 10 minutes and then transferred to a 42 ^{o}C water bath for a 30 second heat shock. The reaction was returned to ice for 2 minutes and then 250 µl SOC medium (Invitrogen, 2 % Tryptone, 0.5 % Yeast Extract, 10 mM NaCl, 2.5 mM KCL, 10 mM $MgCl_2$, 10

mM MgSO$_4$, 20 mM glucose) was added. Transformed cells were then incubated for 1 hour at 37 ^{o}C and plated on selective LB (lysogeny broth) media for growth overnight at 37 ^{o}C.

6.2.9 Plasmid preparation

Plasmids were purified from 6 ml of overnight liquid *E. coli* culture using the QIAprep® Spin Miniprep kit (Qiagen, 27106) according to the manufacturer's protocol. Plasmid DNA was eluted in 50 µl of elution buffer which was passed through the column twice. The plasmid concentration was measured using a NanoDrop 1000 spectrophotometer (Thermo Scientific) as per the manufacturer's instructions.

6.2.10 Sequencing reactions

Sequencing reactions of plasmids were carried out using the BigDye® Terminator v3.1 Cycle Sequencing Kit (Thermo Fisher Scientific, 4337455). A 10 µl reaction was set up with 2 µl ready reaction mix (BigDye v 3.1), 1 µl Big Dye sequencing buffer, 1 µl of 5 mM primer, 500 ng plasmid, up to 10 µl with H$_2$O. Amplification was carried out using the following cycles on a G-STORM® Thermocycler (GT40361); 96 ^{o}C for 60 seconds, followed by 25 cycles of 96 ^{o}C for 10 seconds, 55 ^{o}C for 10 seconds, 60 ^{o}C for 4 minutes, followed by a hold step at 12 ^{o}C. Reactions were sent to Eurofins Genomics for sequencing.

6.3 Generating a heat shock inducible sector line in *U. gibba*

6.3.1 Golden Gate cloning

A construct for the heat shock inducible line was produced using Golden Gate assembly (Weber *et al.*, 2011) in collaboration with Annis Richardson, Samantha Fox, and Chris Whitewoods. Golden Gate cloning uses a modular approach which allows for flexible stacking of large gene constructs into a single binary transformation vector (Engler *et al.*, 2014). Cloning starts with basic modules (promoters - P, 5' UTR - U, signal peptides - S, coding sequences - C, and terminators - T) termed level 0 (L0). These L0 components are

combined to make transcriptional units (L1 modules), which are then combined to make multigene constructs (L2 constructs) which can be transformed into the plant. The system is based on the fact that bacterial type IIS endonuclease restriction enzymes BsaI, BpiI and ESp3l can cut downstream of their recognition sites. In Golden Gate, specific sequences are placed at the cut sites to generate known overhangs which are specific to individual modules. This means that modules may be ligated by T4 ligase in a specific, predetermined order (Weber *et al.*, 2011).

The final construct consists of an NPTII (neomycin phosphotransferase II) cassette conferring kanamycin resistance (position 1), a Cre recombinase under a heat shock inducible promoter (position 2), an mCherry coding sequence flanked by two loxP sites and under a 35S promoter, followed by an eGFP coding sequence (position 3), and an end linker (Figure 6.1). This construct will be referred to as EC71194.
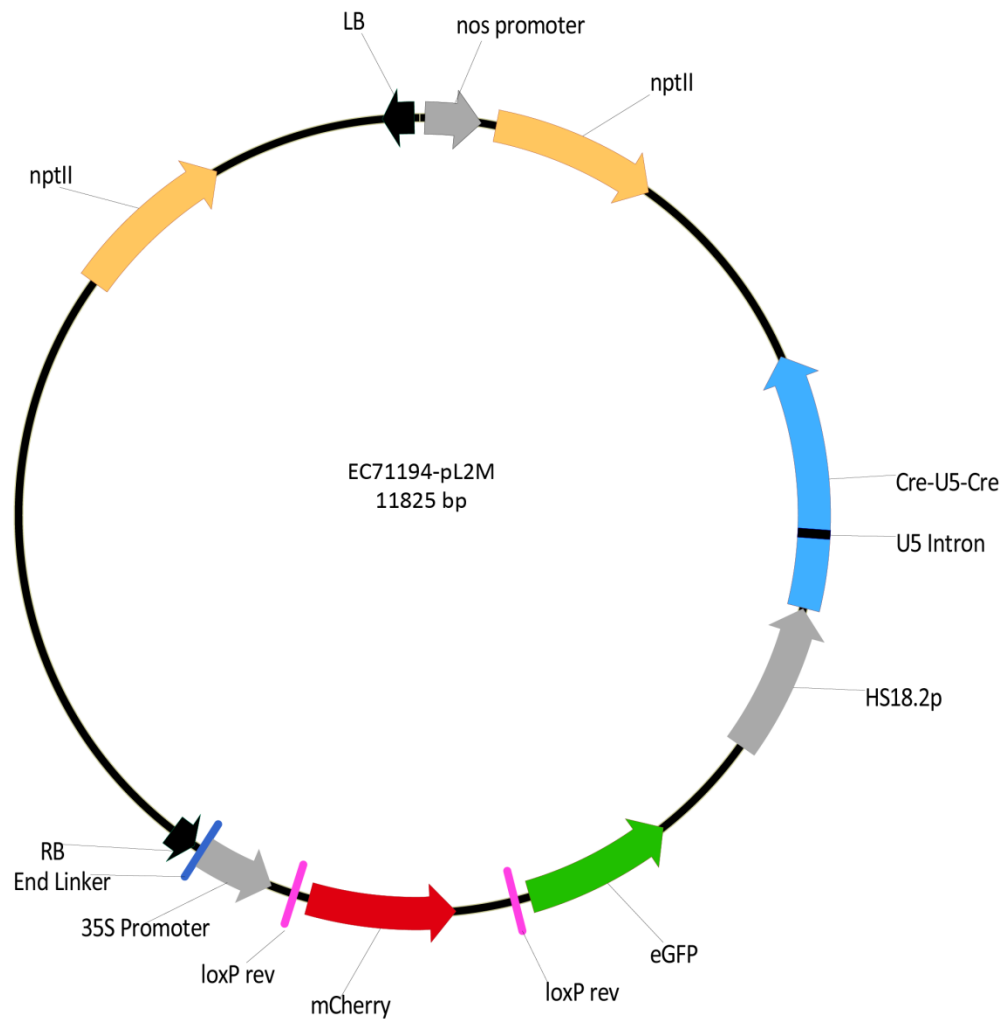
Figure 6.1: Construct for the heat shock inducible sector line (construct EC71194). The construct consists of The L2 backbone vector (pAGM4723-1) containing a kanamycin bacterial resistance cassette (nptII). The left and right boarders (LB and RB) are indicated. These regions are where transfer into the plant is initiated and terminated. The information transferred to the plant includes an nptII cassette conferring kanamycin resistance (orange), a Cre recombinase under a heat shock inducible promoter (blue) (which has a U5 intron inserted- black), an mCherry coding sequence (red) flanked by two loxP sites (pink) and under a 35S promoter (grey), followed by an eGFP coding sequence (green) and an end linker (dark blue).
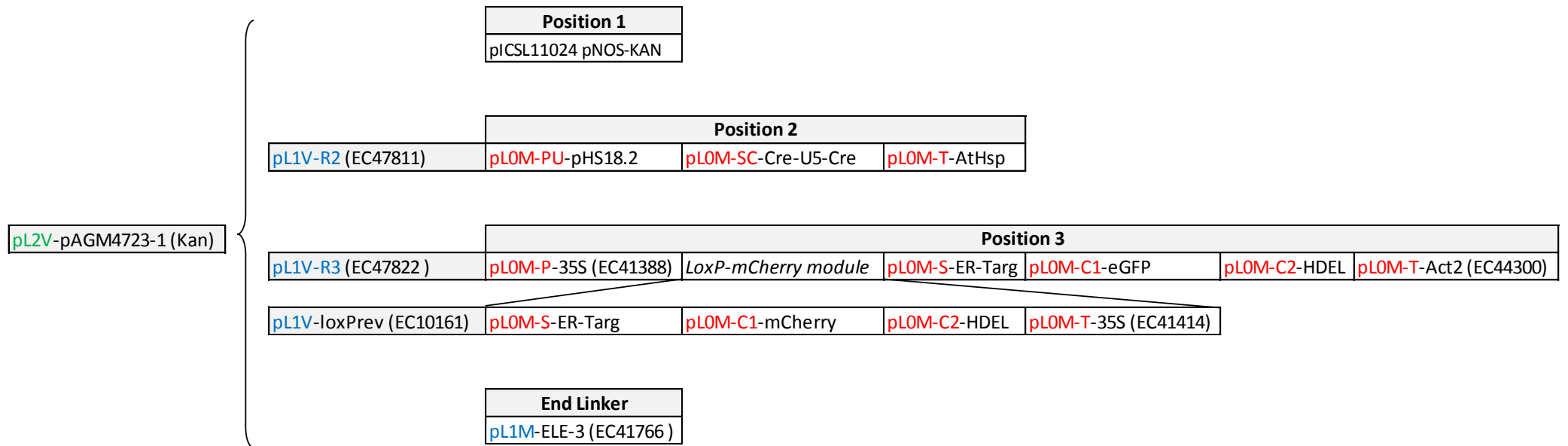
Figure 6.2: Heat shock inducible sector construct components. The pAGM4723-1 backbone vector was used. Components that make up the final level 2 (L2) construct are indicated. Positions 1-3 and the end linker are level 1 (L1) modules which are assembled from L0 components on individual backbone vectors. pL0M (red) indicates plasmid level 0 components, pL1V (blue) indicates plasmid level 1 modules, and pL2V (green) indicates the final level 2 construct. The 'P, U, S, C, T' nomenclature refers to that explained in (Weber *et al.*, 2011). An additional step was required to generate the *LoxP-mCherry module.*

An outline of the components used in the creation of the construct is shown in Figure 6.2 and details are as follows. The L2 backbone vector (pAGM4723-1) containing a kanamycin bacterial resistance cassette, and the L1 module NPTII plant resistance cassette (pICSL11024 (pICH47732::NOSp-NPTII-OCST)) placed in position 1, were obtained from The Sainsbury Laboratory (TSL) (http://synbio.tsl.ac.uk/). The remaining L1 modules were assembled using a protocol modified from (Weber *et al.*, 2011); as detailed below, 'P, U, S, C, T' nomenclature refers to that explained in (Weber *et al.*, 2011).

In position 2, the *heat shock protein 18.2* (*HS18.2*) promoter- PU unit, was fused to a Cre-U5-Cre coding sequence- CS unit, followed by the *HS18.2* terminator from *Arabidopsis*. A U5 intron from the *A. thaliana* U5 small nuclear ribonucleoprotein component (Engler *et al.*, 2014) was included in the Cre coding sequence to prevent it being expressed and recombining during heat shock bacterial transformation. The position 2 components were assembled on a pL1V-R2-47811 backbone obtained from ENSA.

In position 3, a 35S promoter - P unit, was fused to a loxP-mCherry module – U unit (see below for details), followed by an ER targeting signal sequence- S unit, an eGFP coding sequence – C1 unit, an ER retention signal (HDEL) sequence – C2 unit, and an Actin 2 terminator –T unit. The position 3 components were assembled on a pL1V-R3-10161 backbone obtained from ENSA.

The loxP-mCherry module, was assembled in an additional step where we cloned an ER targeting signal sequence- S unit, followed by an mCherry coding sequence – C1 unit, an ER retention signal (HDEL) sequence – C2 unit, and a 35S terminator – T unit, between two loxP sites that were previously added to a pL1V backbone. This is detailed further in (Richardson, 2015).

Finally, an ELE end linker was obtained from ENSA, John Innes Centre, Norwich (pL1M-ELE-3-41766).

6.3.2 Testing the transgenic lines

6.3.2.1 Screening for expression of GFP and mCherry before heat shock

Lines were screened for GFP and mCherry fluorescence and any lines which had GFP fluorescence before heat shock were discarded (Figure 6.3).
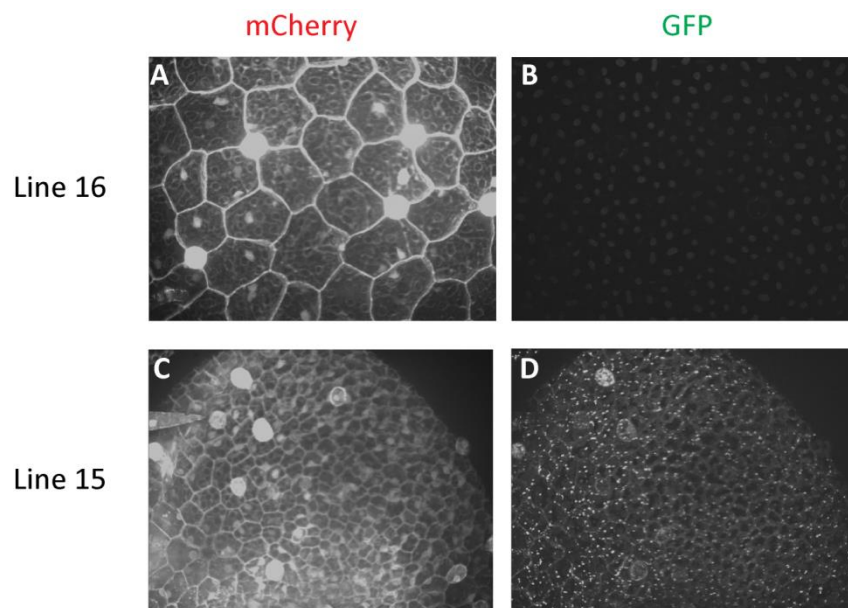
Figure 6.3: Screening heat shock inducible lines for mCherry and GFP expression before heat shock. Example tissue is shown for lines 16 (A-B) and 15 (C-D). Line 16 shows mCherry signal (A) and not GFP signal (B) before heat shock. Line 15 shows mCherry (C) and GFP (D) signal before heat shock. Images are not to scale.

6.3.2.2 Single copy analysis

Single copy analysis was performed by iDnaGENETICS, Norwich. Samples were analysed by qPCR using a multiplexed taqMan reaction assaying for *NPT2* and the 35S promoter. A single copy positive control gene, *CNX3* (cofactor of nitrate reductase and xanthine dehydrogenase), was also used. *CNX3* was reported to be single copy in *U. gibba* (Ibarra-Laclette *et al.*, 2013) and this was confirmed by BLAST analysis within the TGAC and LangeBio genome assemblies. This procedure allows the identification of single copy transgenic plants in the first generation. The results of this analysis are shown in Table 6-1.

Numbers less than 1 may be due to chimeric plants. Plants from each line were put in the glasshouse for flowering so that the next generation could also be screened. No plants had produced seed at the time this thesis was written.

Table 6-1: Single copy analysis results.

Line	Copies *NPT2*	Copies 35S
EC71194-1	0	0.25
EC71194-2	1.5	1
EC71194-11	<1	0.5
EC71194-12	1	0.5
EC71194-13	0	1
EC71194-14	1	1
EC71194-15	1	1
EC71194-16	1	1
EC71194-17	1	1
EC71194-18	3	1-2

Lines EC71194-16 and -17 were used for further heat shock tests and experimental optimisation since they exhibited mCherry signal and no GFP signal before heat shock and had single copy numbers. All data presented in this thesis was collected using line 16.

6.3.2.3 Optimising the heat shock protocol

Heat shocking at 45 °C for between 6 - 8 minutes gave a good spread of GFP induced sectors on the bladder. Less time and the frequency of bladders containing sectors was very low. Any higher and bladders were more likely to have too many sectors so that it was hard to tell if an area of GFP signal was a single sector or was comprised of multiple sectors.

Some individual plants of the selected lines showed large patches of GFP expression before heat shock while others did not. It was not clear whether this was because recombination had occurred accidentally through heat shock or another unknown mechanism in culture. To minimise this effect in my experiments, plants were regularly screened for GFP/ RFP and sub-divided frequently. In each experiment, only plants which did not show GFP signal

before heat shock were used. Control tissue (from the same plant) which was not heat shocked was observed in parallel in each experiment. If there was GFP expression in the control sample, heat shocked tissue from the same parent plant was discarded.

6.4 Heat shock of the inducible transgenic line

Growing tips of the heat shock inducible line, containing a range of bladder sizes, were collected at approximately 2-3 cm in length. The growing tips were placed in six well plates, each well containing 5 ml MS media and 4-6 growing tips. Plates were sealed and floated in a 45 °C water bath for 6-8 minutes. Heat shocked tissue was left to grow at 25 °C for 2 or 4 days before imaging using confocal microscopy (Leica SP5 II confocal) with standard settings for GFP, mCherry and bright–field imaging. Bladders were imaged from the side to allow for staging and to capture visible sectors. Bladders which had sectors close to the midvein or under the mouth were rotated under the coverslip or cut to allow for imaging at multiple angles. Sectors with fainter GFP signal in surrounding cells were discarded from analysis.

6.5 Quadrifid gland polarity analysis

Bladders were incubated overnight in 10 ml water with two drops of 2.5 % w/v Toluidine blue. And were then directly embedded in agarose and scanned in water using OPT as in (Lee *et al.*, 2006) but with no BABB clearing or fixation (as this resulted in a loss of stain).

Quadrifid glands were then analysed in VolViewer software freely available at http://cmpdartsvr3.cmp.uea.ac.uk/wiki/BanghamLab/index.php/VolViewer#Description with the aid of a Matlab function written by Jake Newman. The tip of each quadrifid arm was selected using the Measuring Editor tool, adding vertices to each tip (V1-V4) (Figure 6.4). To do this, clipping planes were used to enable a close view of each quadrifid gland. Vertices were always added with V1 and V2 as a pair along the long axis of the gland and V3 and V4 being a pair on the opposite long axis (defined by a wider angle between the arms in this axis) (Figure 6.4, A). The Matlab function then compares the distance between V1 and V3 (d1) and the distance between V2 and V4 (d2) (Figure 6.4, B, orange and blue lines). A line is added through the centre of each of the pairs of these points and an arrowhead is assigned to the end of the quadrifid with the greatest distance. In the example in Figure 6.4, d2 > d1 and so the arrowhead is positioned at the d2 end (Figure 6.4, C, red line and arrowhead). This eliminates any bias of polarity assignment. The initial orientation of the quadrifid gland is chosen by eye (based on the obtuse angles between opposite arms). This orientation is very clear by eye and so carries much less bias.
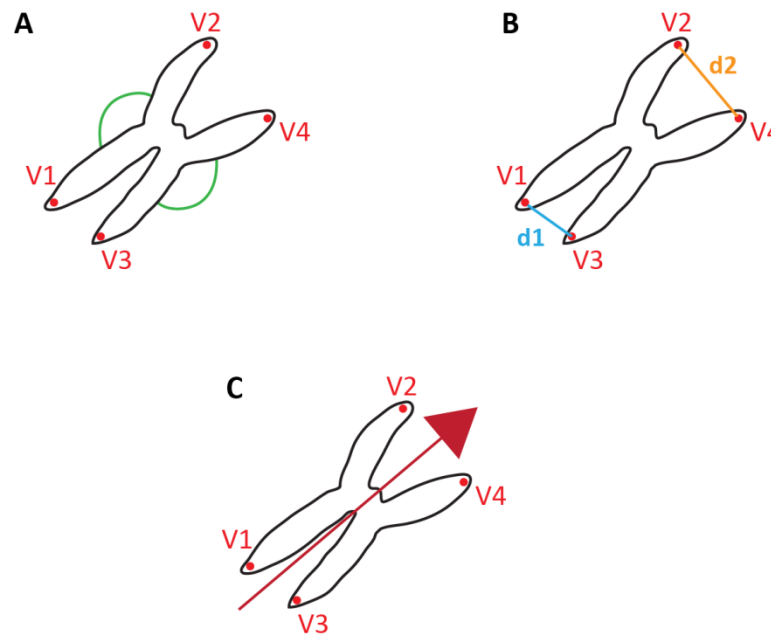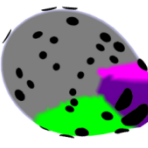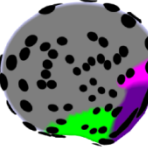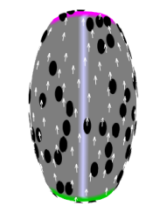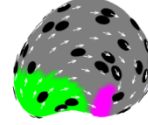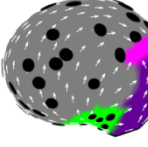
Figure 6.4: Automated assignment of direction in quadrifid gland analysis. (A) The orientation of the quadrifid gland was first determined by eye based on two opposite obtuse angles between quadrifid arms (green angles). Vertices are then marked in pairs (V1 and V2 on one side and V3 and V4 on the other). (B) The distance between V1 and V3 (d1) and between V2 and V4 (d2) are compared. (C) A central line is placed in the middle of the vertices and an arrowhead is added to the end greatest distance between vertices. In this example d2 > d1. Comparisons between vertices and addition of the arrow head and centre line is performed automatically using a Matlab function written by Jake Newman.

6.6 Computational modelling

All models were produced using the Growing Polarised Tissue (GPT) Framework (Kennaway *et al.*, 2011) within software called GFtbox which is available as a MATLAB application from http://cmpdartsvr3.cmp.uea.ac.uk/wiki/BanghamLab/index.php/Software.

General methods and parameters are given below and relate to models described in chapter 2. Table 6-2 gives an overview of the models presented in chapter 2 by number for reference. Throughout this section, models will be referred to by the numbers indicated here. These are the same numbers used to describe the models in chapter 2.

Table 6-2: Model number reference table. Model number is provided along with a description of the specified growth patterns associated with the model and an image of the final canvas shape generated (viewed from the side).

Model number	Description/ specified growth pattern	Final model shape (side view)
1	Isotropic growth across the canvas, no CHIN region.	
2	Isotropic growth across the canvas, CHIN region where areal growth rate is promoted.	
3	Isotropic growth in the main body of the canvas, anisotropic growth at CHIN.	
4	Anisotropic growth across the canvas, polarity field from base to top.	
5	Anisotropic growth across the canvas, polarity from stalk to mouth.	
6	Anisotropic growth across the canvas, increased areal growth rate and anisotropy at CHIN.	
7	Gradient of anisotropy from the MIDVEIN, increased areal growth rate and anisotropy at CHIN.	

6.6.1 The canvas

All bladder models used the same starting canvas which was a 'caplet' (flattened capsule) shape (Figure 6.5). The start shape was based on the default capsule shape found in GFtbox and was set up in such a way that the height of the bladder was parallel to the y axis, the depth of the bladder was parallel to the x axis, and the width of the bladder was parallel to the z axis. The initial canvas was wider than it was tall, and taller than it was deep, with the following dimensions; 55 μm x 68 μm x 84 μm. The canvas started with 2528 total finite elements. The canvas was hollow and the thickness was set to 20 μm with the 'direct' option selected. The mesh editor settings were altered after the thickness of the canvas was set to obtain the correct dimensions of the canvas. These settings are shown in Figure 6.5.

A

B Front **C** Side

y = 68 μm

z = 84 μm

x = 55 μm

D Front section **E** Side section

20 μm

20 μm
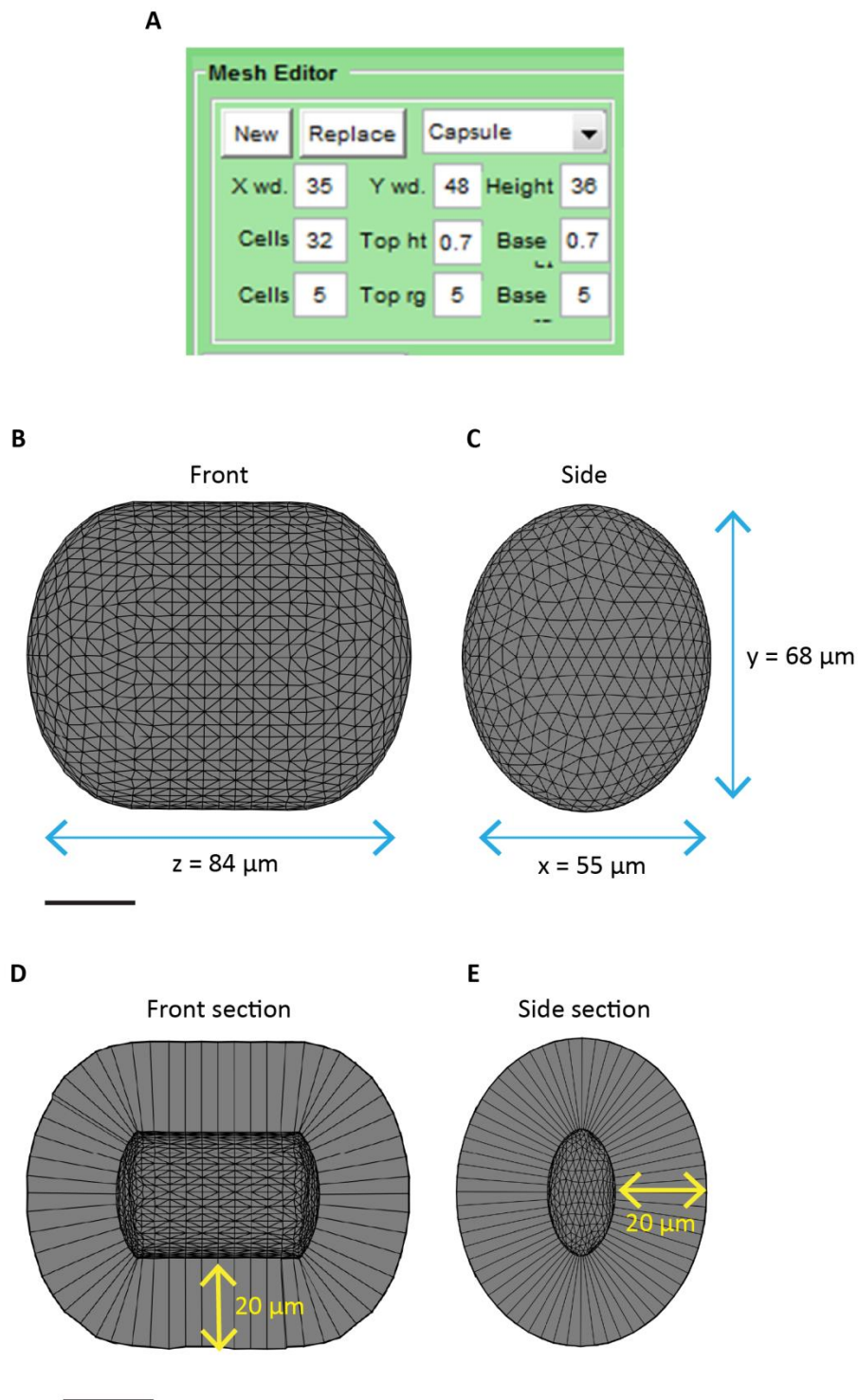
Figure 6.5: Canvas start shape for bladder models. Canvas measurements were based on an 82 μm stage bladder. (A) Mesh editor settings used to generate the 'caplet' start shape based on the default 'capsule' shape. Parameters were set to the values shown to give rise to a start shape which was 84 μm wide in the z axis, 55 μm deep in the x axis, and 68 μm high in the y axis (B-C) where (B) is the canvas viewed from the front, and (C) is the canvas viewed from the side. (D-E) Canvas viewed in front section (D) and side section (E). The thickness of the canvas was set to 20 μm with the 'direct' option selected. The mesh was refined so that the start shape consisted of 2528 finite elements.

6.6.2 Regulatory networks

At the start of each simulation, three regulatory networks are set up; a polariser regulatory network (PRN), a gene regulatory network (GRN), and a growth regulatory network (KRN).

PRN

The PRN controls the activity of + organisers and − organisers which generate polarity information in a graded fashion across the canvas. Polarity points away from + organisers and towards − organisers. Propagation of this polarity is implemented through a signalling factor termed POLARISER (POL) which is produced and degraded at organisers. The production and degradation of POL is regulated by the PRN. A background rate of production and degradation of POL can also be present throughout the canvas.

GRN

A GRN controls the activity of regional factors described below. Each identity or signalling factor had a production rate, diffusion rate, and decay rate.

KRN

The KRN controls the influence of identity and signalling factors on specified growth rates parallel (K_{par}) and perpendicular (K_{per}) to local polarity. Growth rates in K_{par} and K_{per} can be promoted at a given factor using the function *pro*:

$$Pro(k, X) = 1 + KX$$

Growth rates can be inhibited at a given factor using the function *inh*:

$$Inh(k, X) = 1/ (1 + kX)$$

Where 'X' is the factor and 'k' is the coefficient of promotion or inhibition of that factor.

The KRN can also specify the growth rate in thickness (K_{nor}). Growth rates on each surface of the canvas (a and b) may also be specified.

6.6.3 Simulation details

The models each run for a total 30 simulation steps where each step represents 10 hours. The model starts at -100 hours and runs to time 200 hours. At each iteration (simulation step), calculations are made which combine the regulatory and mechanical systems in the following order (Kennaway *et al.*, 2011):

1.) Calculate values and distribution of factors (calculated from their specified interactions designed in the GRN/PRN).

2.) Calculate the extent of factor diffusion (as designed in the GRN/PRN).

3.) Calculate the growth tensor field (specified by the KRN).

4.) Calculate the resulting displacement of each finite element vertex to obtain the computed growth field.

5.) Calculate the region of identity factor expression in the new volume after growth from the displaced field. This involves the concentrations of diffusible factors to be diluted in proportion to the amount of growth, and where regions of immobile factors enlarge, new volumes inherit the factor.

Stresses are discarded after each time-step in all models presented in this work. This is assumed to correspond to plant growth where new material is incorporated into a wall depending on the amount of resultant growth that has occurred, the original properties of the wall will be restored and the stresses will be relaxed (and therefore do not accumulate) (Green *et al.*, 2010).

6.6.4 Factors

Regional factors were added to models by specifying values at each vertex of the finite elements. Factors were used to set up polarity, specify regional growth rates and generate visual plots on the canvas. Identity factors ($i_{FACTORNAME}$) have a fixed value, while signalling

factors ($\mathbf{s}_{FACTORNAME}$) propagate through the canvas over time. Gradients of signalling factors may be fixed at defined realtime points. Visual factors ($\mathbf{v}_{FACTORNAME}$) have a fixed value but do not have any effect on growth in the canvas. It is assumed that factor levels do not dilute with growth. Table 6-3 gives an overview of all factors used in the bladder models along with their position on the canvas, their value, and their relevance in each model. Table 6-4 summarises the final parameters for the diffusible factors used in the models presented along with the applicable model numbers.

Table 6-3: Factors used in the *Utricularia gibba* bladder models. The position of each factor is described along with the x, y, and z coordinates associated with values at each vertex of the finite elements. Factors shaded in green contribute to make the factor referred to as STALK in chapter 2. Factors highlighted in bright green are those factors used as plus organisers in the setup of polarity. Factors highlighted in bright pink are those factors used as minus organisers in the setup of polarity.

Factor	Position	x (:, 1)	y (:, 2)	z (:, 3)	Present in models:	Value
$i_{MIDVEIN}$	Midvein	n/a	n/a	> -4 & < 4	1, 2, 3, 7	1
$s_{MIDVEIN}$	Produced at $i_{MIDVEIN}$ and diffuses across the canvas.	n/a	n/a	n/a	1, 2, 3, 7	0-1
v_{MID}	Midvein	n/a	n/a	> -3 & < 3	All	1
$i_{CENTSTALK}$	At the centre of the stalk intersect.	> 12	< -15	> -12 & < 12	1, 2, 3, 5, 6, 7	1
$s_{CENTSTALK}$	Produced and diffuses from $i_{CENTSTALK}$	n/a	n/a	n/a	1, 2, 3, 5, 6, 7	0-1
i_{STALK}	Generated where the value of $s_{CENTSTALK}$ > 0.2	n/a	n/a	n/a	1, 2, 3, 5, 6, 7	1
i_{MOUTH}	In the mouth region, equivalent to the mouth opening of the bladder.	> -10 & < -5	< -10	> -25 & < 25	1, 2, 3, 5, 6, 7	1
i_{CHIN}	In a band between $i_{NEWSTALK}$ and $i_{MOUTH.}$	> -5 & < 2	< 2	> -23 & < 23	2, 3, 6, 7	1
$POLARISER$	Produced at $i_{CENTSTALK}$ and degraded at i_{MOUTH}	n/a	n/a	n/a	3, 4, 5, 6, 7	0-1
i_{BASE}	At the base of the canvas	> -5 & <5	< -15	> -20 & <20	4	1
i_{TOP}	At the top of the canvas	> -5 & < 5	> -15	> -20 & <20	4	1

Table 6-4: Summary of parameters for the diffusible factors in the *U. gibba* bladder models. Parameters associated with $_{POLARISER}$ are shown in blue. Parameters associated with $s_{CENTSTALK}$ are shown in green. Parameters associated with $s_{MIDVEIN}$ are shown in red.

Parameter	Description	Value	Units	Relevant models
D_{POL}	Diffusion rate of $_{POLARISER}$	100	mm^2 h^{-1}	3, 4, 5, 6, 7
μ_{POL}	Decay rate of $_{POLARISER}$	0.001	h^{-1}	3, 4, 5, 6, 7
b_{POL}	Maximum $_{POLARISER}$ level	1		3, 4, 5, 6, 7
$D_{CENTSTALK}$	Diffusion rate of $s_{CENTSTALK}$	10	mm^2 h^{-1}	1, 2, 3, 5, 6, 7
$\mu_{CENTSTALK}$	Decay rate of $s_{CENTSTALK}$	0.001	h^{-1}	1, 2, 3, 5, 6, 7
$b_{CENTSTALK}$	Maximum $s_{CENTSTALK}$ level	1		1, 2, 3, 5, 6, 7
$D_{MIDVEIN}$	Diffusion rate of $s_{MIDVEIN}$	5	mm^2 h^{-1}	1, 2, 3, 7
$\mu_{MIDVEIN}$	Decay rate of $s_{MIDVEIN}$	0.001	h^{-1}	1, 2, 3, 7
$b_{MIDVEIN}$	Maximum $s_{MIDVEIN}$ level	1		1, 2, 3, 7

6.6.4.1 Setting up the STALK region

The STALK region of the canvas was set up to represent the stalk intersect of the bladder. To set this region up as a smooth curved region rather than a rectangle, a diffusible factor was used ($s_{CENTSTALK}$) which diffuses from $i_{CENTSTALK}$ which is present in a small region in the centre of the final STALK region. i_{STALK} is then positioned at realtime >= -1 in the region where $s_{CENTSTALK}$ is greater than 0.2.

6.6.4.2 Polarity parameters

In models 3, 4, 5, 6, and 7, a polarity field was used to allow anisotropic growth to be specified in at i_{CHIN} (model 3), or across the whole canvas (models 4, 5, 6, and 7). The parameters for POLARISER were a diffusion rate of 100 and a background degradation rate of 0.001. POLARISER was produced at plus organisers with a value of 1 and degraded at minus organisers to a value of 0. The resulting gradient of POLARISER was fixed:

m.morphogenclamp(((i_{PLUS} ==1)|(i_{MINUS} ==1)), polariser_i) = 1;

6.6.5 Growth parameters

Growth parameters for each model are given below. For a reference of each model by number see Table 6-2 above. Specified growth on the a and b surfaces of the canvas was equal in all cases. Multiple values of K_{par} and K_{per} are given where different parameters were explored.

Model 1 growth parameters

$K_{par} = 0.10 .pro(\textbf{s}_{MIDVEIN})$

$K_{per} = 0.10 .pro(\textbf{s}_{MIDVEIN})$

$K_{nor} = 0.01$

Model 2 growth parameters

$K_{par} = 0.10 .pro(\textbf{s}_{MIDVEIN}, \textbf{i}_{CHIN})$

$K_{per} = 0.10 .pro(\textbf{s}_{MIDVEIN}, \textbf{i}_{CHIN})$

$K_{nor} = 0.01$

Model 3 growth parameters

$K_{par} = 0.10 .pro(\textbf{s}_{MIDVEIN}, \textbf{i}_{CHIN}) .inh(\textbf{s}_{CENTSTALK})$

$K_{per} = 0.10 .pro(\textbf{s}_{MIDVEIN}, \textbf{i}_{CHIN}) .inh(\textbf{s}_{CENTSTALK})$

$K_{nor} = 0.01$

Model 4 growth parameters

K_{par} = either 0.16, 0.17, 0.18

K_{per} = either 0.14, 0.13, 0.12

K_{nor} = 0.01

Model 5 growth parameters

K_{par} = either 0.16, 0.17, 0.18, 0.19, 0.20

K_{per} = either 0.14, 0.13, 0.12, 0.11, 0.10

K_{nor} = 0.01

Model 6 growth parameters

K_{par} = 0.17 .pro(i_{CHIN}) .inh($s_{CENTSTALK}$)

K_{per} = 0.13 .pro(i_{CHIN}) .inh($s_{CENTSTALK}$)

K_{nor} = 0.01

Model 7 growth parameters

K_{par} = 0.13 .pro(i_{CHIN}, $s_{MIDVEIN}$) .inh($s_{CENTSTALK}$)

K_{per} = 0.13 .pro(i_{CHIN}, $s_{MIDVEIN}$) .inh($s_{CENTSTALK}$)

K_{nor} = 0.01

6.7 Tissue fixation and preparation for *in situ* hybridisation and immunolocalisations on sliced tissue

U. gibba circinnate apexes were collected into either 4 % paraformaldehyde (PBS pH 7, Water, 16 % paraformaldehyde solution (Electron Microscopy Sciences, 15710) with 4 % DMSO and 0.1 % Triton X) or FAA (50 % ethanol, 5 % acetic acid, 3.7 % formaldehyde (sigma Aldrich, F8775), water, 1 % DMSO and 0.1 % Triton X), for *in situ* hybridisation or immunolocalisation respectively. Tissue in solution was placed under vacuum pressure for three rounds of 10 minutes, or until the samples dropped to the bottom of the solution. Samples were incubated at 4 ° C overnight.

Samples were removed from the paraformaldehyde and washed with cold 0.85 % saline for 30 minutes at 4 °C, followed by a cold 50 % ethanol/0.85 % saline solution for 3 hours at 4 °C. Samples were then transferred to 70 % ethanol/0.85 % saline for a further 3 hours. The solution was then replaced with fresh 70 % ethanol/0.85 % saline and samples were stored at 4 °C. The FAA solution was removed and replaced with cold 50 % ethanol for 3 hours at 4 °C, followed by cold 70 % ethanol for 3 hours at 4 °C. The solution was then exchanged for fresh 70 % ethanol and samples were stored at 4 °C.

All samples were transferred to mesh biopsy cassettes (Sakura) in 70 % ethanol. These were placed in a Tissue-Tek® vacuum infiltration processor (VIP) machine (Sakura) with the following programme:

Table 6-5 Tissue- Tek® VIP machine program for paraffin embedded samples

Step	Solution	Time (hours)	Temperature (°C)	Pressure/Vacuum cycle (P/V)	Agitation
1	70 % EtOH	4	35	on	on
2	80 % EtOH	4	35	on	on
3	90 % EtOH	4	35	on	on
4	100 % EtOH	4	35	on	on
5	100 % EtOH	4	35	on	on
6	100 % EtOH	4	35	on	on
7	Xylene	4	35	on	on
8	Xylene	4	35	on	on
9	Xylene	4	35	on	on
10	Paraffin Wax	4	60	on	on
11	Paraffin Wax	4	60	on	on
12	Paraffin Wax	4	60	on	on
13	Paraffin Wax	4	60	on	on

Samples were then embedded in blocks of paraffin wax using the Tissue-Tek® TEC (Sakura) embedding machine and kept at 4 °C until sectioning.

Samples embedded in wax blocks were sliced in 8 µm thick ribbons using a microtome (Reichet-Jung 2030). Tissue slices were mounted on Polysine™ microscope slides (VWR, 631-0107) with water. Slides were left to dry on a 37 °C hotplate for 48 hours to ensure the slices were dry and flat on the slide. Once dried, slides were stored covered at 4 °C.

6.8 Immunolocalisations

6.8.1 Antibodies

Details on the homology of UgPIN1a, b, and c, and the design of the UgPIN1 antibodies can be found in chapter 3. *UgPIN1* sequences were confirmed using PCR before probe design.

Four different primary antibodies were used in this work. The HISTONE 3 (H3) (D1H2) XP Rabbit commercial antibody was used as a positive control for the immunolocalisation

protocol (New England Biolabs, 4499S). Antibodies against UgPIN1a, b, and c were designed during this project and produced by Cambridge Research Biochemicals, raised in rabbit. Table 6-6 gives information on each of the UgPIN1 antibodies.

Table 6-6: UgPIN1 antibodies. The target sequence for each antibody is shown along with the amino acid numbers in the UgPIN1a, b, or c protein sequence.

Antibody	Target sequence	Amino acids
UgPIN1a	VSPIRTRSPEGEE	284-296
UgPIN1b	RQSSYANPGLDEEN	278-291
UgPIN1c	SPRHSNFGNSGFDEEN	276-291

Standard anti-rabbit Alexa 647, and anti-rabbit Alexa 594 conjugated secondary antibodies were used (from Life Technologies).

6.8.2 Immunolocalisation protocol

The protocol published in Conti & Bradley, (2007) was followed with the following modifications. Tissue was fixed in either formaldehyde acetic acid solution (FAA), or with a pre-fixation in methanol acetic acid followed by FAA fixation. Details of these fixatives are given above (6.7). All blocking solutions contained 3 % BSA (Bovine Serum Albumen, Sigma Aldrich) instead of 5 % milk. Blocking was carried out in 3 % BSA in PBS with 0.3 % triton X for 3 hours. Antibodies were diluted with 3 % BSA in PBS. The dilutions used for each antibody are shown in Table 6-7. In some cases a range of dilutions was explored so the table gives the dilution which produced the clearest signal in each case. All secondary antibodies were used in a 1:200 dilution. The primary antibody was incubated overnight at 4 °C. The secondary antibody was incubated for 3 hours at room temperature. The final BCIP/NBT staining steps in the Conti & Bradley, 2007 protocol were not followed, since the

secondary antibodies used were fluorescently tagged. Slides were additionally stained with 0.1 % calcofluor (Fluorescent Brightener 28, Sigma, F3543) for 20 minutes.

Table 6-7: Dilutions used for each primary antibody. Antibodies were diluted in 3 % BSA in PBS.

Antibody	Dilution
UgPIN1a	1:500
UgPIN1b	1:500
UgPIN1c	1:200
H3	1:200

6.8.3 Imaging

Samples were mounted with 1 % DABCO (1,4-diazabicyclo[2.2.2]octane) (Sigma, D2, 780-2) and imaged on the Leica SP5 II confocal microscope. Standard settings for Alexa 594 and Alexa 647 fluorophore detection were used. Calcofluor was detected using the 405 nm laser with PMT detectors set to 400 nm-480 nm. Sequential scans were used to image calcofluor signal and Alexa 594/ 647 alternately in one scan.

6.9 *In situ* hybridisations

6.9.1 Probe design

Homologues of my genes of interest were found in the published *U. gibba* genome or transcriptome using phylogenetic analysis. Protein sequences were identified using a local BLAST of sequences from *Arabidopsis*. A range of published genomes were searched to make the phylogenetic analysis more robust. Sequences with good homology to candidate genes were converted to FASTA format and aligned using CLUSTALW (Thompson *et al.*, 1994). A neighbour joining tree was then generated based on the protein sequences using Mega5 (Tamura *et al.*, 2011). The JTT model was used with pairwise deletion and 500 bootstrap replications. The correct target sequence was then identified based on this

phylogeny. Primers were designed to amplify approximately 500 bp unique fragments of the target gene in varying positions.

6.9.2 Probe production

Fragments of the target gene were amplified from purified *Utricularia gibba* cDNA by PCR using primers described in Table 0-1. The fragment was then cloned into the pCR®4-TOPO® vector using the Invitrogen Life Technologies TOPO®TA Cloning® kit according to the manufacturers guidelines. The ligation product was transformed into One Shot® TOP10 chemically competent *E. coli* (Invitrogen, C4040) using heat-shock as described in the manufacturer's protocol. Cells were plated on selective LB media containing 50 µg/ml kanamycin. Colonies were analysed using colony PCR. Chosen colonies were streaked onto new LB plates containing 50 µg/ml kanamycin. Single colonies were then selected and grown overnight in LB/ kanamycin broth, shaking at 30 °C. Plasmids were extracted from 6 ml of culture using the QIAprep Spin Miniprep kit (Qiagen, 27106) as per the manufacturer's instructions. Clones were validated via sequencing.

RNA probes were produced using the protocol published in Coen *et al.* (1990) with the following modifications. The T7 or T3 transcription start site and the probe coding sequence were amplified using PCR. The PCR product was then purified using the QIAGEN QIAquick PCR purification kit (QIAGEN, 28106) as per the manufacturer's instructions. Approximately 1 µg of purified PCR product was digoxigenin-UTP labelled using T7 or T3 RNA polymerase. Probes were washed in 70 % EtOH and resuspended in 50 µl RNAse free H_2O and then stored at -20 °C.

6.9.3 *In situ* hybridisation protocol

The protocol used was based on that published in Coen *et al.* (1990) and is as follows. Slides were placed in metal racks and rehydrated in the following solutions in order:

Solution	Time
Histoclear	10 min
Histoclear	10 min
100 % EtOH	1 min
100 % EtOH	1 min
95 % EtOH	1 min
85 % EtOH, 0.85 % saline	1 min
50 % EtOH, 0.85 % saline	1 min
30 % EtOH, 0.85 % saline	1 min
0.85 % saline	2 min
PBS	2 min

Sections were then treated with pronase or proteinase K to digest the cell wall proteins. The enzymatic reaction was stopped using glycine and sections were then dehydrated through an ethanol series as follows:

Solution	Time
Pronase (0.125 mg/ml in pronase buffer: 50 mM Tris-HCl pH 7.5, 5mM EDTA) Or	12 min
Proteinase K (10 µg/ml in pronase buffer)	15 min
Glycine (0.2 % in PBS)	3 min
PBS	2 min
4 % Paraformaldehyde in PBS	10 min
PBS	2 min
PBS	2 min
Acetic anhydride (5 µl/ ml in 0.1 M triethanolamine, pH 8)	10 min
PBS	2 min
0.85 % saline	2 min

30 % EtOH, 0.85 % saline	1 min
50 % EtOH, 0.85 % saline	1 min
85 % EtOH, 0.85 % saline	1 min
95 % EtOH	1 min
100 % EtOH	1 min
100 % EtOH	Kept at 4 $^{\circ}$C for up to 2 hours

Probes were prepared for hybridisation of each slide with a mix of 2 µl probe, 2 µl RNAse free H$_2$O, and 4 µl deionised formamide per slide. Probes were denatured at 80 $^{\circ}$C for 2 minutes and then kept on ice. The probe solution was then made up to 100 µl/ slide by adding the appropriate volume of hybridisation buffer (hybridisation salts with a final concentration of 300 mM NaCl, 10 mM Tris-HCl pH 6.8, 10 mM NaPO$_4$, 5 mM EDTA added to 50 % deionised formamide, 25 % dextran sulphate, 1.25 % tRNA, 2.5 % Denhardt's salts (Thermo Scientific, 1 % BSA, 1 % Ficoll, 1 % polyvinylpyrrolidone in water), 8.75 % H$_2$O).

Ethanol was allowed to evaporate from the slides and 100 µl hybridisation buffer/probe solution was added to each slide. Slides were then covered with a plastic coverslip (Sigma, Hybri-slips H0 784-1006A) avoiding bubbles. Slides were placed in a humid chamber lined with paper soaked in 2X SSC, 50 % formamide, the chamber was sealed and incubated at 50 $^{\circ}$C overnight for hybridisation.

Slides were soaked in 2x SSC until the coverslips could be removed easily. Slides were washed in 0.2x SSC at 55 $^{\circ}$C for 35 minutes. Slides were then washed twice more in pre heated 0.2x SSC at 55 $^{\circ}$C for 25 minutes. Incubation in the following solutions was then carried out to digest any excess probe that was not hybridised:

Solution	Time	Temperature
NTE buffer (500 mM NaCl, 10 mM Tris-HCl pH 7.5, 1 mM EDTA)	5 min	37 $^{\circ}$C
NTE buffer	5 min	37 $^{\circ}$C
NTE buffer with 20 µg/ ml RNase A	30 min	37 $^{\circ}$C
NTE buffer	5 min	RT
NTE buffer	5 min	RT

Antibody staining was carried out through the following solutions at room temperature:

Solution	Time
Buffer 1 (100 mM Tris-HCl pH 7.5, 150 M NaCl)	5 min
Buffer 2 (0.5 % blocking reagent (Roche) in buffer 1)	1 hour
Buffer 3 (1 % BSA, 0.3 % Triton X-100 in buffer 1)	30 min
Buffer 4 (Anti-digoxigenin-AP (Sigma, A7906) 1:3000 in buffer 3)	90 min
Buffer 1 with 0.3 % Triton X-100	4 x 25 min
Buffer 1	5 min
Buffer 5 (buffer 5a (100 mM Tris-HCl pH 9.5, 100 M MaCl) + buffer 5b (0.5 M MgCl$_2$)	5 min
Buffer 6 (buffer 5 + 2 µl/ ml NBT and 1.5 µl/ ml BCIP)	Overnight in dark or until signal develops

To stop development of the signal further, slides were washed with water and then kept in water at 4 °C. Slides were imaged using a Leica DM6000 microscope.

6.10 Whole genome sequencing of *U. gibba*

6.10.1 DNA extraction for sequencing

DNA was extracted as described in 6.2.4.2. The concentration of DNA was assessed by Qubit analysis following the manufacturer's protocol for the Qubit dsDNA BR Assay Kit. The DNA concentrations obtained are shown below.

Sample	Concentration (ng/µl)
BA	89.8
CPS	84.8
Morley	57.0
Bonn	51.0
Czech	87.8

6.10.2 Sequencing

Sequencing was carried out by TGAC, Norwich. An Illumina barcode DNA TruSeq library was generated and then sequencing was performed on the Illumina HiSeq 2000 platform using 100 bp paired end reads. The service included data QC, basecalling and formatting.

6.11 EMS mutagenesis of *U. gibba* tissue

6.11.1 Treating plant tissue with EMS

U. gibba (BA line) plants were grown up in sterile culture for EMS treatment. Plant material was treated with; 0.01 %, 0.05 %, 0.010 %, 0.15 %, 0.2 %, or 0.25 % EMS (ethyl methanesulphonate) diluted in 0.02 % tween 20 (Sigma-Aldrich, P9416). Treatment was carried out on propagated *U. gibba* tissue which was divided into pieces that were just

small enough to fill approximately half of a 50 ml falcon tube. Tissue was incubated with the EMS solution overnight in 50 ml falcon tubes which were continually agitated for 18 hours. Treated tissue was then passed through a series of 10 x 20 minute washes in 40 ml 0.02 % tween. Finally, tissue was washed twice in water. Plants were initially placed in the growth room under standard growth conditions and incubated overnight in water. Tissue was then divided further into separate M1 plants in the glasshouse (each division consisted of approximately 5 cm of stolon.

Appendices

Appendix 1: Oligonucleotides used in this project

Table 0-1 describes all oligonucleotides used in this project.

Table 0-1: Oligonucleotides used in this work.

Gene and Scaffold ref	Description/use	5'-3' primer
UgFIL1 (Scf00036:146709..148057)	Used to amplify a *UgFIL1* probe for *in situ* hybridization. Designed from published genome sequence.	Forward: GCTCTGCTATGTTCATTGCCAAGTC Reverse: CACATCATCTCCCTCCTGCTGG
UgH4 (Scf00351:42131..42439)	Used to amplify a *UgH4* probe for *in situ* hybridization. Designed from published genome sequence.	Forward: GTCTGGACGAGGCAAGGGC Reverse: CTAACCGCCGAATCCGTACAGAG
UgPIN1a (Ug_TG_Scf59)	Sequencing primers used to confirm *UgPIN1a* sequence in the BA line genome before antibody design.	**Primer set 1** Forward: GAGACTCTGTTGCCGCATTG Reverse: CTGACTTACAGCCCCAGGAC **Primer set 2** Forward: GTACCACGTGATGACGGC Reverse: GGTAGTAGAGGAGTGCCACG **Reverse to start** CCGATTCCATTTCCACTTC **Forward to stop** GAAGAAAGGGAAAGGGATGC **Reverse to stop** GTGAACATGTAATCCATTCATCATCC
UgPIN1b (Ug_TG_Scf234)	Sequencing primers used to confirm *UgPIN1b* sequence in the BA line genome	**Primer set 1** Forward: CTTGCAGTCCCATCTCCTTG Reverse: CATTGCTTCACCTGCTGTG

	before antibody design.	**Primer set 2** Forward: GATCTCCCTCACAGACCTCTATC Reverse: TGATTGGGAGGGCTATCAAC **Reverse to start** GATGTCGCCCGCAGTATCTG **Forward to stop** CCCACAAGTGTGATGACGAG **Middle forward** ACTTGTCATGGGCATTCCTC **Middle reverse** CCAATGAGGCTGGAGTATGTG
UgPIN1c (Ug_TG_Scf6792)	Sequencing primers used to confirm *UgPIN1c* sequence in the BA line genome before antibody design.	**Primer set 1** Forward: GAGACTTGCAGGTTTCAACAAAG Reverse: CGAATCCTTGTCTGAATGAACC **Primer set 2** Forward: TGTCCTTGCAGCTGTTGTTC Reverse: CCCCAACAGGATGTAGTACACG **Reverse to start** TCAACATTCTCGCACCTCTG **Forward to stop** CTTACTCCAGCCTCATTGGC **Middle forward** GGACAAGATGGGAAGATCCA **Middle 2 forward** TTTCGGGAACTCAGGATTTG **Middle reverse** GAAGATCTTTGCCGACATCATG

Appendix 2: Confirmed *UgPIN1* sequences

The sequences below were confirmed by PCR using primers described in Table 0-1.

UgPIN1a

ATGATCTCTCTTACAGACCTCTACCATGTCCTTGCAGCTGTTGTTCCTCTCTACGTTGCAATGATTCTG
GCGTATGGATCAGTGAAATGGTGGAAAATTTTCACCCCTGATCAGTGCTCTGGGATCAACAGATTC
GTTGCACTTTTCGCTGTTCCTCTTCTCTCGTTCCACTTCATCTCCACCAATAATCCCTACGCCATGAAC
TACCGCTTCATCGCCGCCGACACTCTGCAGAAACTCATTGTTCTTGCTGTTCTGGCTGTCTGGTCCAG
ACTCAGCTCCAGGGGATCCCTTGAATGGTCCATTACACTGTTTTCTTTGTCAACTCTCCCAAACACGC
TGGTTATGGGCATCCCTCTTCTGAAAGGGATGTACGGAGACTTCTCTGGGAGTTTAATGGTCCAGA
TTGTTGTGCTTCAATGCATCATCTGGTACACCTTGATGCTCTTCTTGTTTGAGTACAGAGGTGCGAG
AATGTTGATCGCTGAGCAGTTTCCAGACACTGCTGGTGACATTATTTCGTTCAGAGTTGATTCGGAC
ATCATTTCTTTGGATGGTAAGGAGCCATTACAGACGGAAGCGGAAGTTGGACAAGATGGGAAGAT
CCATGTTACTGTCCGAAAATCAGCGAGTTCCAGGTCTGAAATCTTTTCAAGAAGATCACACGGTCCG
AACTCCGGTCTCTCTTTGACACCCCGTCCCTCCAATTTGACAAACGCAGAGATTTACTCTCTTCAGTC
ATCCCGAAATCCAACACCAAGGGGCTCCAGTTTCAATCACACCGATTTCTATTCAATGGTGAACGGT
AAAAGCGCCTTGAGTGCTAGTCCAAGGCATTCCAATTTCGGGAACTCAGGATTTGATGAGGAGAAT
CAAGTACGAGTCACCGGCGGTTATGGTGGTTCTGCAGCCGCCGGAATATTCTCTCCGGCTACCGGA
CCTAATGCGAAAAAGAAGGCAAACGGGCATGATGTCGGCAAAGATCTTCACATGTTTGTGTGGAG
TTCAAGTGCTTCTCCAGTTTCTGAAGGAGGGATCCATGTTTTCAGAGGAGGCGAATATGGAAATGA
GGTCACCGTGGGACCTCATCCTAAAGAGTATGATGATTTCGGGAGAGAAGAGTTCAGCTTCGGGA
ACAAACATGGACCAAATGGCCCAGATGCATCTAAACTCGCATCGAGCTCCACGGCGGAGCTCCGAA
CCAAGAGCGGTGGCGATGCCAAGGCGAATGCCATGCCGCCCACCAGTGTGATGACGAGGCTGATT
CTGATCATGGTTTGGAGAAAGCTGATCAGAAATCCCAACACTTACTCCAGCCTCATTGGCCTCACCT
GGTCTCTAGTCTCGTTCAGATGGCACATTGAGATGCCTGTTATCGTTGCCAAATCGATTTCCATCCTG
TCTGATGCCGGCCTCGGGATGGCGATGTTTAGTCTCGGTTTGTTCATGGCGCTTCAGCCAAAGATCA
TCGCCTGCGGGAAGTCGATCGCCGCCTTCTCGATGGCCATCCGGTTCCTCACAGGCCCGGCCGTCA
TGGCTGCAGCATCGATAGCCGTTGGACTGAGAGGCGTGCTGCTGCACGTCGCAATAGTACAGGCC
GCTCTTCCACAAGGAATCGTCCCCTTCGTCTTCGCAAAGGAGTACAACGTTCACCCCGACATTCTCA
GCACCGGGGTGATCTTCGGAATGCTGATAGCGCTCCCCATAACTCTCGTGTACTACATCCTGTTGGG
GTTGTGA

UgPIN1b

ATGATCTCCCTCACAGACCTCTATCATGTCCTGACCGCGGTGGTTCCTCTCTACGTGGCCATGATTTT
GGCTTATGGCTCGGTGAAGTGGTGGAAGATCTTCACCCCGGACCAATGCTCCGGCATCAACAGATT
TGTCGCCCTTTTTGCCGTTCCATTGCTCTCTTTCCATTTCATCTCCACCAACAATCCCTATGCCATGAA
CTACCGTTTCATAGCCGCTGACACTTTGCAGAAACTCATAGTTCTTGCAGTTCTCGCAGTCTGGTCCA
GGCTGAGCTCCAGAGGTTCCCTTGAATGGTCCATTACTCTCTTTTCCTTGTCCACACTACCGAATACA

CTTGTCATGGGCATTCCTCTCTTGAAAGGGATGTACGGCGACTTCTCCGGGAGTTTAATGGTCCAGA
TCGTTGTTCTCCAGTGCATCATTTGGTACACATTGATGCTGTTCTTGTTTGAGTTCAGAGGAGCGAG
GATGCTTATTGCTGAACAGTTCCCAGATACTGCGGGCGACATCATTTCTTTCAGGGTTGATTCAGAC
ATTATTTCGTTGGACGGGAGAGATCCTCTCCAGACGGAGACGGAGGTTGGTGAAGACGGCAAGAT
TCACGTGACTGTTCGAAAATCAGCCAGCTCGAGATCTGAAATCTTCTCAAGAGGATCGCATGGTCC
GAAGTCGGGACTCTCCTTGACTCCTCGTCCGTCTAACTTAACCAATGCCGAGATTTACTCACTTCAAT
CGTCGAGAAATCCTACCCCAAGAGGCTCCAGTTTCAACCACGCTGATTTCTATACGATGGTGAACG
GGAAAAACGCTATCAGTCACAGTCCAAGGCAATCGAGTTATGCGAACCCTGGATTAGATGAGGAG
AACCAATCACGAGTTAACACTAACGCAGGAGGTGGATATGCTCCTCCTGCAACCACCGGAATATTC
TCTCCTGCTGCGAAAAAGAAGGCGAACGGTCACGAAAGCAGCAAGGATCTTCACATGTTTGTCTGG
AGTTCGAGTGCTTCTCCAGTTTCCGAACGAGGGATTCATGTCTTCCGAGGAGGTGAATATGGGAAT
GAGCTTAACTTGGGACCTCATCCTAAAGAATACGATGAGTTTGGGCGAGATGACTTCAGCTTCGGG
AACAAACAAGGTGCTGATCCACTGAAGCTGGGATCAAGCTCCAAGGCTGAGCTCCGGACAAAAAG
TGGAAACGACGACACGAAACCGGCGGCCATGCCACCCACAAGTGTGATGACGAGACTGATTCTGA
TCATGGTGTGGCGGAAGCTGATCAGAAATCCCAACACATACTCCAGCCTCATTGGCCTCACTTGGTC
CTTGGTCTCATTCAGGTGGCATCTTGAGATGCCGGCCATAGTTGCAAAATCTATTTCCATCCTGTCA
GACGCTGGTCTAGGAATGGCTATGTTTAGTCTTGGACTGTTCATGGCGCTGCAGCCTAAAATCATTG
CCTGTGGTAACTCCGTGGCGGCCTTTTCCATGGCGGTTCGCTTTCTTACTGGACCGGCAGTCATGGC
TGCAGCTTCCGTTGCGGTAGGACTAAGGGGCGTGCTCCTACGTGTGGCGATTGTGCAGGCTGCTCT
TCCGCAAGGAATAGTCCCTTTCGTGTTTGCCAAGGAGTACAATGTGCATCCCAAGATCCTTAGCACT
GGGGTGATATTTGGAATGTTGATAGCCCTCCCAATCACCCTAGTGTATTACATCCTACTGGGGCTCT
GA

UgPIN1c

ATGATAAGTTCCAAGGACTTGTACCACGTGATGACGGCGATGGTGCCGTTGTACGTTGCCATGGCA
TTGGCCTACGCCTCCGTCAAGTGGTGGAAGATATTCACGCCGGAACAGTGCTCCGGCATCAACCGC
TACGTGGCCCTCTTCGCCGTCCCTCTTCTCTCCTTCCATTTCATTGCTACAAACGATCCCTACGCCATG
AATTTCAGGTTCATAGTAGCCGATACGCTGCAGAAGCTGATGATTCTCGGGATCCTCTCTCTGTACG
TGAGGTTCAGCAGACAGGGCTCCTTCGAACAGACCATTACCTTCTTCTCCCTCTCCACCCTCCCCAAC
ACCCTGGTGATTGGGATCCCGTTGCTGGAAGGGATGTACGGCGAGTTTTGCGGAGGACTGATGGT
GCAGATCGTGGTGCTGCAGTGCATCATCTGGTACACTCTGATGCTCTTCATGTTCGAGTATAGGGCC
GCCATGATTCTCATATCCGATCGCTTCCCGGAGACGGCTGATTCGATCATTTCGATCCGCGTGGAAT
CCGACGTGGTATCTCTCCAGCAGGAGCAGCCGCTGGAGACGGTGGTGGGAGATGTCAGAGAAGA
CGGCAAGTTCCACGTCACGGTGAGGCTATCGAATGCCGAGATCTACTCCGTTCAATCCTCGATGAA
TCCGACGCCCCGGGGATCCAGCGCGCGATCCACGTCTCCAATAAGAAAATTAGATGCGGGTGGCC
CTGAAGCGGATCCAGTCTTCCTCGGGAGCTCAACGGGCTCCTCTGTTTCCGGCAGAGTTTTCGTTGC
CAGCCCAACACATCATCATCATCATCATCATCATGCGAAGGAAATCAGATTTGTTTCTCCCATCAGA
ACAAGATCCCCGGAAGGGGAGGAAATGGAAGTGGAAATGGAATCGGAAAAGAGTCCAACAGATG
ATTTGGCGGAGAAGAAAGGGAAAGGGATGCCTCCCACCAAAGTAATGACGAGGCTGTTACTCGTT
ATGGTTTGGCGGAAGCTTATAAGGAATCCCAACACTTACTCCAGCTTCATTGGCCTCTTCTGGTCTCT
CATCTCCTTCAGGTGGGAGGTGGAGATGCCTCCCATAGTCGCCAAGTCCATCTCCATCTTATCTGAT
ACGGGACTCGGCATGGCCATGTTCAGCCTCGGGCTGTTCATGGCGTTGCAACCGAGGATGATAGC

ATGCGGGAAGACGATGGTGACCTTTGCCATCGCCGTGAGATTCATCATCGGCCCCGCCTTCATGGC
CATCGCTTCTCTCATCTCCGGCATCGGCGGCGTCCTCCTAAGTGTCGCAATCGTTCAGGTTATATTCG
GGATGCTGCTAGCGGTACCCGTGGCGCTCCTCTACTACCTCGTCCTGGGGCTGTAAGTCAGTGTAT
GTAA

Appendix 3: *In situ* hybridisation probe sequences

The probes below were amplified using primers described in Table 0-1.

UgFIL1 probe sequence

GCTCTGCTATGTTCATTGCCAAGTCTGTGACACCGTTCTCGCGGTGAGTGTTCCCTGCACGAGCTTG
TTCAAGACGGTGACTGTGAGATGCGGCCACTGCACCACTCTCCTCTCTGTGTATATGAGGACGCCG
CTTCATCCCGCCGGCGCCCACCAACTTCTTCAGGGCCACCCCTTCTTCTCCCCTCAGAACCTCTTGGA
GGAGATCAGGAATTCTCCAGCAAATGTGTTCATCAACCAGCCCAACCCCAACCCTGTCCGCAGCGG
CAGCATCGATGAGCTCCCCAAGCCACCTGCTGCTAATCGACCGCCGGAGAAAAGACAGCGAGTCCC
CTCCGCCTACAACCGCTTCATCAAGGACGAGATCCAACGCATCAAGGCTGGAAACCCTGATATCAG
TCACAGGGAGGCCTTCAGTGCAGCTGCCAAAAACTGGGCCCACTTTCCGCACATCCACTTCGGTCTC
ATGCCCGACCAGCCGGTGAAGAAGACGAATGTGTGCCAGCAGGAGGGAGATGATGTG

UgH4 probe sequence

GTCTGGACGAGGCAAGGGCGGAAAGGGACTTGGAAAGGGCGGTGCAAAGCGTCACCGGAAGGT
TCTACGGGACAACATCCAGGGGATCACGAAGCCTGCAATACGCCGTCTGGCCAGAAGAGGCGGCG
TCAAACGTATTTCTGGCCTGATCTACGAGGAAACCCGCGGAGTTCTCAAGATTTTCTTGGAGAATGT
CATACGCGATGCCGTCACCTACACCGAGCACGCGCGGAGGAAGACGGTTACCGCCATGGACGTCG
TTTACGCTCTGAAAAGACAAGGCCGAACTCTGTACGGATTCGGCGGTTAG

References

Abley, K., De Reuille, P., Strutt, D., Bangham, A., Prusinkiewicz, P., Marée, A., Grieneisen, V., & Coen, E. (2013). An intracellular partitioning-based framework for tissue cell polarity in plants and animals. *Development*, 140(10), 2061–74.

Abley, K., Sauret-Güeto, S., Marée, A., & Coen, E. (2016). Formation of polarity convergences underlying shoot outgrowths, *Elife*, 5:e18165.

Abremski, K., & Hoess, R. (1984). Bacteriophage P1 Site-specific Recombination purification and properties of the cre recombinase protein. *The Journal of Biological Chemistry*, 259(3), 1509–1514.

Adler, P. N. (2002). Planar signaling and morphogenesis in *Drosophila*. *Developmental Cell*, 2(5), 525–535.

Alonso, J. M., Stepanova, A. N., Leisse, T. J., Kim, C. J., Chen, H., Shinn, P., Stevenson, D. K., Zimmerman, J., Barajas, P., Cheuk, R., Gadrinab, C., Heller, C., Jeske, A., Koesema, E., Meyers, C. C., Parker, H., Prednis, L., Ansari, Y., Choy, N., Deen, H., Geralt, M., Hazari, N., Hom, E., Karnes, M., Mulholland, C., Ndubaku, R., Schmidt, I., Guzman, P., Aguilar-Henonin, L., Schmid, M., Weigel, D., Carter, D. E., Marchand, T., Risseeuw, E., Brogden, D., Zeko, A., Crosby, W. L., Berry, C. C., & Ecker, J. R. (2003). Genome-wide insertional mutagenesis of *Arabidopsis thaliana*. *Science*, 301(5633), 653–7.

Arber, A. (1941). On the morphology of the pitcher-Leaves in *Heliamphora*, *Sarracenia*, *Darlingtonia*, *Cephalotus*, and *Nepenthes*. *Annals of Botany*, 5(20), 563–578.

Barbier De Reuille, P., Bohn-Courseau, I., Ljung, K., Morin, H., Carraro, N., Godin, C., & Traas, J. (2006). Computer simulations reveal properties of the cell–cell signaling network at the shoot apex in *Arabidopsis*. *PNAS*, 103(5), 1627–1632.

Baskin, C., & Baskin, J. (1998). Seeds: ecology, biogeography, and, evolution of dormancy and germination. *Academic Press*.

Baskin, T. I. (2001). On the alignment of cellulose microfibrils by cortical microtubules: a review and a model. *Protoplasma*, 215, 150–171.

References

Bell, D. T., Rokich, D. P., McChesney, C. J., & Plummer, J. A. (1995). Effects of temperature, light and gibberellic acid on the germination of seeds of 43 species native to Western Australia. *Journal of Vegetation Science*, 6(6), 797–806.

Bennett, M., Leitch, I., Price, J., & Johnston, S. (2003). Comparisons with *Caenorhabditis* (100 Mb) and *Drosophila* (175 Mb) using flow cytometry show genome size in *Arabidopsis* to be 157 Mb and thus 25 % Larger than the Arabidopsis Genome Initiative Estimate of 125 Mb. *Annals of Botany*, 91(5), 547–557.

Bilsborough, G., Runions, A., Barkoulas, M., Jenkins, H., Hasson, A., Galinha, C., Laufs, P., Hay, A., Prusinkiewicz, P., & Tsiantis, M. (2011). Model for the regulation of *Arabidopsis thaliana* leaf margin development. *PNAS*, 108(8), 3424–3429.

Blilou, I., Xu, J., Wildwater, M., Willemsen, V., Paponov, I., Friml, J., Heidstra, R., Aida, M., Palme, K., & Scheres, B. (2005). The PIN auxin efflux facilitator network controls growth and patterning in *Arabidopsis* roots. *Nature*, 433, 39–44.

Bosch, M., Cheung, A., & Hepler, P. (2005). Pectin methylesterase, a regulator of pollen tube Growth. *Plant Physiology*, 138(3), 1334–1346.

Boudaoud, A. (2010). An introduction to the mechanics of morphogenesis for plant biologists. *Trends in Plant Science*, 15(6), 353–360.

Bouyer, D., Kirik, V., & Hülskamp, M. (2001). Cell polarity in *Arabidopsis* trichomes. *Seminars in Cell & Developmental Biology*, 12(5), 353–356.

Bratcher, C., Dole, J., & Cole, J. (1993). Stratification improves seed germination of five native wildflower species. *Horticultural Science*, 28(9), 899–901.

Brunoud, G., Wells, D. M., Oliva, M., Larrieu, A., Mirabet, V., Burrow, A. H., Beeckman, T., Kepinski, S., Traas, J., Bennett, M. J., & Vernoux, T. (2012). A novel sensor to map auxin response and distribution at high spatio-temporal resolution. *Nature*, 482(7383), 103–6.

Byrne, M. (2012). Making leaves. *Current Opinion in Plant Biology*, 15, 24–30.

Cheng, Y., Dai, X., & Zhao, Y. (2006). Auxin biosynthesis by the YUCCA flavin monooxygenases controls the formation of floral organs and vascular tissues in *Arabidopsis*. *Genes & Development*, 20, 1790-1799.

Cheng, Y., Dai, X., & Zhao, Y. (2007). Auxin synthesized by the YUCCA flavin monooxygenases is essential for embryogenesis and leaf formation in *Arabidopsis*. *The Plant cell*, 19(8), 2430–9.

Chormanski, T., & Richards, H. (2012). An architectural model for the bladderwort *Utricularia gibba* (Lentibulariaceae). *Journal of the Torrey Botanical Society*, 139(2), 137–148.

Cieslak, M., Runions, A., & Prusinkiewicz, P. (2015). Auxin-driven patterning with unidirectional fluxes. *Journal of experimental botany*, 66(16), 5083–102.

Coen, E., & Rebocho, A. (2016). Resolving conflicts: modeling genetic control of plant morphogenesis. *Developmental Cell*, in press.

Coen, E., Rolland-Lagan, A.-G., Matthews, M., Bangham, J. A., & Prusinkiewicz, P. (2004). The genetics of geometry. *PNAS*, 101(14), 4728–4735.

Coen, E., Romero, J., Doyle, S., Elliott, R., Murphy, G., & Carpenter, R. (1990). *FLORICAULA*: a homeotic gene required for flower development in *Antirrhinum majus*. Cell, 63(6), 1311–22.

Colbert, T., Till, B. J., Tompa, R., Reynolds, S., Steine, M. N., Yeung, A. T., McCallum, C. M., Comai, L., & Henikoff, S. (2001). High-throughput screening for induced point mutations. *Plant Physiology*, 126(2), 480–484.

Conte, V., Muñoz, J. J., & Miodownik, M. (2008). A 3D finite element model of ventral furrow invagination in the *Drosophila melanogaster* embryo. *Journal of the Mechanical Behavior of Biomedical Materials*, 1(2), 188–198.

Conti, L., & Bradley, D. (2007). TERMINAL FLOWER1 is a mobile signal controlling *Arabidopsis* architecture. *The Plant cell*, 19(3), 767–78.

Cosgrove, D. J. (2005). Growth of the plant cell wall. *Nature Reviews: Molecular Cell Biology*, 6(11), 850–861.

Cosgrove, D. J., Li, L. C., Cho, H.-T., Hoffmann-Benning, S., Moore, R. C., & Blecker, D. (2002). The growing world of expansins. *Plant and Cell Physiology*, 43(12), 1436–1444.

References

Dong, J., MacAlister, C., & Bergmann, D. (2009). BASL controls asymmetric cell division in *Arabidopsis*. *Cell*, 137(7), 1320–1330.

Dupuy, L., Mackenzie, J., & Haseloff, J. (2010). Coordination of plant cell division and expansion in a simple morphogenetic system. *PNAS*, 107(6), 2711–2716.

Eghobor, S., Umar, A., Munir, G., Abubakar, A., & Collins, O. (2015). Comparative study of *Moringa oleifera* seed germination enhancement using gibberellic acid in varying concentrations. *International Journal of Applied Research*, 1(13), 79–80.

Eldridge, T. (2014). An intergrative analysis of fruit shape in *Capsella rubella* and *Arabidopsis thaliana*. PhD thesis manuscript.

Eldridge, T., Langowski, L., Stacey, N., Jantzen, F., Moubayidin, L., Sicard, A., Southam, P., Kennaway, R., Lenhard, M., Coen, A., & Ostergaard, L. (2016). Fruit shape diversity in the Brassicaceae is generated by varying patterns of anisotropy. *Development*, 143, 3394–3406.

Ellison, A. M., & Gotelli, N. J. (2008). Energetics and the evolution of carnivorous plants-Darwin's "most wonderful plants in the world." *Journal of Experimental Botany*, 60(1), 19–42.

Engler, C., Youles, M., Gruetzner, R., Ehnert, T.-M., Werner, S., Jones, J. D. G., Patron, N. J., & Marillonnet, S. (2014). A Golden Gate modular cloning toolbox for plants. *ACS Synthetic Biology*, 3(11), 839–843.

Eran, S., Marder, M., & Swinney, H. L. (2004). Leaves, flowers and garbage bags: making waves. *American Scientist*, 92, 254–261.

Farquharson, M., Harvie, R., & McNicol, A. M. (1990). Detection of messenger RNA using a digoxigenin end labelled oligodeoxynucleotide probe. *Journal of Clinical Pathology*, 43(5), 424–428.

Federici, F., Dupuy, L., Laplaze, L., Heisler, M., & Haseloff, J. (2012). Integrated genetic and computation methods for *in planta* cytometry. *Nature Methods*, 9(5), 483–485.

Fischer, U., Ikeda, Y., Ljung, K., Serralbo, O., Singh, M., Heidstra, R., Palme, K., Scheres, B., & Grebe, M. (2006). Vectorial information for *Arabidopsis* planar polarity is mediated by combined AUX1, EIN2, and GNOM activity. *Current Biology*, 16, 2143-2149.

Franck, D. (1975). Early histogenesis of the adult leaves of *Darlingtonia californica* (Sarraceniaceae) and its bearing on the nature of epiascidiate foliar appendages. *American Journal of Botany*, 62(2), 116.

Franck, D. (1976). The morphological interpretation of epiascidiate leaves. *The Botanical Review*, 42(3), 345-387.

Fukushima, K., Fujita, H., Yamaguchi, T., Kawaguchi, M., Tsukaya, H., & Hasebe. (2015). Oriented cell division shapes carnivorous pitcher leaves of *Sarracenia purpurea*. *Nature Communications*, 6: 6450.

Fukushima, K., & Hasebe, M. (2014). Adaxial-abaxial polarity: The developmental basis of leaf shape diversity. *Genesis*, 52(1), 1–18.

Gallois, J-l, Woodward, C, Venugopala Reddy, G, Sablowski, R. (2002). Combined SHOOT MERISTEMLESS and WUSCHEL trigger ectopic organogenesis in *Arabidopsis*. *Development*, 129, 3207–3217.

Gleissberg, S., Groot, E. P., Schmalz, M., Eichert, M., Kölsch, A., & Hutter, S. (2005). Developmental events leading to peltate leaf structure in *Tropaeolum majus* (Tropaeolaceae) are associated with expression domain changes of a *YABBY* gene. *Development Genes & Evolution*, 215(6), 313–319.

Grebe, M. (2004). Ups and downs of tissue and planar polarity in plants. *Bioessays*, 26, 719-729.

Green, A., Kennaway, R., Hanna, A., Bangham, A., & Coen, E. (2010). Genetic control of organ shape and tissue polarity. *PLoS Biology*, 8(11), e1000537.

Green, P. B. (1965). Pathways of cellular morphogenesis: a diversity in *Nitella*. *The Journal of Cell Biology*, 27(2), 343–363.

Greene, E. A., Codomo, C. A., Taylor, N. E., Henikoff, J. G., Till, B. J., Reynolds, S. H., Enns, L. C., Burtner, C., Johnson, J. E., Odden, A. R., Comai, L., & Henikoff, S. (2003). Spectrum of chemically induced mutations from a large-scale reverse-genetic screen in *Arabidopsis*. *Genetics*, 164(2), 731–40.

References

Greilhuber, J., Borsch, T., Müller, K., Worberg, A., Porembski, S., & Barthlott, W. (2006). Smallest angiosperm genomes found in Lentibulariaceae, with chromosomes of bacterial size. *Plant Biology*, 8(6), 770–777.

Groot, S. P. C., & Karssen, C. M. (1987). Gibberellins regulate seed germination in tomato by endosperm weakening: a study with gibberellin-deficient mutants. *Planta*, 171(4), 525–531.

Hamant, O., Heisler, M. G., Jönsson, H., Krupinski, P., Uyttewaal, M., Bokov, P., Corson, F., Sahlin, P., Boudaoud, A., Meyerowitz, E. M., Couder, Y., & Traas, J. (2008). Developmental patterning by mechanical signals in *Arabidopsis*. *Science*, 322, 1650–5.

Harumoto, T., Ito, M., Shimada, Y., Kobayashi, T. J., Ueda, H. R., Lu, B., & Uemura, T. (2010). Atypical cadherins dachsous and fat control dynamics of noncentrosomal microtubules in planar cell polarity. *Developmental Cell*, 19(3), 389–401.

Heath, I. B. (1974). A unified hypothesis for the role of membrane bound enzyme complexes and microtubules in plant cell wall synthesis. *Journal of Theoretical Biology*, 48(2), 445–449.

Heisler, M. G., Hamant, O., Krupinski, P., Uyttewaal, M., Ohno, C., Jönsson, H., Traas, J., & Meyerowitz, E. M. (2010). Alignment between PIN1 polarity and microtubule orientation in the shoot apical meristem reveals a tight coupling between morphogenesis and auxin transport. *PLoS Biology*, 8(10), e1000516.

Heisler, M. G., Ohno, C., Das, P., Sieber, P., Reddy, G. V., Long, J. A., & Meyerowitz, E. M. (2005). Patterns of auxin transport and gene expression during primordium development revealed by live imaging of the *Arabidopsis* inflorescence meristem. *Current Biology*, 15(21), 1899–1911.

Hervieux, N., Dumond, M., Sapala, A., Smith, R. S., Boudaoud, A., Hamant, O., Routier-Kierzkowska, A.-L., Kierzkowski, D., & Roeder, A. H. K. (2016). A mechanical feedback restricts sepal growth and shape in *Arabidopsis*. *Current Biology*, 26, 1019-1028.

Hoess, R. H., Ziese, M., & Sternberg, N. (1982). P1 site-specific recombination: Nucleotide sequence of the recombining sites. *Biochemistry*, 79, 3398–3402.

Ibarra-Laclette, E., Albert, V. A., Pérez-Torres, C. A., Zamudio-Hernández, F., de Ortega-Estrada, M. J., Herrera-Estrella, A., & Herrera-Estrella, L. (2011). Transcriptomics and molecular evolutionary rate analysis of the bladderwort (*Utricularia*), a carnivorous plant with a minimal genome. *BMC Plant Biology*, 11: 101.

Ibarra-Laclette, E., Lyons, E., Hernández-Guzmán, G., Pérez-Torres, C. A., Carretero-Paulet, L., Chang, T.-H., Lan, T., Welch, A. J., Juárez, M. J. A., Simpson, J., Fernández-Cortés, A., Arteaga-Vázquez, M., Góngora-Castillo, E., Acevedo-Hernández, G., Schuster, S. C., Himmelbauer, H., Minoche, A. E., Xu, S., Lynch, M., Oropeza-Aburto, A., Cervantes-Pérez, S. A., de Jesús Ortega-Estrada, M., Cervantes-Luevano, J. I., Michael, T. P., Mockler, T., Bryant, D., Herrera-Estrella, A., Albert, V. A., & Herrera-Estrella, L. (2013). Architecture and evolution of a minute plant genome. *Nature*, 498(7452), 94–98.

Jansen, J. G., Vrieling, H., van Teijlingen, C. M., Mohn, G. R., Tates, A. D., & van Zeeland, A. A. (1995). Marked differences in the role of O6-alkylguanine in hprt mutagenesis in T-lymphocytes of rats exposed in vivo to ethylmethanesulfonate, N-(2-hydroxyethyl)-N-nitrosourea, or N-ethyl-N-nitrosourea. *Cancer research*, 55(9), 1875–82.

Jönsson, H., Heisler, M., Shapiro, B., Meyerowitz, E., & Mjolsness, E. (2006). An auxin-driven polarized transport model for phyllotaxis. *PNAS*, 103(5), 1633–1638.

Keith, D. A. (1997). Combined effects of heat shock, smoke and darkness on germination of *Epacris stuartii* Stapf., an endangered fire-prone Australian shrub. *Oecologia*, 112(3), 340–344.

Kennaway, R., Coen, E., Green, A., & Bangham, A. (2011). Generation of diverse biological forms through combinatorial interactions between tissue polarity and growth. *PLoS Computational Biology*, 7(6), e1002071.

Khan, A. A. (1968). Inhibition of gibberellic acid-induced germination by abscisic acid and reversal by cytokinins. *Plant Physiol*, 43, 1463–1465.

Kim, G. T., Tsukaya, H., Saito, Y., & Uchimiya, H. (1999). Changes in the shapes of leaves and flowers upon overexpression of cytochrome P450 in *Arabidopsis*. *PNAS*, 96(16), 9433–9437.

References

Koornneef, M. (2002). Classical mutagenesis in higher plants. *Molecular Plant Biology*, 1, 1–11.

Křeček, P., Skůpa, P., Libus, J., Naramoto, S., Tejos, R., Friml, J., & Zažímalová, E. (2009). The PIN-FORMED (PIN) protein family of auxin transporters. *Genome Biology*, 10(12), 249.

Kuchen, E. E., Fox, S., Reuille, P. B. de, Kennaway, R., Bensmihen, S., Avondo, J., Calder, G. M., Southam, P., Robinson, S., Bangham, A., & Coen, E. (2012). Generation of leaf shape through early patterns of growth and tissue polarity. *Science*, 335, 1092–1097.

Kurowska, M., Daszkowska-Golec, A., Gruszka, D., Marzec, M., Szurman, M., Szarejko, I., & Maluszynski, M. (2011). TILLING - a shortcut in functional genomics. *Journal of Applied Genetics*, 52(4), 371–390.

Lawrence, P. (1966). Gradients in the insect segment: the orientation of hairs in the milkweed bug *Oncopeltus fasciatus*. *Journal of Experimental Biology*, 44, 607–620.

Lawrence, P., Struhl, G., & Casal, J. (2007). Planar cell polarity: one or two pathways? *Nature Reviews Genetics*, 8, 555–563.

Lee, K., Avondo, J., Morrison, H., Blot, L., Stark, M., Sharpe, J., Bangham, A., & Coen, E. (2006). Visualizing plant development and gene expression in three dimensions using optical projection tomography. *The Plant Cell*, 18(9), 2145–56.

Llorens, C., Argentina, M., Bouret, Y., Marmottant, P., & Vincent, O. (2012). A dynamical model for the *Utricularia* trap. *Journal of The Royal Society*, 9(76), 3129–3139.

Lloyd, F. (1942). The carnivorous plants. Waltham Mass.

Lockhart, J. A. (1965). An analysis of irreversible plant cell elongation. *Journal of Theoretical Biology*, 8(2), 264–275.

Marcon, L., Arqués, C. G., Torres, M. S., & Sharpe, J. (2011). A computational clonal analysis of the developing mouse limb bud. PLoS *Computational Biology*, 7(2), e1001071

Martinez, C. C., Koenig, D., Chitwood, D. H., & Sinha, N. R. (2016). A Sister of PIN1 gene in tomato (*Solanum lycopersicum*) defines organ initiation patterns by maintaining epidermal auxin flux. *Developmental Biology*, http://dx.doi.org/10.1016/j.ydbio.2016.08.011.

Matilla, A. J. (2000). Ethylene in seed formation and germination. *Seed Science Research*, 10(10), 111–126.

McCallum, C., Comai, L., Greene, E., & Henikoff, S. (2000). Targeting induced local lesions in genomes (TILLING) for plant functional genomics. *Plant Physiology*, 123(2), 439–442.

McQueen-Mason, S., Durachko, D., & Cosgrove, D. (1992). Two endogenous proteins that induce cell wall extension in plants. *The Plant Cell*, 4, 1425–1433.

Meierhofer, H. (1902). Beitrage zur Anatomie und Entwickelungsgeschichte der Utricularia-Blasen. *Flora*, 90, 84–114.

Mirabet, V., Das, P., Boudaoud, A., & Hamant, O. (2011). The role of mechanical forces in plant morphogenesis. *Annu. Rev. Plant Biol*, 62, 365–85.

Mitchison, G. J. (1980). A model for vein formation in higher plants. *Proceedings of the Royal Society of London B: Biological Sciences*, 207, 79-109.

Moreira, B., & Pausas, J. G. (2012). Tanned or burned: the role of fire in shaping physical seed dormancy. *PLoS ONE*, 7(12).

Nikolić, R., Mitić, N., Miletić, R., & Nešković, M. (2006). Effects of cytokinins on *in vitro* seed germination and early seedling morphogenesis in *Lotus corniculatus* L. *Journal of Plant Growth Regulation*, 25(3), 187–194.

O'Connor, D. L., Runions, A., Sluis, A., Bragg, J., Vogel, J. P., Prusinkiewicz, P., & Hake, S. (2014). A division in PIN-mediated auxin patterning during organ initiation in grasses. *PLoS Computational Biology*, 10(1), 21–24.

Oegema, T., & Fletcher, R. A. (1972). Factors that influence dormancy in milkweed seeds. *Canadian Journal of Botany*, 50(4), 713–718.

Olofsson, J., Sharp, K. A., Matis, M., Cho, B., Axelrod, J. D.(2014). Prickle/spiny-legs isoforms control the polarity of the apical microtubule network in planar cell polarity. *Development*, 141(14), 2866–74.

Overvoorde, P., Fukaki, H., & Beeckman, T. (2010). Auxin control of root development, *Cold Spring Harb Perspect Biol* 2010;2:a0015371–17.

References

Parry, G., Marchant, A., May, S., Swarup, R., Swarup, K., James, N., Graham, N., Allen, T., Martucci, T., Yemm, A., Napier, R., Manning, K., King, G., & Bennett, M. (2001). Quick on the uptake: Characterization of a family of plant auxin influx carriers. *Journal of Plant Growth Regulation*, 20(3), 217–225.

Péret, B., Swarup, K., Ferguson, A., Seth, M., Yang, Y., Dhondt, S., James, N., Casimiro, I., Perry, P., Syed, A., Yang, H., Reemmer, J., Venison, E., Howells, C., Perez-Amador, M. A., Yun, J., Alonso, J., Beemster, G. T. S., Laplaze, L., Murphy, A., Bennett, M. J., Nielsen, E., & Swarup, R. (2012). *AUX/LAX* genes encode a family of auxin influx transporters that perform distinct functions during *Arabidopsis* development. *The Plant Cell*, 24(7), 2874–85.

Plummer, J., & Bell, D. (1995). the effect of temperature, light and gibberellic acid (ga3) on the germination of australian everlasting daisies (Asteraceae, Tribe Inuleae). *Australian Journal of Botany*, 43(1), 93.

Popławski, N. J., Swat, M., Scott Gens, J., & Glazier, J. A. (2007). Adhesion between cells, diffusion of growth factors, and elasticity of the AER produce the paddle shape of the chick limb. *Physica A: Statistical Mechanics and its Applications*, 373, 521–532.

Poppinga, S., Weisskopf, C., Westermeier, A. S., Masselter, T., & Speck, T. (2015). Fastest predators in the plant kingdom: functional morphology and biomechanics of suction traps found in the largest genus of carnivorous plants. *AoB Plants*, 8, doi:10.1093/aobpla/plv140.

Prusinkiewicz, P., & Runions, A. (2012). Computational models of plant development and form. *New Phytologist*, 193, 549–569.

Rahman, M., Adamec, L., & Kondo, K. (2001). Chromosome numbers of *Utricularia*. *Chromosome Science*, 5, 105–108.

Rebocho, A., Southam, P., Kennaway, R., Bangham, A., & Coen, E. (2016). Generation of shape complexity through tissue conflicts. Submitted to *eLife*.

Reinhardt, D., Frenz, M., Mandel, T., & Kuhlemeier, C. (2005). Microsurgical and laser ablation analysis of leaf positioning and dorsoventral patterning in tomato. *Development*, 132, 15-26.

Reinhardt, D., Mandel, T., & Kuhlemeier, C. (2000). Auxin regulates the initiation and radial position of plant lateral organs. *The Plant Cell*, 12(4), 507–18.

Richardson, A. (2015). The role of tissue cell polarity in monocot development. PhD Thesis Manuscript.

Richardson, A., Rebocho, A., & Coen, E. (2016). Ectopic *KNOX* expression affects plant development by altering tissue cell polarity and identity. *The Plant Cell*, tpc.00284.2016.

Rutishauser, R. (2015). Evolution of unusual morphologies in Lentibulariaceae (bladderworts and allies) and Podostemaceae (river-weeds): a pictorial report at the interface of developmental biology and morphological diversification. *Annals of Botany*, 117(5), 811–832.

Rutishauser, R., & Brugger, J. (1992). Structural and developmental diversity of *Utricularia* traps. *Carnivorous Plant Newsletter*, 21, 68–74.

Saini, H., Bassi, P., & Spencer, M. (1985). Seed germination in *Chenopodium album* L: relationships between nitrate and the effects of plant hormones. *Plant Physiology*, 77(4), 940–943.

Sari, A., Morales, M., & Simon, J. (2001). Ethephon can overcome seed dormancy and improve seed germination in purple coneflower species *Echinacea angustifolia* and *E. pallida*. *Hort Technology*, 11(2), 202–205.

Sauret-Güeto, S., Schiessl, K., Bangham, A., Sablowski, R., & Coen, E. (2013). *JAGGED* controls *Arabidopsis* petal growth and shape by interacting with a divergent polarity field. *PLoS Biology*, 11(4), e1001550.

Sawa, S., Watanabe, K., Goto, K., Liu, Y. G., Shibata, D., Kanaya, E., Morita, E. H., & Okada, K. (1999). *FILAMENTOUS FLOWER*, a meristem and organ identity gene of *Arabidopsis*, encodes a protein with a zinc finger and HMG-related domains. *Genes & Development*, 13(9), 1079–88.

Scarpella, E., Marcos, D., Friml, J., & Berleth, T. (2006). Control of leaf vascular patterning by polar auxin transport. *Genes & Development*, 20(8), 1015–1027.

Shapiro, L., McAdams, H. H., & Losick, R. (2002). Generating and exploiting polarity in bacteria. *Science*, 298, 1942-1946.

References

Sieburth, L. E., Drews, G. N., Meyerowitz, E. M. (1998). Non-autonomy of *AGAMOUS* function in flower development: use of a Cre/*loxP* method for mosaic analysis in *Arabidopsis*. *Development*, 125(21), 4303–12.

Siegfried, K. R., Eshed, Y., Baum, S. F., Otsuga, D., Drews, G. N., & Bowman, J. L. (1999). Members of the *YABBY* gene family specify abaxial cell fate in *Arabidopsis*. *Development*, 126(18), 4117–28.

Skordilis, A., & Thanos, C. A. (1995). Seed stratification and germination strategy in the Mediterranean pines *Pinus brutia* and *P. halepensis*. *Seed Science Research*, 5(3), 151–160.

Smith, R., Guyomarc'h, Mandel, T., Reinhardt, D., Kuhlemeier, C., & Prusinkiewicz, P. (2006). A plausible model of phyllotaxis. *PNAS*, 103(5), 1301–1306.

Solly, J. E. (2015). Regulation of thallus shape in the liverwort *Marchantia polymorpha*. PhD Thesis Manuscript.

Stephenson, P., Baker, D., Girin, T., Perez, A., Amoah, S., King, G. J., Østergaard, L., Østergaard, L. (2010). A rich TILLING resource for studying gene function in *Brassica rapa*. *BMC Plant Biology*, 10: 62.

Sternberg, N., & Hamilton, D. (1981). Bacteriophage P1 site-specific recombination. *Journal of Molecular Biology*, 150(4), 467–486.

Stewart, E. R., & Freebairn, H. T. (1969). Ethylene, seed germination, and epinasty. *Plant Physiology*, 44(7), 955–958.

Stoma, S., Lucas, M., Chopard, J., Schaedel, M., Trass, J., & Godin, C. (2008). Flux-based transport enhancement as a plausible unifying mechanism for auxin transport in meristem development. *PLoS Computational Biology*, 4(10), e1000207.

Strutt, D. I. (2001). Asymmetric localization of frizzled and the establishment of cell polarity in the *Drosophila* wing. *Molecular Cell*, 7(2), 367–375.

Strutt, D. I. (2002). The asymmetric subcellular localisation of components of the planar polarity pathway. *Seminars in Cell & Developmental Biology*, 13(3), 225–231.

Sussex, I. (1951). Experiments on the cause of dorsiventrality in leaves. *Nature*, 167(4251), 651–652.

Tamura, K., Peterson, D., Peterson, N., Stecher, G., Nei, M., & Kumar, S. (2011). MEGA5: molecular evolutionary genetics analysis using maximum likelihood, evolutionary distance, and maximum parsimony methods. *Molecular Biology And Evolution*, 28(10), 2731–9.

Taylor, P. (1994). The genus *Utricularia* : a taxonomic monograph. Royal Botanical Gardens, Kew.

Thompson, J. D., Higgins, D. G., & Gibson, T. J. (1994). CLUSTAL W: improving the sensitivity of progressive multiple sequence alignment through sequence weighting, position-specific gap penalties and weight matrix choice. *Nucleic Acids Research*, 22(22), 4673–4680.

Till, B. J., Reynolds, S. H., Greene, E. A., Codomo, C. A., Enns, L. C., Johnson, J. E., Burtner, C., Odden, A. R., Young, K., Taylor, N. E., Henikoff, J. G., Comai, L., & Henikoff, S. (2003). Large-scale discovery of induced point mutations with high-throughput TILLING. *Genome Research*, 13, 524–530.

Till, B. J., Reynolds, S. H., Weil, C., Springer, N., Burtner, C., Young, K., Bowers, E., Codomo, C. A., Enns, L. C., Odden, A. R., Greene, E. A., Comai, L., Henikoff, S. (2004). Discovery of induced point mutations in maize genes by TILLING. *BMC Plant Biology*, 4: 12.

Townsley, B., & Sinha, N. (2012). A new development: evolving concepts in leaf ontogeny. *Annual Review of Plant Biology*, 63(1), 535–562.

Trinh, L., McCutchen, D., Bonner-Fraser, M., Fraser, S., Bumm, L., & McCauley, D. (2007). Fluorescent *in situ* hybridization employing the conventional NBT/BCIP chromogenic stain. *BioTechniques*, 42(6), 756-759.

Truernit, E., Bauby, H., Dubreucq, B., Grandjean, O., Runions, J., Barthelemy, J., & Palauqui, J.-C. (2008). High-resolution whole-mount imaging of three-dimensional tissue organization and gene expression enables the study of phloem development and structure in *Arabidopsis*. *The Plant Cell*, 20(6), 1494–1503.

Tsuge, T., Tsukaya, H., & Uchimiya, H. (1996). Two independent and polarized processes of cell elongation regulate leaf blade expansion in *Arabidopsis thaliana* (L.) Heynh. *Development*, 122(5), 1589–1600.

References

Uauy, C., Paraiso, F., Colasuonno, P., Tran, R. K., Tsai, H., Berardi, S., Comai, L., Dubcovsky, J. (2009). A modified TILLING approach to detect induced mutations in tetraploid and hexaploid wheat. *BMC Plant Biology*, 9(1), 115.

Veleba, A., Bures, P., Adamec, L., Smarda, P., Lipnerova, I., & Horova, L. (2014). Genome size and genomic GC content evolution in the miniature genome-sized family Lentibulariaceae. *New Phytologist,* 203(1), 22–28.

Vincent, O., Weißkopf, C., Poppinga, S., Masselter, T., Speck, T., Joyeux, M., Quilliet, C., & Marmottant, P. (2011). Ultra-fast underwater suction traps. *Proceedings of the Royal Society B: Biological Sciences,* DOI: 10.1098/rspb.2010.2292.

Vrieling, H., Simons, J., Arwert, F., Natarajan, A., & van Zeeland, A. (1985). Mutations induced by X-rays at the HPRT locus in cultured Chinese hamster cells are mostly large deletions. *Mutation Research Letters*, 144(4), 281–286.

Waites, R., & Hudson, A. (1995). *phantastica*: a gene required for dorsoventrality of leaves in *Antirrhinum majus*. *Development*, 121, 2143–2154.

Wang, P., Cheng, T., Wu, S., Zhao, F., Wang, G., Yang, L., Lu, M., Chen, J., & Shi, J. (2014). Phylogeny and molecular evolution analysis of *PIN-FORMED 1* in Angiosperm. *PLoS ONE*, 9(2), e89289.

Wang, Y., & Nathans, J. (2007). Tissue/planar cell polarity in vertebrates: new insights and new questions. *Development*, 134(4), 647–58.

Weber, E., Engler, C., Gruetzner, R., Werner, S., & Marillonnet, S. (2011). A modular cloning system for standardized assembly of multigene constructs. *PLoS ONE*, 6(2), e16765.

Wenzel, C., Schuetz, M., Yu, Q., & Mattsson, J. (2007). Dynamics of *MONOPTEROS* and *PIN-FORMED1* expression during leaf vein pattern formation in *Arabidopsis thaliana*. *Plant Journal*, 49(3), 387–398.

Whaley, W. G., & Whaley, C. Y. (1942). A developmental analysis of inherited leaf patterns in *Tropaeolum*. *American Journal of Botany*, 29(3), 195-200.

Williamson, R. (1990). Alignment of cortical microtubules by anisotropic wall stresses. *Australian Journal of Plant Physiology*, 17(6), 601-603.

Wiśniewska, J., Xu, J., Seifertová, D., Brewer, P., Růžička, K., Blilou, I., Rouquié, D., Benková, E., Scheres, B., & Friml, J. (2006). Polar PIN localization directs auxin flow in plants. *Science*, 312, 883–883.

Wu, X., Dabi, T., & Weigel, D. (2005). Requirement of homeobox gene *STIMPY/WOX9* for *Arabidopsis* meristem growth and maintenance. *Current Biology* 15(5), 436-440.

Yamaguchi, T., Nukazuka, A., & Tsukaya, H. (2012). Leaf adaxial-abaxial polarity specification and lamina outgrowth: evolution and development. *Plant & Cell Physiology*, 53(7), 1180–94.

Yang, Y., Hammes, U. Z., Taylor, C. G., Schachtman, D. P., & Nielsen, E. (2006). High-affinity auxin transport by the AUX1 influx carrier protein. *Current Biology* 16, 123-1127.